The Connection Between Mass and Light in Galaxy Clusters

Proefschrift

ter verkrijging van
de graad van Doctor aan de Universiteit Leiden,
op gezag van Rector Magnificus prof. mr. C.J.J.M. Stolker,
volgens besluit van het College voor Promoties
te verdedigen op woensdag 7 september 2016
klokke 10:00 uur

door

Cristóbal Sifón Andalaft
geboren te Punta Arenas, Chili in 1986

Promotiecommissie

Promotor:	Prof. dr. Konrad Kuijken	
Co-Promotor:	Dr. Henk Hoekstra	
Overige leden:	Prof. dr. August Evrard	(University of Michigan)
	Prof. dr. Huub Röttgering	
	Prof. dr. Joop Schaye	
	Dr. Frank van den Bosch	(Yale Universtiy)

A Dani y Martina

Cover design: Andrés Castillo.

Front cover: Background image: Galaxy cluster MACS J0717.5+3745, with matter (blue, from weak lensing) and gas (red, from X-ray imaging) distributions overlaid. Image credit: NASA, ESA, CXC, C. Ma, H. Ebeling, and E. Barrett (University of Hawaii/IfA), et al., and STScI. Front image: Leiden Observatory, picture by Daniela Egas.

Back cover: Hubble Space Telescope image of the galaxy cluster ACT-CL J0102−4915, “El Gordo”. Image credit: NASA, ESA, J. Jee (University of California, Davis), J. Hughes (Rutgers University), F. Menanteau (Rutgers University and University of Illinois, Urbana-Champaign), C. Sifón (Leiden Observatory), R. Mandelbum (Carnegie Mellon University), L. Barrientos (Universidad Católica de Chile), and K. Ng (University of California, Davis).

Contents

1. Introduction **1**
1.1. Galaxies and their dark matter haloes 2
1.2. Galaxy clusters in a nutshell 4
1.2.1. Mass proxies and cosmological leverage 5
1.3. Mass and light in cluster galaxies 7
1.3.1. Tidal effects on cluster galaxies 7
1.4. This thesis 8

2. Strong lensing analysis of PLCK G004.5−19.5 at $z = 0.52$ **11**
2.1. Introduction 12
2.2. Observations and data analysis 12
2.2.1. SZ and X-ray data 12
2.2.2. Optical imaging 13
2.2.3. Optical spectroscopy 13
2.3. Strong lensing analysis 15
2.3.1. Strong lensing model 15
2.3.2. External constraints 17
2.4. Radio emission 18
2.5. Conclusions 22

3. Dynamical masses of galaxy clusters selected through the Sunyaev-Zel'dovich effect **25**
3.1. Introduction 26
3.2. Data and observations 28
3.2.1. The Atacama Cosmology Telescope 28
3.2.2. ACT SZ-selected clusters in the equator 28
3.2.3. Gemini/GMOS spectroscopy 29
3.2.4. SALT/RSS spectroscopy 31
3.2.5. Archival data 31
3.2.6. Comparison between redshift measurements 32
3.3. Velocity Dispersions and Dynamical Masses 32
3.3.1. Velocity dispersion measurements 32
3.3.2. Calibrating velocity dispersions with the Multidark simulation 33

3.3.3. From velocity dispersions to dynamical masses . . . 38
3.3.4. Dynamical mass estimates . . . 40
3.3.5. Comparison to SZ-derived masses . . . 42
3.3.6. Cluster substructure . . . 45
3.3.7. The impact of centring on the BCG . . . 46
3.4. Notable clusters . . . 47
3.4.1. Previously studied ACT clusters . . . 47
3.4.2. ACT-CL J0218.2−0041 . . . 48
3.4.3. ACT-CL J0326.8−0043 . . . 48
3.4.4. ACT-CL 2050.5−0055 . . . 50
3.4.5. ACT-CL J2055.4+0105 . . . 51
3.4.6. ACT-CL J2302.5+0002 . . . 52
3.5. Conclusions . . . 52
3.A. Eddington bias and selection effects . . . 53
3.B. Velocity histograms . . . 56

4. Galaxy alignments in massive clusters from ~14,000 spectroscopic members 59
4.1. Introduction . . . 60
4.2. Data . . . 61
4.2.1. Cluster sample and photometry . . . 61
4.2.2. Spectroscopic data . . . 63
4.3. Galaxy samples . . . 64
4.3.1. Spectroscopic members and dynamical masses . . . 64
4.3.2. Red sequence members . . . 66
4.3.3. Photometric redshift contamination . . . 73
4.3.4. Control samples . . . 73
4.4. Measuring intrinsic alignments . . . 74
4.4.1. Different alignment signals . . . 74
4.4.2. Shape measurements . . . 75
4.4.3. Systematic effects . . . 76
4.5. Results . . . 77
4.5.1. Satellite radial alignment . . . 78
4.5.2. Satellite-BCG alignment . . . 82
4.5.3. Satellite-satellite alignment . . . 83
4.5.4. Is there an agreement on the level of galaxy alignments in groups and clusters? . . . 84
4.6. Contamination to cosmic shear measurements . . . 85
4.6.1. Linear alignment model . . . 86
4.6.2. Halo model . . . 86
4.6.3. Impact of alignments within haloes on the power spectra . . . 87
4.7. Conclusions . . . 89

5. The masses of satellites in GAMA galaxy groups from 100 square degrees of KiDS weak lensing data 91
5.1. Introduction . . . 92
5.2. Galaxy samples . . . 94
5.2.1. Lens galaxies: satellites in the GAMA galaxy group catalogue . . . 94
5.2.2. Lensed background sources: the Kilo-Degree Survey . . . 96
5.3. Galaxy-galaxy lensing of satellite galaxies . . . 97

5.3.1. The satellite lensing signal . . . 99
5.3.2. Host group contribution . . . 100
5.3.3. Satellite contribution . . . 102
5.4. Results . . . 104
5.4.1. Fitting procedure . . . 104
5.4.2. Group masses and mass-concentration relation . . . 105
5.4.3. The masses of satellite galaxies . . . 107
5.4.4. The average subhalo mass . . . 108
5.4.5. Sensitivity to contamination in the group catalogue . . . 109
5.5. Conclusions . . . 110
5.A. Full satellite lensing correlation matrix and the contribution from sample variance . . . 110

6. The galaxy-subhalo connection in low-redshift galaxy clusters from weak gravitational lensing 113
6.1. Introduction . . . 114
6.2. Weak galaxy-galaxy lensing . . . 116
6.2.1. Statistical errors: data covariance . . . 117
6.3. Data set . . . 117
6.3.1. Cluster and lens galaxy samples . . . 117
6.3.2. Source galaxy sample . . . 120
6.4. Bias assessment and calibration through image simulations . . . 121
6.4.1. Shape measurements . . . 122
6.4.2. Obscuration and contamination by cluster members . . . 124
6.4.3. Resulting lensing signal . . . 125
6.5. Satellite galaxy-galaxy lensing model . . . 126
6.5.1. Host cluster contribution . . . 126
6.5.2. Subhalo contribution . . . 127
6.5.3. Fitting procedure . . . 128
6.6. The connection between mass and light in satellite galaxies . . . 128
6.6.1. The subhalo-to-stellar mass relation . . . 128
6.6.2. Subhalo mass segregation . . . 131
6.6.3. Host clusters . . . 135
6.7. Conclusions . . . 135
6.A. Lens-induced bias on the shape measurements . . . 137

Bibliography 139

Nederlandse Samenvatting 151

Resumen en Castellano 157

Curriculum Vitae 163

Acknowledgements 165

1 | Introduction

Our view of the Cosmos changed dramatically during the first third of the 20th century. The idea of a deterministic, stationary Universe governed by Newtonian dynamics with absolute measures of time and space had to be abandoned as Quantum Mechanics and the Special and General Theories of Relativity revolutionized our understanding of the very small, the very fast and the very large, respectively, along with our notions of space and time themselves.

It was not long until astronomical observations revolutionized our understanding of the Universe just a little more and, with that, our very own place in it. The year 1920 was host to one of the most famous astronomical discussions ever to take place. In what was termed "the Great Debate," Harlow Shapley and Heber D. Curtis discussed (among other topics) the extent of the Milky Way and its place in the Universe (Shapley & Curtis 1921; a thorough review of the debate and its context is presented by Trimble 1995). Shapley argued that the Milky Way, with a size of up to 100 kpc (with 1 kpc = 3,260 light years), encompassed the entire Universe, while Curtis argued that other "spiral nebulae" were distinct galaxies much like our own Milky Way (which, he argued, was much smaller and hosted the Sun in its very centre). The issue was settled not long after, thanks to the observation of Cepheid variable stars in the Andromeda nebula by Hubble (1925). It was already known at that time that a Cepheid's distance can be inferred by measuring the duration of its variability cycle, since they follow a tight period-luminosity relation. While Shapley was right that the Sun is not located at the centre of the Milky Way, Curtis was right about the nebulae: Hubble's observations were definitive proof that these spiral nebulae could not be part of our Galaxy, and marked the birth of *extragalactic* astronomy.

A few years later, Hubble (1929) showed that there exists a linear relation between the distance and the velocity of galaxies other than the Milky Way (now known as Hubble's law), which became the first solid evidence for an expanding Universe. He based this inference on measurements of i) the period of Cepheid stars (from which he inferred their luminosities and thereby their distances) and ii) the Doppler shift of their spectra, using spectroscopic observations made by Vesto Slipher. Detailed discussions of pre-1929 observations of receding galaxies and an expanding Universe are presented by Trimble (2012, 2013).

Then, in 1933 Zwicky showed that galaxies in galaxy clusters move faster than the sum of their masses would be able to hold gravitationally, and inferred that there must be 10 to 100 times more mass hidden from us. Decades later, Rubin et al. (1980) came to the same conclusion by studying the motions of stars within spiral galaxies. Zwicky's observations are now credited as the discovery of dark matter (e.g., Trimble 1987; Einasto 2013).

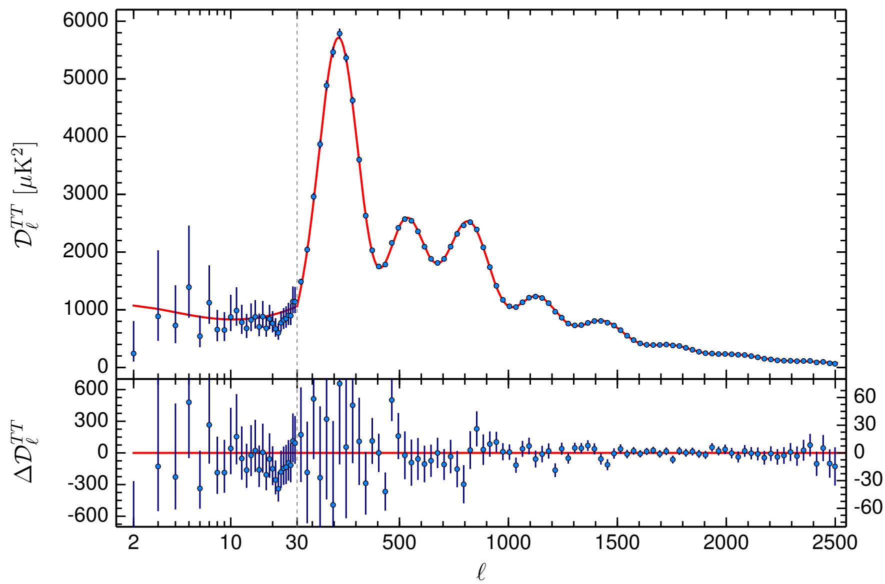

Figure 1.1: The top panel shows the cosmic microwave background temperature power spectrum measured by the *Planck* satellite (blue points with errorbars) and the best-fit ΛCDM model (red curve). The bottom panel shows the residuals when subtracting the best-fit model from the data points. The agreement, over three orders of magnitude in scale, is remarkable. Figure from Planck Collaboration (2015a).

Our modern 'Λ cold dark matter' (ΛCDM) standard model of cosmology came to be complete with four additional ingredients: primordial nucleosynthesis (the theory that the lightest chemical elements formed during the big bang; Alpher et al. 1948); the discovery of the cosmic microwave background (CMB) by Penzias & Wilson (1965), predicted by the hot big bang hypothesis (Dicke et al. 1965); the development of the inflationary model, which explains the homogeneity of the CMB with a brief period of exponential growth in the very early Universe (Guth 1981); and the discovery of the Universe's accelerated expansion (Riess et al. 1998; Perlmutter et al. 1999). We use the term 'dark energy' to refer to the cause of this accelerated expansion, whatever it may be, and is represented by the "Λ" in ΛCDM. Dark energy makes up approximately 70% of the energy density of the Universe, while dark matter amounts to about 25%. Consequently, only about 5% of the Universe corresponds to 'normal' luminous matter (Spergel et al. 2003; Planck Collaboration 2015a). The success of this model is summarized most spectacularly by measurements of the CMB temperature power spectrum, the latest and most precise of which was presented by Planck Collaboration (2015a) and is reproduced in Figure 1.1.

1.1. Galaxies and their dark matter haloes

The cosmological model introduced above predicts that structure grows hierarchically: small structures form first and then merge to give rise to larger structures. This continuous mass accretion and merging process has given rise to what we term the 'Cosmic Web', a

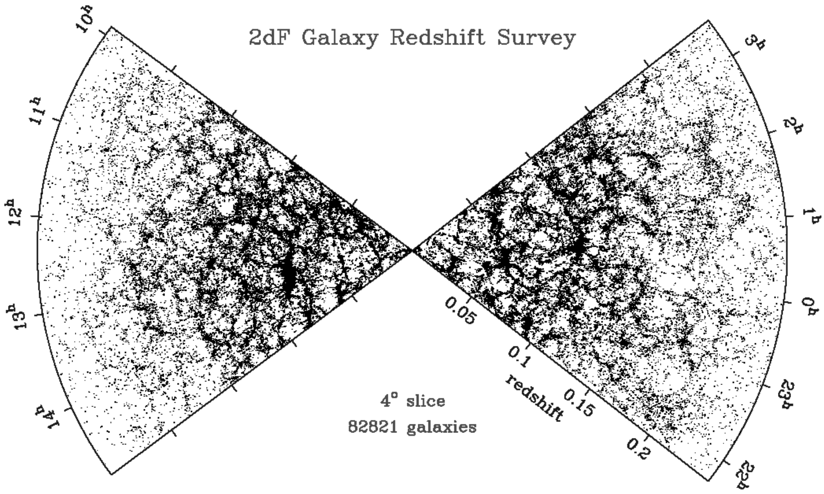

Figure 1.2: The local ($z < 0.2$) cosmic web as seen by the 2-degree Field Galaxy Redshift Survey. Each black dot is a galaxy with a spectroscopic redshift. Figure from Peacock (2002).

complicated arrangement of galaxies into 'voids', 'sheets', 'filaments' and 'knots'. Figure 1.2 shows the local ($z < 0.2$) cosmic web as seen by the 2-degree Field Galaxy Redshift Survey (Colless et al. 2001).

Numerical simulations show that dark matter traces the same cosmic web as galaxies. Although we cannot observe dark matter directly, we can measure its consequences on observable galaxies. According to the General Theory of Relativity, the local curvature of space is intimately linked to the local mass distribution, so that space is curved around mass overdensities, and more so for more massive overdensities. This local curvature of space deflects the path of light coming from galaxies located behind the overdensity in question (called *lens* hereafter), so that light that from these galaxies circumvents the lens. As a result, the apparent shapes of galaxies in the background of the lens (referred to as *sources* hereafter) are elongated preferentially along the tangent of the lens mass distribution, and the strength of this elongation is proportional to the surface mass density around the lens. If the background source is close enough to the line of sight to the centre of the lens, then this deflection of light produces multiple images of the same source; we call this effect *strong lensing*. If the source is extended (for instance, a spiral galaxy), some of these images may show up as strong lensing *arcs*. Further out, the effect is a very weak distortion of the shape of sources, and can only be measured as a statistical, average coherent distortion of the shapes of the population of background sources. This regime is referred to as *weak lensing*. Figure 1.3 illustrates the effect of gravitational lensing on a population of background sources by a galaxy cluster, where both the strong and weak lensing regimes can be observed.

Strong and weak lensing offer complementary probes of the mass distribution in galaxies and galaxy clusters, allowing us to map their mass distributions separately on small and large scales, respectively. Strong lensing gives the most detailed view of the inner regions of individual galaxies, and can constrain the initial stellar mass function in galaxies and the density profile of dark matter haloes, which is a stringent test of the ΛCDM model (for a review, see Courteau et al. 2014). Weak lensing, on the other side, reveals the average relation between stellar and total mass. For instance, Hudson et al. (2015) used weak lensing

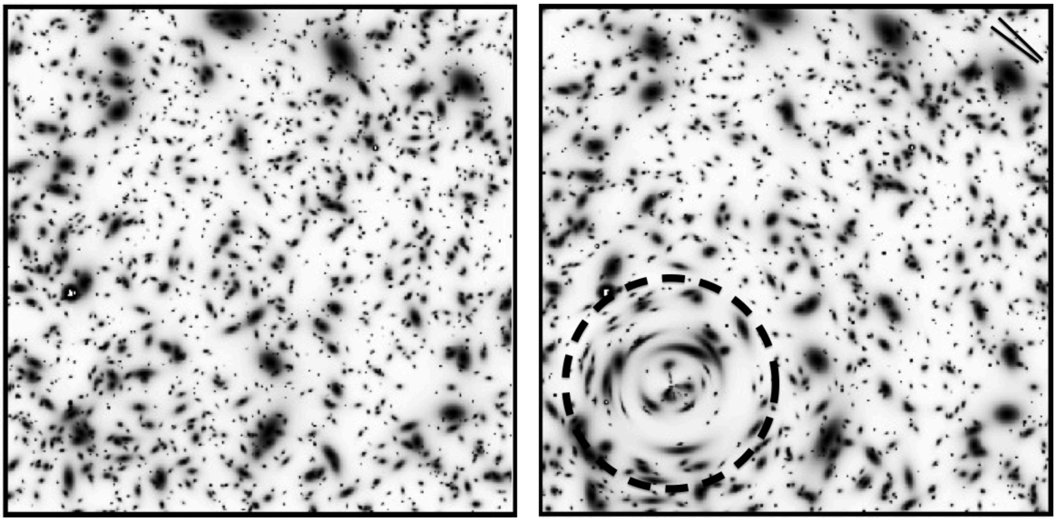

Figure 1.3: Illustration of the gravitational lensing effect. The left panel shows a simulated population of galaxies, whose images are distorted in the right panel by the presence of a massive galaxy cluster located at the centre of the dashed black circle (the cluster is not shown in either panel). The images of galaxies approximately within the dashed circle are affected by strong lensing: they are multiply-imaged because their light reaches us through more than one path (though this effect is not obvious in the figure), and they look highly distorted by the cluster. Outside the circle, the image of each galaxy is only very slightly distorted and the effect must be measured statistically. This is illustrated by the two sticks at the top right of the right panel: the lower stick shows the average true orientation of galaxies near the corner, while the upper stick shows the average orientation of the lensed images. Figure from Mellier (1999).

measurements around galaxies at $0.3 < z < 0.7$ to show that blue galaxies form stars just as efficiently as they accrete dark matter from their surroundings, while the stellar mass fraction of red galaxies decrease with time, consistent with the hypothesis that they grow purely by accretion of dark matter. This picture is summarized in Figure 1.4.

The picture above applies to *central* galaxies—the galaxies living at the centres of their dark matter haloes. Galaxies that are not central galaxies are referred to as *satellite* galaxies, and they have a very different interaction with their environment. We take a closer look at satellite galaxies in Section 1.3.

1.2. Galaxy clusters in a nutshell

As mentioned above, galaxies and their dark matter haloes are distributed following a complicated pattern termed the cosmic web. At the intersections of this cosmic web lie galaxy clusters, the most massive gravitationally-bound structures formed so far in the Universe. As the name suggests, galaxy clusters are objects in which galaxies abound—a massive cluster can host hundreds of bright galaxies (e.g., Abell 1958). However, this simple description was rendered insufficient early on by Zwicky (1933, discussed above). We now know that galaxy clusters, with sizes of 1–2 Mpc and masses of up to a few times $10^{15}\,\mathrm{M}_\odot$, are mostly made of dark matter (roughly 80% of their mass); only about 2% of their mass is in stars, while the remaining 18% is in a hot ionized gas with temperatures exceeding 10^7 K that can be observed at X-ray wavelengths (e.g., Sarazin 1986).

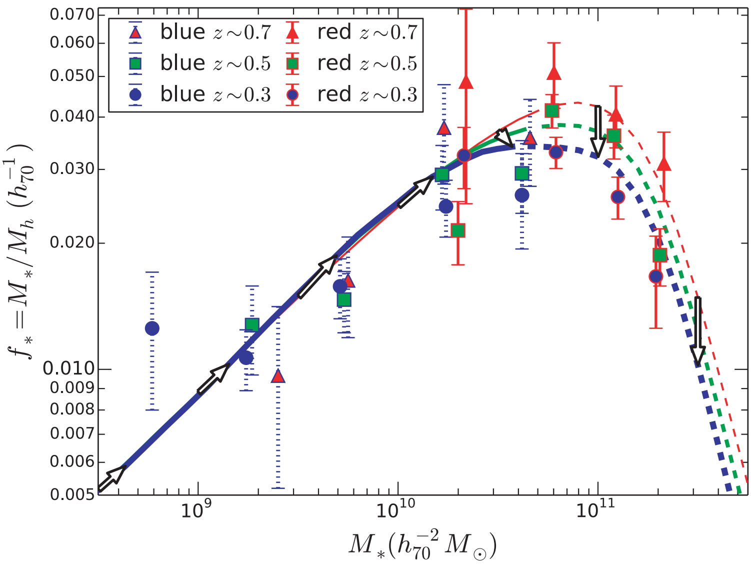

Figure 1.4: Evolution in the stellar mass fraction, f_*, over $0.3 < z < 0.7$ from weak lensing measurements combined with independent measurements of stellar masses. Data points with red and blue errorbars refer to red and blue galaxies, respectively. The lines correspond to a model where blue galaxies evolve by forming stars at a rate equal to the rate of dark matter accretion (whereby their stellar mass grows just as much as their dark matter mass), while red galaxies evolve only by the accretion of dark matter, and their stellar mass content does not evolve. White arrows show the evolution of the stellar mass fraction of a single galaxy in this model. The model provides a good fit to the data. Figure from Hudson et al. (2015).

1.2.1. Mass proxies and cosmological leverage

Galaxy clusters can be used to quantify the ability of the Universe to aggregate matter and therefore serve as powerful cosmological probes. The number of clusters in the Universe at a given time—and their masses—depends on the matter density of the Universe, usually parametrized as $\Omega_\mathrm{m} \equiv \rho_\mathrm{m}/\rho_\mathrm{c}$ (where ρ_c is the 'critical' density needed for the Universe to be flat), the size of density fluctuations left after the inflationary period, parametrized by σ_8, and the rate of expansion in the Universe, which can be quantified by the dark energy density, $\Omega_\Lambda \equiv \rho_\Lambda/\rho_\mathrm{c}$.

Exploiting clusters as cosmological probes requires knowledge of their masses, which is not an easy quantity to estimate. While gravitational lensing—the deflection of light due to the mass–induced curvature of space—provides a direct measurement of the surface mass density (which can be deprojected into a total mass under some assumptions), it has not been generally available for large samples of clusters.

Because of this, considerable effort has been devoted to characterize a variety of mass *proxies*—observable quantities that, we hope, depend on mass in as simple a manner as possible, but also that are readily measurable with current capabilities. The most obvious of these is the number of galaxies, usually referred to as 'richness', which has received considerable attention in recent years. Although initial attempts found that the richness was a very noisy mass proxy, recent studies have found that a properly-defined richness can be as good a proxy as any other (Rykoff et al. 2012; Andreon 2015). Also common are X-ray–derived mass proxies, including the X-ray luminosity, the gas temperature and the gas mass. Of these, the gas mass shows the least scatter (Mahdavi et al. 2013) but is the most difficult to obtain,

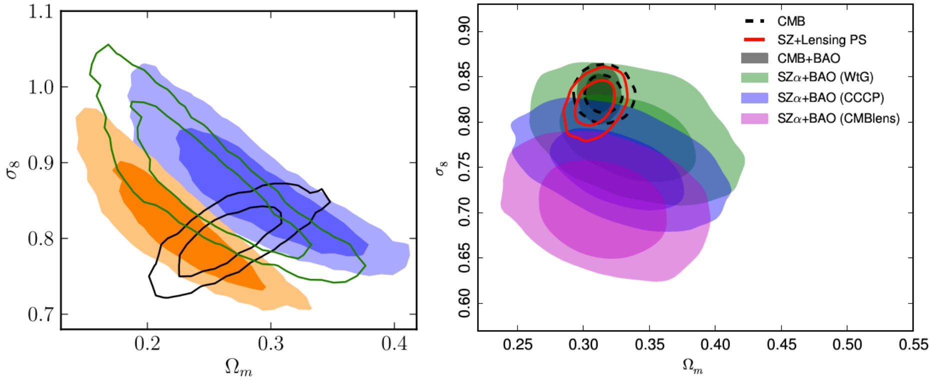

Figure 1.5: Constraints on cosmological parameters Ω_m and σ_8 from galaxy clusters detected by the Atacama Cosmology Telescope (left, from Hasselfield et al. 2013) and the *Planck* satellite (right, from Planck Collaboration 2015c) through their SZ effect. Black contours in the left and right panel show constraints from primary CMB measurements by the WMAP and *Planck* satellites, respectively. The broader, coloured contours show different assumptions about the scaling between SZ effect and mass. Clearly, this dominates the uncertainty budget on cosmological parameters.

and is currently only available for rather small samples.

A novel mass proxy, which has only been measurable in recent years thanks to new, sensitive high-resolution millimeter-wave surveys, is the Sunyaev-Zel'dovich (SZ, Sunyaev & Zel'dovich 1972) effect. The SZ effect is produced by the interaction of CMB photons with the hot electrons in galaxy clusters; this interaction increases the energy of CMB photons and creates 'holes' in observations at frequencies around 150 GHz in the direction of galaxy clusters. In a sense, therefore, observing the SZ effect is like seeing the shadow of a galaxy cluster. Because it is a CMB observable, the SZ surface brightness is independent of the redshift of the cluster producing it, and SZ surveys reveal the most massive clusters at all redshifts (Hasselfield et al. 2013; Bleem et al. 2015).[1] In contrast, X-ray or optical observations reveal flux from the clusters themselves and are therefore generally limited to rather low redshift. In addition, the relation between SZ effect and mass has been predicted to have very little scatter (at a level of 5–10%; e.g., Motl et al. 2005; Battaglia et al. 2012), although observations have shown that these predictions were rather optimistic (Benson et al. 2013; Sifón et al. 2013).

Massive galaxy clusters at high redshift have a particularly strong leverage on cosmological parameters (Vikhlinin et al. 2009), so SZ surveys are well-suited for cosmological parameter inference; the characterization of the SZ effect as a mass proxy is an active field of study. Figure 1.5 shows the constraints on cosmological parameters from galaxy clusters detected in the SZ survey by the Atacama Cosmology Telescope (ACT, Hasselfield et al. 2013) and the *Planck* satellite (Planck Collaboration 2015c). Both analyses found that the main limitation to the constraining power is given by the unknown conversion from SZ effect to cluster mass (rather than statistical uncertainties), even though the ACT analysis is based on only 15 clusters.

[1] This is not true for the SZ survey carried out with the *Planck* satellite, which is mostly limited to $z < 0.6$ (Planck Collaboration 2015b). This is because high-redshift clusters have a small angular extent, so their SZ signal is diluted by the large beam of *Planck* (roughly $5'$).

1.3. Mass and light in cluster galaxies

The galaxies we readily see in galaxy clusters tell us the story of a harsh, unforgiving environment: unlike the spiral galaxies (or 'nebulae') known since time immemorial (but whose spiral nature was discovered by William Parsons, 3rd Earl of Rosse, in 1845, and whose physical properties have only been characterized over the course of the past century), galaxies in clusters are typically of elliptical shape and a distinct reddish colour (Dressler 1980; Gladders & Yee 2000). This difference arises because galaxies entering clusters suffer the fast removal of their cold (~ 10 K) gas (which can collapse to form stars); the galaxies are then left only with old stars, which on average look redder than the bluer young stars (hence the colour of spiral galaxies).

This transformation is facilitated mainly by three distinct effects. *Galaxy harassment* is the process by which a galaxy removes the gas from another galaxy due to a high-speed encounter or fly-by (Moore et al. 1996). *Ram pressure stripping* is the removal of galactic gas by the gas in the intracluster medium, because the galaxy is traversing it at high speed (Gunn & Gott 1972; Nulsen 1982). Finally, *strangulation* refers to the process by which the strong tidal forces produced by the gravitational potential of the cluster remove the cold gas from the galaxy (Larson et al. 1980). Whatever the exact relevance of each mechanism, these effects seem to remove the star formation fuel from galaxies on relatively short timescales of about 1 billion years or less (e.g. Haines et al. 2013; Muzzin et al. 2014). Moreover, the evidence suggests that these effects are strong enough to suppress star formation even in low-mass galaxy groups (Haines et al. 2015; Balogh et al. 2016).

1.3.1. Tidal effects on cluster galaxies

Because galaxies do not follow radial orbits within clusters, they are subject to strong tidal torques from the cluster's gravitational potential. These torques have an effect on both the shapes and the masses of cluster galaxies.

Regarding the shapes, the tidal torques tend to align the galaxies such that their major axes point towards the centre of the host cluster. In numerical simulations of dark matter (where gravity is the only force present), this process is very efficient, and dark matter *subhaloes* are tidally aligned with the host dark matter halo after the first pericentre passage, and remain aligned thereafter (e.g., Kuhlen et al. 2007; Pereira & Bryan 2010). However, simulations that incorporate gas and stars have shown that the case is not so clear-cut for galaxies. These simulations show that there is a degree of *mis*alignment between the two components, such that the alignment of stellar light in galaxies is probably much weaker than that of the dark matter. Observational constraints on the strength of these cluster galaxy alignments, if any, can also have a strong impact on ongoing and upcoming cosmic shear surveys such as the Kilo-Degree Survey (KiDS, de Jong et al. 2015) or Euclid (Laureijs et al. 2011), as these *intrinsic* alignments are anti-correlated with the apparent alignment of background sources produced by gravitational lensing (Hirata & Seljak 2004). If not accounted for, they could introduce significant biases on cosmological parameters inferred from cosmic shear measurements.

If the visible parts of galaxies undergo such dramatic changes when they become satellites, similar effects might apply to the dark component. Just like in isolated galaxies and galaxy clusters, dark matter is expected to be the dominant mass component in cluster galaxies; exactly how much so is not well known. In fact, the same tidal forces that might cause galaxies to align also act to transfer mass from the satellite galaxy to the host cluster.

Statistical measurements of this *tidal stripping* effect are particularly challenging: in addition to the difficulty of measuring the masses of galaxies in general, one must be able to identify galaxies belonging to clusters in the first place.

Measuring the total masses of cluster galaxies has implications not only for models of galaxy formation and evolution, but also for cosmology. Specifically, the energy of the postulated dark matter particle defines the amount of mass that is contained in substructures within the large scale structure (i.e., galaxies in clusters, or satellite galaxies around massive galaxies). A universe where dark matter is "warm" produces less substructure than one where dark matter is "cold" (e.g., Libeskind et al. 2013). Therefore the fraction of mass in cluster galaxies (relative to the total mass of a galaxy cluster) depends on the energy of the dark matter particle. The cold dark matter model provides a good description of large-scale structure observations and is the most widely-accepted scenario (e.g., Blumenthal et al. 1984; Frenk & White 2012); accurate measurements of cluster galaxy masses would provide a complementary test of it.

1.4. This thesis

In this thesis we use a variety of observations and techniques to study the connection between the mass and light contents of galaxy clusters from different perspectives. The implications of different aspects of this connection have been briefly outlined above and are discussed in more detail in each chapter.

In **Chapter 2** we characterize PLCK G004.5−19.5, a galaxy cluster recently discovered by the *Planck* satellite through its SZ effect. We present the first optical images of this cluster, measure its redshift ($z = 0.52$) and identify multiple images of a lensed background galaxy, which allows us to perform a strong lensing analysis. We also show that PLCK G004.5−19.5 hosts diffuse radio emission—the tell-tale sign of cluster mergers and, to this day, an extremely rare sight at $z > 0.4$.

In **Chapter 3** we use extensive spectroscopic observations of galaxy clusters detected through the Sunyaev-Zel'dovich effect to measure the velocity dispersions of their member galaxies. Taking previous results from hydrodynamical simulations, we convert these velocity dispersions into cluster masses and compare them to the strength of the SZ effect, with the aim of characterizing the latter to allow its use for cosmological parameter inference. We pay particular attention to sources of uncertainty and scatter in the determination of the velocity dispersions, and conclude that the dominant uncertainty comes from the identification of member galaxies, which poses an irreducible uncertainty on velocity dispersions as mass proxies.

In the second half of this thesis we turn our attention to the galaxies residing in clusters. In particular, in **Chapter 4** we investigate the alignment of the shapes of cluster galaxies. We base our study on a sample of 90 clusters with deep, wide-field observations devised for accurate weak lensing measurements. We first perform a thorough literature search for spectroscopic redshifts with which to select galaxies physically belonging to these clusters, resulting in a sample of more than 14,000 cluster galaxies. We then measure the orientations of cluster galaxies to see if there are any signs of alignment of galaxies within clusters. We place upper limits on the strength of these alignments and show that these upper limits are within the statistical uncertainty expected for ongoing cosmic shear surveys.

In **Chapter 5** we exploit the overlap between the spectroscopic Galaxy And Mass Assembly survey (GAMA) and the deep photometric Kilo-Degree Survey to measure the masses of satellite galaxies in galaxy groups using weak gravitational lensing, with the aim of constraining the segregation of group galaxies by mass. The spectroscopic nature of the galaxy group catalogue ensures we can do this essentially free of contamination from both non-group galaxies and central galaxies. **Chapter 5** represents a first step in understanding the connection between cluster galaxies and dark matter haloes from weak gravitational lensing.

Finally, in **Chapter 6** we extend the lensing measurements of **Chapter 5** to more massive galaxy clusters using the dataset produced for **Chapter 4**. Using weak lensing measurements of the masses of cluster galaxies, we constrain the stellar-to-subhalo mass relation and study the mass segregation of cluster galaxies. We find results that are broadly consistent with expectations but conclude, in fact, that the primary limiting aspect is the lack of precise theoretical predictions on the link between dark and luminous matter in cluster galaxies.

2 | Strong lensing analysis of PLCK G004.5−19.5 at $z = 0.52$

The recent discovery of a large number of galaxy clusters using the Sunyaev-Zel'dovich (SZ) effect has opened a new era on the study of the most massive clusters in the Universe. Multi-wavelength analyses are required to understand the properties of these new sets of clusters, which are a sensitive probe of cosmology. We aim at a multi-wavelength characterization of PLCK G004.5−19.5, one of the most massive X-ray validated SZ effect–selected galaxy clusters discovered by the *Planck* satellite. We have observed PLCK G004.5−19.5 with GMOS on the 8.1m-Gemini South Telescope for optical imaging and spectroscopy, and performed a strong lensing analysis. We also searched for associated radio emission in published catalogs. An analysis of the optical images confirms that this is a massive cluster, with a dominant central galaxy (the BCG) and an accompanying red sequence of galaxies, plus a 14″–long strong lensing arc. Longslit spectroscopy of 6 cluster members shows that the cluster is at $z = 0.516 \pm 0.002$. We also targeted the strongly lensed arc, and found $z_{\rm arc} = 1.601$. We use LensTool to carry out a strong lensing analysis, from which we measure a median Einstein radius $\theta_{\rm E}(z_{\rm s} = 1.6) \simeq 30''$ and estimate an enclosed mass $M_{\rm E} = 2.45^{+0.45}_{-0.47} \times 10^{14}\,{\rm M}_\odot$. By extrapolating an NFW profile we find a total mass $M_{500}^{\rm SL} = 4.0^{+2.1}_{-1.0} \times 10^{14}\,{\rm M}_\odot$. Including a constraint on the mass from previous X-ray observations yields a slightly higher mass, $M_{500}^{\rm SL+X} = 6.7^{+2.6}_{-1.3} \times 10^{14}\,{\rm M}_\odot$, consistent with the value from strong lensing alone. High-resolution radio images from the TIFR GMRT Sky Survey at 150 MHz reveal that PLCK G004.5−19.5 hosts a powerful radio relic on scales $\lesssim 500$ kpc. Emission at the same location is also detected in low resolution images at 843 MHz and 1.4 GHz. This is one of the higher redshift radio relics known to date.

Cristóbal Sifón, Felipe Menanteau, John P. Hughes,
Mauricio Carrasco, & L. Felipe Barrientos,
2014, A&A, 562, A43

2.1. Introduction

In the last few years, the Sunyaev-Zel'dovich (SZ) effect has proven to be an effective method to find massive galaxy clusters at all redshifts, with results from the Atacama Cosmology Telescope (ACT, e.g., Marriage et al. 2011b; Hasselfield et al. 2013), the South Pole Telescope (SPT, e.g., Williamson et al. 2011; Reichardt et al. 2013) and the *Planck* satellite (e.g., Planck Collaboration 2011a, 2014b) already yielding a few hundred newly discovered clusters up to $z \sim 1.4$. The SZ effect is a distortion in the Cosmic Microwave Background (CMB) spectrum in the direction of galaxy clusters caused by inverse Compton scattering of CMB photons by the hot electrons in the intracluster gas (Sunyaev & Zel'dovich 1972). Multi-wavelength follow-up observations of SZ-selected clusters have confirmed the unique potential of the SZ effect for detecting the most massive clusters in the Universe (e.g., Benson et al. 2013; Sifón et al. 2013), with the SZ-discovered El Gordo and SPT-CL J2344−4243 being two of the most extreme galaxy clusters ever known (Menanteau et al. 2012; McDonald et al. 2012). As expected, many of these clusters display strong lensing features (Menanteau et al. 2010b), a good indication that these are very massive systems.

Observations of these strongly lensed background galaxies offer one of the most robust ways of constraining the mass of a cluster, providing a direct measure of the mass within the Einstein radius (see Kneib & Natarajan 2011, for a recent review). In combination with other probes (such as X-rays and weak lensing), strong lensing analyses have provided some of the most complete mass distribution models for galaxy clusters, even allowing for the determination of the 3-dimensional configuration in some cases (e.g., Morandi et al. 2010; Limousin et al. 2013).

Here, we present a multi-wavelength analysis of PLCK G004.5−19.5, one of the most massive, hot and X-ray luminous galaxy clusters discovered by the *Planck* satellite via the SZ effect and validated with *XMM-Newton* X-ray observations (Planck Collaboration 2011b). We perform a strong lensing analysis from optical imaging and spectroscopy, and show from archival radio imaging that PLCK G004.5−19.5 hosts a powerful radio relic.

All uncertainties are quoted at the 68.3% (1σ) confidence level. We assume a flat ΛCDM cosmology with $\Omega_{\rm m} = 0.3$ and $H_0 = 70\,{\rm km\,s^{-1}\,Mpc^{-1}}$. Total masses, X-ray and SZ measurements are reported within a radius r_{500}, which encloses a mean density 500 times the critical density of the Universe at the corresponding redshift. All quantities reported by Planck Collaboration (2011b) (reproduced in Section 2.2.1) have been corrected to the spectroscopic redshift $z = 0.516$. All magnitudes are in the AB system.

2.2. Observations and data analysis

2.2.1. SZ and X-ray data

PLCK G004.5−19.5 was discovered through its SZ effect by the *Planck* satellite. With a signal-to-noise ratio (S/N) of 5.9 in the Early Science release, it is just below the S/N threshold of 6.0 set for the *Planck* Early SZ sample (Planck Collaboration 2011a)[1]. Despite this relatively low S/N, it has a strong integrated SZ signal, $Y_{500} = (1.90 \pm 0.19) \times 10^{-4}\,{\rm Mpc}^2$, where $Y \equiv \int y\, d\Omega$. Here, y is the usual Compton parameter and the integral is over the solid

[1]PLCK G004.5–19.5 has been included in the new *Planck* SZ catalog (Planck Collaboration 2014b) with a S/N of 6.15.

angle of the cluster. We use the $Y-M$ scaling relation of Planck Collaboration (2011c) to estimate a mass $M_{500}^{\rm SZ} = (10.4 \pm 0.7) \times 10^{14}\,{\rm M}_\odot$.

PLCK G004.5−19.5 was subsequently validated using *XMM-Newton* (Planck Collaboration 2011b), which confirmed that it is an extended X-ray source. Moreover, the observed energy of the Fe K emission line allowed a redshift determination $z_{\rm Fe} = 0.54$, making it the highest-redshift cluster of the initial *Planck–XMM-Newton* validation program. The X-ray analysis of Planck Collaboration (2011b) proves that PLCK G004.5−19.5 is a hot, massive cluster, with an X-ray luminosity[2] (in the [0.1-2.4] keV band) of $L_{\rm X} = 1.6 \times 10^{45}\,{\rm erg\,s^{-1}}$, an integrated temperature $kT_{\rm X} = 10.2{\pm}0.5$ keV and a gas mass $M_{\rm gas} = 1.3{\times}10^{14}\,{\rm M}_\odot$. Combined, the latter two give a pseudo-Compton parameter $Y_{\rm X} \equiv kT_{\rm X}M_{\rm gas} = (13.3 \pm 0.9) \times 10^{14}{\rm M}_\odot$ keV. With this latter value, Planck Collaboration (2011b) estimate a total mass $M_{500}^{\rm X} = (9.6 \pm 0.5) \times 10^{14}\,{\rm M}_\odot$.

2.2.2. Optical imaging

PLCK G004.5−19.5 was observed on UT 2012 July 19 with the *gri* filters with GMOS on the Gemini-South Telescope (ObsID:GS-2012A-C-1, PI:Menanteau), with exposure times of 8×60 s, 8×90 s and 8×150 s respectively. Observations were performed with photometric conditions and seeing $\sim 0\farcs6$. Images were coadded using SWarp (Bertin et al. 2002) and photometry was performed using SExtractor (Bertin & Arnouts 1996) in dual mode, using the *i*-band for detection. Figure 2.1 shows the combined *gri* image[3] of PLCK G004.5−19.5, which shows clearly that there is an overdensity of red elliptical galaxies with a central dominant Brightest Cluster Galaxy (BCG) close to the X-ray peak. Figure 2.1 also reveals the presence of several strong lensing features, most notably a giant arc to the West of the BCG, roughly 14″ long.

Each galaxy is assigned a photometric redshift by fitting Spectral Energy Distributions (SEDs) to the *gri* photometry using the BPZ code (Benítez 2000) including correction for galactic extinction as described in Menanteau et al. (2010a,b). Typical uncertainties are $\delta z/(1+z) \simeq 0.09$. The photometric redshift of the cluster, $z_{\rm phot} = 0.51 \pm 0.02$, was estimated as in Menanteau et al. (2010a,b) and is consistent with the spectroscopic redshift (Section 2.2.3). We consider as cluster members all galaxies within $\Delta z = 0.03(1+z_0) = 0.045$ of $z_0 = 0.51$ and brighter than $m^\star + 2 \simeq 22.9$ in the *i*-band, for a total 222 photometrically-selected members. (Here $m^\star$ is the characteristic luminosity of the Schechter (1976) function as found by Blanton et al. (2003), passively evolved to z_0.[4]) Selecting galaxies from a color-magnitude diagram instead or imposing a brighter membership cut have no influence on the results.

2.2.3. Optical spectroscopy

We performed longslit spectroscopy of PLCK G004.5−19.5 on UT 2012 July 20 with GMOS, with $0\farcs75$-wide slits with three pointings, two aimed at confirming cluster members and one targeting the most prominent strongly lensed background galaxy. The data were reduced using pygmos[5] (Sifón et al. 2013), with an average wavelength calibration root-mean-square (rms) uncertainty of 0.4Å. Redshifts were measured by cross-correlating the spectra with Sloan Digital Sky Survey (Abazajian et al. 2009) template spectra using the iraf package rvsao (Kurtz & Mink 1998). The six confirmed cluster members are listed

[2] The uncertainties in the X-ray values from Planck Collaboration (2011b) do not include systematic errors and have been dropped when negligible.

[3] Created with stiff (Bertin 2012).

[4] For reference, the BCG has a luminosity $L = 9.5L^\star$.

[5] `http://www.strw.leidenuniv.nl/~sifon/pygmos/`

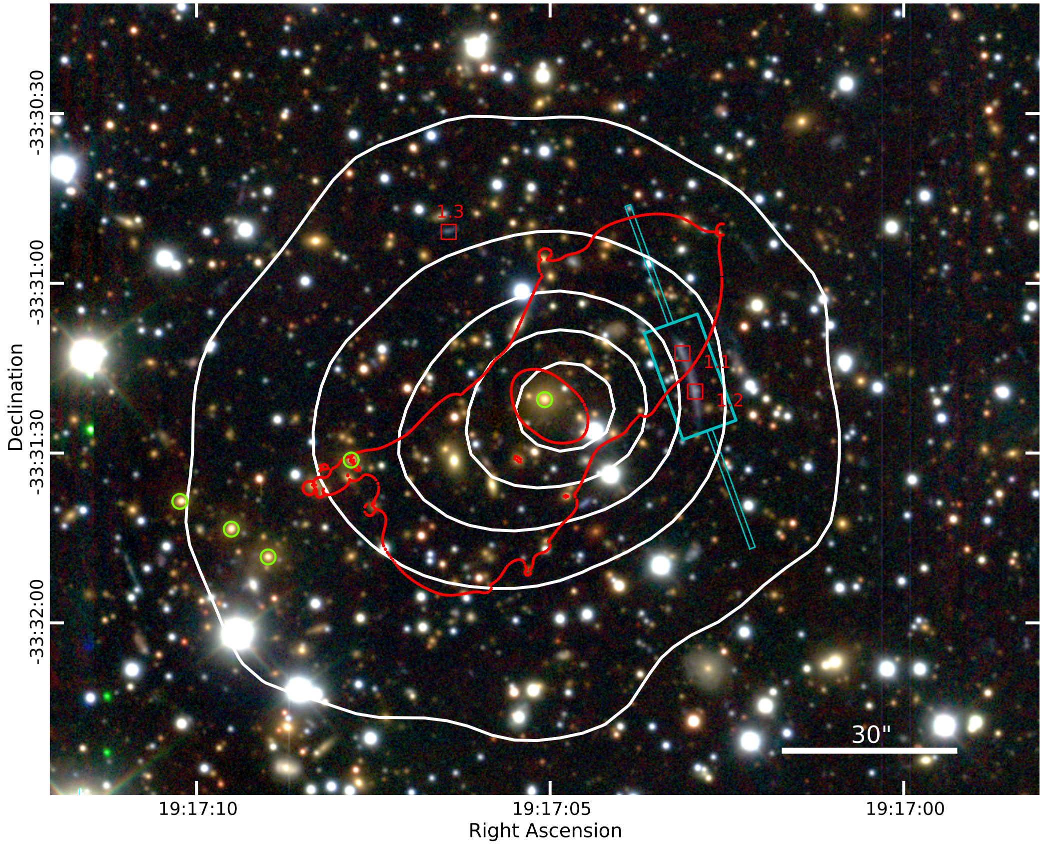

Figure 2.1: GMOS *gri* pseudo-color image of the central region of PLCK G004.5−19.5. North is up, east is left. X-ray surface brightness contours from *XMM-Newton* are overlaid in white. Spectroscopic cluster members are marked by green circles; only 5 out of 6 are visible in the shown region, the sixth member is ~ 760 kpc to the E-SE of the BCG. Red squares mark the position of the 3 confirmed multiple images, while we show in red the critical curve for $z_s = 1.6$. The thin cyan box shows the slit used to get the spectrum of the arc ($1''$ across) ; the wide cyan box shows the region zoomed-in in the left panel of Figure 2.2. The thick white line in the bottom right shows a $30''$ scale, corresponding to 188 kpc at $z = 0.516$.

in Table 2.1 and are shown in Figure 2.1 by green circles. They are all red, passive elliptical galaxies and have a rest-frame velocity dispersion $\sigma \sim 860\,\mathrm{km\,s^{-1}}$ (which is likely not representative of the cluster velocity dispersion). The median redshift of these 6 members, $z = 0.516 \pm 0.002$, is adopted as the cluster redshift (with uncertainties given by $\sigma\sqrt{\pi/2N}$).

The left panel of Figure 2.2 shows a zoomed-in view of the brightest lensed galaxy. Two brightness peaks can be identified, which we interpret as two blended strong lensing images of a single source (see Section 2.3). The top-right panel shows the 2d spectrum along the arc, where a faint continuum can be distinguished between the north and south images. The red inset histogram shows the normalized counts for each row over the spectral range shown, after an iterative 3σ-clipping rejection so that bad pixels and emission lines are not included in the counts. This histogram shows that the decrease in brightness is significant between the two peaks but that this region is, in turn, still detected at high significance. The middle- and bottom-right panels show the 1d spectra of the two brightness peaks. Both spectra clearly

Table 2.1: Spectroscopically confirmed cluster members.

ID	RA (hh:mm:ss)	Dec (dd:mm:ss)	i mag.[a] (AB mag)	Redshift[b]
1[c]	19:17:05.08	−33:31:20.6	18.47	0.5199 ± 0.0005
2	19:17:07.80	−33:31:31.2	19.74	0.5126 ± 0.0005
3	19:17:08.98	−33:31:48.4	19.16	0.5074 ± 0.0004
4	19:17:09.49	−33:31:43.5	19.70	0.5150 ± 0.0003
5	19:17:10.20	−33:31:38.5	19.83	0.5176 ± 0.0003
6	19:17:14.40	−33:31:57.5	20.48	0.5187 ± 0.0002

[a]`MAG_AUTO` from SExtractor. [b]Errors as given by RVSAO. [c]Brightest Cluster Galaxy.

show 5 redshifted FeII absorption lines with rest-frame wavelengths 2344.2, 2374.5, 2382.8, 2586.6 and 2600.2 Å. The median redshift of these 5 pairs of lines is $z_{\rm arc} = 1.6008 \pm 0.0002$. The bottom spectrum also shows three emission lines (seen in the 2d spectrum as well), which correspond to Hβ and [OIII]$\lambda\lambda$4958,5007Å from a foreground compact star-forming galaxy at $z = 0.203$, for which Hα emission is also observed but not shown in Figure 2.2. A small, bright, blue blob is indeed seen overlapping with the south knot (just West of the latter), which we interpret as this foreground galaxy.

2.3. Strong lensing analysis

2.3.1. Strong lensing model

The strong lensing analysis was performed using the Markov Chain Monte Carlo (MCMC) code LensTool (Kneib 1993; Jullo et al. 2007), as follows. The cluster is modelled with an ellipsoidal Navarro-Frenk-White (NFW, Navarro et al. 1995) profile for the main halo, plus a truncated Pseudo-Isothermal Elliptical Mass Distribution (PIEMD, Kassiola & Kovner 1993; Kneib et al. 1996) with a constant mass-to-light ratio for the 222 brightest cluster members (see Section 2.2.2). A PIEMD halo is modelled by three parameters: the core radius, $r_{\rm core}$, the size of the halo (the cut-off radius), $r_{\rm cut}$, and the velocity dispersion, σ_0, which scale with galaxy luminosity as (Jullo et al. 2007):

$$r_{\rm core} = r^{\star}_{\rm core} \left(L/L^{\star}\right)^{1/2} \tag{2.1a}$$

$$r_{\rm cut} = r^{\star}_{\rm cut} \left(L/L^{\star}\right)^{1/2} \tag{2.1b}$$

$$\sigma_0 = \sigma^{\star}_0 \left(L/L^{\star}\right)^{1/4}, \tag{2.1c}$$

where $L^{\star} = 6.6 \times 10^{10}\,\mathrm{L}_{\odot}$. The total mass of the galaxy is then given by

$$M = (\pi/G) \left(\sigma^{\star}_0\right)^2 r^{\star}_{\rm cut} \left(L/L^{\star}\right). \tag{2.2}$$

We fix $r^{\star}_{\rm core} = 0.3$ kpc, and $r^{\star}_{\rm cut}$ and $\sigma^{\star}_0$ are free parameters. The centre of the NFW halo is fixed to the peak of the X-ray emission (located at RA=19:17:04.6, Dec=−33:31:21.9; Planck Collaboration 2011b). Therefore the mass model has six free parameters: four for the main NFW halo and two for the PIEMD haloes.

As can be seen in the red inset histogram of Figure 2.2, there is a decrease in brightness in the middle of the arc in between two prominent brightness peaks. We interpret this as

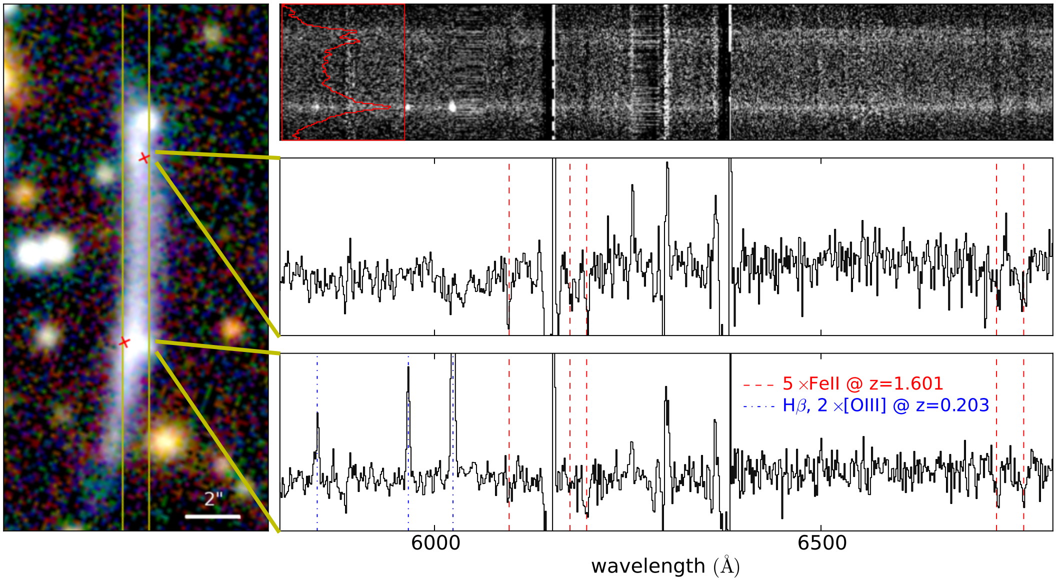

Figure 2.2: Strong lensing giant arc. The left panel shows a $10'' \times 20''$ close-up gri image of the arc (cyan box in Figure 2.1), with the red crosses marking the location where LensTool predicts the images to be. The thin yellow lines outline the position of the slit and the thick yellow lines mark the approximate locations of the knots from where the 1D spectra are shown. The right panels show the arc spectrum in the wavelength range $5800-6800$. The top right panel shows the GMOS 2d spectrum. The image is 105 pixels, corresponding to $15.''3$, from top to bottom. The red histogram (inset) shows the total counts in each row over the shown spectral range, after an iterative 3σ-clipping to remove bad pixels and emission lines. This highlights the decrease in brightness (and the significance of the continuum) between the two images. The middle and bottom panels show, respectively, the 1d spectra of the northern (source 1.1) and southern (source 1.2) peaks seen in the lensed arc, each marked by a yellow "wedge" in the left panel. In these, the red dashed lines mark the 5 FeII absorption lines at $z = 1.601$ and the blue dash-dotted lines mark the emission lines from a foreground galaxy at $z = 0.203$, only seen in the south spectrum. The vertical axes in these two panels are in arbitrary units.

the merging of two images of the background galaxy and use this double-imaged arc with $z_{\rm arc} = 1.6$ as a constraint for the lens model, and identify a third image of the same source to the North-East of the BCG (labelled 1.3 in Figure 2.1). The positions and photometry of these three images are listed in Table 2.2.

The total mass model is therefore optimized using the 222 brightest members (including the six spectroscopic members) and the three images for the background galaxy at $z = 1.601$. We adopt a positional uncertainty $\Delta\mathbf{x} = 1.''4$ for the multiple images. The goodness-of-fit for the best model is $\chi^2_{\rm red}/{\rm d.o.f.} = 0.15$, with a rms error on the image positions of $0.''22$. The total mass distribution is moderately elongated along the plane of the sky, approximately aligned with the light distribution. The best-fit values for the six free parameters plus the posterior masses and radii are listed in Table 2.3 (see also Section 2.3.2).

Following Meneghetti et al. (2011), the Einstein radius is estimated as the median distance of the tangential critical curves to the cluster centre. We find $\theta_{\rm E}(z_{\rm s} = 1.6) = 30.''3^{+1.4}_{-3.9}$, corresponding to a physical distance $r_{\rm E} \simeq 190$ kpc. Assuming a symmetric lens, the mass inside this region is $M_{\rm E} = 2.45^{+0.45}_{-0.47} \times 10^{14}\,{\rm M}_\odot$. Integrating the 3-dimensional NFW profile for the main halo, we obtain $M^{\rm SL}_{500} = 4.0^{+2.1}_{-1.0} \times 10^{14}\,{\rm M}_\odot$.The corresponding radius, $r^{\rm SL}_{500} = 0.93^{+0.16}_{-0.08}$ Mpc, is estimated from M_{500} assuming a spherical cluster. We note that the values at r_{500}

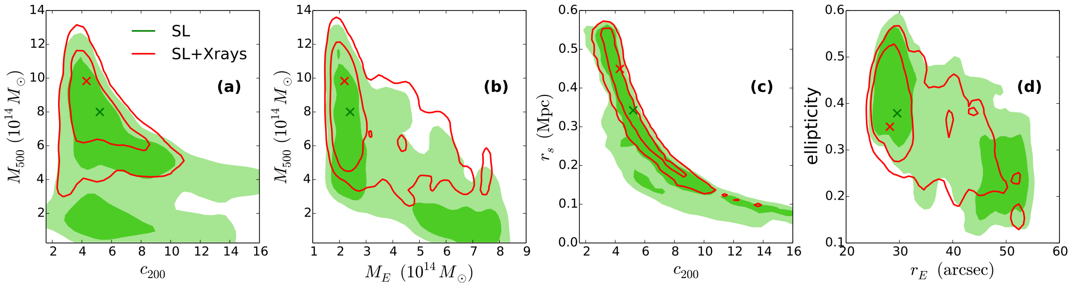

Figure 2.3: Joint 2D posterior distributions of c_{200} and M_{500} (panel *a*), $M_{\rm E}$ and M_{500} (panel *b*), c_{200} and $r_{\rm s}$ (panel *c*), and $r_{\rm E}$ and θ (panel *d*). Contours are at the 68% and 95% levels. Filled green contours show constraints from strong lensing alone and red contours show the constraints when $M_{500}^{\rm X}$ is included as an independent constraint. Crosses show the corresponding maximum likelihood estimates.

Table 2.2: Images of the strongly lensed galaxy.

Source	RA (hh:mm:ss)	Dec (dd:mm:ss)	r mag.[a] (AB mag)	$g-r$[b] (AB mag)
1.1	19:17:03.14	−33:31:12.5	21.42 ± 0.01	0.40 ± 0.03
1.2	19:17:02.97	−33:31:19.0	21.42 ± 0.01	0.39 ± 0.02
1.3	19:17:06.45	−33:30:50.8	23.75 ± 0.03	0.35 ± 0.05

[a]`MAG_ISO` from SExtractor. [b]Difference of `MAG_APER`'s from SExtractor.

are an extrapolation of the strong lensing information.

Recently, Zitrin et al. (2012) derived a representative distribution of Einstein radii from a sample of $\sim 10{,}000$ clusters from the SDSS optically-selected sample of Hao et al. (2010). They found a log-normal Einstein radius distribution with mean and standard deviation $\langle \log(\theta_{\rm E}^{\rm eq}/{\rm arcsec})\rangle = 0.73 \pm 0.32$ for background sources at $z_{\rm s} \sim 2$. For comparison to Zitrin et al. (2012) and others, we estimate the equivalent Einstein radius to be $\theta_{\rm E}^{\rm eq}(z_{\rm s} = 1.6) \simeq 25''$. PLCK G004.5−19.5 is a 2σ outlier from this mean relation; therefore it can be said to be within the 5% strongest lensing clusters in the Universe.

2.3.2. External constraints

We run LensTool again including a prior in the mass, from the X-ray mass estimated by Planck Collaboration (2011b) as implemented by Verdugo et al. (2011). As mentioned in Section 2.2.1, however, the reported uncertainties are unrealistically small. As a more realistic estimate, we take the intrinsic scatter in the latest $Y_{\rm X}-M$ relation by Mahdavi et al. (2013) of 22%, measured by combining weak lensing and X-ray observations. Thus the additional constraint in the total mass is the following Gaussian prior:

$$M_{500}^{\rm X} = (9.6 \pm 2.1) \times 10^{14}\,{\rm M}_\odot \tag{2.3}$$

measured at $r_{500}^{\rm X} = 1245$ kpc.[6] The same excersise for the SZ mass, assuming an uncertainty of 18% corresponding to the central value of the intrinsic scatter in the $Y_{\rm SZ}-M$ measured by

[6]Note that in LensTool the X-ray constraint to the strong lensing model is given as a fixed mass M at a fixed radius r (with a mass uncertainty), not explicitly as the mass at a given overdensity.

Table 2.3: Marginalized posterior estimates of the strong lensing model with and without the X-ray mass constraint.

Parameter[a]	Symbol	SL	SL+X	units
Main NFW Halo				
Ellipticity	e	$0.40^{+0.07}_{-0.09}$	$0.37^{+0.08}_{-0.07}$	
Position Angle[b]	θ	52^{+7}_{-3}	53^{+2}_{-1}	deg
Scale radius	r_s	$0.10^{+0.17}_{-0.04}$	$0.39^{+0.07}_{-0.08}$	Mpc
Concentration[c]	c_{200}	$4.0^{+5.0}_{-0.8}$	$4.1^{+1.8}_{-0.6}$	
PIEMD Halos				
Cut-off radius	$r^{\star}_{\mathrm{cut}}$	47^{+13}_{-20}	25^{+28}_{-14}	kpc
Velocity dispersion	$\sigma^{\star}_0$	225^{+42}_{-23}	106^{+37}_{-53}	$\mathrm{km\,s^{-1}}$
Derived Parameters				
Einstein Mass	M_{E}	$2.45^{+0.45}_{-0.47}$	$2.46^{+0.31}_{-0.59}$	$10^{14}\mathrm{M}_{\odot}$
Einstein Radius	r_{E}	$30.3^{+1.4}_{-3.9}$	$30.0^{+0.6}_{-3.5}$	arcsec
Total Mass	M_{500}	$4.0^{+2.1}_{-1.0}$	$6.7^{+2.6}_{-1.3}$	$10^{14}\mathrm{M}_{\odot}$
Radius	r_{500}	$0.93^{+0.16}_{-0.08}$	$1.10^{+0.14}_{-0.07}$	Mpc

[a]All parameters have uniform priors. [b]Position angle West of North. [c]The concentration is defined as $c_{200} = r_{200}/r_s$.

Sifón et al. (2013) using dynamical masses and SZ measurements from ACT, gives

$$M^{\mathrm{SZ}}_{500} = (10.4 \pm 1.9) \times 10^{14}\,\mathrm{M}_{\odot} \tag{2.4}$$

We only use Equation 2.3 because both measurements are very similar and because they are both measured at the same radius, determined from the X-ray scaling relation (Planck Collaboration 2011b) and are therefore not independent. The posterior distributions are shown for various combinations of parameters for the two different models in Figure 2.3, highlighting degeneracies in the strong lensing model.

The X-ray constraint pushes the mass to a higher value which is marginally consistent with the strong lensing only (SL) model. Notably, the SL model allows for a low-M_{500}, high-M_{E} (through a high r_{E}), high-concentration and low-ellipticity solution which is marginally excluded by the model including the X-ray constraint (SL+X). The marginalized posterior mass is $M^{\mathrm{SL+X}}_{500} = 6.7^{+2.6}_{-1.3} \times 10^{14}\,\mathrm{M}_{\odot}$. Although the contours are broader in the SL model, the maximum likelihood estimate (MLE) and marginalized 68% range of M_{E} (and r_{E}) are mostly unaffected by the inclusion of the X-ray constraint, with a posterior estimate $M^{\mathrm{SL+X}}_{\mathrm{E}} = 2.46^{+0.31}_{-0.59} \times 10^{14}\mathrm{M}_{\odot}$. This is expected, since r_{E} is directly constrained by the strongly lensed images, independently of the mass profile of the cluster.

2.4. Radio emission

Radio relics and radio haloes are diffuse, non-thermal emission features that have no obvious connection with individual cluster galaxies and are often associated with merging activity in massive clusters of galaxies (see Feretti et al. 2012, for a recent review). We searched for such features around PLCK G004.5−19.5 in the high-resolution 150 MHz images

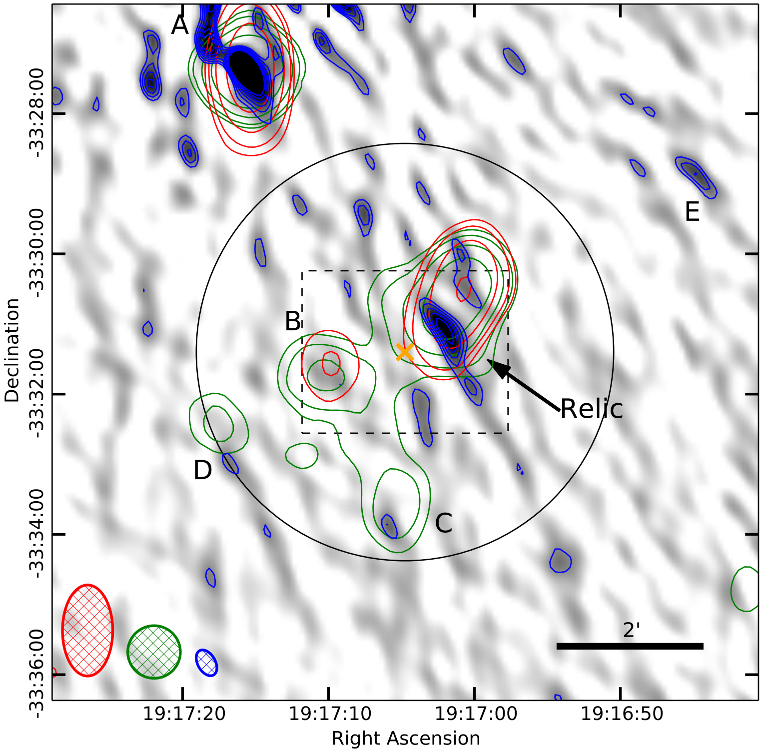

Figure 2.4: $10' \times 10'$ TGSS 150 MHz intensity map around PLCK G004.5−19.5, with contours in blue. Contours are shown at $(3,5,7,15)\times\sigma$, where σ is the background rms. NVSS 1.4 GHz and SUMSS 843 MHz contours are shown in green and red, respectively. Both contour sets are in units of $(3,5,10,20)\times\sigma$. The orange cross shows the position of the BCG. The dashed black rectangle is the region shown in Figure 2.1 and the black circle marks $r_{500}^{\rm SL+X} = 1.12$ Mpc. The black bar in the bottom right marks a scale of $2'$. The SUMSS, NVSS and TGSS beams are shown from left to right, respectively, in the bottom left corner (hatched ellipses).

of the TIFR GMRT Sky Survey (TGSS)[7] Data Release 5 and in VizieR[8] (Ochsenbein et al. 2000) for additional archival data.

Figure 2.4 shows the intensity map at 150 MHz from the TGSS with blue contours at (3, 5, 7, 15)σ, where $\sigma = 11.9\,\mathrm{mJy\,beam}^{-1}$ is the background rms level. Green and red contours show 1.4 GHz and 843 MHz emission from the NRAO VLA Sky Survey (NVSS; Condon et al. 1998) and the Sydney University Molonglo Sky Survey (SUMSS; Mauch et al. 2003), respectively. Both sets of contours are shown at (3, 5, 10, 20)σ, where $\sigma = 0.51\,\mathrm{mJy\,beam}^{-1}$ and $2.0\,\mathrm{mJy\,beam}^{-1}$ in the NVSS and SUMSS images, respectively. There is significant ($> 5\sigma$) emission around PLCK G004.5−19.5 in all three frequencies at coincident locations. Moreover, this emission is extended in the TGSS and NVSS images.

We identify a tangentially extended radio relic in the TGSS image, coincident with emission at the other frequencies, although this emission is barely resolved in SUMSS and NVSS (the extent of the emission is roughly 2 beams in both low-resolution images). The multi-frequency properties of this relic are given in Table 2.4. Radio relics span a wide range of

[7]http://tgss.ncra.tifr.res.in/

[8]http://vizier.u-strasbg.fr/viz-bin/VizieR

Table 2.4: Radio Relic

Source Name	RA[a] (hh:mm:ss)	Dec[a] (dd:mm:ss)	Freq. (MHz)	Beam (″×″)	F_ν[b] (mJy)	Size[c] (″×″)	P.A.[d] (deg)
GMRT173_01[e]	19:17:01.94	−33:31:12.6	150	24 × 15	382 ± 80	84 × 19	28 ± 5
SUMSS J191701−333033	19:17:01.50(16)	−33:30:33.7(2.5)	843	51 × 43	51 ± 4	70 × 62	136 ± 3
NVSS 1917101−333035	19:17:01.75(08)	−33:30:35.6(1.3)	1400	45 × 45	37 ± 2	74 × 50	146 ± 1

[a]Nominal uncertainties on the last two digits in parentheses. [b]Integrated Flux. [c]Major and minor axes. [d]Position angle West of North. [e]Position uncertainties from TGSS are $\sim 4''$.

Table 2.5: Other Sources in the Radio Images.

Source	Name	RA (hh:mm:ss)	Dec (dd:mm:ss)	F_ν (mJy)	Size ($'' \times ''$)	P.A. (deg)
	GMRT243_01[a,b]	19:17:16.71	−33:27:11.8	540 ± 75	39×19	43
A	NVSS J191715−332722	19:17:15.89(05)	−33:27:22.2(0.7)	35.7 ± 0.5	47×45	176
	SUMSS J191715−332720	19:17:15.75(11)	−33:27:20.6(2.0)	71.5 ± 2.7	73×49	165
B	NVSS J191710−333144	19:17:10.90(28)	−33:31:44.7(3.3)	11.2 ± 0.8	74×55	102
	SUMSS J191710−333139[c]	19:17:10.55(37)	−33:31:39.0(4.6)	8.8 ± 1.0	57×52	3
C	NVSS J191705−333333	19:17:05.94(32)	−33:33:33.6(8.0)	7.7 ± 0.5	81×49	173
D	NVSS J191717−333224	19:17:17.84(52)	−33:32:24.4(5.7)	3.7 ± 0.1	57×42	132
E	GMRT163_01[b]	19:16:45.13	−33:28:48.9	161 ± 41	71×14	34

See Notes in Table 2.4. [a]Blended in the TGSS catalog. [b]Position uncertainties from TGSS are $\sim 4''$. [c]Not in the SUMSS catalog.

spectral indices, α (where $F_\nu \propto \nu^{-\alpha}$), from $\alpha \sim 1$ up to $\alpha \sim 3$ (Feretti et al. 2012). We give a preliminary estimate of the integrated spectral index of the relic by fitting a power-law to the 150 MHz flux combined with NVSS and SUMSS, one at a time. From both combinations we measure $0.9 \lesssim \alpha \lesssim 1.4$ at the 68% level. Measuring the spectral index from all three frequencies gives a shallower but consistent spectral index $\alpha \sim 0.7 - 1.1$, suggesting that the emission at 843 MHz and/or 1.4 GHz may be contaminated by unresolved point sources, thus boosting the flux and lowering α. A spectral index measured using both 843 MHz and 1.4 GHz would be more affected by this contamination since these two frequencies are closer together (in log-space) than any of them is to the TGSS frequency.

We confirm that there are no X-ray point sources associated with any of the radio emission from the *XMM-Newton* image. As with the relic, sources A, B, C and E have no counterparts in the optical images, nor in the Near Infrared (NIR) from the 2 Micron All Sky Survey (2MASS, Skrutskie et al. 2006) or the Mid Infrared (MIR) from the Wide-field Infrared Survey Explorer All Sky Survey (WISE, Wright et al. 2010), within their nominal position uncertainties. Source D has two plausible counterparts from the 2MASS and WISE (merged into one source) catalogs. Both are stars, and are also seen in our optical images. It is therefore likely that source D is a radio point source. Given its high flux and shape in the TGSS image, source A is also likely a point source, or two blended point sources.

Because the relic elongation is approximately in the same direction as the TGSS beam and source E, we use source E (which can be regarded as noise-dominated, being much less significant and not detected at any other frequency) as a control for the significance of the relic accounting for the TGSS beam. As seen from Tables 2.4 and 2.5, both the relic and source E have similar sizes and position angles. Figure 2.4 shows however that the relic is much more significant than source E. Moreover, the following exercise shows that in the case of source E, the large size is a consequence of the background noise and the beam, whereas the source we associate to the radio relic is significantly extended over the background. We re-measured fluxes for these two sources on images in which we masked all pixels with values below $3\sigma = 35.7\,\mathrm{mJy\,beam^{-1}}$. More than half the emission associated with source E comes from pixels with $< 3\sigma$ emission, and the major axis is halved in this masked map. From the relic, in contrast, we still measure $\sim 70\%$ of the total flux, and the major axis is 75% of the size measured in the original map.

2.5. Conclusions

We present a multi-wavelength analysis of PLCK G004.5−19.5, one of the massive galaxy clusters recently discovered by the *Planck* satellite using the SZ effect. Optical confirmation from GMOS imaging clearly shows a red sequence of galaxies with a dominant BCG, both undisputable characteristics of galaxy clusters. There is also a strongly lensed giant arc which is composed of two partially merged images of a background galaxy. Spectroscopy of 6 cluster members plus the giant arc show that the cluster is at $z = 0.516 \pm 0.002$ and that the arc is at $z_{\rm arc} = 1.601$. With these data we have performed a strong lensing analysis, confirming a third image for the source producing the arc. We use LensTool to obtain a mass model for the cluster including the contribution from cluster galaxies, and estimate an Einstein mass $M_{\rm E} = 2.45^{+0.45}_{-0.47} \times 10^{14}\,\mathrm{M_\odot}$, within a median Einstein ring $r_{\rm E} \simeq 190$ kpc, corresponding to an angular size $\theta_{\rm E}(z_{\rm s} = 1.6) \simeq 30''$. Compared to the universal Einstein ring distribution derived by Zitrin et al. (2012), PLCK G004.5−19.5 is among the 5% strongest gravitational lenses in the Universe. By integrating the 3-dimensional NFW profile we estimate $M_{500}^{\rm SL} = 4.0^{+2.1}_{-1.0} \times 10^{14}\,\mathrm{M_\odot}$. We also run LensTool including a Gaussian prior for the X-ray mass estimated by Planck

Collaboration (2011b) and find $M_{500}^{\mathrm{SL+X}} = 6.7^{+2.6}_{-1.3} \times 10^{14}\,\mathrm{M}_{\odot}$, marginally consistent with the mass estimated from strong lensing alone. The Einstein mass does not change significantly when including the X-ray constraint, because the latter is constrained directly by the strongly lensed galaxy. The inclusion of the X-ray mass constraint does help to exclude a high-mass, low-concentration solution which is allowed by the strong lensing-only model.

Examination of archival high-resolution radio data from the TIFR GMRT Sky Survey at 150 MHz reveals the presence of a radio relic at approximately 250 kpc from the cluster centre. Significant emission is also detected in low-resolution images from NVSS at 1.4 GHz and SUMSS at 843 MHz. A preliminary measurement of the integrated spectral index yields $\alpha \sim 0.9 - 1.4$. We find no detectable point sources contributing significantly to the radio emission in the *XMM-Newton* or Gemini images, nor from archival observations in the NIR or MIR. This radio emission likely originated from recent merging activity, but the available data do not allow for a detailed study of possible merging events. The origin of the radio emission will be addressed with future observations.

3 | Dynamical masses of galaxy clusters selected through the Sunyaev-Zel'dovich effect

We present galaxy velocity dispersions and dynamical mass estimates for 44 galaxy clusters selected via the Sunyaev-Zel'dovich (SZ) effect by the Atacama Cosmology Telescope. Dynamical masses for 18 clusters are reported here for the first time. Using N-body simulations, we model the different observing strategies used to measure the velocity dispersions and account for systematic effects resulting from these strategies. We find that the galaxy velocity distributions may be treated as isotropic, and that an aperture correction of up to 7% in the velocity dispersion is required if the spectroscopic galaxy sample is sufficiently concentrated towards the cluster centre. Accounting for the radial profile of the velocity dispersion in simulations enables consistent dynamical mass estimates regardless of the observing strategy. Cluster masses M_{200} are in the range $(1-15)\times10^{14}\,\mathrm{M}_\odot$. Comparing with masses estimated from the SZ distortion assuming a gas pressure profile derived from X-ray observations gives a mean SZ-to-dynamical mass ratio of 1.10 ± 0.13, but there is an additional 0.14 systematic uncertainty due to the unknown velocity bias; the statistical uncertainty is dominated by the scatter in the mass-velocity dispersion scaling relation. This ratio is consistent with previous determinations at these mass scales.

Cristóbal Sifón, Nick Battaglia, Matthew Hasselfield, Felipe Menanteau, and the ACT collaboration,
2016, MNRAS, 461, 248

3.1. Introduction

Galaxy clusters are a sensitive probe of cosmology. Populating the high-end of the mass function, their number density depends strongly on the matter density in the Universe, Ω_m, and the amplitude of matter fluctuations, σ_8 (see, e.g., the review by Allen et al. 2011). Their potential as cosmological probes, however, depends critically on our knowledge of survey selection effects and baryon physics. Survey selection effects are usually properly accounted for through analytical considerations (e.g., Vikhlinin et al. 2009), numerical simulations (e.g., Sehgal et al. 2011; Sifón et al. 2013), or modeled self-consistently with scaling relations and cosmological parameters (e.g., Pacaud et al. 2007; Mantz et al. 2010; Rozo et al. 2010; Benson et al. 2013; Hasselfield et al. 2013; Bocquet et al. 2015). In contrast, incomplete knowledge of baryonic physics poses a serious and still not well understood challenge to the accuracy with which galaxy clusters can constrain cosmological parameters, and is currently the dominant systematic effect (e.g., Benson et al. 2013; Hasselfield et al. 2013).

The Sunyaev-Zel'dovich (SZ) effect (Zel'dovich & Sunyaev 1969; Sunyaev & Zeldovich 1980) is a distortion in the cosmic microwave background (CMB) temperature produced by inverse-Compton scattering of CMB photons by free electrons in the hot ($T > 10^7\,\mathrm{K}$) intracluster medium (ICM) of a galaxy cluster. The SZ effect has a distinct frequency dependence such that, in the direction of a massive cluster, the temperature of the sky increases at frequencies larger than 218 GHz while below this frequency the temperature decreases. The amplitude of this distortion is described by the line-of-sight–integrated Compton parameter, $y \propto n_e T_e$, or its solid-angle integral, $Y = \int y\,\mathrm{d}\Omega$. Its surface brightness is independent of redshift which, to first order, means that surveying the sky at millimetre wavelengths reveals all clusters above a fixed mass to high redshift, resulting in a relatively simple selection function.

Both numerical simulations (Springel et al. 2001b; da Silva et al. 2004; Motl et al. 2005; Nagai 2006; Battaglia et al. 2012) and analytical studies (Reid & Spergel 2006; Afshordi 2008; Shaw et al. 2008) predict that the SZ effect should correlate with mass with low (of order 10%) intrinsic scatter, although observations correlating the SZ effect with different mass proxies from X-rays (Bonamente et al. 2008; Andersson et al. 2011; Planck Collaboration 2011c; Benson et al. 2013; Rozo et al. 2014b), optical richness (High et al. 2010; Planck Collaboration 2011d; Menanteau et al. 2013; Sehgal et al. 2013), weak lensing (Hoekstra et al. 2012; Marrone et al. 2012; Planck Collaboration 2013; Gruen et al. 2014) and galaxy velocity dispersion (Sifón et al. 2013; Ruel et al. 2014; Rines et al. 2016) find a larger intrinsic scatter between mass and Y of about 20%. The effect of cluster physics mentioned above, coupled to systematic effects arising from the use of different instruments (Mahdavi et al. 2013; Rozo et al. 2014a), dominate the uncertainties in these scaling relations. This uncertainty has been most notoriously highlighted by the tension in inferred cosmological parameters between the primary CMB and SZ cluster counts found by the Planck satellite (Planck Collaboration 2015c), and can be reduced by larger, more detailed analyses involving independent mass proxies and ICM tracers.

Velocity dispersions have been well studied as a proxy for galaxy cluster mass, dating back to the first such scaling relation reported by Evrard (1989), and are independent of the ICM properties that determine the SZ effect.[1] Extensive tests on numerical simulations have shown that the 3-dimensional galaxy velocity dispersion is a low-scatter mass proxy but, not surprisingly, projection effects including cluster triaxiality and large-scale structure significantly increase the scatter (White et al. 2010; Saro et al. 2013). The scatter at fixed

[1] Some degree of correlation may still exist, however, because different observables are affected by the same large scale structure (White et al. 2010).

velocity dispersion in observed samples is as large as a factor two (Old et al. 2014, 2015).[2] Importantly, the biases on these measurements (typically $\lesssim 25\%$ for $\gtrsim 30$ observed galaxies) are much smaller than the observed scatter (Old et al. 2015), meaning that velocity dispersions remain a valuable, unbiased mass calibrator for sufficiently large cluster samples. In this paper we make use of spectroscopic data to estimate line-of-sight galaxy velocity dispersions (referred to as σ in the remainder of this section) and dynamical masses of galaxy clusters selected through their SZ effect using the Atacama Cosmology Telescope (ACT, Marriage et al. 2011b; Hasselfield et al. 2013).

In Sifón et al. (2013), we used the $\sigma - M$ scaling relation of Evrard et al. (2008) to estimate dynamical masses of a subset of these clusters. Evrard et al. (2008) calibrated this scaling relation using a suite of N-body simulations, using dark matter particles to estimate velocity dispersions. They showed that the velocity dispersions of dark matter particles in N-body simulations are robust to variations in cosmology and to different simulation codes. However, galaxies, which are used as observational tracers to measure the velocity dispersion, do not necessarily sample the same velocity distribution as the dark matter particles. Both galaxies and dark matter subhaloes (the analogues of galaxies in N-body simulations) feel dynamical friction, which distorts their velocity distribution and biases their dispersion with respect to dark matter particles. Additionally, subhaloes are tidally stripped and disrupted such that they can drop below the subhalo identification limit of a particle simulation. The lower-velocity subhaloes are more likely to be disrupted, thus the surviving subhaloes have a larger velocity dispersion which again biases the velocity dispersion of subhaloes (e.g., Faltenbacher & Diemand 2006).

The result of these effects is referred to as velocity bias, denoted $b_{\rm v} \equiv \sigma_{\rm gal}/\sigma_{\rm DM}$ (e.g., Carlberg 1994; Colín et al. 2000). Baryonic effects are significant when quantifying the amplitude of $b_{\rm v}$: recent high-resolution hydrodynamical simulations show significant differences in the velocity dispersions of subhaloes versus DM particles (roughly +7%, which translates to a $\sim 20\%$ bias in mass), but comparatively little difference between galaxies and dark matter subhaloes (e.g., Lau et al. 2010; Munari et al. 2013; Wu et al. 2013).[3] Additionally, the amplitude of $b_{\rm v}$ depends on the brightness of the observed galaxies: the velocity dispersion of brighter galaxies is generally biased low, but this can be counteracted by selecting a sample of ($\gtrsim 30$) galaxies with a representative brightness distribution (Old et al. 2013; Wu et al. 2013). In apparent contradiction with this, Guo et al. (2015a,b) used measurements of the clustering of luminous red galaxies (LRGs) to infer a *negative* velocity bias for satellite galaxies. Moreover, they found that *less* luminous LRGs have a stronger velocity bias of about 90%, while more luminous LRGs have velocities consistent with those of DM particles. This result can be reconciled with those of the above simulations by noting that any given cluster[4] typically has less than ten LRGs—both Old et al. (2013) and Wu et al. (2013) find that taking the N brightest galaxies gives rise to a velocity bias of roughly 0.9, if $N \lesssim 10$.

Since observationally one uses galaxies to calculate σ, biases may be introduced if one uses a $\sigma - M$ scaling relation calibrated from simulations using dark matter particles, such as that of Evrard et al. (2008), but does not account for the aforementioned complexities.

[2]In theory, the caustic technique provides a lower-scatter mass proxy than simple velocity dispersions (Gifford et al. 2013); however, it has been shown to produce similar scatter in more realistic settings (Old et al. 2014, 2015). In this respect, machine learning algorithms may become a promising alternative (Ntampaka et al. 2015b,a).

[3]Selecting galaxies by stellar mass instead of total mass reduces the strength of the velocity bias (e.g., Faltenbacher & Diemand 2006; Lau et al. 2010).

[4]Note that both the simulations and the observations of Guo et al. (2015a,b) refer to clusters with masses well below $10^{15} \mathrm{M}_\odot$.

Therefore, in this paper we use the scaling relation of Munari et al. (2013), calibrated on simulated *galaxies* instead of dark matter particles, to relate velocity dispersions to cluster masses.

We present our SZ-selected cluster sample and describe the observations, data reduction and archival compilation in Section 3.2. In Section 3.3 we describe our velocity dispersion and dynamical mass estimates, including an assessment of our different observing strategies using mock observations on numerical simulations (Section 3.3.2), a comparison to SZ-derived masses (Section 3.3.5) and an investigation of cluster substructure (Section 3.3.6). We highlight interesting individual clusters in Section 3.4 and summarize the main results in Section 3.5.

We assume a flat ΛCDM cosmology[5] with $\Omega_\mathrm{m} = 0.3$ and $H_0 = 70\,\mathrm{km\,s^{-1}\,Mpc^{-1}}$. Throughout this work we quote measurements (e.g., masses, M_Δ) at a radius r_Δ, within which the average density is Δ times the critical density of the Universe at the corresponding redshift, where $\Delta = \{200, 500\}$.

3.2. Data and observations

In this section we detail the cluster sample, our follow-up observations and data processing, and archival data with which we supplement our observations. In summary, we study 44 SZ-selected clusters, of which 28 are in the celestial equator and are the focus of this paper, and 16 clusters are part of the southern survey and were studied in Sifón et al. (2013). We summarize our observing runs and sources of archival data in Table 3.1.

3.2.1. The Atacama Cosmology Telescope

The Atacama Cosmology Telescope (ACT) is a 6-meter off-axis Gregorian telescope located at an altitude of 5200 m in the Atacama desert in Chile, designed to observe the CMB at arcminute resolution. Between 2007 and 2010, ACT was equipped with three 1024-element arrays of transition edge sensors operating at 148, 218, and 277 GHz (Fowler et al. 2007; Swetz et al. 2011), although only the 148 GHz band has been used for cluster detection. In this period, ACT observed two regions of the sky, one covering 455 sq. deg. to a typical depth of 60 μK centred around declination $-53°$ (the "southern" survey, Marriage et al. 2011b,a), and one covering 504 sq. deg. around the celestial equator, with a typical depth of 44 μK (the "equatorial" survey, Hasselfield et al. 2013). For details on the observational strategy of ACT and map making procedure see Dünner et al. (2013).

In the remainder of this section we describe ACT detections and follow-up observations of clusters in the equatorial survey. Details about the detection and optical confirmation of clusters in the southern survey can be found in Marriage et al. (2011b) and Menanteau et al. (2010b), respectively. The spectroscopic observations are described in Sifón et al. (2013) and the latest SZ measurements are given in Hasselfield et al. (2013).

3.2.2. ACT SZ-selected clusters in the equator

Galaxy clusters were detected in the 148 GHz band by matched-filtering the maps with the pressure profile suggested by Arnaud et al. (2010), fit to X-ray selected local ($z < 0.2$)

[5] Assuming Planck-level uncertainties in Ω_m and H_0 (Planck Collaboration 2015a) introduces a < 5% difference in the reported masses, accounting for their influence on both member selection (through changes in projected physical distances) and the adopted scaling relation.

clusters, with varying cluster sizes, θ_{500}, from $1.'18$ to $27'$. A signal-to-noise (S/N) ratio map was extracted from each of these matched-filtered maps and all pixels with $\mathrm{S/N} > 4$ were considered as cluster candidates. Cluster properties were extracted only from the map with $\theta_{500} = 5.'9$. The properties depend weakly on the exact shape of the profile as discussed in Hasselfield et al. (2013).

Because of the complete overlap of ACT equatorial observations with Sloan Digital Sky Survey Data Release 8 (SDSS DR8, Aihara et al. 2011) imaging, *all* cluster candidates were assessed with optical data (Menanteau et al. 2013). With DR8, clusters can be confidently detected up to $z \approx 0.5$. Moreover, 270 sq. deg. of the ACT survey overlap with the deep, co-added SDSS Stripe82 region (S82, Annis et al. 2014), which allows the detection of the cluster red sequence up to $z \approx 0.8$. Confirmed clusters are all those $\mathrm{S/N} > 4$ candidates for which there are at least 15 galaxies within $1\,h^{-1}\,\mathrm{Mpc}$ of the brightest cluster galaxy and with a photometric redshift within $0.045(1+z)$ of the cluster redshift. We additionally targeted candidate high-redshift, high S/N candidates with near infrared K_s-band imaging with the ARC 3.5m telescope at the Apache Point Observatory, which allowed us to confirm five additional clusters at $z \gtrsim 1$.[6]

A total of 68 clusters were confirmed, of which 19 (all at $z > 0.65$) were new detections. This sample has been divided into three subsamples: a complete sample of clusters within S82 at $z < 1$ and with $\mathrm{S/N} > 5$ (the "cosmological" sample, containing 15 clusters), a uniform sample of 34 clusters within S82, and an incomplete sample of 19 clusters up to $z \approx 0.7$ in the shallower DR8 region. Confirmed clusters in S82 have redshifts up to $z \approx 1.3$ (with the aid of near infrared data for the higher redshifts). See Menanteau et al. (2013) for more details on the optical and infrared confirmation of clusters in the equatorial survey.

3.2.3. Gemini/GMOS spectroscopy

We observed 20 clusters from the equatorial sample with the Gemini Multi-Object Spectrograph (GMOS, Hook et al. 2004) on the Gemini-South telescope, split in semesters 2011B (ObsID:GS-2011B-C-1, PI:Barrientos/Menanteau) and 2012A (ObsID:GS-2012A-C-1, PI:Menanteau), prioritizing clusters in the cosmological sample at $0.3 < z < 1.0$. All observations followed our setup for the southern sample (Sifón et al. 2013). We first selected as targets those galaxies with photometric redshifts within $\Delta z = 0.1$ of the cluster photometric redshift and prioritized bright galaxies as allowed by the multi-object spectroscopy (MOS) masks. The only major difference in strategy from Sifón et al. (2013) is that, owing to the SDSS photometry, we targeted galaxies out to larger radii than in the southern observations, in which we were bound by the roughly $5'$ fields of view of our targeted optical follow-up with 4m-class telescopes (Menanteau et al. 2010b). We followed this approach because of the indication, especially from numerical simulations, that the velocity dispersion is a decreasing function of radius; therefore an unbiased velocity dispersion estimate is predicted only if galaxies are sampled out to approximately the cluster's virial radius (e.g., Girardi et al. 1998; Biviano et al. 2006; Mamon et al. 2010). We observed 2-3 masks per cluster along the (visually identified) major axis of the galaxy distribution. In order to obtain a wide sky coverage, these masks were mostly non-overlapping in the sky, even though this meant we had fewer targets per unit area. We detail the differences with the southern strategy, and address the impact of these differences in our measurements, in Section 3.3.2.

[6] One of these clusters, ACT-CL J0012.0–0046, associated with an overdensity of red galaxies at $z = 1.36$ by Menanteau et al. (2013), is detected at much lower significance in new, more sensitive SZ observations performed with ACTPol (M. Hilton et al., in prep).

Table 3.1: Summary of spectroscopic observations and sources of archival data. The last column lists the number of clusters observed in each program. Previously published data have the corresponding references. All SDSS clusters have been observed by us in one of the listed programs as well.

Instrument / Archival source	Semester	Program	PI	Data reference	Sample	N_{cl}
VLT/FORS2	2009B	084.A-0577	Infante	Sifón et al. (2013)	South	3
	2010B	086.A-0425	Infante	Sifón et al. (2013)	South	2
Gemini/GMOS	2009B	GS-2009B-Q-2	Barrientos	Sifón et al. (2013)	South	4
	2010B	GS-2010B-C-2	Barrientos/Menanteau	Sifón et al. (2013)	South	10
	2011B	GS-2011B-C-1	Barrientos/Menanteau	this work	Equator	12
	2012A	GS-2012A-C-1	Menanteau	this work	Equator	8
SALT/RSS	2012A	2012-1-RSA_UKSC_RU-001	Hilton/Hughes	Kirk et al. (2015)	Equator	1
	2012B	2012-2-RSA_UKSC_RU-001	Hilton/Hughes	Kirk et al. (2015)	Equator	2
	2013A	2013-1-RSA_RU-001	Hilton/Hughes	Kirk et al. (2015)	Equator	1
	2013B	2013-2-RSA_RU-002	Hilton/Hughes	Kirk et al. (2015)	Equator	3
SDSS DR12	–	–	–	Alam et al. (2015)	Equator	20
HeCS	–	–	–	Rines et al. (2013)	Equator	3
NED	–	–	–	Soucail et al. (1988), Dressler et al. (1999)	Equator	1

We used PYGMOS[7] (Sifón et al. 2013), an automated Python/PyRAF script[8] that goes from raw data to one-dimensional spectra, including bias subtraction, flat field correction, wavelength calibration, cosmic ray rejection (van Dokkum 2001) and sky subtraction. Redshifts[9] were measured by cross-correlating the spectra with template spectra from SDSS[10] using XCSAO within IRAF's RVSAO package[11] (Kurtz & Mink 1998).

3.2.4. SALT/RSS spectroscopy

We also observed seven clusters in S82 with the Robert Stobie Spectrograph (RSS, Burgh et al. 2003) on the Southern African Large Telescope (SALT), using multi-object spectroscopy. Details of these observations are given in Kirk et al. (2015). Target selection and redshift measurements were carried in a similar, but not identical, fashion to the GMOS observations of the equatorial clusters. The data were prepared with PYSALT (Crawford et al. 2010), after which they were reduced with standard IRAF[12] functions. Redshift measurements are also obtained with XCSAO. ACT-CL J0045.2−0152 is the only cluster that was observed both with Gemini and SALT, but there are only two galaxies in our final catalogue observed with both telescopes.

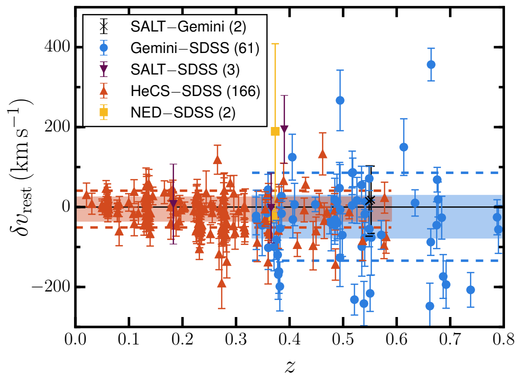

Figure 3.1: Comparison of redshifts from all spectroscopic datasets to SDSS measurements (for overlapping galaxies), shown as $\delta v_{\rm rest} = c\,(z_1 - z_2)/(1+z_2)$, where $z_2 = z_{\rm SDSS}$ (except for the black crosses, where $z_2 = z_{\rm Gemini}$). All redshifts are in the heliocentric frame. Red, yellow, purple and blue points correspond to redshifts from the HeCS survey (Rines et al. 2013), from NED for Abell 370, and from our SALT/RSS and Gemini/GMOS campaigns, respectively, while black crosses compare our redshift measurements between SALT/RSS and Gemini/GMOS. Individual uncertainties correspond to the quadrature sum of the uncertainties from both measurements. Red and blue shaded regions show uncertainties on the weighted means for HeCS−SDSS and Gemini−SDSS, respectively, and dashed horizontal lines show standard deviations. The number of matches per data set pair are given in parentheses in the legend.

3.2.5. Archival data

In order to enlarge the sample of studied clusters and member galaxies, we also compiled archival data for the equatorial sample. Specifically, we searched the SDSS Data Release 12 (DR12, Alam et al. 2015) database[13]. We retrieved all galaxies with a valid redshift (that is, with `z>0` and `zWarning=0`) within a cluster-centric distance of 20′ (corresponding to several times r_{200} for most clusters) and found a total of 2001 galaxies (most of which are not cluster members; see Section 3.3) in the direction of 25 of the ACT equatorial clusters observed with Gemini or SALT. Of the galaxies with SDSS spectra, 61 were also observed by us with

[7] `http://www.strw.leidenuniv.nl/~sifon/pygmos/`
[8] PyRAF is a product of the Space Telescope Science Institute, which is operated by AURA for NASA.
[9] All redshifts presented here are in the heliocentric frame.
[10] `http://www.sdss.org/DR7/algorithms/spectemplates/index.html`
[11] `http://tdc-www.harvard.edu/iraf/rvsao/`
[12] `http://iraf.noao.edu/`
[13] `http://skyserver.sdss9.org/public/en/home.aspx`

Gemini, and three with SALT. We compare these repeat observations in Section 3.2.6. There are additionally four clusters in the equatorial sample with dedicated archival observations; we did not observe any of these clusters ourselves. We briefly describe these data below.

The Hectospec Cluster Survey (HeCS, Rines et al. 2013) was designed to measure the masses of galaxy clusters at $0.1 < z < 0.3$ out to the infall regions of clusters (typically around $4r_{200}$), targeting more than four hundred objects per cluster within a radius of $30'$ (corresponding to 6 Mpc at $z = 0.2$). The three clusters below $z = 0.3$ in the cosmological sample of Hasselfield et al. (2013) were targeted by Rines et al. (2013), namely ACT-CL J0152.7+0100 (Abell 267), ACT-CL J2129.6+0005 (RX J2129.6+0005) and ACT-CL J2337.6+0016 (Abell 2631). We include these three clusters in our analysis. Rines et al. (2013) also measured redshifts using XCSAO; we use only galaxies with redshift quality flags `'Q'` or `'?'`, which correspond to secure redshifts for high- and medium-quality spectra, respectively (Rines et al. 2013).

Additionally, the cluster ACT-CL J0239.8−0134 ($z = 0.375$) is the well-studied, HST Frontier Fields[14] cluster Abell 370. Despite extensive lensing studies (e.g. Medezinski et al. 2010; Richard et al. 2010; Hoekstra et al. 2012; von der Linden et al. 2014a), there is no modern spectroscopic data on this cluster. A search in the NASA/IPAC Extragalactic Database[15] (NED) gives roughly 100 galaxies with redshifts in the range $0.30 \leq z \leq 0.45$, which safely includes all potential cluster members (we then run our membership algorithm on these galaxies, see Section 3.3.1). These galaxies go out to $6'$ in radius. For homogeneity, we limit ourselves to redshifts measured either by Soucail et al. (1988) or Dressler et al. (1999) since these two sources make up the majority ($\approx 90\%$) of galaxies returned by NED. We assign to each galaxy an uncertainty at the level of the last non-zero digit.

3.2.6. Comparison between redshift measurements

There are many overlapping galaxies between SDSS and other data, as well as two overlapping galaxies between our SALT/RSS and Gemini/GMOS observations of ACT-CL J0045.2−0152. We compare the spectroscopic redshifts between the different measurements in Figure 3.1. There is good agreement between the different datasets. In particular, the inverse-variance-weighted average differences in rest-frame velocity (defined as $\delta v_{\rm rest} = c(z_1 - z_2)/(1 + z_2)$) are $\delta v_{\rm rest} = -24.2 \pm 53.1\,{\rm km\,s^{-1}}$ (where the errorbar is the uncertainty on the mean) between GMOS and SDSS, with a standard deviation $\sigma_{\delta v} = 110\,{\rm km\,s^{-1}}$, and $\delta v_{\rm rest} = -5.1 \pm 30.0\,{\rm km\,s^{-1}}$ between HeCS and SDSS, with $\sigma_{\delta v} = 46\,{\rm km\,s^{-1}}$. The standard deviations are 2.07 and 1.39 times the average XCSAO errors, respectively. We conclude that XCSAO underestimates the true cross-correlation velocity uncertainty by up to a factor two, consistent with previous determinations (e.g., Quintana et al. 2000; Boschin et al. 2004; Barrena et al. 2009). HeCS spectra have a higher S/N than GMOS spectra; therefore it is possible that the level of underestimation depends on the S/N of the spectrum.

3.3. Velocity Dispersions and Dynamical Masses

3.3.1. Velocity dispersion measurements

We use the shifting gapper method developed by Fadda et al. (1996) as implemented in Sifón et al. (2013) to select cluster members, as follows. Assuming the BCG to correspond

[14] `http://www.stsci.edu/hst/campaigns/frontier-fields/`
[15] `http://ned.ipac.caltech.edu`

to the cluster centre[16] (the impact of this assumption is assessed in Section 3.3.7), we bin galaxies by their (projected) cluster-centric distance in bins of at least 250 kpc and 10 galaxies. Therefore member selection in clusters with fewer than 20 redshifts was performed using a single bin (i.e., a standard sigma-clipping). A visual inspection of the phase-space diagrams of clusters with few members suggests that this choice is better than the 15 galaxies used in Sifón et al. (2013), where clusters had an average 65 members over a smaller area of the sky.[17] In each bin in projected distance we sort galaxies by the absolute value of their peculiar velocity (taken initially with respect to the median redshift of potential cluster members). In practice, this means we assume that clusters are symmetric in the radial direction. We then select a main body of galaxies having peculiar velocities $|v_i| < |v_{i-1}| + 500\,\mathrm{km\,s^{-1}}$, where the index i runs over all galaxies in a given radial bin. In other words, the main body is composed, in each radial bin, by the group of galaxies intersecting $v = 0$ and bound by velocity differences of less than 500 $\mathrm{km\,s^{-1}}$. All galaxies with peculiar velocities less than $1000\,\mathrm{km\,s^{-1}}$ away from the main body are considered cluster members. Modifying the velocity gaps does not have a noticeable impact on our results—all clusters have well defined boundaries in velocity space. This process is iterated, updating the cluster redshift and the radial binning, until the number of members converges (usually two to three iterations).

At every step in the member selection process, cluster redshifts and velocity dispersions are calculated as the biweight estimators of location and scale (i.e., the central value and dispersion, respectively, see equations 5 and 9 of Beers et al. 1990), respectively. We correct the velocity dispersion for individual redshift uncertainties (Danese et al. 1980), but this is a $<1\%$ correction for $\sigma = 1000\,\mathrm{km\,s^{-1}}$. We estimate 68% uncertainties in cluster redshifts and velocity dispersions by bootstrapping over all galaxies within 3σ of the measured velocity dispersion, which is always larger than the velocity limit defined by the shifting gapper. Therefore we include galaxies which are rejected by our member selection algorithm, and thus account for uncertainties arising from membership selection in the redshift and velocity dispersion uncertainties. We find that the membership selection process increases the statistical uncertainties in the mass by a median 2% for the full sample (but by $> 20\%$ for nine clusters where a large number of objects are rejected by the member selection algorithm). Such a small value is dominated by the southern clusters where, since we targeted the central regions only, the number of galaxies rejected by our algorithm is small compared to the number of members (only 2%, compared to 24% of galaxies rejected for the equatorial clusters). For comparison, we also implement a Bayesian algorithm to estimate velocity dispersions statistically accounting for an interloper component with constant spatial density (Wojtak et al. 2007; Andreon et al. 2008). The Bayesian analysis yields velocity dispersions, as well as uncertainties, that are consistent with our analysis.

Cluster redshifts and velocity dispersions are listed in Table 3.2. We show velocity histograms of clusters in the equatorial and southern samples in Figures 3.13 and 3.14, respectively.

3.3.2. Calibrating velocity dispersions with the Multidark simulation

To estimate a possible bias in the velocity dispersions arising from the different optical observations, especially between our southern and equatorial campaigns, we use mock observations of dark matter haloes in the Multidark simulation (Prada et al. 2012). Here we want

[16]The only exception is ACT-CL J2302.5+0002, which we discuss in Section 3.4.6.

[17]The difference in the dynamical masses (which are reported in Section 3.3.4) between using 10 or 15 galaxies as a minimal bin size in the shifting gapper is six%, well within the reported errorbars.

Table 3.2: Redshifts, velocity dispersions and dynamical masses of ACT SZ-selected clusters. The horizontal line separates equatorial and southern clusters. Clusters in the cosmological samples of Hasselfield et al. (2013) have a "Cosmo" suffix in the second column. The third and fourth columns give the total number of members, $N_{\rm m}$, and the number of members within r_{200}, N_{200}. We list the maximum radius at which we have spectroscopic members, $r_{\rm max}$, and the velocity dispersion of all members, $\sigma(<r_{\rm max})$, as well as the quantities calculated specifically within r_{200}. Uncertainties in the masses do not include the scatter in the $\sigma-M$ scaling relation. Alternative cluster names are given in Menanteau et al. (2013).

Cluster	Sample	$N_{\rm m}$	N_{200}	$z_{\rm cl}$	$\sigma(<r_{\rm max})$ (km s^{-1})	$r_{\rm max}$ (r_{200})	σ_{200} (km s^{-1})	r_{200} (Mpc)	M_{200} (10^{14} M$_\odot$)
ACT-CL J0014.9−0057	S82-Cosmo	62	45	0.5331 ± 0.0007	806 ± 91	1.75	850 ± 108	1.31 ± 0.16	4.5 ± 1.6
ACT-CL J0022.2−0036	S82-Cosmo	55	44	0.8048 ± 0.0014	961 ± 124	1.71	1025 ± 164	1.33 ± 0.20	6.6 ± 3.0
ACT-CL J0045.2−0152	DR8	56	44	0.5483 ± 0.0010	930 ± 77	1.40	967 ± 88	1.45 ± 0.12	6.3 ± 1.6
ACT-CL J0059.1−0049	S82-Cosmo	44	23	0.7870 ± 0.0012	884 ± 150	1.82	874 ± 206	1.19 ± 0.28	4.6 ± 3.2
ACT-CL J0119.9+0055	S82	16	14	0.7310 ± 0.0011	725 ± 128	1.06	786 ± 149	1.10 ± 0.20	3.4 ± 1.9
ACT-CL J0127.2+0020	S82	46	46	0.3801 ± 0.0008	994 ± 106	0.92	991 ± 108	1.64 ± 0.17	7.5 ± 2.3
ACT-CL J0152.7+0100	S82-Cosmo	253	144	0.2291 ± 0.0004	931 ± 41	2.57	1065 ± 54	1.89 ± 0.09	9.7 ± 1.4
ACT-CL J0206.2−0114	S82-Cosmo	40	23	0.6758 ± 0.0010	570 ± 105	2.02	625 ± 164	0.94 ± 0.25	2.0 ± 1.6
ACT-CL J0215.4+0030	S82-Cosmo	14	11	0.8622 ± 0.0026	1386 ± 262	1.27	1256 ± 268	1.57 ± 0.33	11.7 ± 7.3
ACT-CL J0218.2−0041	S82-Cosmo	61	41	0.6727 ± 0.0008	723 ± 76	1.80	790 ± 92	1.12 ± 0.12	3.4 ± 1.1
ACT-CL J0219.9+0129	DR8	10	10	0.3651 ± 0.0014	1001 ± 224	0.56	963 ± 215	1.66 ± 0.36	7.6 ± 5.0
ACT-CL J0223.1−0056	S82-Cosmo	38	27	0.6632 ± 0.0011	829 ± 96	1.25	911 ± 165	1.31 ± 0.23	5.3 ± 2.8
ACT-CL J0239.8−0134	DR8	75	75	0.3751 ± 0.0009	1216 ± 128	0.64	1183 ± 128	1.94 ± 0.19	12.2 ± 3.7
ACT-CL J0241.2−0018	S82	36	26	0.6872 ± 0.0013	830 ± 132	1.70	905 ± 160	1.28 ± 0.22	5.1 ± 2.6
ACT-CL J0256.5+0006	S82-Cosmo	78	78	0.3625 ± 0.0008	1185 ± 102	0.59	1144 ± 102	1.89 ± 0.16	11.2 ± 2.8
ACT-CL J0320.4+0032	S82	25	25	0.3847 ± 0.0014	1284 ± 209	0.56	1236 ± 215	2.03 ± 0.34	14.3 ± 7.1
ACT-CL J0326.8−0043	S82-Cosmo	62	59	0.4471 ± 0.0006	897 ± 96	1.21	927 ± 101	1.49 ± 0.15	6.0 ± 1.8
ACT-CL J0342.7−0017	S82	19	19	0.3072 ± 0.0015	941 ± 173	0.80	930 ± 173	1.64 ± 0.29	6.9 ± 3.7
ACT-CL J0348.6−0028	S82	15	15	0.3449 ± 0.0010	642 ± 117	0.51	614 ± 112	1.10 ± 0.19	2.2 ± 1.1
ACT-CL J2050.5−0055	S82-Cosmo	33	14	0.6226 ± 0.0007	539 ± 120	2.32	511 ± 97	0.79 ± 0.14	1.1 ± 0.6
ACT-CL J2050.7+0123	DR8	47	47	0.3339 ± 0.0009	1046 ± 104	0.92	1043 ± 103	1.76 ± 0.16	8.8 ± 2.4
ACT-CL J2055.4+0105	S82	55	52	0.4089 ± 0.0005	759 ± 77	1.11	778 ± 78	1.29 ± 0.12	3.8 ± 1.1
ACT-CL J2058.8+0123	DR8	16	16	0.3285 ± 0.0014	1109 ± 196	0.65	1080 ± 191	1.86 ± 0.31	10.2 ± 5.2
ACT-CL J2128.4+0135	DR8	59	56	0.3856 ± 0.0006	895 ± 116	1.12	906 ± 119	1.51 ± 0.19	5.9 ± 2.2
ACT-CL J2129.6+0005	S82-Cosmo	291	68	0.2337 ± 0.0005	786 ± 39	5.05	859 ± 91	1.56 ± 0.15	5.5 ± 1.6
ACT-CL J2154.5−0049	S82-Cosmo	52	42	0.4904 ± 0.0011	918 ± 108	1.42	964 ± 121	1.51 ± 0.18	6.6 ± 2.3
ACT-CL J2302.5+0002	S82	47	39	0.5199 ± 0.0007	648 ± 67	1.16	671 ± 63	1.06 ± 0.11	2.4 ± 0.7
ACT-CL J2337.6+0016	S82-Cosmo	154	51	0.2769 ± 0.0007	853 ± 52	4.85	879 ± 96	1.56 ± 0.16	5.7 ± 1.7

Table 3.2: *Continued.*

Cluster	Sample	N_{m}	N_{200}	z_{cl}	$\sigma(<r_{\mathrm{max}})$ ($\mathrm{km\,s^{-1}}$)	r_{max} (r_{200})	σ_{200} ($\mathrm{km\,s^{-1}}$)	r_{200} (Mpc)	M_{200} ($10^{14}\,\mathrm{M_{\odot}}$)
ACT-CL J0102–4915	South-Cosmo	86	81	0.8700 ± 0.0010	1273 ± 114	1.18	1284 ± 117	1.55 ± 0.13	11.3 ± 2.9
ACT-CL J0215–5212	South	54	54	0.4803 ± 0.0009	1027 ± 110	0.83	1018 ± 111	1.59 ± 0.16	7.6 ± 2.3
ACT-CL J0232–5257	South	63	63	0.5561 ± 0.0007	924 ± 87	0.66	900 ± 86	1.35 ± 0.12	5.2 ± 1.4
ACT-CL J0235–5121	South	80	80	0.2775 ± 0.0005	1044 ± 93	0.48	994 ± 92	1.74 ± 0.15	8.0 ± 2.0
ACT-CL J0237–4939	South	65	65	0.3343 ± 0.0007	1290 ± 91	0.39	1210 ± 91	2.01 ± 0.14	13.1 ± 2.7
ACT-CL J0304–4921	South	61	61	0.3917 ± 0.0007	1098 ± 98	0.51	1050 ± 96	1.71 ± 0.15	8.7 ± 2.2
ACT-CL J0330–5227	South-Cosmo	71	71	0.4417 ± 0.0008	1247 ± 96	0.46	1182 ± 98	1.85 ± 0.14	11.6 ± 2.7
ACT-CL J0346–5438	South	88	88	0.5297 ± 0.0007	1081 ± 76	0.77	1066 ± 75	1.60 ± 0.10	8.3 ± 1.6
ACT-CL J0438–5419	South-Cosmo	63	63	0.4212 ± 0.0009	1268 ± 109	0.56	1221 ± 108	1.93 ± 0.16	12.9 ± 3.2
ACT-CL J0509–5341	South-Cosmo	74	71	0.4601 ± 0.0005	860 ± 79	1.13	865 ± 82	1.38 ± 0.12	4.9 ± 1.3
ACT-CL J0521–5104	South	19	19	0.6742 ± 0.0018	941 ± 194	0.97	940 ± 198	1.35 ± 0.28	5.9 ± 3.6
ACT-CL J0528–5259	South	55	44	0.7676 ± 0.0010	934 ± 114	1.45	984 ± 125	1.30 ± 0.16	5.9 ± 2.1
ACT-CL J0546–5345	South-Cosmo	45	40	1.0668 ± 0.0013	1020 ± 138	1.20	1018 ± 148	1.13 ± 0.15	5.5 ± 2.3
ACT-CL J0559–5249	South-Cosmo	25	25	0.6094 ± 0.0016	1085 ± 136	0.86	1078 ± 137	1.55 ± 0.19	8.3 ± 3.0
ACT-CL J0616–5227	South-Cosmo	18	18	0.6837 ± 0.0015	1156 ± 193	0.75	1139 ± 190	1.58 ± 0.25	9.5 ± 4.5
ACT-CL J0707–5522	South	58	58	0.2958 ± 0.0005	838 ± 82	0.66	816 ± 83	1.44 ± 0.14	4.6 ± 1.3

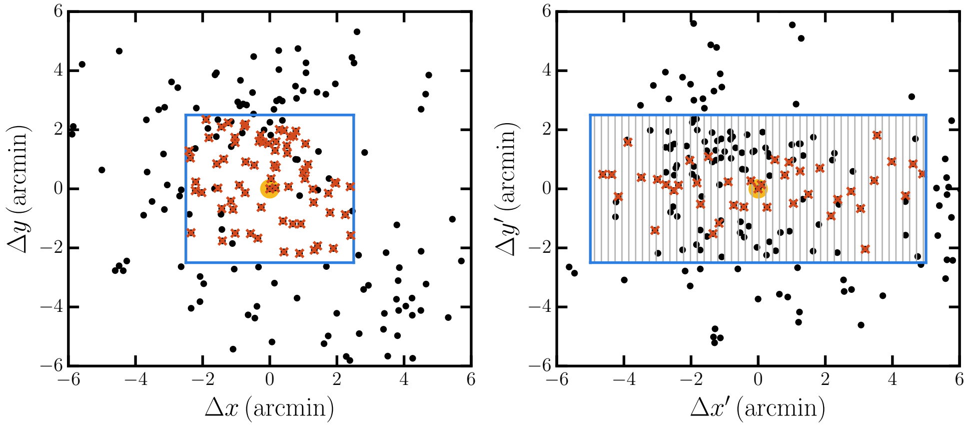

Figure 3.2: The two simulated observational strategies, for a Multidark halo of mass $M_{200} = 1.76 \times 10^{15}\mathrm{M}_{\odot}$. The same halo is shown in both panels; in the right panel axes are rotated such that the slits are placed along the horizontal axis. Angular distances are scaled to $z = 0.5$; at this redshift, the size r_{200} of this halo corresponds to $7.'6$.. Black dots are all halo members, of which red crosses are used to calculate the velocity dispersion. The orange circle in the middle marks the central subhalo, which is always used to calculate the velocity dispersion, and the blue rectangle outlines the field of view. Left: the southern strategy, in which we observed up to 70 randomly selected members in the central $5' \times 5'$. Right: the equatorial strategy, in which we observed an average 25 members inside a $10' \times 5'$ field of view along the major axis of the subhalo distribution. Grey vertical stripes show the mask slit boundaries, and only one galaxy is observed per slit.

to understand whether there is a relative bias between the two strategies compared to the "true" velocity dispersion. By "true" we mean the line-of-sight velocity dispersion obtained using all the subhaloes found in the simulation within r_{200}, where r_{200} is measured directly in the simulation as the distance from the centre of mass within which the density is 200 times the critical density. We begin by describing the Multidark simulation and then describe our mock observations of subhaloes that follow our real observing strategies.

We used haloes from the Multidark BDMW database (Riebe et al. 2013) constructed from the N-body Multidark MDPL simulation (Prada et al. 2012). The Multidark simulation is an N-body simulation containing 3840^3 dissipationless particles in a box of length $1\,h^{-1}$Gpc and run using a variation of the Gadget2 code (Springel 2005). The halo catalog was constructed using a spherical over-density halo finder that used the bound density maxima algorithm (BDM, Klypin & Holtzman 1997) with an over-density criterion of 200 times the critical density of the Universe. The cosmology used in the simulation is a concordance ΛCDM model that is consistent with Planck Collaboration (2014a); the parameters are $\Omega_{\Lambda} = 0.69$, $\Omega_{\rm m} = 0.31$, $\Omega_{\rm b} = 0.048$, $h = 0.68$, and $\sigma_8 = 0.82$. The small differences in cosmological parameters between the simulations and those adopted by us ($\Omega_{\rm m} = 0.3$, $h = 0.7$) have no impact on our results.

We select all haloes at $z = 0$ more massive than $10^{14}\,h^{-1}\mathrm{M}_{\odot}$ and containing a minimum number of 50 subhaloes more massive than $10^{12}\,h^{-1}\mathrm{M}_{\odot}$. A total of 572 haloes meet these criteria. We created mock observations of the Multidark haloes by implementing distinct algorithms for the southern and equatorial strategies to mimic our observational strategies. While the southern campaign was confined to areas $\approx 5' \times 5'$ around the BCGs, for the equatorial sample we tried to observe as far out as possible (see Section 3.2.3). First, we scaled projected distances of the subhaloes to $z = 0.5$, the median redshift of our sample. As our sample spans $0.25 < z < 1.06$, an observing field of fixed angular extent contains different fractions of r_{200}. However, as we show below, the most important parameter is the radial coverage. There is therefore no extra information in scaling distances to different redshifts.

We note that our goal in this section is not to test the membership selection algorithm, and we therefore only include subhaloes in Multidark within r_{200}. Unbound subhaloes may appear to be part of a cluster in projection, and this can bias velocity dispersion measurements. However, the same member selection and velocity dispersion algorithms used here were applied to mock catalogs including this 'interloper' population in Old et al. (2015), who showed that despite this our method is able to recover unbiased mass measurements. Instead, we aim to assess any intrinsic, *relative* biases introduced in our sample by having different observing strategies. We account for the impact of these projection effects as a systematic uncertainty in our final estimate of the dynamical mass uncertainties (see Section 3.3.4).

To simulate the southern observations, we observed up to 70 galaxies in the inner $5' \times 5'$ randomly. Given the resolution of Multidark, we were typically able to "observe" 45 subhaloes following this strategy. To recreate the equatorial observations we first identified the approximate major axis of the subhalo distribution for each cluster by taking the mean direction of the 10 largest distances between cluster members. We then created a MOS mask with slits of length $8''$ along this major axis (axis x' as per the right panel of Figure 3.2), and observed exactly one subhalo in each slit (unless there were no subhaloes in the slit area). To define which subhalo to "observe," we selected an object from each slit with a Gaussian distribution around the cluster major axis such that we preferentially, but not exclusively, observed subhaloes close to the line passing through the central subhalo (representing the BCG). This setup led to, on average, 25 subhaloes observed per cluster for the equatorial strategy. Figure 3.2 illustrates our southern and equatorial spectroscopic strategies applied to a halo of the Multidark simulation. Because the number of "observed" subhaloes per halo is lower than the number of observed galaxies per cluster, the statistical uncertainties in the velocity dispersions from the mock observations overestimate the measured uncertainties per cluster. This, however, does not compromise our assessment of a bias introduced by either strategy, and is compensated by the large number of simulated haloes used. We note that the strategies defined above are generalizations (e.g., some clusters in the equator have denser sampling and out to smaller radii). We apply the relevant corrections (see below) to all clusters irrespective of the sample they belong to (that is, southern or equatorial sample), solely based on their particular observational setup.

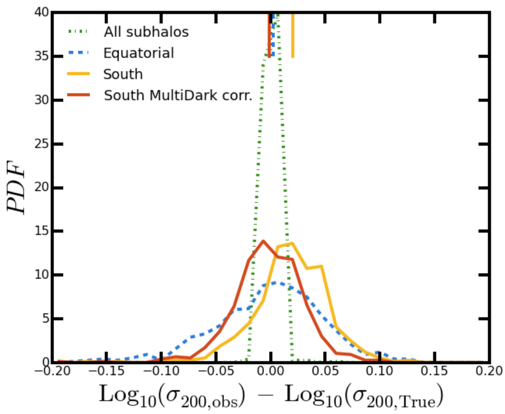

Figure 3.3: Probability distribution functions of the residuals between the measured and true velocity dispersions in the Multidark simulation, in logarithmic space. The dash-dotted green, dashed blue, and solid yellow lines show the differences using all subhaloes, an average of 25 subhaloes with the equatorial strategy, and an average of 45 subhaloes with the southern strategy, respectively. The red solid line shows the residuals in the southern strategy after correcting for incomplete sky coverage (see Section 3.3.2). Vertical lines at the top of the figure show the median values.

The residuals in the recovered velocity dispersions with respect to the true halo velocity dispersion (i.e., that determined using all subhaloes, typically 60) are shown in Figure 3.3 for each observational strategy. As a consistency check, we also show the residuals determined from measuring the velocity dispersion from all subhaloes within r_{200}, as determined iteratively from the mock observations following the procedure described in Section 3.3.1, which are consistent with the true velocity dispersions within the statistical uncertainty. This comparison shows that the adopted scaling relation (see Section 3.3.3) is consistent with the scaling of Multidark haloes and that, in an ideal case where we observe all subhaloes, our estimates of both σ_{200} and r_{200} (and thereby M_{200}) are unbiased.

Figure 3.3 also shows the distribution of velocity dispersions recovered from the simulations for both our observing strategies. For the equatorial strategy the velocity dispersions are unbiased, meaning that the velocity distributions are well sampled within the statistical precision we require—there is no bias introduced by sampling galaxies along a particular direction (but see Skielboe et al. 2012, for evidence of a preferred direction for the velocity distribution in galaxy clusters). The velocity distribution derived from the southern strategy is, on the other hand, biased by 0.02 dex (corresponding to $\approx 5\%$) on average, which is consistent with the picture of a decreasing velocity dispersion outward from the cluster centre (e.g., Mamon et al. 2010). We correct for this bias by measuring the *true* integrated velocity dispersion profiles for Multidark haloes and scaling them up to $\sigma_{200} \equiv \sigma(r = r_{200})$. We list the radial correction $\sigma(< r)/\sigma_{200}$ and the associated scatter in Table 3.3, and show it in Figure 3.4. While the spread increases towards small apertures, the correction is $< 10\%$ at all radii. However, at small radii the scatter is large and must be included in the error estimate when measuring velocity dispersions. We apply this correction to each halo when observed with the southern strategy and are able to recover unbiased velocity dispersions (see Figure 3.3).

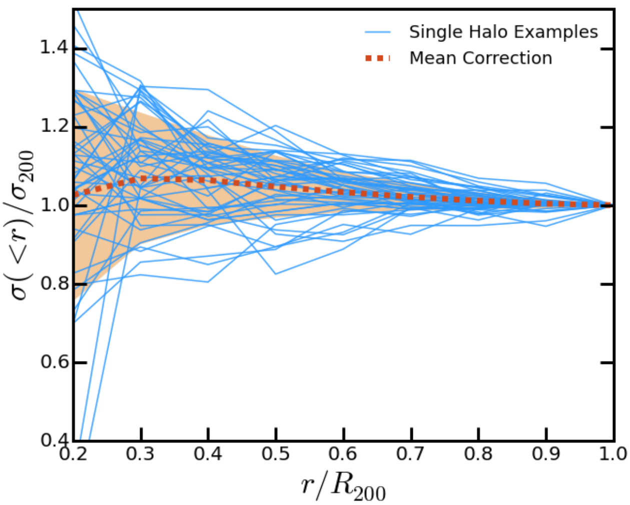

Figure 3.4: Enclosed one-dimensional velocity dispersion, $\sigma(< r)$, as a function of radius, r, for subhaloes in Multidark, normalized to σ_{200} and r_{200}, respectively. The red dashed line is the mean value, and the orange region encloses 68% of the haloes. Blue lines are a random subset of the Multidark haloes. The data for this figure are presented in Table 3.3.

3.3.3. From velocity dispersions to dynamical masses

In Sifón et al. (2013), we used the $\sigma - M_{200}$ scaling relation of Evrard et al. (2008) to estimate dynamical masses. As discussed in Section 3.1, the scaling relation of Evrard et al. (2008) was calibrated from a suite of N-body simulations using dark matter particles to estimate velocity dispersions. However, the galaxies, from which velocity measurements are made in reality do not sample the same velocity distribution as the dark matter (hereafter DM) particles. They feel dynamical friction and some are tidally disrupted, which distorts their velocity distribution and biases their dispersion (e.g., Carlberg 1994; Colín et al. 2000). Recent high resolution hydrodynamical simulations of “zoomed” cosmological haloes have shown that there is a significant difference between the velocity distributions of DM particles and galaxies themselves; whether galaxies (i.e., overdensities of stars in hydrodynamical simulations) or dark matter subhaloes are used makes comparatively little difference (Munari et al. 2013). Results from state-of-the art numerical simulations depend on the exact definition of a galaxy and the member selection applied, but the current consensus is that galaxies are biased high (i.e., at a given mass the velocity dispersion of galaxies or subhaloes is larger than that of DM particles) by 5−10% with respect to DM particles (Lau et al. 2010; Munari et al. 2013; Wu et al. 2013), translating into a positive 15−20% bias in dynamical masses when using DM particles. This is illustrated in Figure 3.5: DM particles are not significantly impacted by either dynamical friction or baryonic physics; therefore the scaling relations for DM particles are essentially the same for all simulations. In contrast, dark matter subhaloes are affected by baryons in such a way that including baryonic feedback (most importantly feedback from active galactic nuclei (AGN), but also from cooling and star formation) makes their velocity dispersions much more similar to those of simulated galaxies. This means we can rely on our analysis of the previous section, based on dark matter subhaloes, to correct the velocity dispersions measured for ACT clusters, and then estimate dynamical masses using predictions obtained either from galaxies or subhaloes. The difference between the Saro et al. (2013) and Munari et al. (2013) galaxy scaling relations depends on the details of the semi-analytic and hydrodynamical implementations used in Saro et al. (2013) and Munari et al. (2013), respectively. The different cosmologies used in the Millenium simulation (in particular, $\sigma_8 = 0.9$; Springel et al. 2005) by Saro et al. (2013) and the simulations by Munari et al. (2013) ($\sigma_8 = 0.8$) may also play a role.

r/r_{200}	$\langle\sigma(<r)/\sigma_{200}\rangle$
0.2	1.03 ± 0.27
0.3	1.07 ± 0.17
0.4	1.06 ± 0.11
0.5	1.05 ± 0.08
0.6	1.03 ± 0.05
0.7	1.02 ± 0.04
0.8	1.01 ± 0.02
0.9	1.00 ± 0.01
1.0	1.00 ± 0.00

Table 3.3: Ratio of one-dimensional velocity dispersion within an aperture r, $\sigma(<r)$, to the one-dimensional velocity dispersion within r_{200}, σ_{200}, estimated using subhaloes in the Multidark simulation. Uncertainties are the standard deviations. These values are plotted in Figure 3.4.

We therefore use the scaling relation between the projected galaxy velocity dispersion and mass estimated by Munari et al. (2013), obtained from zoomed-in hydrodynamical simulations of dark matter haloes, that includes prescriptions for cooling, star formation, and AGN feedback,

$$\sigma_{200} = A_{\rm 1D} \left[\frac{h\,E(z)\,M_{200}}{10^{15}{\rm M}_\odot} \right]^\alpha \tag{3.1}$$

where σ_{200} is the 3-dimensional velocity dispersion of galaxies within r_{200}, divided by $\sqrt{3}$ (i.e., the line-of-sight velocity dispersion in a spherical cluster), $E(z) = [\Omega_\Lambda + (1+z)^3\Omega_{\rm m}]^{1/2}$, $A_{\rm 1D} = 1177 \pm 4.2\,{\rm km\,s^{-1}}$, and $\alpha = 0.364 \pm 0.002$. The intrinsic scatter *at fixed mass* in Equation 3.1 is of order 5%, or ≈15% in mass (Munari et al. 2013), but this value does not include the effect of interlopers (that is, impurity in the member sample), which can increase the intrinsic scatter by up to a factor two (Biviano et al. 2006; Mamon et al. 2010; White et al. 2010; Saro et al. 2013). This is an irreducible uncertainty since there is always a fraction of contaminating galaxies that cannot be identified by their peculiar velocities because they overlap with the velocity distribuion of actual members (see, e.g., figure 10 of White et al. 2010). Hence we adopt a figure of 30% for each cluster's mass uncertainty arising from interlopers in the member sample. Note that we automatically account for the velocity bias, $b_{\rm v}$, by adopting a scaling relation based on simulated galaxies rather than dark matter particles[18] (see Section 3.3.4 for further discussion).

The velocity dispersion measurements were obtained for a pre-selected set of clusters, and the sample was not further refined based on these measurements. So although the measurements are affected by noise and intrinsic scatter, we can expect positive and negative noise and scatter excursions to be equally likely. The dynamical mass measurements on this sample are thus not affected by Eddington bias; this is discussed further in Section 3.A. We therefore calculate dynamical masses by directly inverting Equation 3.1, which gives $\sigma(M)$, in order to obtain $M(\sigma)$. For this computation we take the uncertainty on σ to be normal, and report the mean and standard deviation of $M(\sigma)$ after propagating the full error distribution.[19] We note that this procedure can yield biased dynamical masses if velocity dispersion and SZ effect measurements are correlated for individual clusters (Evrard et al. 2014). In fact, we may expect some degree of correlation between any pair of observables for a given cluster, because the same large scale structure is affecting all cluster observables (White et al. 2010). We defer a proper treatment of correlations between observables to future work.

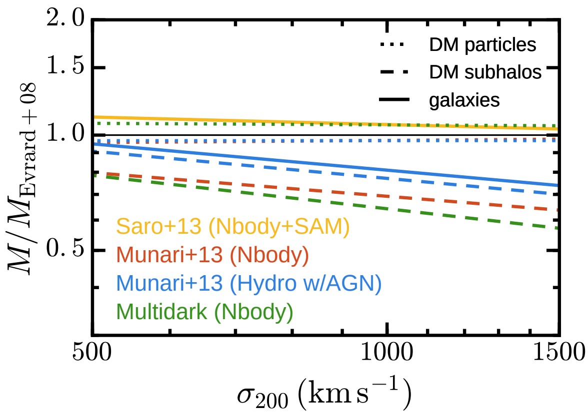

Figure 3.5: Comparison between different $\sigma-M$ scaling relations, relative to the scaling relation of dark matter particles derived by Evrard et al. (2008). Dotted, dashed and solid lines show scaling relations for dark matter particles, dark matter subhaloes and galaxies, respectively. We show the scaling relation for galaxies derived from a semi-analytic model implemented in a dark matter-only simulation by Saro et al. (2013) in yellow. Red and blue lines show the scaling relations derived from dark matter-only and full hydrodynamical simulations, respectively, by Munari et al. (2013), and the green lines show scaling relations from the Multidark simulation. In this work, we calculate dynamical masses using the scaling relation given by the blue solid line.

3.3.4. Dynamical mass estimates

The masses thus estimated are listed in Table 3.2, along with the redshifts, velocity dispersions, number of members used and r_{200}. We also list the radius at which our spectroscopic coverage ends, r_{max}, and the initial velocity dispersion measured within r_{max}. Below we summarize the corrections applied with respect to our analysis in Sifón et al. (2013) and then present a detailed account of uncertainties entering our dynamical mass estimates, before comparing our mass estimates with masses derived from SZ measurements.

Two sources of bias are now accounted for that were not included in Sifón et al. (2013). The first is the radial coverage of spectroscopic members (which was discussed, but not corrected for, in Sifón et al. 2013) which includes (i) an iterative calculation of the velocity dispersion within r_{200} only for 24 clusters with $r_{\mathrm{max}} > r_{200}$ and (ii) a correction to the velocity

[18] We assume that the spatial distribution of simulated galaxies is identical to that in real clusters.

[19] The error distribution is normal in σ but not in $M \propto \sigma^{1/\alpha}$ (with $1/\alpha \approx 3$). Therefore the mean mass is not the cube of the central value of σ. This difference depends only on the measurement uncertainty and for our sample its median is 3%, with a maximum of 16% for ACT-CL J0206.2−0114.

Table 3.4: Individual cluster mass uncertainty budget, given as a fraction of cluster mass. Central values are the medians of the cluster distributions and uncertainties are 16th and 84th percentiles; upper limits are 84th percentiles. The median is equal to zero for all values with upper limits. "Reported" uncertainties correspond to those in Table 3.2, which arise from the combination of the three effects preceding them, while "total" uncertainties include the 30% scatter from the $\sigma - M$ scaling relation, which is fixed for all clusters, added in quadrature. The 15% uncertainty in the velocity bias is an overall uncertainty on the average masses.

Source	Equator	South	All
Statistical	$0.31^{+0.21}_{-0.08}$	$0.25^{+0.09}_{-0.03}$	$0.28^{+0.20}_{-0.06}$
Member selection	$0.14^{+0.18}_{-0.14}$	< 0.01	$0.04^{+0.18}_{-0.04}$
Multidark correction	< 0.12	$0.07^{+0.18}_{-0.07}$	< 0.18
Reported	**0.36**	**0.26**	**0.31**
Scatter in $M(\sigma)$	0.30	0.30	0.30
Total	**0.47**	**0.40**	**0.44**
Velocity bias uncertainty	0.15	0.15	0.15

dispersion, based on the velocity dispersion profile of subhaloes in the Multidark simulation (see Figure 3.4), for 20 clusters with $r_{\rm max} < r_{200}$. Over the full sample these two situations produce a net correction of −5%, compared to applying no correction as in Sifón et al. (2013). The second source of bias is the relation between the velocity dispersion of dark matter particles and that of galaxies. We account for this difference by using the $\sigma - M$ scaling relation of galaxies derived by Munari et al. (2013), which gives average masses 20% lower than those derived from the scaling relation of Evrard et al. (2008) used in Sifón et al. (2013). In addition, we have updated the minimum bin size in our member selection algorithm (cf. Section 3.3.1), which lowers the masses by an average 6% with respect to the value adopted in Sifón et al. (2013). Because of these updates to our analysis, for the southern clusters we report masses that are, on average, (71 ± 8)% of those reported in Sifón et al. (2013).

We present a breakdown of the contributions to individual cluster mass uncertainties for the equatorial and southern samples in Table 3.4. The uncertainty budget is dominated by the scatter induced by interlopers. Based on the discussion presented in Section 3.3.3, we estimate that this uncertainty amounts roughly to 30% in mass. Because this contribution corresponds to a constant uncertainty for all clusters, we do not include them in the uncertainties reported in Table 3.2. We do recommend this 30% systematic (i.e., that cannot be reduced by observing more galaxies) uncertainty to be added to the reported uncertainties in any cosmological analysis that uses these dynamical masses, and we include it in our calculation of the SZ mass bias in Section 3.3.5. Similarly, based on the discussion in Section 3.1, we adopt a 15% systematic uncertainty arising from the unknown velocity bias (5% in velocity; e.g., Wu et al. 2013). This 15% essentially accounts for i) the fact that our galaxy sample may not correspond to the galaxy samples used by Munari et al. (2013) to arrive at Equation 3.1 (because the velocity bias is luminosity-dependent), and ii) differences in scaling relations compared to that of Munari et al. (2013) that may arise because of different hydrodynamical implementations (each producing a different velocity bias). The unknown velocity bias therefore limits our constraints on the SZ mass bias (see Section 3.3.5).

Statistical uncertainties are the dominant contribution to the reported uncertainties, with a median contribution of 28% of the cluster mass. Uncertainties from member selection and the scatter in the correction of Table 3.3 are subdominant. We note here that by "member selection" we mean uncertainties arising from including or rejecting particular galaxies through the shifting gapper. The true uncertainty from contaminating galaxies is included in the scaling relation scatter as discussed in Section 3.3.3. We make this distinction because there is a fraction of false members which cannot be identified observationally via their peculiar velocities (e.g., Mamon et al. 2010; White et al. 2010; Saro et al. 2013). For the SZ-selected clusters of the South Pole Telescope survey, Ruel et al. (2014) found that the uncertainty from member selection, estimated by "pseudo-observing" their stacked cluster, depends on the number of galaxies observed. For the number of members we observed (which is roughly a factor two larger than the average number of members observed by Ruel et al. 2014), their estimate of the combined statistical and member selection uncertainty is consistent with ours.

3.3.5. Comparison to SZ-derived masses

The usefulness of clusters for constraining cosmological parameters depends on the accurate calibration of the cluster mass scale. Calibrated SZ masses are especially informative because SZ surveys yield large samples of clusters reaching to high redshifts. While our dynamical and SZ mass proxies may have non-trivial mass or redshift-dependence, the data in our study permit us to constrain the average bias between these proxies within the mass range probed in this study.

We compare the dynamical masses to the SZ-derived masses, $M_{500}^{\rm SZ}$, in Figure 3.6. For the purpose of this comparison we rescale dynamical masses to M_{500} using the mass-concentration relation of Dutton & Macciò (2014). The SZ-derived masses assume a scaling relation between the SZ effect (specifically, Y_{500}) and mass based on the pressure profile of Arnaud et al. (2010), derived from X-ray observations of local ($z < 0.2$) clusters, and have been corrected for Eddington bias as detailed in Hasselfield et al. (2013), assuming a 20% intrinsic scatter in Y_{500} at fixed true mass (the "UPP" masses of Hasselfield et al. 2013). We refrain from fitting a scaling relation to these data since this requires a proper calibration of the survey selection effects and accounting for the mass function and cosmological parameters; the dynamical mass–SZ scaling relation and inferred cosmological parameters will be presented in a future paper.

Beyond the assumptions used to obtain the SZ masses, any additional bias in the inferred mass relative to the true cluster mass is often parametrized in terms of the SZ mass bias, $1-b_{\rm SZ}$ (e.g., Planck Collaboration 2015c), defined by the relation $\langle M_{\rm SZ}|M_{\rm true}\rangle = (1-b_{\rm SZ})M_{\rm true}$. An understanding of this calibration is essential to the cosmological interpretation of cluster counts from SZ surveys. Similarly, our dynamical masses may be biased proxies for the true cluster mass. Following Hasselfield et al. (2013), we parametrize this bias with $\beta_{\rm dyn}$, defined by $\langle M_{\rm dyn}|M_{\rm true}\rangle \equiv \beta_{\rm dyn} M_{\rm true}$. For the remainder of this section we use the word "bias" to refer to systematic effects on the sample, such as "Eddington bias," that do not average down to an expectation value of zero with an increasing sample size.

The SZ and dynamical mass data permit us to place limits on the ratio $(1-b_{\rm SZ})/\beta_{\rm dyn}$ by comparing the average SZ and dynamical masses of the clusters from the cosmological sample. We first combine the dynamical masses into a single characteristic mass

$$\bar{M}_{\rm dyn} \equiv \frac{\sum_i w_i M_{i,\rm dyn}}{\sum_i w_i}, \tag{3.2}$$

where the $M_{i,\rm dyn}$ represent the individual dynamical mass measurements, and the w_i are weighting factors. For this analysis we set all $w_i = 1$, but see below for further discussion of the choice of weights. We also compute the error, through standard error analysis.[20] For the SZ masses, we form the analagous sum, $\bar{M}_{\rm SZ} \equiv (\sum_i w_i M_{i,\rm SZ})/(\sum_i w_i)$. Note that the weights

[20] The error in $\bar{M}$ is $(\sum_i w_i^2 \epsilon_i^2)^{1/2}/(\sum_i w_i)$, where ϵ_i is the error in M_i.

w_i used in this expression are the same weights used to compute $\bar{M}_{\rm dyn}$; this is essential to obtaining an unbiased answer when we later combine the two characteristic masses.

Each mass measurement is contaminated by intrinsic scatter and noise, in the sense that

$$\bar{M}_{i,\rm dyn} = M_{i,\rm true} e^{\xi_i} + \delta M_i, \tag{3.3}$$

where $\delta M_{i,\rm true} \sim \mathcal{N}(0, \epsilon_i)$ is the contribution from measurement noise, and $\xi_i \sim \mathcal{N}(0, 0.3)$ is the contribution from intrinsic scatter. The expectation value for δM_i is zero, while the expectation value of e^{ξ_i} is 1.046. So when we combine our measurements into a characteristic mass we expect that

$$\langle \bar{M}_{\rm dyn} \rangle = \frac{\sum_i w_i \langle M_{i,\rm dyn} \rangle}{\sum_i w_i} = 1.046\, \beta_{\rm dyn} \frac{\sum_i w_i M_{i,\rm true}}{\sum_i w_i}. \tag{3.4}$$

For the combination of the SZ masses, the expectation value is $\langle \bar{M}_{\rm SZ} \rangle = 1 - b_{\rm SZ}$, because the skewness introduced by intrinsic scatter has already been fully accounted for in the calculation of the $M_{\rm SZ}$ values used here by Hasselfield et al. (2013). Taking the ratio of these two characteristic masses gives

$$\frac{\langle \bar{M}_{\rm SZ} \rangle}{\langle \bar{M}_{\rm dyn} \rangle} = \frac{(1 - b_{\rm SZ})}{1.046\, \beta_{\rm dyn}}. \tag{3.5}$$

Our measured values of $\bar{M}_{\rm SZ}$ and $\bar{M}_{\rm dyn}$ thus provide a useful meaurement of $(1 - b_{\rm SZ})/\beta_{\rm dyn}$. (We show in Section 3.A that this ratio is unbiased.) For the 21 clusters in the cosmological sample, the characteristic dynamical mass under uniform weights is $\bar{M}_{\rm dyn} = (4.8 \pm 0.5) \times 10^{14} \mathrm{M}_\odot$, and the characteristic SZ mass is $\bar{M}_{\rm SZ} = (5.0 \pm 0.2) \times 10^{14} \mathrm{M}_\odot$. The ratio of calibration factors is then

$$\frac{(1 - b_{\rm SZ})}{\beta_{\rm dyn}} = 1.10 \pm 0.13\,(\mathrm{stat.}) \pm 0.14\,(\mathrm{syst.}) \tag{3.6}$$

where the 0.14 systematic uncertainty arises from the 15% fractional uncertainty on the average dynamical masses due to the unknown velocity bias discussed in Section 3.3.4. We note again that, in computing Equation 3.6, we have accounted for the 30% scatter in the $M(\sigma)$ relation (see Section 3.3.3) which is not included in the cluster mass uncertainties reported in Table 3.2 and shown in Figure 3.6. Recent estimates of the SZ mass bias combining weak lensing measurements and SZ mass estimates from Planck Collaboration (2015b) have found $M_{\rm SZ}/M_{\rm WL} \approx 0.7$ (von der Linden et al. 2014b; Hoekstra et al. 2015). These measurements were then used as priors for the cosmological analysis of Planck SZ-selected clusters (under the assumption that $\langle M_{\rm WL} \rangle = \langle M_{\rm true} \rangle$, Planck Collaboration 2015c), highlighting the importance of calibrating these biases. We note that both von der Linden et al. (2014b) and Hoekstra et al. (2015) probed higher masses than we do. In fact, both works found evidence (at 95% confidence) for a mass-dependent bias which, at the typical masses of ACT clusters, is consistent with our estimate. Similar to us, Rines et al. (2016) found no evidence that the mass ratio $\langle \bar{M}_{\rm SZ} \rangle / \langle \bar{M}_{\rm dyn} \rangle$ is different from unity, using dynamical masses estimated with the caustic technique, in a mass regime similar to ours.

Battaglia et al. (2016) used a stacked weak lensing measurement on a subset of these clusters, which they fit using hydrodynamical simulations, and found an SZ mass bias $1 - b_{\rm SZ} = \bar{M}_{\rm SZ}/\bar{M}_{\rm WL} = 0.98 \pm 0.28$ (assuming $\langle M_{\rm WL} | M_{\rm true} \rangle = M_{\rm true}$, as has been assumed in recent studies). This value has been computed with weights that depend on the weak lensing measurements.

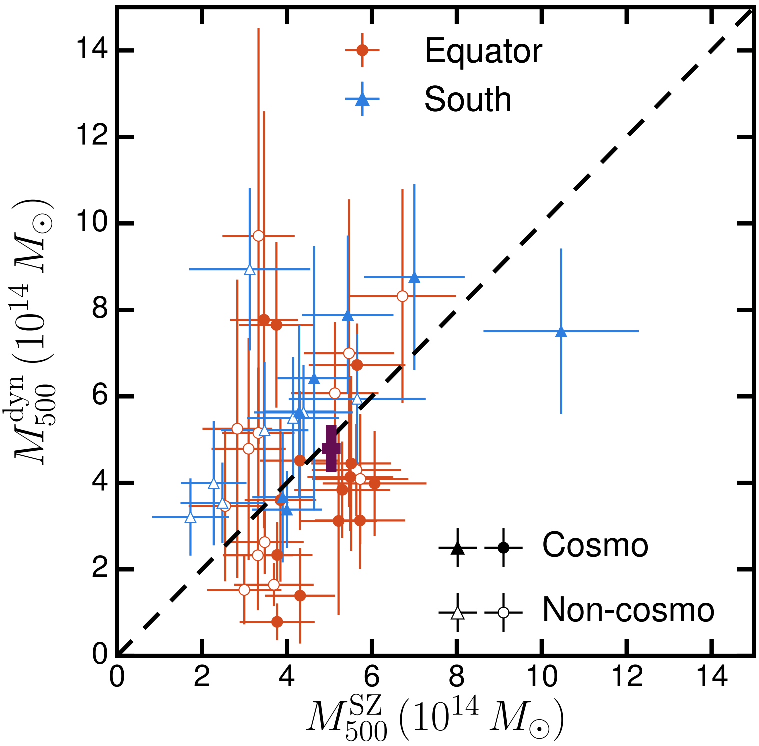

Figure 3.6: Comparison of dynamical and SZ-derived masses. Red circles and blue triangles show clusters in the equatorial and southern samples, respectively. Uncertainties on dynamical masses correspond to those reported in Table 3.2, and for clarity do not include the 30% scatter in the $M(\sigma)$ relation. The dashed line shows equality and the purple cross shows the average SZ and dynamical masses of the combined southern and equatorial cosmological samples (filled symbols), calculated including the 30% intrinsic scatter in the $M(\sigma)$ relation on the dynamical masses. There is an additional 15% overall uncertainty on dynamical masses arising from the unknown galaxy velocity bias. See Section 3.3.5 for details.

As a consistency check, we estimate the average dynamical mass of the nine clusters used by Battaglia et al. (2016), using the same weak lensing weights, and find $\bar{M}_{\rm dyn-WL} = (4.7 \pm 1.4) \times 10^{14} {\rm M}_\odot$, which implies a mass ratio $\bar{M}_{\rm dyn-WL}/\bar{M}_{\rm WL} = 0.98 \pm 0.33$. Therefore the dynamical masses are consistent with the weak lensing masses derived by Battaglia et al. (2016).

We have used uniform weights $w_i = 1$ to obtain the ratio in Equation 3.6, but one might expect that more carefully chosen weights could provide a more precise answer. In fact the weights should be chosen with some care, as it is possible to introduce a bias into this ratio if one permits the weights to depend too much on the measured data themselves. For example, if we take weights $w_i = 1/\epsilon_{i,\rm dyn}^2$ (where $\epsilon_{i,\rm dyn}$ is the measurement uncertainty on the velocity dispersion of cluster i), we find that clusters with low dynamical mass are more strongly weighted, because the dynamical mass uncertainties are strongly correlated with the dynamical mass measurements. However, the SZ masses are limited by sample selection effects to lie above some minimum value, and the characteristic SZ mass under these weights is almost twice the characteristic dynamical mass. A somewhat weaker effect is that these weights (i.e., the w_i above) have the potential to introduce a sort of Eddington bias into the computation, even though we carefully constructed a sample for which the dynamical mass measurements were unbiased. By re-weighting the clusters in a way that is correlated with the dynamical mass measurements themselves, we are effectively sub-selecting for measurements that are more likely to have scattered below the true mass values.

To avoid such biases, one should not incorporate dynamical mass or its uncertainty into the weights. Similarly, one should be wary of using the measured SZ masses and uncertainties to set the weights. In the present data, using weights $w_i = 1/\epsilon^2_{i,\mathrm{SZ}}$ or $w_i = M^2_{i,\mathrm{SZ}}/\epsilon^2_{i,\mathrm{SZ}}$ changes the resulting ratio by +3 or -2%, respectively, without reducing the uncertainty. We discuss alternative weighting schemes in Section 3.A.

3.3.6. Cluster substructure

Probes of substructure within a galaxy cluster provide information on a cluster's dynamical state: for example, whether or not a recent merger event has occurred. Since the thermodynamic properties of clusters vary depending on their dynamical state, a measurement of the amount of substructure provides an important additional cluster property. Of particular interest to SZ experiments is how the integrated Y parameter fluctuates with dynamical state. Simulations have shown that Y can fluctuate by tens of percent shortly after merger events (e.g., Poole et al. 2007; Wik et al. 2008; Krause et al. 2012; Nelson et al. 2012), and that the intrinsic scatter of the $Y - M$ scaling relation for a subsample of relaxed clusters is smaller than for the entire sample (e.g., Battaglia et al. 2012; Yu et al. 2015). The latter conclusion was also reached by Sifón et al. (2013), albeit with low statistical significance.

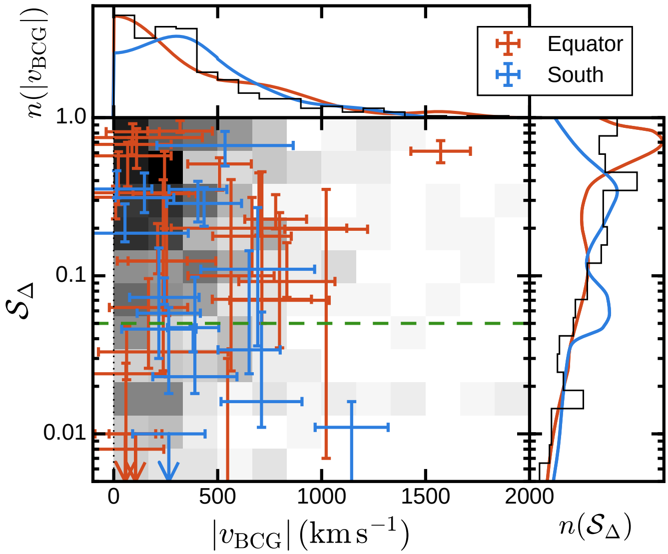

Figure 3.7: Comparison between BCG peculiar velocity and DS test significance level for the southern (blue) and equatorial (red) samples, and haloes in the Multidark simulation (grey scale background, where zero is white and one is black, and black histograms). The green, dashed horizontal line shows the threshold $\mathscr{S}_\Delta = 0.05$, below which the DS test is usually considered to provide evidence for substructure. The top and right panels show the corresponding histogram for the Multidark simulation and the summed probability distribution functions for the southern (blue) and equatorial (red) clusters, normalized to subtend the same area as the histograms.

Because of the sparser spectroscopic sampling used for the equatorial clusters, it is more difficult to identify localized substructure than it is with our dense sampling of the southern clusters (which is, however, confined to a smaller region of the cluster). We therefore refrain from a detailed, cluster-by-cluster analysis of substructure in the equatorial sample as we did for the southern clusters in Sifón et al. (2013). However, it is still valuable to study the presence of substructure in the sample as a whole, to be able to compare between our equatorial and southern samples, and whether the SZ selects different cluster populations than other techniques.

We use two quantities used by Sifón et al. (2013) to study cluster substructure. The first is the peculiar velocity of the BCG, $v_{\rm BCG} = c(z_{\rm BCG} - z_{\rm cl})/(1+z_{\rm cl})$, where $z_{\rm cl}$ is the cluster redshift listed in Table 3.2. Based on the results of Section 3.2.6, we assume an error of $100\,{\rm km\,s^{-1}}$ on $v_{\rm BCG}$. The second estimator we use is the DS test (Dressler & Shectman 1988), which measures the deviation of the velocity distribution in localized regions of a cluster with respect to the cluster as a whole through the statistic $\Delta = \sum_i \delta_i$, where

$$\delta^2 = \frac{N_{\rm local}}{\sigma^2}\left[(\bar{v}_{\rm local} - \bar{v})^2 + (\sigma_{\rm local} - \sigma)^2\right]^2 \tag{3.7}$$

is calculated for each galaxy, where $\bar{v}_{\rm local}$ and $\sigma_{\rm local}$ are the mean and dispersion of the velocity distribution of the $N_{\rm local}$ nearest neighbors, where typically $N_{\rm local} = \sqrt{N_{200}}$. For each cluster we compare Δ to 1000 realizations where we shuffle the galaxy velocities, keeping their positions fixed. $\mathscr{S}_\Delta$ is then the probabilitiy to exceed the Δ measured for the clusters, given statistical fluctuations as determined through these realizations. We calculate 68% level uncertainties on $\mathscr{S}_\Delta$ by varying $N_{\rm local}$ in the range $\sqrt{N_{200}} - 3 \leq N_{\rm local} \leq \sqrt{N_{200}} + 3$. Typically, $\mathscr{S}_\Delta < 0.05$ is taken as evidence for substructure (Pinkney et al. 1996). See Sifón et al. (2013) for more details.

We compare in Figure 3.7 the distributions of (absolute values of) BCG peculiar velocities, $|v_{\rm BCG}|$, and $\mathscr{S}_\Delta$ to those found in the Multidark simulation. In general, the southern sample shows more evidence of substructure than the equatorial sample through the DS test, with 38% and 22%, respectively, having $\mathscr{S}_\Delta < 0.05$. In turn, 31% of Multidark clusters fulfill this criterion. Two-sided Kolmogorov-Smirnov tests, however, show no evidence of the distributions of either $\mathscr{S}_\Delta$ or $|v_{\rm BCG}|$ being different between the southern, equatorial and Multidark samples (all p-values from the KS tests are $\gtrsim 0.20$). In Sifón et al. (2013), we selected clusters as non-relaxed (i.e., containing substructure) if, among other properties, they had $|v_{\rm BCG}| > 0$ at 95% confidence. In the southern sample 50% of clusters pass this test, while 41% (11/27) of the clusters in the equatorial sample do. This 40–50% rate of non-relaxed clusters is somewhat lower than fractions found for X-ray– and optically–selected clusters (e.g., Böhringer et al. 2010; Wen & Han 2013). Using mock cluster observations, Lin et al. (2015) showed that the SZ significance can be boosted by up to 10% for cool core (i.e., relaxed) clusters depending on the redshift, cuspiness and size of the cluster. This would then lead to a preferential selection of relaxed clusters, qualitatively consistent with our results. The fact that this bias is not apparent when comparing to Multidark clusters may relate to the fact that Multidark is a dark matter only simulation, but a detailed comparison is beyond the scope of this work.

3.3.7. The impact of centring on the BCG

As mentioned in Section 3.3.1, we have assumed that the BCGs correspond to the centre of the cluster potential. In this section we estimate the impact of this assumption on the reported masses.

We first re-calculate the velocity dispersions for all clusters assuming that the cluster centre is the centre of light instead of the BCG. To estimate the centre of light we take the luminosity-weighted average position of photometric members using photometric redshifts estimated by Menanteau et al. (2013) using the Bayesian Photometric Redshift (BPZ) code (Benítez 2000). The average mass ratio is $\langle M_{\rm CoL}/M_{\rm BCG}\rangle = 1.01 \pm 0.09$ with a standard deviation of 0.16, which is within the quoted mass uncertainties. Note that Viola et al. (2015) have shown, using weak lensing measurements, that the centre of light is generally significantly offset from the true cluster centre while BCGs are, on average, consistent with being at the centre of the cluster potential.

We also looked for clusters whose BCG cannot be identified unambiguously because there are other similarly bright member galaxies. Three southern (ACT-CL J0215−5212, ACT-CL J0232−5257 and ACT-CL J0521−5104) and four equatorial (ACT-CL J0239.8 −0134, ACT-CL J0256.5+0006, ACT-CL J2055.4+0105 and ACT-CL J2302.5+0002) clusters fall under this category (see Menanteau et al. 2010b, 2013, for optical images of ACT clusters; Section 3.4 for more detailed comments on some of these clusters). We estimate the masses of these clusters once more, taking the next most probable BCG candidate (where this is determined by visual inspection) as the cluster centre. In all cases the mass difference is well within the reported uncertainties.

From these two tests we conclude that uncertainties due to the choice of cluster centre are within the quoted errorbars and therefore cluster centring does not introduce any biases or additional uncertainties on our mass estimates.

3.4. Notable clusters

In this section we describe notable clusters in the equatorial sample in more detail; similar notes on southern clusters can be found in Sifón et al. (2013). We first summarize ACT clusters that have been studied in detail elsewhere and then discuss new clusters.

3.4.1. Previously studied ACT clusters

El Gordo (ACT-CL J0102−4915, $z = 0.87$, Menanteau et al. 2012) is probably the most massive cluster known at $z > 0.8$ (Jee et al. 2014b). It is a merging system composed of two roughly equal-mass subclusters colliding approximately perpendicular to the line-of-sight (Zitrin et al. 2013; Jee et al. 2014b), probably seen about 1 Gyr after core passage (Ng et al. 2015). It hosts the highest-redshift known radio relics and halo (Lindner et al. 2014). Its dynamical mass ($M_{200} = (1.13 \pm 0.29) \times 10^{15}\,\mathrm{M}_\odot$, cf. Table 3.2) is significantly smaller than the total mass estimated from weak lensing ($M_{200} = (2.84 \pm 0.51) \times 10^{15}\,\mathrm{M}_\odot$, Jee et al. 2014b), but the former can be expected to be biased when such an extreme system is assumed to be composed of a single component (as is the case here for consistency with the rest of the sample). As a result of the major merger, the total stellar mass in El Gordo is lower than the expectation based on its SZ effect (Hilton et al. 2013).

ACT-CL J0022.2−0036 ($z = 0.81$) is the highest-significance detection in the S82 sample (Hasselfield et al. 2013). The dynamical mass is consistent with independent mass estimates from weak lensing (Miyatake et al. 2013), optical richness and high-resolution SZ measurements (Reese et al. 2012), giving an inverse-variance-weighted average mass of $M_{200} = (7.8 \pm 0.9) \times 10^{14}\mathrm{M}_\odot$ (see also the discussion in Menanteau et al. 2013).

ACT-CL J0256.5+0006 ($z = 0.36$) was studied in detail by Knowles et al. (2015). It is one of the lowest-mass systems known to host a giant radio halo, which is likely produced by the interaction of two systems with a mass ratio of approximately 2:1 being observed prior to the first core crossing. The merging scenario is supported by the velocity distribution (ACT-CL J0256.5+0006 has $\mathscr{S}_\Delta < 0.01$ at 68% confidence) and X-ray observations; there are two X-ray peaks coincident with two dominant galaxies. The velocity dispersions of the two components suggests that the reported mass, which assumes a single component, may be biased high by roughly 40%, an amount comparable to the quoted uncertainty.

ACT-CL J0320.4+0032 ($z = 0.385$) is one of the few clusters whose BCG is known to host a type II quasar (Kirk et al. 2015). The low number of observed members precludes a detailed analysis of the cluster structure, but we note that a maximally-predictive histogram (Knuth 2006) of the galaxy velocities shows two peaks and a somewhat asymmetric distribution (see Figure 3.14), which suggests that ACT-CL J0320.4+0032 is a dynamically young cluster.

3.4.2. ACT-CL J0218.2−0041

ACT-CL J0218.2−0041 ($z = 0.673$) is one of the lowest-mass clusters in the sample (Table 3.2). In addition to the cluster itself, we have identified in our spectroscopic data an overdensity of eight galaxies at $z = 0.82$. Their velocity dispersion, while not necessarily representative of this system's velocity dispersion, is $\sigma_{\rm gal} = 880\,{\rm km\,s^{-1}}$, which would suggest a mass $M > 10^{14}{\rm M}_{\odot}$. We additionally identified a structure of 12 galaxies around $z = 0.73$ which, although it only spans $6000\,{\rm km\,s^{-1}}$, has $\sigma_{\rm gal} = 2320\,{\rm km\,s^{-1}}$, suggesting that the structure is probably not collapsed.

Two of the three structures have velocity dispersions that suggest cluster-sized systems. The fact that we detect these overdensities, instead of non-members being scattered in redshift space, suggests that ACT-CL J0218.2−0041 may be associated with a larger cosmic structure along the line of sight, with two relatively massive clusters at $z = 0.67$ and $z = 0.82$ possibly connected by a filament (the $z = 0.73$ structure). For comparison, we also detected additional galaxy overdensities in the lines of sight of ACT-CL J0235−5121 (7 galaxies at $z = 0.44$) and ACT-CL J0215.4+0030 (8 galaxies at $z = 0.39$), which have $\sigma_{\rm gal} = 280\,{\rm km\,s^{-1}}$ and $\sigma_{\rm gal} = 170\,{\rm km\,s^{-1}}$, respectively. This shows that low-mass groups may in fact be identified with our observations—that is, the structures detected behind ACT-CL J0218.2−0041 are not likely to be low mass groups. This large-scale scenario is also appealing given the low mass of ACT-CL J0218.2−0041. It would be interesting to explore the impact of this structure on the measured SZ effect, and similarly on X-ray emission, but this is deferred to future work.

3.4.3. ACT-CL J0326.8−0043

ACT-CL J0326.8−0043 ($z = 0.447$) was first discovered as part of the Massive Cluster Survey (MACS J0326.8−0043, Ebeling et al. 2001). The left panel of Figure 3.8 shows a SDSS gri image of the centre of the cluster, with 1.4 GHz contours from the Faint Images of the Radio Sky at Twenty centimetres (FIRST, Becker et al. 1995) survey overlaid in white. The BCG (which we refer to simply as J0326 in the remainder of this section) shows strong emission lines across the optical spectrum (Figure 3.8, right panel). Because our Gemini/GMOS spectrum is not flux-calibrated we use the line measurements from the SDSS MPA/JHU Value-Added Galaxy Catalog (Brinchmann et al. 2004) throughout. We cannot distinguish whether the emission in J0326 is dominated by star formation or an AGN from the line ratio diagnostic introduced by Lamareille (2010), appropriate for high-redshift ($z > 0.4$) objects for which Hα falls outside the optical wavelength range (specifically, $\log([{\rm O\,II}]\lambda\lambda3726+3729/{\rm H}\beta) = 0.57 \pm 0.03$ and $\log([{\rm O\,III}]\lambda5007/{\rm H}\beta) = -0.23 \pm 0.03$).

The left panel of Figure 3.8 shows that there is additionally significant 1.4 GHz emission from a point source whose peak is offset $1.''2$ (7 kpc) from the BCG (but note that the positional uncertainty in the FIRST source is $\approx 1''$), but again the nature of the emission cannot be determined. In the case of star forming galaxies with no AGN contamination, the 1.4 GHz luminosity can be used as an unobscured tracer of star formation. The 1.4 GHz luminosity of the source associated to the BCG is $\log L_{1.4}/({\rm W\,Hz^{-1}}) = 24.0$, which at face value

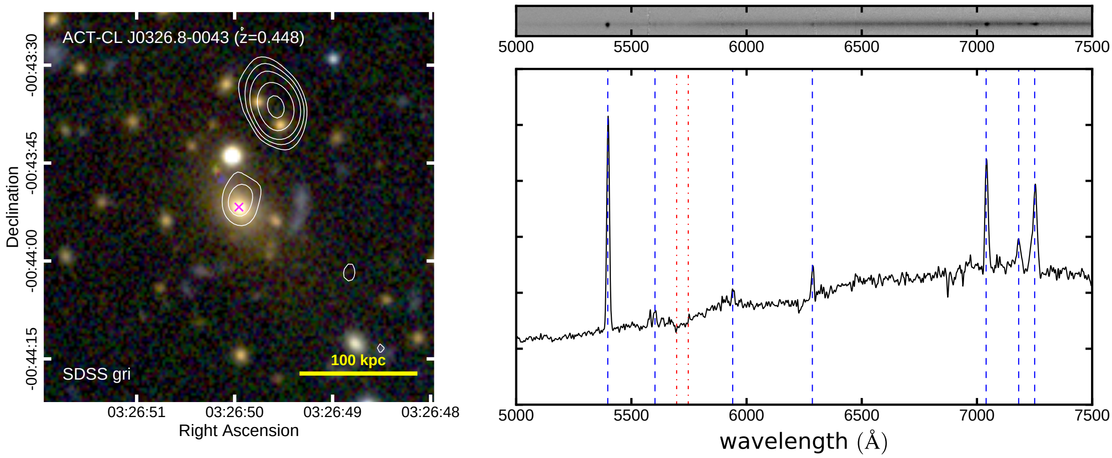

Figure 3.8: The BCG of ACT-CL J0326.8−0043 at $z = 0.45$. Left: Optical gri image from SDSS with 1.4 GHz contours from the FIRST survey overlaid in white and shown at $(3,5,8,15,25)\sigma$ levels, where $\sigma = 0.14\,\mathrm{mJy\,beam^{-1}}$. The BCG is marked with a magenta cross and the thick yellow line in the bottom-right corner is 100 kpc wide, corresponding to $17.''4$ at the cluster redshift. North is up and East is left. Right: Optical one- (bottom) and two-dimensional (top) Gemini/GMOS spectra. The former is smoothed with a 3-pixel boxcar. In the bottom panel, detected emission lines are marked with dashed blue lines (in order of increasing wavelength: [O II], Ne III, Hδ, Hγ, Hβ and [O III]$\lambda\lambda$4959, 5007); the Ca II K,H absorption doublet is marked with dash-dotted red lines. The asymmetric broadening of the [O III]λ5007 line is an artifact introduced by interpolating the GMOS chip gaps. The vertical axis is in arbitrary units.

implies a star formation rate (SFR) of several hundred $\mathrm{M_\odot\,yr^{-1}}$ (Hopkins et al. 2003). In contrast, the [O II]λ3727 doublet suggests a SFR of a few tens of $\mathrm{M_\odot\,yr^{-1}}$. Systems with such marked differences in estimated SFRs are almost always AGN hosts (J. Brinchmann, private communication). Chang et al. (2015) fitted spectral energy distributions to optical SDSS data plus mid infrared data from the Wide-field Infrared Survey Explorer (WISE, Wright et al. 2010) of one million objects. For J0326 they estimated a best-fit star formation rate of $\mathrm{SFR} = 15^{+10}_{-5}\,\mathrm{M_\odot\,yr^{-1}}$, consistent with the radio emission being dominated by nuclear activity. If this is the case then J0326 is a new Type II AGN BCG (Type I AGNs are characterized by broad components in the [O III] lines), similar to the case of the BCG of ACT-CL J0320.4+0032 recently reported by Kirk et al. (2015) and noted in Section 3.4.1. Therefore J0326 probably adds to the very sparse sample of Type II AGNs in BCGs (see references in Kirk et al. 2015).

Gilmour et al. (2009) analyzed a 10 ks *Chandra* observation of ACT-CL J0326.8−0043 and found no evidence for an X-ray point source in the BCG location to suggest the presence of an AGN; however, the observations are too shallow to draw any firm conclusions. While available X-ray data are not sufficient to establish the cooling rate in the cluster core, all evidence points to a fairly relaxed cluster. There is no evidence for substructure from the velocity distribution; $v_{\mathrm{BCG}} = 205 \pm 147\,\mathrm{km\,s^{-1}}$ suggests the BCG is located at the centre of the potential; and the magnitude gap to the second-brightest member (based on photometric redshifts to avoid a bias due to spectroscopic incompleteness) is relatively large, $\Delta m_{12} = 1.62$, which is also an indication of a dynamically old cluster (e.g., Wen & Han 2013).

3.4.4. ACT-CL 2050.5−0055

The BCG of ACT-CL 2050.5−0055 ($z = 0.623$; hereafter simply "the BCG") has the highest peculiar velocity of all BCGs in the ACT sample. In fact, the BCG is rejected by our member selection algorithm, with a peculiar velocity of $v_{\rm BCG} = -(1572 \pm 143)\,{\rm km\,s^{-1}}$, different from zero at 11σ, compared with a cluster velocity dispersion $\sigma_{200} = (511 \pm 97)\,{\rm km\,s^{-1}}$, the lowest σ_{200} in the entire sample (cf. Table 3.2). The BCG also has a redshift in the SDSS catalogue, $z_{\rm SDSS} = 0.6133 \pm 0.0002$, which would make $v_{\rm BCG}$ more negative by about $200\,{\rm km\,s^{-1}}$ (compared to $z_{\rm Gemini} = 0.6141 \pm 0.0003$). For the purpose of this discussion, this difference is not important and we will continue to use $z_{\rm Gemini}$ throughout. Such a high $v_{\rm BCG}$ probably originated as a result of either merging activity or strong galaxy-galaxy interactions in the centre (Martel et al. 2014). Regarding the possibility of a cluster-scale merger, the DS test does not reveal any evidence for substructure, although we do not have enough member galaxies to draw firm conclusions. As seen in Figure 3.7, there are haloes in our Multidark sample that have comparable BCG velocities but they tend to have lower values of $\mathscr{S}_\Delta$ than ACT-CL 2050.5−0055.

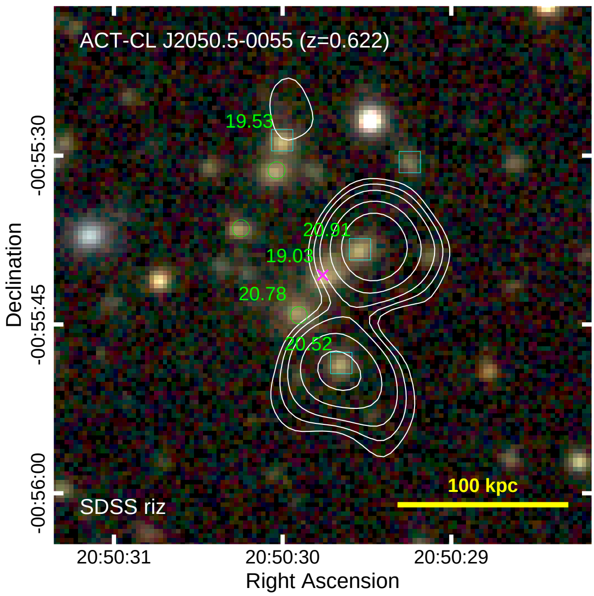

Figure 3.9: Optical *riz* image of the central region of ACT-CL J2050.5−0055 ($z = 0.62$) from SDSS, with 1.4 GHz contours from the FIRST survey overlaid in white at $(3,5,8,15,25)\sigma$ levels, where $\sigma = 0.15\,{\rm mJy beam^{-1}}$. The BCG is marked with a magenta cross; cyan squares show other spectroscopically confirmed cluster members and green circles show bright photometric redshift members. Greeen numbers to the top-left of the five brightest cluster members correspond to dereddened i-band magnitudes from SDSS. The thick yellow line in the bottom-right corner is 100 kpc wide, corresponding to $14.''7$ at the cluster redshift. North is up and East is left.

Studying a sample of 452 BCGs in low-redshift clusters, Coziol et al. (2009) found that BCGs have, on average, $|v_{\rm BCG}| = 0.32\sigma$ (where σ is the cluster velocity dispersion), with only three BCGs having velocities $|v_{\rm BCG}| > 2\sigma$. In comparison, the BCG of ACT-CL 2050.5−0055 has $v_{\rm BCG} = -(3.1 \pm 0.7)\,\sigma_{200}$.[21] Similarly, all the BCGs studied by Coziol et al. (2009) have $|v_{\rm BCG}| < 1500\,{\rm km\,s^{-1}}$. Therefore the BCG of ACT-CL 2050.5−0055 is unique in this respect; it will be interesting to study the conditions that led to such high $|v_{\rm BCG}|$. All other spectroscopic members in the cluster centre (Figure 3.9) have peculiar velocities between -550 and $350\,{\rm km\,s^{-1}}$, consistent with the low cluster velocity dispersion.

Figure 3.9 shows FIRST contours overlaid on an SDSS *gri* image of the central region of ACT-CL 2050.5−0055. There are two point-like sources coinciding with two galaxies within 100 kpc from the BCG. The integrated 1.4 GHz luminosities of the northern and southern sources are $\log L_{1.4}/({\rm W Hz^{-1}}) = 25.1$ and 25.0, respectively. Such high luminosities suggest that indeed these are point sources rather than extended emission originating in the ICM.

[21] Including the BCG in the member sample by hand increases the cluster velocity dispersion to $\sigma_{200} = (607 \pm 107)\,{\rm km\,s^{-1}}$, yielding $v_{\rm BCG} = -(2.6 \pm 0.5)\,\sigma_{200}$.

All spectroscopic members shown in Figure 3.9 have spectra typical of passive, elliptical galaxies with no signs of activity, with strong Ca II K,H absorption and no optical emission lines.

We also show in Figure 3.9 the deredenned i-band magnitudes from the SDSS catalog for the five brightest galaxies (spectroscopic and photometric members). The BCG is brighter than any other galaxy by 0.5 mag. In combination with its central location relative to the galaxy distribution, it is unlikely that the BCG is not the central galaxy of the cluster. In particular, the galaxies that coincide with radio sources are only the third and fifth brightest galaxies, making it unlikely that any of them is the central galaxy. We conclude that misidentification of the central galaxy is unlikely to explain the high $|v_{\rm BCG}|$ reported for this cluster.

3.4.5. ACT-CL J2055.4+0105

As mentioned in Section 3.3.7, the identification of the BCG is not obvious for this cluster at $z = 0.409$. In fact, we identify four galaxies along a straight line extending 1.2 Mpc SE of the BCG (the BCG is the one further NW of the four), the faintest of which is only 0.86 mag fainter than the BCG (all four galaxies are spectroscopically confirmed). Two of the four galaxies (the first and third brightest, and in the NW-SE line joining them, which are separated by 940 kpc) have extended light envelopes characteristic of cD galaxies. Only the fiducial BCG is clearly surrounded by a large overdensity of red galaxies, suggesting it is indeed the central galaxy. The fact that its peculiar velocity is consistent with zero also supports this scenario. The “alternative BCG” velocity (of $-700\,\mathrm{km\,s^{-1}}$) shown in Figure 3.14 corresponds to this secondary cD galaxy; the other two galaxies have peculiar velocities of less than 400 $\mathrm{km\,s^{-1}}$.

Overall, this elongated configuration with multiple dominant galaxies strongly suggests that this cluster is undergoing a major merger between at least two massive subclusters, and possibly more. The DS test does not reveal any evidence for substructure ($\mathscr{S}_\Delta = 0.81 \pm 0.10$), but we note that this is also the case for El Gordo (Sifón et al. 2013). This is because the DS test (nor, indeed, dynamical information in general) is not sensitive to mergers happening along the plane of the sky. As with other clusters described in this section, more data would be required for a detailed assessment of this system.

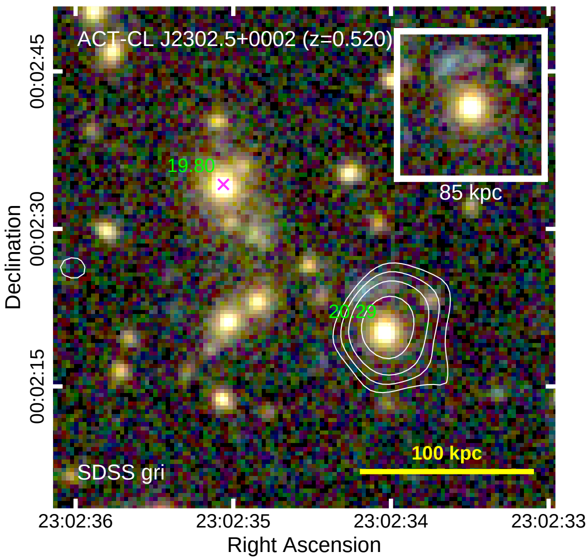

Figure 3.10: Optical SDSS gri image of the inner 300 kpc of ACT-CL J2302.5+0002. Symbols, labels and contours are as in Figure 3.9. The inset in the top-right corner is 85 kpc on a side and shows the region around the second-brightest galaxy without the radio contours, which show what appears to be a strongly lensed background image.

3.4.6. ACT-CL J2302.5+0002

ACT-CL J2302.5+0002 at $z = 0.520$ is also one of the lowest-mass clusters in the sample. We show the central 300 kpc of this cluster in Figure 3.10, which shows strong evidence that the brightest galaxy is not the *central* cluster galaxy: the second-brightest galaxy, 130 kpc away, shows strong 1.4 GHz emission and what appears to be a strongly lensed background galaxy around it. The coordinates given by Menanteau et al. (2013) indeed correspond to the brightest galaxy, but for our purposes we take the second-brightest galaxy as the cluster centre. ACT-CL J2302.5+0005 is therefore the only cluster for which we do not take the brightest galaxy as the cluster centre in Section 3.3. As mentioned in Section 3.3.7, adopting either galaxy as the centre gives consistent mass estimates; using the brightest galaxy instead of the central one we obtain $M_{200} = (1.9 \pm 0.7) \times 10^{14}\mathrm{M}_\odot$, compared to the fiducial value of $M_{200} = (2.4 \pm 0.7) \times 10^{14}\mathrm{M}_\odot$. We do not detect any optical emission lines in either galaxy.

Although such clear examples of brightest galaxies not being the central galaxy are rare, the value of the separation between the two galaxis is not uncommon (Skibba et al. 2011; Martel et al. 2014). Martel et al. (2014) have argued that the positional offset of the BCG is not as robust an indication of major mergers as the velocity offset, v_BCG/σ, where σ is the cluster velocity dispersion. As shown in Figure 3.14, both galaxies have large peculiar velocities, with $v = -470\,\mathrm{km\,s^{-1}}$ ($v/\sigma_{200} = 0.70$) and $v = -600\,\mathrm{km\,s^{-1}}$ ($v/\sigma_{200} = 0.89$) for the central and brightest galaxies, respectively. Similar to (but less extreme than) the BCG in ACT-CL J2050.5−0055, these peculiar velocities—especially given the small cluster velocity dispersion—strongly suggest that ACT-CL J2302.5+0002 is undergoing a major merger (Martel et al. 2014), but the available data do not allow us to perform a more detailed analysis.

3.5. Conclusions

We have carried out a spectroscopic follow-up effort of ACT SZ-selected clusters in the equatorial survey in the redshift range $0.3 < z < 0.9$. Combined with our previous follow-up program of the southern clusters and archival data, we present velocity dispersions and dynamical masses for 44 clusters at $0.24 < z < 1.06$ with a median of 55 spectroscopic members per cluster.

We calibrate our velocity dispersion measurements using the Multidark simulation, taking into account the spectroscopic coverage of clusters which is qualitatively different for southern and equatorial clusters, owing to the different optical imaging available (namely, targeted $5' \times 5'$ observations in the south and full SDSS coverage in the equator, Figure 3.2). We find that velocity dispersions are unbiased so long as the measurement includes galaxies out to r_{200} but the azimuthal distribution of spectroscopic targets is not important for our purposes (see Section 3.3.2 and Figure 3.3). We use the average radial velocity dispersion profile of subhaloes in Multidark to correct measurements for clusters whose coverage does not reach r_{200} and include the uncertainties from this correction (Table 3.3) in the reported velocity dispersions.

We use a scaling relation between galaxy velocity dispersion and cluster mass derived from zoomed cosmological hydrodynamical simulations to infer dynamical masses consistently for the full sample of clusters with spectroscopic observations. We make a detailed assessment of the different contributions to the reported mass uncertainties, which are dominated by a ≈30% scatter in the scaling relation induced by interlopers, triaxiality and the intrinsic scatter of the relation. Because this is a constant value, we do not include this contribution in the reported cluster mass uncertainties but recommend that it be included in cosmological analyses derived from these data. Statistical uncertainties from our average 55 members per cluster are comparable to said scatter, while uncertainties from member selection and the spectroscopic aperture selection are subdominant.

The updated dynamical mass estimates of the southern clusters are, on average, 71% of the masses presented in Sifón et al. (2013). This overall difference results from (i) accounting for the observing strategies used to get the galaxy redshifts when calculating cluster velocity dispersions (Section 3.3.2), and (ii) using a $\sigma - M_{200}$ scaling relation that includes the effects of baryonic physics and dynamical friction (Section 3.3.3). We find that masses derived from the SZ effect assuming a scaling relation based on the pressure profile of Arnaud et al. (2010) are consistent with the dynamical masses and report a mass bias which results from the combination of the dynamical mass bias and the SZ bias, $(1 - b_{\mathrm{SZ}})/\beta_{\mathrm{dyn}} = \bar{M}_{500}^{\mathrm{SZ}}/\bar{M}_{500}^{\mathrm{dyn}} = 1.10 \pm 0.13$, with an additional 0.14 systematic uncertainty due to the unknown galaxy velocity bias (see Figure 3.6 and Section 3.3.5), consistent with previous estimates from the literature if one accounts for the different mass regimes. Hasselfield et al. (2013) used the dynamical masses of Sifón et al. (2013) as prior information on the cosmological analysis derived from the SZ cluster counts and found that dynamical masses suggested a higher σ_8 than other cosmological probes. The new, lower dynamical masses will bring the estimate of σ_8 down. A cosmological analysis incorporating these new dynamical mass estimates will be presented in a future paper.

We also highlight five newly-characterized clusters. ACT-CL J0218.2−0041 ($z = 0.67$) appears to be part of a structure where two cluster-sized systems are connected by a filament along the line of sight. The BCG of ACT-CL J0326.8−0043 ($z = 0.45$) is likely a rare Type II AGN host which also seems to be associated with strong radio emission. The BCG of ACT-CL 2050.5−0055 ($z = 0.62$) has a peculiar velocity of $v_{\mathrm{BCG}} = 3\sigma_{200}$ and is surrounded by double-peaked (probably point-source) radio emission. ACT-CL J2055.4+0105 ($z = 0.41$) has four bright, locally-dominant galaxies separated by 1.2 Mpc along a straight line. Finally, ACT-CL J2302.5+0002 ($z = 0.52$) is a clear example of the brightest galaxy not being the central cluster galaxy, confirmed by the presence of a strong lensing arc around the second-brightest galaxy. Further follow-up studies will reveal more details about these intriguing systems.

The uncertainty on the average dynamical mass is dominated by the scatter in the $\sigma - M$ relation (see Table 3.4), which cannot be significantly reduced by observing more galaxies per cluster. Ntampaka et al. (2015b) recently developed a machine learning approach to measure dynamical masses which incorporates information about the distribution of galaxies and their velocities to predict cluster masses, which has been successfully applied to mock observations that include the effects of impurity and incompleteness, reducing the errors by up to 60% (Ntampaka et al. 2015a). Further tests on more realistic galaxy catalogues will assess its effectiveness in measuring galaxy cluster masses in real observations.

3.A. Eddington bias and selection effects

In this appendix we discuss the SZ and dynamical mass measurements in the context of understanding potential biases, such as Eddington bias (Eddington 1913), that might affect the comparison of the two mass proxies. We then demonstrate with a simple simulation that the method used in Section 3.3.4 to determine the ratio $(1 - b_{\mathrm{SZ}})/\beta_{\mathrm{dyn}}$ is unbiased.

The SZ masses used in this work have been corrected for Eddington bias by Hasselfield et al. (2013). The calculation accounts for the fact that the underlying mass function is falling steeply as mass increases, so a direct inversion of $y_{SZ}(M)$ gives a biased estimate of $M(y_{SZ})$ (Evrard et al. 2014). The computation of the correction requires certain assumptions, such as the form of the cluster mass function and the survey selection function, which is constructed assuming a particular model for the SZ signal and an assumption about the degree of intrinsic scatter. Under these assumptions the correction is then computed in a Bayesian framework, with the posterior probability of a cluster's mass given by $P(M|y) \propto P(y|M)n(M)$, where the likelihood $P(y|M)$ accounts for intrinsic scatter and measurement noise and the prior $n(M)$ is the cluster mass function (see section 3.2 of Hasselfield et al. 2013).

Aside from the modelling assumptions, it is important to note that the correction is no longer valid if we change the underlying distribution of cluster masses upon which the ACT selection is effectively acting. For example, if we were to remove objects from the sample based on some auxiliary information (such as X-ray flux, or membership in an optical cluster survey), then we would risk complicating the underlying mass function and invalidating the Eddington bias correction applied in Hasselfield et al. (2013).

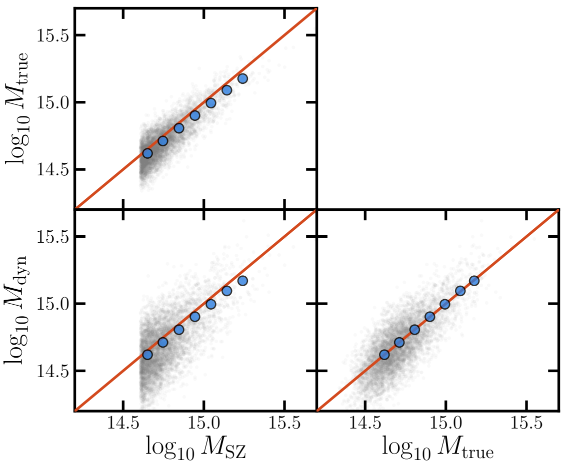

Figure 3.11: Comparison of SZ, dynamical, and true cluster masses for a mock catalog that incorporates a simple model for noise, scatter and selection effects. The gray points are individual mock clusters. The blue points show the mean masses for several bins in M_{SZ}.

However, there are many ways to sub-sample the ACT sample without changing the validity of the Eddington bias correction. Restricting the survey to a smaller region of the sky, or to a particular redshift range[22] does not affect the Eddington bias correction. Although less obvious, it is also true that raising the S/N threshold of the catalog does not change the correction (though of course this will change the membership of the sample). While the S/N threshold affects the survey selection function (which we take to mean the probability that a cluster of some mass and redshift would be included in the sample), it does not affect the underlying distribution of masses which we should consider when working with a particular cluster that has been detected. In a Bayesian framework, the posterior distribution for any one cluster's mass is not dependent on the overall survey selection function. The cosmological sample considered in this work satisfies the requirements above, and so we take the masses of Hasselfield et al. (2013), which have been corrected for Eddington bias, to be unbiased on average.

The dynamical masses presented in this work were obtained for all clusters passing certain redshift and S/N cuts (i.e., those in the cosmological sample of Hasselfield et al. 2013), and the present measurements were not used to refine the sample further. Though noise and scatter will certainly affect the velocity dispersion measurements, we expect positive and negative noise (or scatter) excursions to be equally likely. The dynamical mass measurements thus constitute a complete set of "follow-up" observations for the sample, and are not affected by

[22]The redshift cut can in principle affect the bias correction due to uncertainty in the cluster redshifts; in practice the redshift uncertainties are small enough that this is not significant.

Eddington bias.

While the descriptions above can be justified formally (see Evrard et al. 2014), we illustrate their validity using mock catalogs of SZ and dynamical mass measurements. We draw a large number of masses, $M_{\rm true}$, from a realistic cluster mass function, considering a single redshift. We create SZ and dynamical mass proxy measurements by adding intrinsic scatter (at the 20 and 30% levels, respectively) and measurement noise (fixed at $10^{14}\,\mathrm{M}_\odot$ and $2\times10^{14}\,\mathrm{M}_\odot$, respectively) to the true masses. Then we simulate the effect of SZ selection by keeping only mock clusters with $M_{\rm SZ} > 4\times10^{14}\,\mathrm{M}_\odot$.

In Figure 3.11 we show these mock clusters, and demonstrate that if we bin the objects according to their $M_{\rm SZ}$ measurement, we see Eddington bias effects in $M_{\rm SZ}$ relative to the true cluster mass, but $M_{\rm dyn}$ is not biased. In the real observations, the Eddington bias in $M_{\rm SZ}$ is corrected by modeling the mass function and SZ scaling relation. For the mock study we simply fit a constant bias factor to the binned $M_{\rm SZ}$ and M_{true} points and use it to correct the individual mock $M_{\rm SZ}$ values.

We then take a random subsample consisting of 20 mock clusters, to roughly match the size of the real sample considered in this work. We compute the characteristic SZ and dynamical mass of these clusters, under uniform weights, as was done in Section 3.3.5. The resulting ratio is consistent, as expected, with unity. This subsample and the characteristic masses are plotted in Figure 3.12.

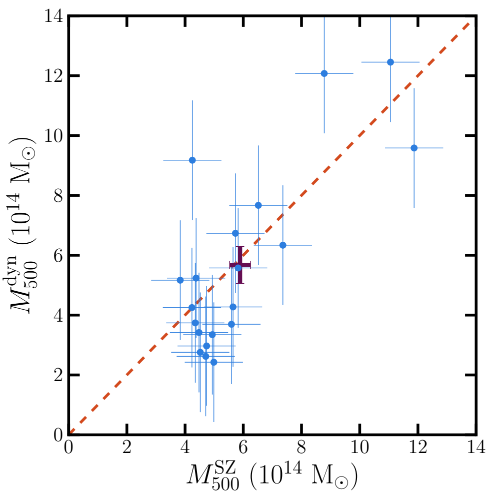

Figure 3.12: Masses of 20 clusters drawn from a large mock catalog that simulates noise, scatter, and selection effects. Purple cross shows the mean characteristic SZ and dynamical mass, computed under uniform weights. As in Figure 3.6, errorbars in the individual masses include only the noise contribution and not intrinsic scatter.

We also repeat the entire procedure for alternative weighting schemes. We find that weighting schemes that incorporate the measured dynamical masses are significantly biased. For example, if we take the weights to be the inverse square of the combined measurement error and intrinsic scatter, the characteristic dynamical mass is 10% lower, on average, than the characteristic SZ mass. Such biases are also seen in weights that include the fractional measurement error (which requires the input of the measured mass), or weights that incorporate the intrinsic scatter contribution (which scales in proportion to the measured mass). The real data contain additional correlations between dynamical mass and measurement error beyond those modeled in this simple simulation, because more massive clusters also tend to have more galaxies that can be used to measure the dispersion. For these reasons it is clear that one should not incorporate the dynamical mass measurements and errors into the weights unless the impact can be fully modelled.

In constrast, for this simulation we find that weighting by the inverse square of the SZ mass error (including the contribution from intrinsic scatter) does not bias the mass comparison. This is because we have already corrected the SZ masses to make them unbiased, even under weights (or selection choices) that depend on the measured SZ mass.

3.B. Velocity histograms

We show in Figures 3.13 and 3.14 the velocity histograms for all clusters (only member galaxies are shown). We show histograms with bins of $400\,\mathrm{km\,s^{-1}}$ and with a constant bin size that maximizes the predictive power of the histogram in a Bayesian sense (Knuth 2006)[23].

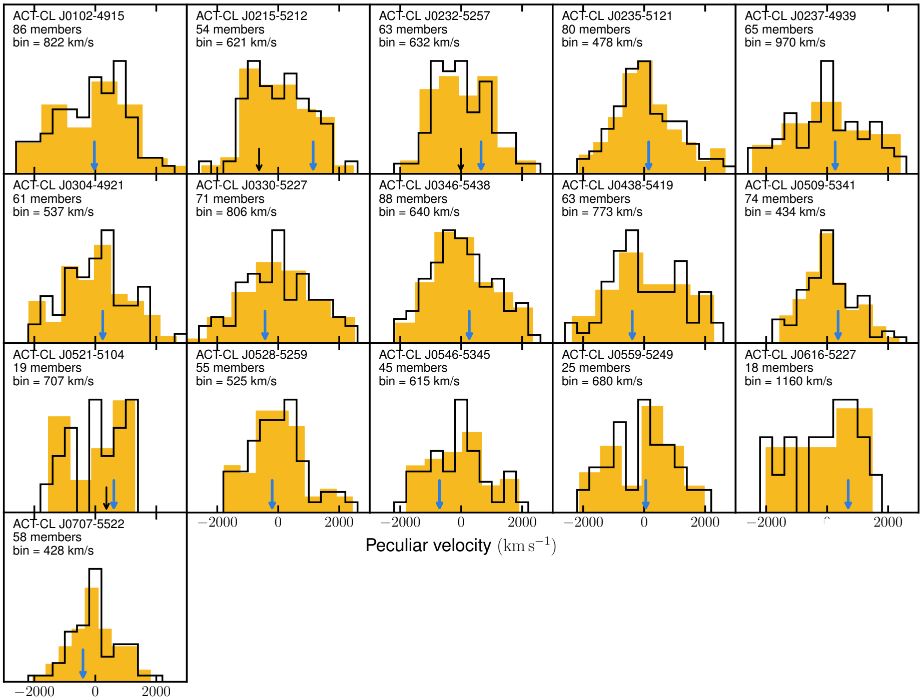

Figure 3.13: Velocity histograms of all clusters in the southern sample. Black empty histograms have a bin size of $400\,\mathrm{km\,s^{-1}}$ and filled yellow histograms have a bin size indicated in the legend, which is such that the predictive power of the histogram (i.e., the likelihood that the next datum will fall in a given bin) is maximized using a bayesian approach. We show normalized counts and list the number of members in each cluster in the legends (see also Table 3.2). Blue arrows mark the BCG velocities and, where applicable, smaller black arrows mark peculiar velocities of alternative choices for the BCG (see Sections 3.3.7 and 3.4). BCG velocities have a typical uncertainty of $\approx 100\,\mathrm{km\,s^{-1}}$.

[23]We use the version implemented in the `plotting` library of `astroML` (VanderPlas et al. 2012).

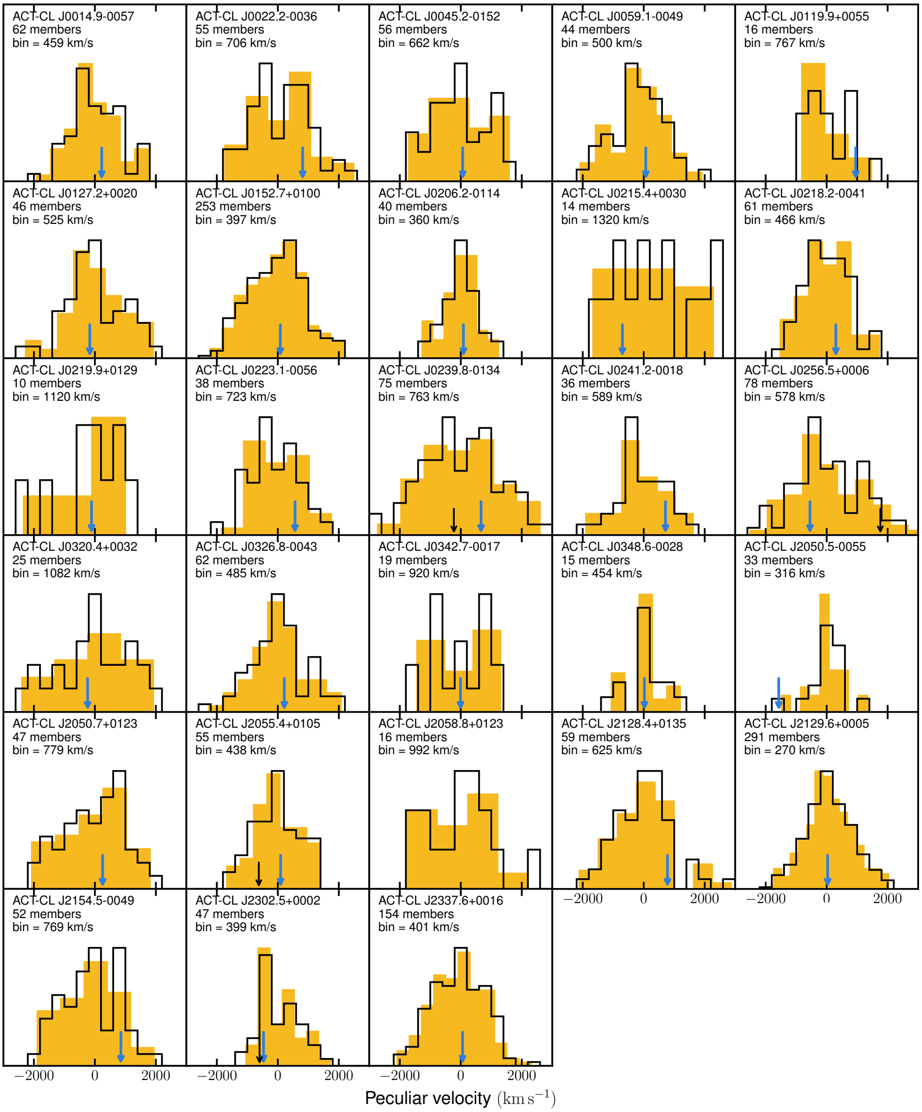

Figure 3.14: Rest-frame velocity histograms of all clusters in the equatorial sample. Styles are the same as Figure 3.13. We do not know the redshift of the BCG of ACT-CL J2058.8+0123.

4 | Galaxy alignments in massive clusters from ~14,000 spectroscopic members

Torques acting on galaxies lead to physical alignments, but the resulting ellipticity correlations are difficult to predict. As they constitute a major contaminant for cosmic shear studies, it is important to constrain the intrinsic alignment signal observationally. We measured the alignments of satellite galaxies within 90 massive galaxy clusters in the redshift range $0.05 < z < 0.55$ and quantified their impact on the cosmic shear signal. We combined a sample of 38,104 galaxies with spectroscopic redshifts with high-quality data from the Canada-France-Hawaii Telescope. We used phase-space information to select 14,576 cluster members, 14,250 of which have shape measurements and measured three different types of alignment: the radial alignment of satellite galaxies toward the brightest cluster galaxies (BCGs), the common orientations of satellite galaxies and BCGs, and the radial alignments of satellites with each other. Residual systematic effects are much smaller than the statistical uncertainties. We detect no galaxy alignment of any kind out to at least $3r_{200}$. The signal is consistent with zero for both blue and red galaxies, bright and faint ones, and also for subsamples of clusters based on redshift, dynamical mass, and dynamical state. These conclusions are unchanged if we expand the sample with bright cluster members from the red sequence. We augment our constraints with those from the literature to estimate the importance of the intrinsic alignments of satellites compared to those of central galaxies, for which the alignments are described by the linear alignment model. Comparison of the alignment signals to the expected uncertainties of current surveys such as the Kilo-Degree Survey suggests that the linear alignment model is an adequate treatment of intrinsic alignments, but it is not clear whether this will be the case for larger surveys.

Cristóbal Sifón, Henk Hoekstra, Marcello Cacciato, Massimo Viola, Fabian Köhlinger, Remco F. J. van der Burg, David J. Sand, & Melissa L. Graham,
2015, A&A, 575, A48

4.1. Introduction

Tidal torques tend to align triaxial satellite galaxies toward the centre of the larger "host" gravitational potential as they orbit around its centre. This mechanism is well established in numerical simulations, where galaxies are typically locked pointing toward the centres of clusters, possibly with brief periodic misalignments depending on the specific orbit, well within a Hubble time (e.g., Ciotti & Dutta 1994; Altay et al. 2006; Faltenbacher et al. 2008; Pereira et al. 2008; Pereira & Bryan 2010). In a hierarchical clustering scenario, this effect could be coupled with alignments arising from the nonlinear evolution of structure. Therefore the patterns and evolution of galaxy alignments—if any—contain important information about the initial conditions that gave rise to the present-day cosmic web, as well as the formation history and environments of galaxies.

Additionally, these galaxy alignments (commonly referred to as "intrinsic," as opposed to apparent, alignments) are a potential contaminant of cosmic shear, which is a measurment of the coherent distortions of galaxies in the background of a matter distribution. While the signal from these intrinsic alignments is weak enough that it is not relevant for weak lensing measurements of galaxy clusters (and in general cluster members can be identified and removed to a sufficient level), it is a concern for large-area cosmic shear surveys, which are more susceptible to this contamination, and where the requirements on precision and accuracy are more stringent. The contamination induced by these galaxy alignments into cosmic shear measurements can be divided into two effects. The first effect is the tidal alignment of galaxies with similar formation histories, so-called intrinsic-intrinsic or II signal. Since this effect is restricted to pairs with common formation or evolutionary histories, this II signal can be avoided by selecting pairs of galaxies with large angular and/or redshift separations (e.g., King & Schneider 2002; Heymans & Heavens 2003; Heymans et al. 2004). The second effect is more subtle and more difficult to control: the same gravitational field that aligns galaxies within a halo is responsible for the deflection of the light coming from background galaxies (Hirata & Seljak 2004). This effect is referred to as gravitational-intrinsic or GI signal (for consistency, the lensing signal itself is referred to as gravitational-gravitational, or GG, signal). In tomographic analyses, it is possible to account for this effect through its distinct redshift dependence (King 2005; Joachimi & Schneider 2008; Zhang 2010b,a) or, inversely, to measure it from cosmic shear data by boosting its signal while suppressing the contribution from gravitational lensing (Joachimi & Schneider 2010). This cross-correlation has recently been shown to exist also between galaxy-galaxy lensing and CMB lensing (Hall & Taylor 2014; Troxel & Ishak 2014). Intrinsic alignments can also be modeled directly in cosmic shear data and marginalized over to extract cosmological parameters (Joachimi & Bridle 2010; Heymans et al. 2013). In an attempt to identify a consistent model for galaxy shapes and alignments, Joachimi et al. (2013a,b) have tried to match semi-analytical models to galaxies from the COSMOS survey (Scoville et al. 2007) and find that the intrinsic alignment contamination to upcoming cosmic shear surveys should be $< 10\%$.

Recent large photometric and spectroscopic surveys such as the 2-degree Field redshift survey (2dF, Colless et al. 2001) and the Sloan Digital Sky Survey (SDSS, York et al. 2000) have allowed the study of galaxy alignments out to several tens of Mpc exploiting cross-correlation techniques, with robust direct detections of the GI signal up to $z \sim 0.7$ between galaxy samples with large line-of-sight separations (Mandelbaum et al. 2006a; Hirata et al. 2007; Joachimi et al. 2011), although Mandelbaum et al. (2011) reported a null detection. However, the II signal is much weaker than the GI signal in nontomographic studies at intermediate redshifts typical of these surveys, and has typically eluded detection (e.g., Mandelbaum et al. 2006a, 2011; Blazek et al. 2012).

On smaller scales the history of these measurements goes back further, but the issue is far from settled. Early measurements of galaxy alignments focused on galaxy clusters, trying to understand galaxy formation and (co-)evolution. Rood & Sastry (1972) were the first to claim a detection of a preferential direction of galaxies in clusters. Specifically, they found that satellite galaxies in Abell 2199 tend to point in the direction of the major axis of the BCG. However, most subsequent measurements have been consistent with random orientations of satellite galaxies in clusters (e.g., Hawley & Peebles 1975; Thompson 1976; Dekel 1985; van Kampen & Rhee 1990; Trevese et al. 1992; Panko et al. 2009; Hung & Ebeling 2012), although some authors have also claimed significant nonrandom orientations of these cluster satellites (e.g., Djorgovski 1983; Godłowski et al. 1998, 2010; Baier et al. 2003; Plionis et al. 2003).

More recent studies have focused on smaller mass galaxy groups, where the number of objects is much larger. Similar to the results summarized above, most of these measurements are consistent with no alignments (Bernstein & Norberg 2002; Hao et al. 2011; Schneider et al. 2013; Chisari et al. 2014), although there are claims of significant detections (e.g., Pereira & Kuhn 2005; Faltenbacher et al. 2007b).[1] Interestingly, although this effect might be expected to be stronger for more massive haloes, Agustsson & Brainerd (2006) found that satellite galaxies are radially aligned in galaxy-scale haloes. However, Hao et al. (2011) and Schneider et al. (2013) have shown that the results can depend on the method used to estimate the direction of the satellite galaxies, so each result must be taken with care.

In general, there is clear tension between observations and numerical N-body simulations, with the latter predicting much higher signals than have been observed. This discrepancy can be attributed, for instance, to a misalignment between stars and dark matter, such that stars—being more centrally concentrated than dark matter—react more slowly and less strongly to tidal torquing from the parent halo (Pereira & Bryan 2010; Tenneti et al. 2014). Whatever the physical reasons of this discrepancy, the potential impact of the choice of intrinsic alignment *model* on cosmological parameter estimation (Kirk et al. 2012) makes it imperative that we know the level of intrinsic alignments to high precision at all relevant mass and spatial scales, and this can only be achieved through detailed observations.

In this work, we study the alignments of galaxies in clusters from a sample of galaxy clusters with high-quality photometric observations and a large number of spectroscopic redshifts from archival sources. We measure different kinds of alignments, assess systematic errors, and use the halo model to characterize galaxy alignments in the context of upcoming cosmic shear analyses.

We adopt a flat ΛCDM cosmology with $\Omega_\Lambda = 0.7$, Ω_m and $H_0 = 70\,\mathrm{km\,s^{-1}\,Mpc^{-1}}$. To calculate the power spectra, we use $\sigma_8 = 0.8$, $\Omega_b h^2 = 0.0245$, and $n_s = 1.0$. All magnitudes are `MAG_AUTO` from SExtractor in the AB system, and all absolute magnitudes and luminosities are in the rest frame of the corresponding cluster.

4.2. Data

4.2.1. Cluster sample and photometry

The cluster sample is drawn from two large, nonoverlapping X-ray selected cluster surveys carried out with the Canada-France-Hawaii Telescope (CFHT), namely the Multi-Epoch

[1] We discuss sources of this discrepancy in light of recent results in Section 4.5.4.

Nearby Cluster Survey (MENeaCS; Sand et al. 2012) and the Canadian Cluster Comparison Project (CCCP; Hoekstra et al. 2012). MENeaCS performed multi-epoch observations of 57 clusters in the redshift range $0.05 < z < 0.15$, aimed at measuring the supernova Ia rate in these clusters. For this, clusters were observed using the g and r bands with MegaCam. CCCP was designed to study the scaling relations between different tracers of mass in galaxy clusters, and includes 50 clusters in the redshift range $0.15 < z < 0.55$. Of these, 20 clusters had archival *B*- and *R*-band data taken with the CFH12k camera, and 30 clusters were observed with the g and r bands with MegaCam (Hoekstra 2007; Hoekstra et al. 2012).

The data were reduced using the Elixir pipeline (Magnier & Cuillandre 2004), and processed further following the method outlined in van der Burg et al. (2013), which is summarized below. In order to simplify point spread function (PSF) modeling for shape measurements, we homogenized the PSF across the entire field-of-view by finding a locally-varying convolution kernel that makes the PSF circular and Gaussian everywhere (Kuijken 2008). This PSF homogenization was done for each exposure, after which the individual exposures were co-added. By applying a Gaussian weight function to measure aperture fluxes we optimized color measurements in terms of S/N (see Kuijken 2008 and van der Burg et al. 2013, Appendix A). This gaussianization process introduces correlations in pixel noise, which we do not account for. As we show in Section 4.4.3, this is not a problem for the present analysis.

We performed object detection with SExtractor (Bertin & Arnouts 1996) in dual-image mode, using the r (or R) band as detection image. All sources were detected in the r-band image obtained by stacking the nonhomogenized images. Photometric zero points were calibrated using the stellar locus regression (SLR) software developed by Kelly et al. (2014)[2]. SLR uses the known colors of stars to obtain solutions for the photometric zero points of any photometric catalogue, correcting for instrumental response and atmospheric and Galactic extinctions (see also High et al. 2009). We used the Two-Micron All Sky Survey (2MASS, Skrutskie et al. 2006) J-band star catalogue in addition to our MegaCam g and r, or CFH12k B and R, observations as inputs to the SLR. We retrieved extinction values in the J band from the NASA/IPAC Extragalactic Database (NED)[3], which use the reddening measurements of Schlafly & Finkbeiner (2011). With these two colors, plus the absolute photometric calibrations of 2MASS (including the extinction correction), we obtained absolute zero points for the CFHT catalogues. For clusters within the SDSS footprint we also use the SDSS *griz* photometry to check for consistency, from which we conclude that SLR-corrected zero points are calibrated to an absolute uncertainty of ~ 0.01 mag. Galaxies were separated from stars by visual inspection of the magnitude-size[4] plane for each cluster individually. Stars occupy a well-defined region in this plane, having essentially a single size up to the saturation flux. Given that the stacks generally have a sub-arcsecond sized PSF, galaxies used here are large compared to the PSF and are therefore easily distinguishable from stars.

We computed r-band absolute magnitudes, M_r, using EzGal[5] (Mancone & Gonzalez 2012), using a passive evolution Charlot & Bruzual 2007 (unpublished, see Bruzual & Charlot 2003) single burst model with solar metallicity and formation redshift $z_f = 5$.

[2] `https://code.google.com/p/big-macs-calibrate/`
[3] `http://ned.ipac.caltech.edu/`
[4] Here, sizes are given by `FLUX_RADIUS` from SExtractor.
[5] `http://www.baryons.org/ezgal/`

Table 4.1: Spectroscopic catalogues.

Source	Total redshifts	Unique redshifts	Clusters	Avg. unique per cluster
		Compilations		
NED	16,125	9,161	79	116
WLTV	1,613	1,399	2	700
CNOC	1,427	1,266	10	127
SDSS DR10	14,634	13,995	62	226
HeCS	8,470	8,368	27	310
MENeaCS-spec	1,966	1,966	12	164
		Single-cluster		
Geller et al. (2014)		834	1	834
Ebeling et al. (2014)		1,115	1	1,115
Total		**38,104**	**90**	**423**

4.2.2. Spectroscopic data

We searched for spectroscopic redshifts around all clusters in the MENeaCS+CCCP sample in six archival sources: NED, the WIYN Long-Term Variability survey (WLTV; Crawford et al. 2011), the Canadian Network for Observational Cosmology Survey (CNOC; Yee et al. 1996, 1998; Ellingson et al. 1997; Abraham et al. 1998), the SDSS Data Release 10[6] (DR10; Ahn et al. 2014) which is part of SDSS-III (Ahn et al. 2012) and the Hectospec Cluster Survey (HeCS; Rines et al. 2013). We also include redshifts from the MENeaCS spectroscopic survey (hereafter MENeaCS-spec). When a galaxy was found in more than one of these catalogues, each catalogue replaced the preceding as listed above and in Table 4.1. Thus we included all redshifts from MENeaCS-spec. In NED and in SDSS DR10, we searchws for galaxies with spectroscopic redshifts within a radius of 1 deg. around each cluster, but only galaxies in our photometric catalogues were included in the analysis. From NED, we discarded all flagged redshifts (i.e., all those whose `Redshift Flag` field is not blank) and kept only redshifts with at least 4 significant digits to ensure that only spectroscopic redshifts with enough precision are included. From SDSS we only included galaxies with `zWarning=0`. The NED search includes redshifts obtained as part of large surveys such as the 2dF, the 2MASS spectroscopic survey (2MRS), the WIde-field Nearby Galaxy cluster Survey (WINGS), and the WiggleZ Dark Energy Survey.

Additionally, we included the redshift catalogues of Abell 383 and MACS J0717.5+3745 recently published by Geller et al. (2014) and Ebeling et al. (2014), respectively, which total 1,949 redshifts within our CFHT images. From the catalogue of Ebeling et al. (2014) we used only redshifts with quality flag 1 or 2. We also highlight the redshift catalogue of Abell 2142 by Owers et al. (2011), containing $\sim 1{,}800$ galaxies, which is included as part of the NED catalogue.

Table 4.1 lists the number of (unique) spectroscopic redshifts included from each catalogue and from how many cluster fields they are taken. The largest redshift catalogue(s) for each cluster are listed in Table 4.2, including the largest catalogues within NED; for most clusters the NED redshifts come mainly from one or two large catalogues (with $\gtrsim 90\%$ of redshifts). The final spectroscopic sample is summarized in the last row of Table 4.1: it contains 38,104 redshifts in the direction of 90 clusters, selected to have at least 30 members, at least 10 of which must be within r_{200} (see Section 4.3.1). The left panel of Figure 4.1 shows the

[6] `http://www.sdss3.org/dr10/data_access/`

redshift distribution of these 90 clusters, compared to the entire MENeaCS+CCCP sample. The analysis in this paper refers only to these 90 clusters, which are listed in Table 4.2.

4.3. Galaxy samples

4.3.1. Spectroscopic members and dynamical masses

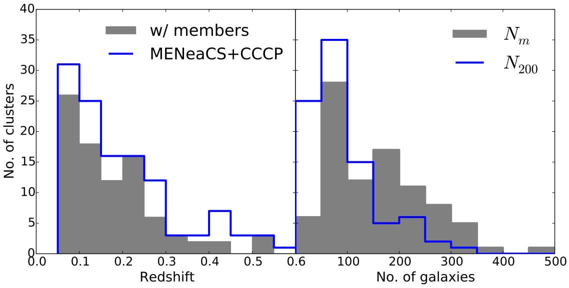

Figure 4.1: Left: redshift distributions of all MENeaCS+CCCP clusters (blue histogram) and clusters used in this study (gray filled histogram). Right: distributions of number of spectroscopic members, N_m (gray filled histogram), and number of spectroscopic members within r_{200}, N_{200} (blue histogram). Abell 2142, with $N_\mathrm{m} = 1052$ and $N_{200} = 731$, is not shown.

Spectroscopic membership is determined using the shifting gapper method (Fadda et al. 1996), slightly adjusted from the implementation of Sifón et al. (2013). We bin galaxies in radial bins of at least 15 galaxies and 250 kpc and, for each radial bin, members are selected as those galaxies that are within $800\,\mathrm{km\,s^{-1}}$ from the main body of galaxies, which is bound by gaps of $400\,\mathrm{km\,s^{-1}}$. The reduction in the velocity gaps compared to Sifón et al. (2013)—who used 1000 and 500 $\mathrm{km\,s^{-1}}$, respectively—is due to the larger number of galaxies used here, producing a distribution that has less obvious gaps in velocity space. In some cases, we introduced a radial cut determined from visual inspection. The left panel of Figure 4.2 shows that the distribution of confirmed cluster members is similar at low and high redshift for luminous ($M_r \lesssim -21$) galaxies but low-luminosity galaxies used here come mainly from low redshift clusters.

We iteratively measure the velocity dispersion, σ_{200}, as the biweight estimator of scale (Beers et al. 1990) using all galaxies within r_{200}, correcting for measurement errors (Danese et al. 1980). Since the measurement uncertainties are not available for all galaxies (most notably, they are not given in NED), we use a fiducial value of $150\,\mathrm{km\,s^{-1}}$ for the uncertainty of all redshifts, which is a conservative estimate for recent measurements, but can be representative of older or low resolution measurements listed in NED. The change in mass introduced by this correction is, in any case, at the percent level for a cluster with $\sigma \sim 1000\,\mathrm{km\,s^{-1}}$.

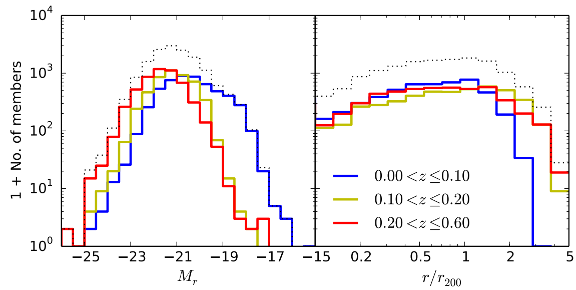

Figure 4.2: Distribution of spectroscopic members. Left: as a function of rest-frame absolute r-band magnitude. Right: as a function of cluster-centric distance in units of r_{200}. The dotted black lines show the distribution of the full sample; the solid lines show the distribution split into three redshift bins of approximately equal number of clusters.

The cluster redshift is determined iteratively in this process as the biweight estimator of location, considering again galaxies within r_{200}. We estimate the mass within r_{200}, namely M_{200}, using the $\sigma_{200} - M_{200}$ relation of Evrard et al. (2008), and estimate $r_{200} = \left[3/(4\pi)\cdot M_{200}/(200\rho_c)\right]^{1/3}$. The resulting σ_{200} is insensitive to uncertainties in r_{200}; varying

r_{200} by ±20% from those obtained from this relation only changes σ_{200} by $\lesssim 5\%$ for every cluster (in other words, velocity dispersion profiles are very close to flat near r_{200}). The uncertainties in the velocity dispersion are obtained from 1,000 jackknife samples drawn from all galaxies with peculiar velocities up to 3 times the cluster velocity dispersion; therefore quoted uncertainties include an estimate of the effect of membership selection. Uncertainties in the dynamical mass are obtained by propagating the uncertainties on the velocity dispersion. The dynamical properties described above are listed in Table 4.2, together with the number of members, $N_{\rm m}$, and the number of members within r_{200}, N_{200}. The right panel of Figure 4.1 shows the distribution of N_{200} and $N_{\rm m}$, the number of members out to arbitrary radius.

In cases where the spectroscopic members do not reach out to r_{200}, we cannot infer σ_{200} directly from the data. We therefore apply a correction to the measured velocity dispersion assuming the isotropic velocity dispersion profile of Mamon et al. (2010) and the mass–concentration relation of Duffy et al. (2008) to get the theoretical expectation for σ_{200} given $\sigma(<r_{\rm max})$. This correction is linear with $r_{\rm max}$ for $r_{\rm max} \gtrsim 0.2r_{200}$, with correction factors 0.93 and 0.81 for the velocity dispersion and mass, respectively, for $r_{\rm max} = 0.6r_{200}$ (i.e., the mass within $0.6r_{200}$ is $0.81M_{200}$), only weakly dependent on mass and redshift. In our sample there are 14 clusters with $r_{\rm max} < r_{200}$, with a median of $r_{\rm max}/r_{200} = 0.69$ and 10th and 90th percentiles of 0.51 and 0.79, respectively. For these clusters, we list the corrected values in Table 4.2.

There are a total of 14,576 cluster members among 90 clusters, 9,054 of which are within r_{200}. The radial distribution of cluster members is shown in the right panel of Figure 4.2. The spectroscopic members on average follow a Navarro-Frenk-White (NFW, Navarro et al. 1995) profile with concentration $c_{200} \sim 2$ (van der Burg et al. 2015). The median redshift of the sample is $z = 0.144$, and the median velocity dispersion is $\sigma_{200} = 881\,{\rm km\,s^{-1}}$ which translates to a median dynamical mass $M_{200} = 7.2 \times 10^{14}\,{\rm M_\odot}$ and a median size $r_{200} \sim 1.7\,{\rm Mpc}$. The distribution of σ_{200} is shown in the bottom panel of Figure 4.3.

In Figure 4.3, we compare the present velocity dispersions to those of Rines et al. (2013); there is a large overlap between the two data sets (see Table 4.1). The two sets of measurements are consistent, with a median ra-

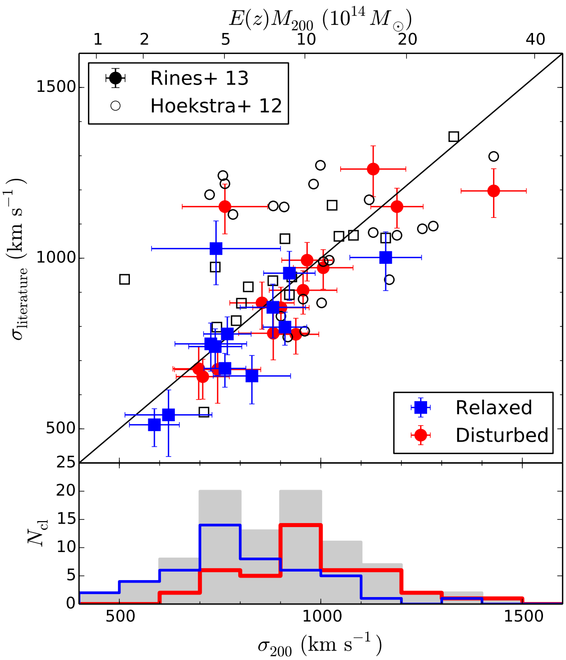

Figure 4.3: Top: comparison between velocity dispersions calculated from spectroscopic members in this work with those in Rines et al. (2013), and with velocity dispersions calculated by fitting a single isothermal sphere to the weak lensing profile (Hoekstra et al. 2012, errorbars not shown for clarity). Squares and circles show relaxed and disturbed clusters, respectively. The black line shows the one-to-one relation, and the top axis shows $E(z)M_{200}$ for a given σ_{200} from the Evrard et al. (2008) relation. Bottom: distribution of velocity dispersions of the full sample. The gray histogram shows the total distribution, with the blue and red histograms showing the distributions for relaxed and disturbed clusters, respectively.

tio $\langle\sigma_{200}/\sigma_{\mathrm{Rines+13}}\rangle = 1.04\pm0.03$. We also show, for comparison, the singular isothermal sphere velocity dispersions fit by Hoekstra et al. (2012) to the weak lensing signal of 39 overlapping clusters, which are also consistent with our measurements to within 2% on average. It is apparent from Figure 4.3 that the agreement between σ_{200} and σ_{WL} is better for relaxed clusters than for disturbed ones, consistent with expectations. For comparison, using the velocity gaps used by Sifón et al. (2013) in our analysis, we obtain velocity dispersions larger than those of Rines et al. (2013) by ∼14%.

4.3.1.1. Dynamical state

We can take further advantage of our large spectroscopic catalogues by studying the dynamical states of clusters. To this end we use the DS test (Dressler & Shectman 1988), which uses both the positions and velocities of galaxies. The DS test gives a measure of substructure by identifying galaxies that do not follow the cluster velocity distribution through the metric

$$\delta^2 = \frac{N_{\mathrm{local}}}{\sigma^2}\left[(\bar{v}_{\mathrm{local}} - \bar{v})^2 + (\sigma_{\mathrm{local}} - \sigma)^2\right]^2, \tag{4.1}$$

where $\bar{v}_{\mathrm{local}}$ and σ_{local} are the local velocity and velocity dispersion, measured for the N_{local} nearest neighbors around a test member, and $\bar{v}$ and σ are the global values. The Δ-statistic is the sum of δ's over all cluster members. This statistic is then measured 5,000 times after shuffling the velocities of cluster members, keeping positions fixed, with the same N_{local}. The substructure significance (hereafter $\mathscr{S}_\Delta$) is the fraction of random samples which have Δ higher than that of the cluster. Errorbars are 68% ranges obtained from 5 runs for each cluster, varying the number of neighbors within $\sqrt{N_{200}}-2 \le N_{\mathrm{local}} \le \sqrt{N_{200}}+2$, and the central value is their median. We run the DS test using only members within r_{200} because r_{200} is very close to the virial radius, beyond which the cluster *should not* be relaxed, by definition.

The DS test is not designed to assess the dynamical state of clusters in general but specifically to find substructure, which furthermore has to have a different spatial and velocity location from the cluster itself. It is therefore incomplete; there are indeed examples of known merging clusters from which the DS test cannot find indications of substructure, most notably mergers along the plane of the sky (e.g., Menanteau et al. 2012; Barrena et al. 2013). This is the case here with Abell 520 (e.g., Jee et al. 2014a), for example. By means of N-body simulations, Pinkney et al. (1996) showed that $\mathscr{S}_\Delta < 0.05$ is a reasonable condition to define a pure, but not necessarily complete, sample of dynamically disturbed clusters. We follow the results of Pinkney et al. (1996) in a conservative way, selecting as disturbed all cluster that are consistent with $\mathscr{S}_\Delta \le 0.05$ within errorbars (52 clusters). All others are classified as relaxed (38 clusters). This is conservative in the sense that we aim to construct a pure sample of relaxed clusters (see Section 4.5.1). Table 4.2 lists $\mathscr{S}_\Delta$ together with the classification for each cluster. We find that more massive clusters tend to be classified as disturbed (D), while less massive clusters are generally relaxed (R); this can be seen in Figure 4.3.

4.3.2. Red sequence members

While spectroscopy provides a clean sample of member galaxies from precise velocities, it suffers from incompleteness mainly due to two practical reasons: 1) obtaining a redshift for a galaxy is expensive; typically it takes ~ 30 minutes of observations for galaxies in low-redshift ($z \lesssim 0.5$) clusters, depending on the telescope and observing conditions; and 2) only a limited number of galaxies can be targeted in a single observation because of slit overlap or fiber collisions.

Table 4.2: Cluster sample, redshifts, and velocity dispersions.

Cluster	z	N_m	N_{200}	σ_{200} (km s^{-1})	M_{200} (10^{14} M$_\odot$)	r_{200} (Mpc)	$\mathscr{S}_\Delta$	Main sources[a]	Main NED sources[b]
Abell 85	0.0555	284	248	967 ± 55	10.0 ± 1.7	2.03 ± 0.12	$0.01^{+0.00}_{-0.00}$(D)	3	14
Abell 115	0.1930	73	73	1028 ± 108	11.2 ± 3.5	2.03 ± 0.21	$0.24^{+0.02}_{-0.07}$(R)	–	1
Abell 119	0.0443	268	255	875 ± 48	7.5 ± 1.2	1.85 ± 0.10	< 0.01(D)	3	7
Abell 133	0.0558	62	59	791 ± 79	5.5 ± 1.7	1.66 ± 0.17	$0.24^{+0.03}_{-0.14}$(R)	–	21
Abell 209[c]	0.2090	110	110	1170 ± 99	16.4 ± 4.1	2.28 ± 0.19	$0.01^{+0.00}_{-0.01}$(D)	–	27
Abell 222[c]	0.2132	76	76	881 ± 79	7.0 ± 1.9	1.72 ± 0.15	$0.30^{+0.04}_{-0.04}$(R)	–	11,33
Abell 223[c]	0.2076	64	64	910 ± 80	7.8 ± 2.1	1.78 ± 0.16	$0.05^{+0.02}_{-0.02}$(D)	–	11,33
Abell 267	0.2291	219	156	1006 ± 74	10.3 ± 2.3	1.95 ± 0.14	< 0.01(D)	3,4	–
Abell 383	0.1885	182	134	918 ± 53	8.1 ± 1.4	1.81 ± 0.11	< 0.01(D)	–	18
Abell 399	0.0718	250	229	1046 ± 47	12.5 ± 1.7	2.18 ± 0.10	< 0.01(D)	5	20
Abell 401	0.0735	104	83	933 ± 81	8.9 ± 2.3	1.94 ± 0.17	$0.32^{+0.19}_{-0.05}$(R)	–	20
Abell 520	0.2007	153	127	1045 ± 73	11.8 ± 2.5	2.05 ± 0.14	$0.27^{+0.04}_{-0.11}$(R)	–	19
Abell 521[c]	0.2469	95	95	1002 ± 95	10.1 ± 2.9	1.92 ± 0.18	$0.06^{+0.02}_{-0.02}$(D)	–	16
Abell 545[c]	0.1577	80	80	1038 ± 89	11.8 ± 3.0	2.08 ± 0.18	$0.07^{+0.02}_{-0.00}$(R)	–	2
Abell 553	0.0670	54	44	665 ± 75	3.3 ± 1.1	1.39 ± 0.16	$0.01^{+0.03}_{-0.00}$(D)	5	–
Abell 586	0.1704	33	21	803 ± 104	5.4 ± 2.1	1.60 ± 0.21	$0.28^{+0.12}_{-0.07}$(R)	3	–
Abell 644[c]	0.0696	31	31	625 ± 96	2.7 ± 1.2	1.31 ± 0.20	$0.67^{+0.11}_{-0.05}$(R)	–	24
Abell 646	0.1266	259	69	707 ± 66	3.8 ± 1.1	1.44 ± 0.13	$0.07^{+0.22}_{-0.04}$(D)	3,4	–

Columns are: (1) cluster name; (2): cluster redshift; (3): number of members out to arbitrary radius; (4): number of members within r_{200}; (5): velocity dispersion of members within r_{200}; (6): total mass within r_{200}; (7): cluster radius r_{200}; (8): significance level of the DS test, the letter in parenthesis shows whether a cluster is classified as disturbed (D) or relaxed (R).

[a]Numbers are: (1): WLTV; (2): CNOC; (3): SDSS; (4): HeCS; (5): MENeaCS-spec. See text for references. [b]catalogues extracted from NED that contribute significantly to each cluster. These are: (1): Barrena et al. (2007); (2): Barrena et al. (2011); (3): Belloni & Roeser (1996); (4): Boschin et al. (2004); (5): Boschin et al. (2009); (6): Braglia et al. (2009); (7): WINGS (Cava et al. 2009); (8): Christlein & Zabludoff (2003); (9): 2dF (Colless et al. 2003); (10): Czoske et al. (2001); (11): Dietrich et al. (2002); (12): Dressler & Gunn (1992); (13): WiggleZ (Drinkwater et al. 2010); (14): Durret et al. (1998); (15): Ebeling et al. (2014); (16): Ferrari et al. (2003); (17): Fisher et al. (1998); (18): Geller et al. (2014); (19): Girardi et al. (2008); (20): Hill & Oegerle (1993); (21): 2MRS (Huchra et al. 2012); (22): Jäger et al. (2004); (23): Liang et al. (2000); (24): Martini et al. (2007); (25): Maurogordato et al. (2008); (26): Maurogordato et al. (2011); (27): Mercurio et al. (2003); (28): Miller et al. (2004); (29): Miller et al. (2006); (30): Oegerle et al. (1995); (31): Owers et al. (2011); (32): Pimbblet et al. (2006); (33): Proust et al. (2000). [c]Spectroscopic members extend out to less than $0.8 r_{200}$.

Table 4.2: *Continued*

Cluster	z	N_m	N_{200}	σ_{200} (km s^{-1})	M_{200} (10^{14} M$_\odot$)	r_{200} (Mpc)	$\mathscr{S}_\Delta$	Main sources^a	Main NED sources^b
Abell 655	0.1271	306	109	938 ± 57	8.8 ± 1.6	1.91 ± 0.12	$0.03^{+0.01}_{-0.02}$(D)	3,4	–
Abell 697	0.2821	215	106	1161 ± 89	15.4 ± 3.6	2.19 ± 0.17	$0.44^{+0.05}_{-0.02}$(R)	3,4	–
Abell 754	0.0546	305	300	959 ± 43	9.8 ± 1.3	2.01 ± 0.09	$0.01^{+0.00}_{-0.00}$(D)	–	8
Abell 780^c	0.0547	33	33	822 ± 113	6.2 ± 2.5	1.73 ± 0.24	$0.01^{+0.01}_{-0.00}$(D)	–	21
Abell 795	0.1385	166	117	768 ± 59	4.9 ± 1.1	1.56 ± 0.12	$0.06^{+0.07}_{-0.02}$(D)	3,4,5	–
Abell 851	0.4038	53	47	999 ± 138	9.3 ± 3.8	1.77 ± 0.24	$0.01^{+0.03}_{-0.01}$(D)	–	3,12
Abell 959	0.2882	67	67	982 ± 101	9.4 ± 2.9	1.85 ± 0.19	$0.08^{+0.04}_{-0.03}$(D)	–	5
Abell 961	0.1275	58	16	740 ± 142	4.4 ± 2.5	1.51 ± 0.29	$0.84^{+0.06}_{-0.13}$(R)	3	–
Abell 963	0.2036	165	85	922 ± 64	8.1 ± 1.7	1.81 ± 0.13	$0.17^{+0.06}_{-0.06}$(R)	3,4	–
Abell 990	0.1421	209	86	829 ± 96	6.1 ± 2.1	1.68 ± 0.19	$0.74^{+0.03}_{-0.05}$(R)	3,4,5	–
Abell 1033	0.1224	170	98	762 ± 52	4.8 ± 1.0	1.56 ± 0.11	$0.59^{+0.08}_{-0.21}$(R)	3,4	–
Abell 1068	0.1393	104	32	740 ± 160	4.3 ± 2.8	1.50 ± 0.32	$0.93^{+0.04}_{-0.04}$(R)	3,4	–
Abell 1132	0.1349	160	55	727 ± 89	4.1 ± 1.5	1.48 ± 0.18	$0.13^{+0.06}_{-0.05}$(R)	3,4	–
Abell 1234	0.1638	54	30	513 ± 86	1.4 ± 0.7	1.03 ± 0.17	$0.87^{+0.06}_{-0.07}$(R)	3,4	–
Abell 1246	0.1920	207	87	956 ± 84	9.1 ± 2.4	1.89 ± 0.17	$0.01^{+0.01}_{-0.00}$(D)	3,4	–
Abell 1285	0.1078	77	51	826 ± 90	6.1 ± 2.0	1.70 ± 0.19	$0.52^{+0.08}_{-0.18}$(R)	5	–
Abell 1361	0.1157	143	46	587 ± 62	2.2 ± 0.7	1.21 ± 0.13	$0.39^{+0.15}_{-0.07}$(R)	3,4	–
Abell 1413	0.1418	124	65	881 ± 81	7.3 ± 2.0	1.78 ± 0.16	$0.72^{+0.07}_{-0.23}$(R)	3,4	–
Abell 1650	0.0841	266	140	720 ± 48	4.1 ± 0.8	1.50 ± 0.10	$0.99^{+0.00}_{-0.02}$(R)	3,5	–
Abell 1651	0.0847	214	138	903 ± 51	8.0 ± 1.4	1.87 ± 0.11	$0.65^{+0.04}_{-0.16}$(R)	–	9,21
Abell 1689	0.1847	252	235	1429 ± 81	30.0 ± 5.1	2.82 ± 0.16	<0.01(D)	3,4	–
Abell 1758	0.2772	133	34	744 ± 107	4.1 ± 1.8	1.41 ± 0.20	$0.11^{+0.06}_{-0.03}$(R)	3,4	–
Abell 1763	0.2323	186	103	1130 ± 81	14.6 ± 3.1	2.18 ± 0.16	<0.01(D)	3,4	–
Abell 1781	0.0622	54	16	419 ± 93	0.8 ± 0.5	0.88 ± 0.19	$0.92^{+0.02}_{-0.19}$(R)	3	–
Abell 1795	0.0629	191	133	778 ± 51	5.2 ± 1.0	1.63 ± 0.11	$0.26^{+0.04}_{-0.09}$(R)	3	21
Abell 1835	0.2506	195	41	762 ± 106	4.5 ± 1.9	1.46 ± 0.20	$0.66^{+0.06}_{-0.23}$(R)	3,4	–
Abell 1914	0.1671	257	146	911 ± 54	7.9 ± 1.4	1.82 ± 0.11	$0.86^{+0.03}_{-0.05}$(R)	3,4	–
Abell 1927	0.0953	138	58	725 ± 58	4.2 ± 1.0	1.50 ± 0.12	$0.25^{+0.02}_{-0.08}$(R)	3,5	–

Table 4.2: *Continued*

Cluster	z	N_{m}	N_{200}	σ_{200} ($\mathrm{km\,s^{-1}}$)	M_{200} ($10^{14}\,\mathrm{M_\odot}$)	r_{200} (Mpc)	$\mathscr{S}_\Delta$	Main sources[a]	Main NED sources[b]
Abell 1942	0.2257	51	27	820 ± 140	5.6 ± 2.9	1.59 ± 0.27	$0.04^{+0.05}_{-0.01}$(D)	3	–
Abell 1991	0.0587	175	99	553 ± 45	1.9 ± 0.5	1.17 ± 0.10	$0.12^{+0.09}_{-0.05}$(R)	3,5	–
Abell 2029	0.0777	317	181	1152 ± 58	16.6 ± 2.5	2.39 ± 0.12	<0.01(D)	3	21
Abell 2033	0.0796	190	88	911 ± 69	8.3 ± 1.9	1.89 ± 0.14	$0.03^{+0.03}_{-0.01}$(D)	3	21
Abell 2050	0.1202	164	82	854 ± 80	6.7 ± 1.9	1.74 ± 0.16	$0.34^{+0.06}_{-0.03}$(R)	3,4	–
Abell 2055	0.1028	154	69	697 ± 64	3.7 ± 1.0	1.44 ± 0.13	$0.04^{+0.02}_{-0.00}$(D)	3,4	21
Abell 2064	0.0734	62	32	675 ± 108	3.4 ± 1.6	1.41 ± 0.22	$0.40^{+0.13}_{-0.05}$(R)	3	–
Abell 2065	0.0725	219	164	1095 ± 67	14.3 ± 2.6	2.28 ± 0.14	$0.03^{+0.01}_{-0.01}$(D)	3	–
Abell 2069	0.1139	331	146	966 ± 63	9.7 ± 1.9	1.98 ± 0.13	$0.01^{+0.00}_{-0.00}$(D)	3,4	–
Abell 2104	0.1547	90	56	1081 ± 126	13.3 ± 4.6	2.17 ± 0.25	$0.22^{+0.09}_{-0.09}$(R)	–	23
Abell 2111	0.2281	256	83	738 ± 66	4.1 ± 1.1	1.43 ± 0.13	$0.46^{+0.09}_{-0.04}$(R)	3,4	29
Abell 2125	0.2466	141	55	857 ± 122	6.4 ± 2.7	1.65 ± 0.23	$0.46^{+0.01}_{-0.26}$(R)	–	28
Abell 2142	0.0903	1052	731	1086 ± 31	13.9 ± 1.2	2.24 ± 0.06	$0.01^{+0.00}_{-0.00}$(D)	3	31
Abell 2163	0.2004	309	290	1279 ± 53	21.5 ± 2.7	2.51 ± 0.10	$0.03^{+0.02}_{-0.01}$(D)	–	25
Abell 2204	0.1507	100	15	782 ± 278	5.1 ± 5.4	1.58 ± 0.56	$0.35^{+0.33}_{-0.12}$(R)	–	32
Abell 2219	0.2255	364	241	1189 ± 65	17.0 ± 2.8	2.30 ± 0.13	<0.01(D)	3,4	4
Abell 2259	0.1602	158	77	901 ± 70	7.7 ± 1.8	1.80 ± 0.14	$0.04^{+0.12}_{-0.01}$(D)	3,4	–
Abell 2261	0.2257	206	76	882 ± 86	7.0 ± 2.0	1.71 ± 0.17	$0.03^{+0.05}_{-0.02}$(D)	3,4	–
Abell 2319[c]	0.0538	83	83	1101 ± 99	14.7 ± 4.0	2.31 ± 0.21	$0.52^{+0.07}_{-0.16}$(R)	–	30
Abell 2390	0.2287	136	92	1120 ± 113	14.3 ± 4.3	2.17 ± 0.22	$0.23^{+0.01}_{-0.10}$(R)	2	–
Abell 2409	0.1454	101	46	826 ± 94	6.0 ± 2.0	1.67 ± 0.19	$0.16^{+0.09}_{-0.03}$(R)	3,5	–
Abell 2440[c]	0.0906	88	88	766 ± 61	4.9 ± 1.2	1.59 ± 0.13	$0.13^{+0.03}_{-0.02}$(R)	3	26
Abell 2495	0.0790	98	46	631 ± 55	2.8 ± 0.7	1.32 ± 0.12	$0.23^{+0.06}_{-0.01}$(R)	3,5	–
Abell 2537	0.2964	175	65	909 ± 85	7.4 ± 2.1	1.70 ± 0.16	$0.05^{+0.04}_{-0.01}$(D)	3	6
Abell 2597	0.0829	39	17	682 ± 131	3.5 ± 2.0	1.42 ± 0.27	$0.37^{+0.15}_{-0.09}$(R)	–	9,13
Abell 2670	0.0763	241	196	919 ± 46	8.5 ± 1.3	1.91 ± 0.10	<0.01(D)	3	21
Abell 2703	0.1140	75	13	657 ± 53	3.1 ± 0.8	1.35 ± 0.11	$0.17^{+0.18}_{-0.05}$(R)	3	–
CL 0024.0+1652	0.3948	229	131	757 ± 48	4.1 ± 0.8	1.35 ± 0.09	<0.01(D)	–	10

Table 4.2: *Continued*

Cluster	z	N_m	N_{200}	σ_{200} ($km\,s^{-1}$)	M_{200} ($10^{14}\,M_\odot$)	r_{200} (Mpc)	$\mathscr{S}_\Delta$	Main sources[a]	Main NED sources[b]
MACS J0717.5+3745	0.5436	468	215	1370±79	22.0±3.8	2.24±0.13	<0.01(D)	–	15
MKW3S	0.0444	125	82	592±49	2.3±0.6	1.25±0.11	$0.83^{+0.06}_{-0.11}$(R)	3	–
MS 0015.9+1609	0.5475	232	122	1330±115	20.0±5.2	2.17±0.19	$0.32^{+0.10}_{-0.18}$(R)	1,2	–
MS 0440.5+0204	0.1962	51	35	742±103	4.3±1.8	1.46±0.20	$0.26^{+0.14}_{-0.13}$(R)	2	–
MS 0451.6−0305	0.5382	247	200	1252±55	16.8±2.2	2.05±0.09	<0.01(D)	1,2	–
MS 1008.1−1224	0.3077	86	85	1028±92	10.6±2.8	1.91±0.17	$0.59^{+0.07}_{-0.11}$(R)	2	22
MS 1224.7+2007	0.3258	33	29	790±95	4.8±1.7	1.46±0.17	$0.57^{+0.23}_{-0.07}$(R)	2,3	–
MS 1231.3+1542	0.2347	84	65	710±57	3.7±0.9	1.38±0.11	$0.87^{+0.03}_{-0.03}$(R)	2,3	–
MS 1358.4+6245	0.3289	189	152	1021±56	10.3±1.7	1.88±0.10	$0.01^{+0.01}_{-0.00}$(D)	2	17
MS 1455.0+2232	0.2565	57	57	928±111	8.0±2.9	1.77±0.21	$0.58^{+0.07}_{-0.24}$(R)	2,3	–
MS 1512.4+3647	0.3719	30	29	960±170	8.4±4.4	1.73±0.30	$0.04^{+0.03}_{-0.00}$(D)	2	–
MS 1621.5+2640	0.4254	70	41	724±82	3.5±1.2	1.27±0.14	$0.17^{+0.20}_{-0.04}$(R)	2	–
RX J0736.6+3924	0.1179	62	28	432±64	0.9±0.4	0.89±0.13	$0.52^{+0.12}_{-0.03}$(R)	3,5	–
ZwCl 0628.1+2502	0.0814	72	66	843±96	6.6±2.2	1.75±0.20	$0.04^{+0.02}_{-0.01}$(D)	5	–
ZwCl 1023.3+1257	0.1425	84	24	622±108	2.6±1.3	1.26±0.22	$0.79^{+0.17}_{-0.17}$(R)	3,4	–
ZwCl 1215.1+0400	0.0773	183	107	902±65	8.0±1.7	1.88±0.14	$0.29^{+0.02}_{-0.04}$(R)	3	–

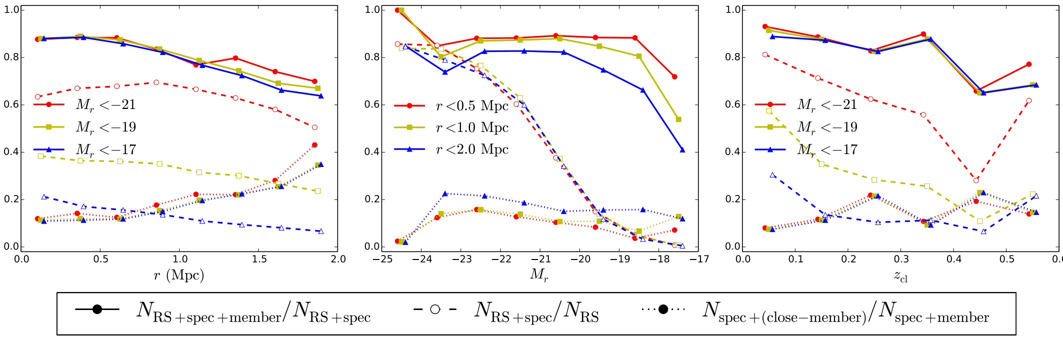

Figure 4.4: Purity of the red sequence (filled symbols with solid lines) and spectroscopic completeness within the red sequence (open symbols with dashed lines). Filled symbols with dotted lines show the fraction of galaxies that are not selected as members but that are within $\Delta z = 0.03(1+z)$ of the cluster, which represents the contamination in an unbiased photometric redshift selection. Left: as a function of cluster-centric distance, for different luminosity limits. Middle: as a function of absolute magnitude, for different radial apertures. Right: as a function of redshift for different luminosity limits, at an aperture of 1 Mpc. Note that points within a given line are independent (each line is a differential distribution), but lines of the same type are not independent from each other.

Being a distinct feature of clusters, the red sequence provides an ideal complement to spectroscopic members. As we show below, for luminous galaxies near the centres of clusters this also provides a clean membership selection, though not as clean as spectroscopy. Using the red sequence *in addition to* the spectroscopic selection ensures that only a small fraction of galaxies need to be included through this more uncertain method, making the purity of the sample very close to 100%.

To find the red sequence in each cluster, we first separate blue and red galaxies by fitting two one-dimensional gaussians to the color distribution of galaxies using an Error-Corrected Gaussian Mixture Model (ECGMM, Hao et al. 2009). We then fit a straight line in color-magnitude space to the red galaxies using a maximum likelihood approach that accounts for intrinsic scatter and the measurement uncertainty in color, iteratively rejecting 2σ outliers. Details will be presented in a forthcoming paper (Sifón et al., in prep).

We assess the purity of the red sequence as a cluster member selection procedure by looking at red sequence members that have redshifts. There are in total 57,885 red sequence galaxies up to $M_r = -17$ and within 2 Mpc, 7,224 of which have a redshift measurement (~12%). Figure 4.4 shows that the red sequence is a high-fidelity member selection method even to large radii. Only the sample of both low-luminosity ($M_r \gtrsim -19$) and distant ($r \gtrsim 1$ Mpc) red sequence members has a lower purity, although the latter is still $\gtrsim 70\%$ for most of this distance-luminosity space. We include in the extended sample all red sequence galaxies more luminous than $M_r = -19$ within 1 Mpc of the cluster centre. Within these parameter boundaries, 84% of red sequence galaxies with a spectroscopic redshift are confirmed cluster members. This level of contamination (16% of red sequence members) has no effects on our results.

The rightmost panel of Figure 4.4 shows that up to $z \sim 0.4$, the purity is extremely high (~90%) but then decreases to ~70%, because above $z \sim 0.4$ the 4000Å break is no longer bracketed by the g and r bands (similarly for the B and R bands). The completeness of the spectroscopic samples does drop noticeably with redshift because of the higher difficulty posed by spectroscopic observations of high redshift clusters.

From a lensing perspective, one other important ingredient in assessing the red sequence is the redshift distribution of the contaminating fraction, which we can quantify using red sequence galaxies that are confirmed to be outside the cluster. If they are sufficiently far behind the cluster, they could in fact be lensed, inducing a signal that we wish to avoid. If instead they are either very close behind or in front of the cluster, then they will not be lensed and will only dilute the signal. Figure 4.5 shows the redshift distribution of red sequence galaxies that are confirmed to be nonmembers through the distance ratio, D_{ls}/D_s, where D_{ls} is the angular diameter distance between the lens (i.e., cluster) and the source galaxy, and D_s is the angular diameter distance to the source. Note that $D_{ls} < 0$ for $z_s < z_l$. Galaxies behind the clusters are lensed, resulting in (apparent) tangential alignments. The amplitude of this effect can be quantified by the "lensing efficiency," β, defined as

$$\beta \equiv \left\langle \max\left(0, \frac{D_{ls}}{D_s}\right)\right\rangle, \tag{4.2}$$

which is typically calculated using photometric redshifts or an average redshift distribution. Note that Equation 4.2 naturally accounts for galaxies in front of the cluster, which do not contain a lensing signal (but do introduce noise), which is especially important when using a generic redshift distribution, or full photometric redshift probability distributions (in which case background galaxies have a nonzero probability of being in front of the cluster). Of the 688 confirmed nonmembers in the red sequence, 496 (72%) are behind the cluster (incuding those immediately behind the cluster), and the lensing efficiency of red sequence nonmembers is $\beta = 0.085$. It is therefore possible that the contaminating red sequence galaxies contain some lensing signal from background galaxies, but within the red sequence selection limits imposed here, this sample is only 16% of the red sequence galaxies. Therefore there is a fraction $\sim 0.72 \times 0.16 \simeq 12\%$ of contaminating galaxies (with $\sim 0.28 \times 0.16 \simeq 4\%$—those in the foreground—adding noise). The lensing signal in these galaxies is $\gamma_{+,\mathrm{rs}} \lesssim 0.11 \cdot \beta \cdot \gamma_+ = 0.11 \cdot 0.085 \cdot 0.10 \approx 9 \times 10^{-4}$, several times smaller than the statistical uncertainties (where $\gamma_+ \approx 0.1$ is a typical shear amplitude in the inner regions of galaxy clusters).

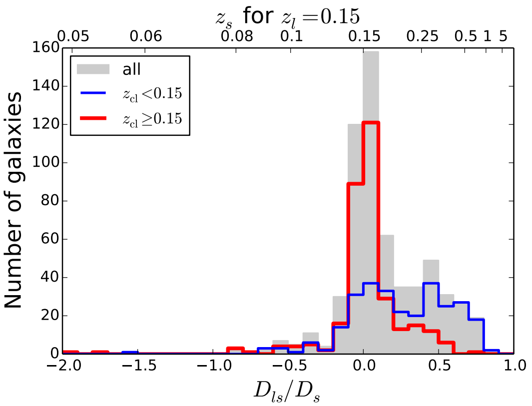

Figure 4.5: Distribution of the distance ratio, D_{ls}/D_s, for red sequence members that are confirmed to be nonmembers of the clusters from spectroscopic redshifts. The gray filled histogram shows red sequence galaxies from all clusters; the blue and red (empty) histograms show the distributions for clusters at low and high redshift, respectively. For illustration, the top axis shows the source redshift for a cluster at $z = 0.15$.

In summary, the red sequence gives a high-fidelity cluster member selection. It is important, however, to restrict this selection to the inner regions of clusters and to luminous galaxies (as shown in Figure 4.4), because the red sequence may contain some lensing signal. The purity of the red sequence as selected here is 84%, so this contamination is not expected to be significant. Adding the red sequence members to the 14,576 spectroscopically confirmed members gives a total of $N_\mathrm{m} + N_\mathrm{rs} = 23{,}041$ members with an estimated contamination of $0.16 \cdot N_\mathrm{rs}/(N_\mathrm{m} + N_\mathrm{rs}) \approx 8\%$.

4.3.3. Photometric redshift contamination

By taking a fixed width in velocity, we can simulate the members found by an accurate, unbiased photometric redshift criterion. The dotted lines in Figure 4.4 show the fraction of galaxies that are within $\Delta z = 0.03(1+z)$ (as expected for large ongoing photometric redshifts) but are not members of the cluster,[7] as determined in Section 4.3.1. The contamination is roughly independent of magnitude at all radii and at a level of $\sim 13\%$ within 1 Mpc of the BCG, rising steeply beyond this radius. In terms of apparent magnitude the curves look similar in the range $m_r \lesssim 23$, the range in which most of the selected red sequence galaxies are found. This contamination rises shallowly with redshift, reaching $\sim 20\%$ at $z \gtrsim 0.3$.

The radial dependence in Figure 4.4 is shown in physical units instead of in units of r_{200} because this is more generally used with photometric surveys where the physical size of each cluster is not known, and Figure 4.4 gives an idea of the apertures that should be used to either search for clusters or characterize the cluster based on a red sequence sample.

Comparing the dotted and solid curves, it seems that there is not such a significant gain in using photo-z's versus the red sequence. A photo-z selection has the advantage that it selects a more representative population of the cluster, and that the red sequence depends on a single color (at least in this implementation) and it becomes less reliable when the 4000Å break is not bracketed by the filters used. This is the case in our study for $z \gtrsim 0.36$. It is also apparent, as with the red sequence, that a photo-z selection becomes significantly contaminated beyond $r \sim 1\,\mathrm{Mpc}$.

Finally, we note that the galaxies we refer to here (shown with the dotted lines) are not cluster members but also do not contribute a lensing signal, because they are too close behind. They are, indeed, likely to be part of the same large-scale structure of the cluster so would probably feel tidal torque from it similar to the actual member galaxies. Thus from the perspective of galaxy alignment measurements these galaxies should not dilute the signal significantly, nor introduce a lensing signal.

4.3.4. Control samples

We construct two catalogues as control samples to assess spurious contributions to our measurements. The shapes of objects in these two samples are unaffected by the cluster (and are mostly unrelated between objects in each sample), so their alignment signals (see Section 4.4) should be consistent with zero. A departure from zero would mean that there is significant residual PSF ellipticity in the images, and therefore that the shape measurements are unreliable.

First, we use all stars in the magnitude range $17 < m_r < 22$, selected as outlined in Section 4.2.1, for a total of 443,321 stars. We choose the bright limit to avoid saturated stars, whereas the faint limit ensures that the star sample is not contaminated by faint, unresolved galaxies.

We also use all spectroscopically confirmed foreground galaxies, which are selected as all galaxies with peculiar velocities more negative than $-10{,}000\,\mathrm{km\,s^{-1}}$ in the rest-frame of the cluster. There are 3,666 spectroscopically confirmed foreground galaxies in the direction of 73 clusters. The clusters with the most foreground galaxies are two high-redshift clusters, namely MS 0451.6−0305 at $z = 0.539$ and MACS J0717.5+3745 at $z = 0.544$, with $N_{\rm fg} = 306$ and $N_{\rm fg} = 304$, respectively.

[7] $\Delta z = 0.03(1+z)$ corresponds to $\approx 10{,}000\,\mathrm{km\,s^{-1}}$ at the median redshift of the sample, $z = 0.15$.

4.4. Measuring intrinsic alignments

We measure the alignment signal of galaxies within clusters by weight-averaging the ellipticity components of all galaxies within a given radial annulus,

$$\langle\epsilon_i\rangle = \frac{\sum_n w_n \epsilon_{i,n}}{\sum_n w_n}, \tag{4.3}$$

with weights equal to

$$w_n = \frac{1}{\epsilon_{\rm int}^2 + \sigma_n^2}, \tag{4.4}$$

where σ_n is the measurement uncertainty on the ellipticity of the n-th galaxy. We assume an intrinsic (i.e., unlensed) galaxy ellipticity dispersion $\epsilon_{\rm int} = \sqrt{\langle\epsilon_i\epsilon_i\rangle} = 0.25$. The uncertainty in Equation 4.3 is equal for both components and is given by $\sigma(\epsilon_i) = \left(\sum_n w_n\right)^{-1/2}$. In this work, we use the shapes of cluster members to measure three kinds of alignment: the alignment of (satellite) galaxies toward the centre of the cluster, the alignment of galaxies with respect to the BCG orientation, and the alignment between satellite galaxies. These three quantities are detailed below.

Throughout, we refer to raw ellipticities as e_i, and to ellipticities that account for instrumental effects (i.e., PSF size in the case of gaussianized images) as ϵ_i.

4.4.1. Different alignment signals

In this section we outline the different rotations we apply to the ellipticity measurements of Section 4.4.2 in order to extract alignment signals within clusters.

4.4.1.1. Satellite radial alignment

We measure the alignment of galaxies with respect to the centre of the cluster using ellipticity components rotated to a frame such that

$$\epsilon_+ = -(\epsilon_1 \cos 2\theta + \epsilon_2 \sin 2\theta) \tag{4.5}$$

$$\epsilon_\times = \epsilon_1 \sin 2\theta - \epsilon_2 \cos 2\theta \tag{4.6}$$

where ϵ_1 and ϵ_2 are the galaxy ellipticities in the cartesian frame, with ϵ_1 measuring the ellipticity in the x and y directions, and ϵ_2 in diagonal directions. Here θ is the azimuthal angle with respect to the centre of the cluster. In this frame, ϵ_+ measures the distortion in the tangential and radial directions while $\epsilon_\times$ measures the distortion at ±45° from the radial direction (see, e.g., Figure 1 of Bernstein & Norberg 2002, for a diagram). Note that the definition of ϵ_+ in Equation 4.5 has the opposite sign to that typically used in weak lensing analyses. For symmetry reasons the cross component, $\langle\epsilon_\times\rangle$, of an ensemble of clusters should be consistent with zero (although a single cluster might have a preferred nonradial alignment direction such that $\langle\epsilon_\times\rangle \neq 0$, the average over an ensemble of clusters must be zero), so it serves as a check for systematic effects. On the other hand, $\langle\epsilon_+\rangle < 0$ indicates that galaxies are preferentially aligned in the tangential direction, as is the case for gravitationally lensed background galaxies, while $\langle\epsilon_+\rangle > 0$ would indicate a radial alignment of the galaxies, which could be the case for cluster members. Finally, $\langle\epsilon_+\rangle = 0$ implies that galaxies are randomly oriented toward the centre of the cluster.

4.4.1.2. Satellite-BCG alignment

To measure the alignment between satellite galaxies and the BCG, we rotate the shapes and coordinates of satellites to a frame where the direction of $\epsilon_1 > 0$ coincides with the major axis of the BCG, namely

$$\begin{aligned} \epsilon_1' &= \epsilon \cos\left[2\left(\phi - \phi_{\rm BCG}\right)\right] \\ \epsilon_2' &= \epsilon \sin\left[2\left(\phi - \phi_{\rm BCG}\right)\right], \end{aligned} \tag{4.7}$$

where ϕ and $\phi_{\rm BCG}$ are the position angles of a satellite galaxy and the BCG, respectively, and $\epsilon \equiv (\epsilon_1^2 + \epsilon_2^2)^{1/2}$ is the ellipticity of the galaxy. In this new frame, the BCG has ellipticity components $\epsilon_1' = \epsilon$ and $\epsilon_2' = 0$. For the BCG position angles we use only GALFIT measurements (see Section 4.4.2.2), since these are expected to be more reliable for galaxies as large as BCGs. Analogous to the radial alignments, $\langle\epsilon_1'\rangle > 0$ implies that satellite galaxies are oriented along the major axis of the BCG, $\langle\epsilon_1'\rangle < 0$ that satellites are oriented along the BCG minor axis, and $\langle\epsilon_1'\rangle = 0$ implies random orientations; ϵ_2' measures diagonal alignments so we expect $\langle\epsilon_2'\rangle = 0$.

4.4.1.3. Satellite-satellite alignment

Finally, we compute the alignment between satellite galaxies within clusters by calculating Equation 4.5 taking every satellite galaxy as a test galaxy (i.e., as the frame for θ). BCGs are excluded from this analysis. This probes potential alignments of galaxies in substructures within the cluster. In principle, if there are N members in a cluster, the number of pairs is equal to $N(N-1)/2$. However, we only use pairs for which a full circle can be averaged, to avoid averages that include mostly objects in the corners of the images where PSF residuals may be larger. This is a concern for massive, low redshift clusters, where $30'$ (half the side of the MegaCam image) is roughly equal to r_{200} in the worst cases. To ensure that the average remains unbiased, therefore, we only include pairs such that the sum of the distance between the test galaxy and the centre of the cluster and the separation between the two satellites is less than 90% of the distance between the cluster centre and the edge of the image.

4.4.2. Shape measurements

Measuring galaxy shapes is a challenging endeavor, especially in the presence of noise and PSF anisotropies (e.g., Massey et al. 2007; Melchior & Viola 2012; Kitching et al. 2013). For large (in units of the PSF), bright objects such as those used here, this should be less of a problem. Moreover, after gaussianization the PSF ellipticity is negligible. In this work we measure the shapes of member galaxies using two different methods, which allows us to test for consistency and robustness of the results. Below we give a brief outline of each method to highlight their differences; more details can be found in the original works.

Shapes are measured from the gaussianized images (Section 4.2.1). The PSF in these images is, by construction, circular, gaussian, and constant across the image. Therefore the shape measurement methods need to account for the blurring of the ellipticity by the PSF, but there are no systematic ellipticities in the images (to a high enough precision, see Section 4.4.3).

4.4.2.1. Kaiser-Squires-Broadhurst (KSB)

KSB was developed for weak lensing measurements by Kaiser et al. (1995) and revised by Hoekstra et al. (1998). It measures shapes by estimating the central second moments I_{ij}

of the image fluxes to measure the two-component polarization

$$e_1 = \frac{I_{11} - I_{22}}{I_{11} + I_{22}};\ e_2 = \frac{2I_{12}}{I_{11} + I_{22}}. \tag{4.8}$$

These measurents are weighted with a circular Gaussian of width r_g, which corresponds to the radius of maximum significance measured by KSB; this weight reduces shot noise in the measurements. Blurring by the PSF is corrected by the so-called pre-seeing shear polarizability, P^γ, which quantifies the effect of the convolution of the PSF to the image polarization, e_i (Luppino & Kaiser 1997; Hoekstra et al. 1998). The corrected ellipticity is then $\epsilon_i = e_i/P^\gamma$.[8] Both e_i and P^γ are measured with the same radius, r_g, for each galaxy.

4.4.2.2. GALFIT

GALFIT was developed by Peng et al. (2002), having in mind the modeling of different components of galaxies for studies of galaxy structure and evolution. It attempts to model the light of a galaxy by fitting a multi-component generalized ellipse given by

$$r = \left(|x|^{c+2} + \left|\frac{y}{q}\right|^{c+2}\right)^{1/(c+2)} \tag{4.9}$$

where a true ellipse has $c = 0$, a boxy shape $c > 0$ and a disky shape $c < 0$; here q is the minor-to-major axes ratio. Additionally, the position angle, ϕ, is defined as the direction of the major axis. GALFIT accounts for the PSF model (in this case a single gaussian for each whole field) when measuring ellipticities. We use a simple Sérsic (1968) model for the surface brightness profile, $\ln I(r) \propto r^{1/n}$. Only galaxies with Sérsic index $0.5 < n < 8$ and with axis ratio $q > 0.15$ are included in the sample. We convert q and ϕ to the same ellipticity measures of KSB through

$$\epsilon_1 = \left(\frac{1-q}{1+q}\right)\cos 2\phi;\ \epsilon_2 = \left(\frac{1-q}{1+q}\right)\sin 2\phi. \tag{4.10}$$

4.4.3. Systematic effects

Because weak lensing measurements rely on averages of a large number of small signals, they are more prone to systematic effects than photometry and require more agressive masks. Therefore some spectroscopic members (all of which are in our photometric catalogue) are not included in the shape catalogues. Moreover, the KSB and GALFIT catalogues are not the same since both have different requirements on, e.g., the size of an object and blending with nearby objects to estimate a reliable shape. Of the 14,576 spectroscopic members, 13,966 have a KSB shape measurement and 13,360 have a GALFIT measurement, with an overlap of 12,160 galaxies and a total of 14,250 galaxies with a shape measurement. Similarly, of 23,041 spectroscopic+RS members, 20,493 have KSB measurements and 18,511 have GALFIT measurements. The smaller number of objects with GALFIT measurements comes mainly from high-redshift galaxies (compare Tables 4.3 and 4.4). This is because small, faint galaxies are harder for GALFIT to fit, while KSB is well-suited to measure the shapes of faint (background) galaxies.

[8] Because the PSF in our images has vanishing ellipticity by construction, the PSF correction of KSB is mathematically exact. This is not the case if the PSF is significantly elliptical.

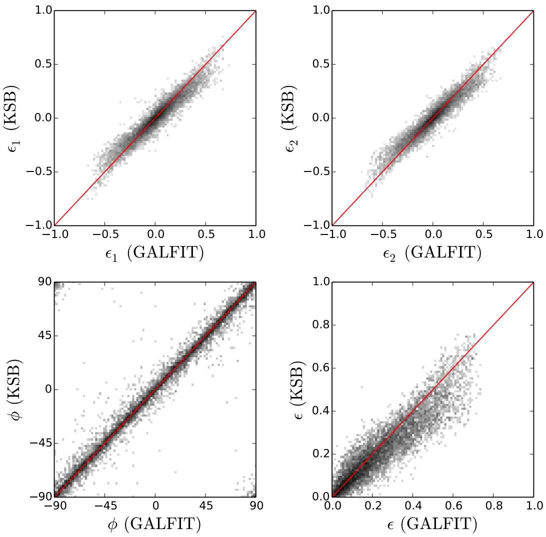

Figure 4.6: Comparison of shape measurements from KSB and GALFIT. Grey scales show the number of points per bin in logarithmic scale. Red lines show $y = x$. Top: Ellipticity components in cartesian coordinates. Bottom left: position angles, ϕ, in degrees. The periodicity of ϕ (of 180 deg) can be seen in the top left and bottom right corners of the plot. Bottom right: galaxy ellipticities.

We only consider galaxies with shape measurements from either method in this work, except for the assessment of the red sequence in Section 4.3.2. Figure 4.6 compares the shape parameters for all spectroscopic members that have valid KSB and GALFIT estimates. While the measurements generally agree, there is a small but noticeable difference for large-ellipticity objects, such that KSB estimates lower ellipticities than GALFIT. This effect is present with more or less the same magnitude for all clusters; it is a genuine difference between the two methods (for our particular dataset), and there is an indication that this effect may be more pronounced for smaller objects. This difference is due to higher-order corrections that are not implemented in KSB, which become important at large ellipticities (Viola et al. 2011). As we show in Section 4.5 this has no impact on our results, so we do not explore this issue further.

As a further test, Figure 4.7 shows the alignment signals of the control samples. As expected, foreground galaxies have a signal consistent with zero in both ellipticity components at all radii, with large errorbars due to small statistics. The average ellipticities of stars are different from zero at significant levels in most of the radial range. However, the average ellipticity is constrained to $\langle\epsilon_i\rangle \lesssim 2\times10^{-4}$ at all radii, an order of magnitude smaller than the statistical errors in the alignments of cluster members. Thus any systematic effects arising from PSF uncertainty or other instrumental biases are controlled to much lower values than the statistical uncertainties, and can be neglected for the purposes of this work.

Finally, the gaussianization of the images makes the PSF round and homogeneous across an image but produces anisotropic (correlated) noise, which could introduce noise bias in our measurements. The level of anisotropy can be assessed by measuring star ellipticities as a function of magnitude: if noise is highly anisotropic then noisier measurements would show, on average, a larger anisotropy than high-S/N measurements. We test this by comparing the ellipticities of stars as a function of magnitude (for $18 \leq m_r \leq 22$), and find that the average ellipticities are consistent with the levels shown in Figure 4.7. Moreover, we use galaxies whose number density drops rapidly beyond $m_r \sim 18$, and are typically 8 times larger than the PSF. We conclude that anisotropic noise can be safely neglected in this study.

4.5. Results

In this section we present and discuss the main results of this paper. We refer to Section 4.4 for details on the calculations that lead to the values reported here and a discussion of systematic effects.

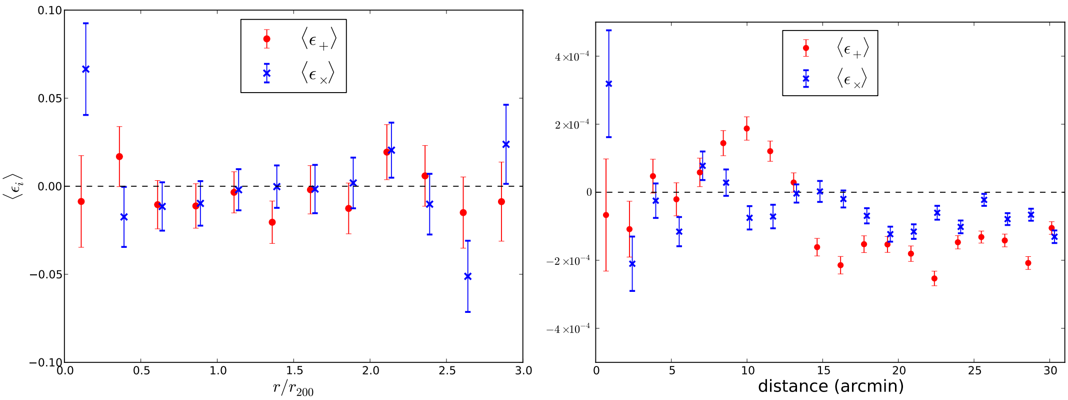

Figure 4.7: Alignment signal from control samples measured with KSB, with data points shifted horizontally for clarity. Left: 3,666 foreground galaxies in the direction of 73 clusters as a function of distance from the cluster, in units of r_{200}. Right: stars in the magnitude range $17 < m_r < 22$ as a function of angular distance from the centre of each cluster. Typically, $r_{200} \sim 10'$. Note the different vertical scales in each plot.

4.5.1. Satellite radial alignment

Figure 4.8 shows the average radial alignment for all spectroscopically confirmed cluster members with good ellipticity measurements from KSB and GALFIT in annuli around the cluster centre. Both methods show that the intrinsic alignment signal of cluster members is consistent with zero across all radii. Hereafter, we choose to quote average values within r_{200} since, strictly speaking, this is the input required by the halo model (see Section 4.6). Within r_{200}, the alignment of spectroscopic members is constrained to an average of $\langle\epsilon_+\rangle = -0.0037 \pm 0.0027$ with KSB and $\langle\epsilon_+\rangle = 0.0004 \pm 0.0031$ with GALFIT at 68% confidence. The cross components are also consistent with zero. Including red sequence members roughly doubles the number of galaxies used and confirms the latter result, with $\langle\epsilon_+\rangle = -0.0022 \pm 0.0020$ and $\langle\epsilon_+\rangle = 0.0000 \pm 0.0026$ with KSB and GALFIT, respectively.

Our results are consistent with the nondetection of satellite radial alignments in massive clusters at $z > 0.5$ (Hung & Ebeling 2012), based on ~ 500 spectroscopic members in the inner ~ 500 kpc of clusters, using imaging from the Hubble Space Telescope (HST), and also with measurements at smaller masses from photometrically-selected galaxy groups from SDSS (Hao et al. 2011; Chisari et al. 2014) and spectroscopically-selected galaxy groups from the Galaxy And Mass Assembly (GAMA) survey (Schneider et al. 2013). Our results suggest that the stars in galaxies within clusters do not feel a strong enough tidal torque to be aligned toward the centre of the cluster, in contrast with results from simulations which find strong alignments even when accounting for differences in the response between stars and dark matter which naturally occurs in hydrodynamical simulations (Pereira & Bryan 2010; Tenneti et al. 2014, Velliscig et al. in prep). An obvious consideration from the observational point of view is miscentring: whether the chosen cluster centre is really the minimum of the cluster potential. This effect can be measured statistically with stacked weak lensing measurements (e.g., George et al. 2012) but is otherwise hard to assess observationally. At least in very relaxed clusters, BCGs are typically very close to the peak of the gas distribution (e.g., Lin & Mohr 2004; Mahdavi et al. 2013), which is closely matched to the dark matter distribution (Faltenbacher et al. 2007a). We can therefore test, to some extent, whether miscentring could be diluting an alignment signal by isolating relaxed clusters as discussed

Table 4.3: Average ellipticity components of spectroscopic members.

	KSB				GALFIT			
Sample	$N_{\rm gal}$[a]	$\langle\epsilon_+\rangle$	$\langle\epsilon_\times\rangle$	$\sigma(\epsilon_i)$[b]	$N_{\rm gal}$[a]	$\langle\epsilon_+\rangle$	$\langle\epsilon_\times\rangle$	$\sigma(\epsilon_i)$[b]
All	8,510	−0.0037	−0.0014	0.0027	8,014	0.0004	−0.0009	0.0031
$z < 0.14$	4,170	0.0002	−0.0000	0.0039	4,612	0.0029	−0.0003	0.0038
$z \geq 0.14$	4,340	−0.0074	−0.0027	0.0038	3,402	−0.0042	−0.0020	0.0053
$M_{200} < 7 \times 10^{14} \mathrm{M}_\odot$	2,287	−0.0059	0.0051	0.0052	2,277	−0.0057	0.0041	0.0057
$M_{200} \geq 7 \times 10^{14} \mathrm{M}_\odot$	6,223	−0.0029	−0.0038	0.0032	5,737	0.0030	−0.0030	0.0037
Relaxed	3,233	−0.0037	−0.0022	0.0044	3,058	−0.0038	−0.0025	0.0050
Disturbed	5,277	−0.0036	−0.0009	0.0034	4,956	0.0031	0.0001	0.0040
$M_r \leq -21$	4,101	−0.0031	−0.0016	0.0039	3,922	0.0009	−−0.0000	0.0044
$M_r > -21$	4,409	−0.0042	−0.0012	0.0038	4,092	−0.0001	−0.0018	0.0044
RS	5,806	−0.0008	−0.0009	0.0033	5,595	0.0010	−0.0001	0.0037
Non-RS	2,704	−0.0099	−0.0025	0.0048	2,419	−0.0012	−0.0031	0.0059

[a]Number of galaxies used for the average, within r_{200}. [b]68% confidence measurement uncertainties on the average ellipticities.

Table 4.4: Average ellipticity components of spectroscopic plus red sequence members.

	KSB				GALFIT			
Sample	N_{gal}	$\langle\epsilon_+\rangle$	$\langle\epsilon_\times\rangle$	$\sigma(\epsilon_i)$	N_{gal}	$\langle\epsilon_+\rangle$	$\langle\epsilon_\times\rangle$	$\sigma(\epsilon_i)$
All	15,905	−0.0022	−0.0021	0.0020	12,930	0.0000	−0.0008	0.0026
$z < 0.14$	6,407	−0.0020	−0.0019	0.0031	6,233	0.0013	0.0002	0.0033
$z \geq 0.14$	9,498	−0.0023	−0.0022	0.0026	6,697	−0.0019	−0.0023	0.0041
$M_{200} < 7 \times 10^{14}\mathrm{M}_\odot$	5,394	−0.0039	−0.0010	0.0034	4,345	−0.0057	0.0009	0.0044
$M_{200} \geq 7 \times 10^{14}\mathrm{M}_\odot$	10,511	−0.0013	−0.0027	0.0024	8,585	0.0031	−0.0017	0.0032
Relaxed	7,504	−0.0034	−0.0051	0.0029	5,903	−0.0044	−0.0038	0.0038
Disturbed	8,401	−0.0011	0.0006	0.0027	7,027	0.0039	0.0018	0.0035
$M_r \leq -21$	5,394	−0.0020	−0.0011	0.0034	4,912	0.0008	0.0004	0.0040
$M_r > -21$	10,511	−0.0023	−0.0026	0.0024	8,018	−0.0005	−0.0017	0.0034

in Section 4.3.1.1. However, as shown in the top-left panel of Figure 4.9, we do not detect any alignment signal neither from relaxed nor from disturbed clusters. Thus we conclude that our results are robust to miscentring effects and that, statistically, satellite galaxies do not align toward the centres of clusters.

As discussed by Hao et al. (2011), the redshift evolution of satellite radial alignments (or lack thereof) contains valuable information as to whether these alignments are produced during the formation of clusters or an evolving product of tidal torques within clusters. The centre-left panel of Figure 4.9 shows that the alignment signal is consistent with zero across redshift, suggesting that neither of these processes is sufficient to sustain radial alignments over cosmological time. Furthermore, the bottom-left panel of Figure 4.9 shows that this nondetection is also independent of cluster mass. We further tested whether any orientation bias, in the sense that we might have clusters viewed preferentially along their major axis, could have any effects on our results. To do this, we divided the cluster sample by BCG elongation, assuming that BCGs that look rounder might actually be elongated along the line-of-sight. Both cluster samples have radial alignments consistent with zero (not shown), arguing that a possible orientation bias is not a problem here.

In any of the two scenarios mentioned above (namely tidal and primordial alignments), radial alignments could show a different pattern for galaxies with different formation histories.

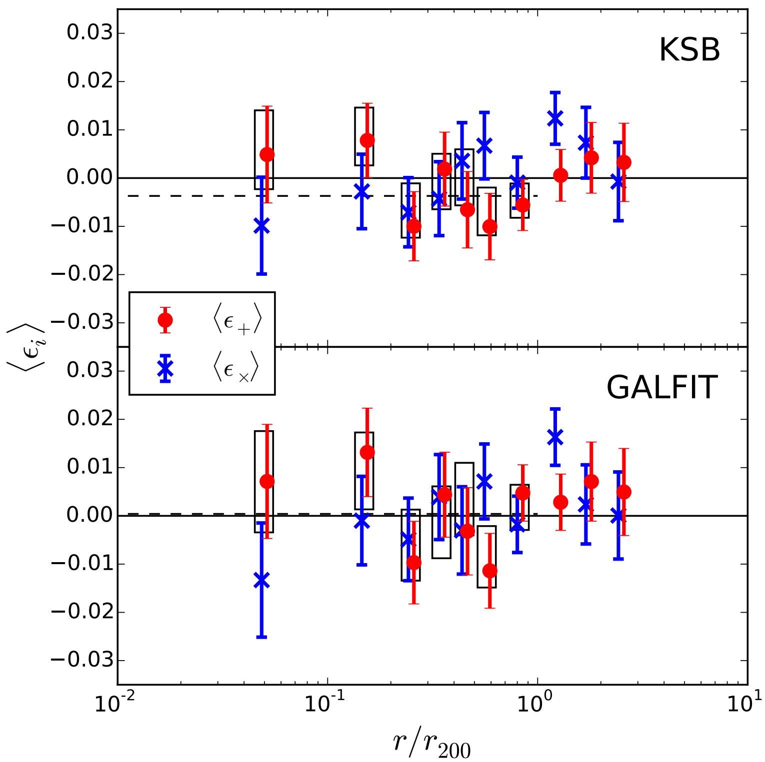

Figure 4.8: Average alignment of all spectroscopically confirmed members out to $3r_{200}$. The top panel shows the results from KSB while the bottom panel shows those from GALFIT. Shaded bands show the 1, 2 and 3σ uncertainties in the overall average and white bars show the 1σ range for $\langle\epsilon_+\rangle$ from the enhanced sample including red sequence members. Points are slightly shifted horizontally for clarity.

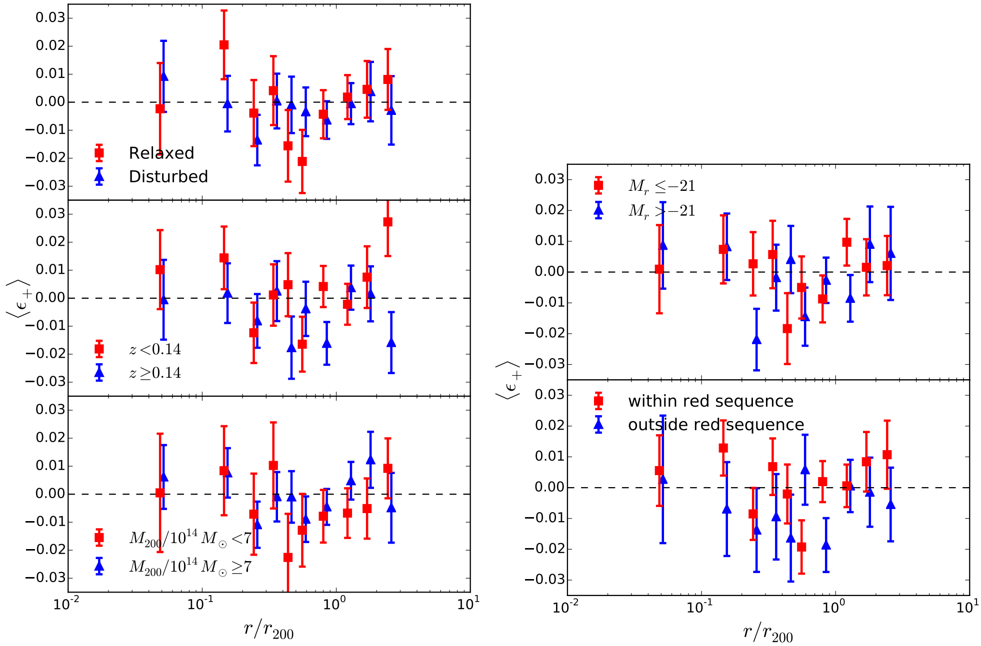

Figure 4.9: Average alignment $\langle \epsilon_+ \rangle$ from KSB for spectroscopically confirmed members, divided by cluster properties (left): by dynamical state (top; see Section 4.3.1.1), redshift (middle), and dynamical mass (bottom), and by galaxy properties (right): by rest-frame r-band absolute magnitude (top) and colour with respect to the red sequence (bottom).

We investigate this by splitting the galaxy sample by galaxy luminosity (as a proxy for galaxy mass) and color—since bluer galaxies have been accreted more recently. To split by galaxy color we use each cluster's red sequence, which depends linearly on apparent magnitude, as outlined in Section 4.3.2. As seen in the right panels of Figure 4.9, we find no radial alignments consistently across galaxy colors and luminosities.

The results discussed above are summarized in Tables 4.3 and 4.4 for spectroscopic and spectroscopic plus red sequence member samples, respectively.

4.5.2. Satellite-BCG alignment

The second type of alignment we explore is the alignment of the satellite orientations with the BCG orientation (cf. Equation 4.7). A large number of observations suggest that BCGs are on average oriented along the major axes of clusters themselves (e.g., Sastry 1968; Binggeli 1982; Faltenbacher et al. 2007b; Niederste-Ostholt et al. 2010; Hao et al. 2011), and there is evidence that the velocity dispersion of satellite galaxies is typically larger along the BCG major axis (Skielboe et al. 2012). It is possible, then, that the BCG orientation represents a preferred infall direction. If this is the case, it is possible that galaxies would be aligned toward this infall direction.

Figure 4.10 shows the alignment of galaxies with the major axis of the BCGs measured with KSB as a function of radius, for the full sample of spectroscopic plus red sequence members. As in the case of radial alignments, the data are also consistent with no satellite-BCG alignments at all distances. The average KSB signal within r_{200} is $\langle \epsilon_1' \rangle = -0.0021 \pm 0.0022$; the average GALFIT signal is $\langle \epsilon_1' \rangle = -0.0024 \pm 0.0029$. We also split the sample as in the preceeding section, and find no signal for all galaxy and cluster subsamples. As a consistency check, we also find that the distribution of position angles, $|\phi - \phi_{\rm BCG}|$, is consistent with a random distribution.

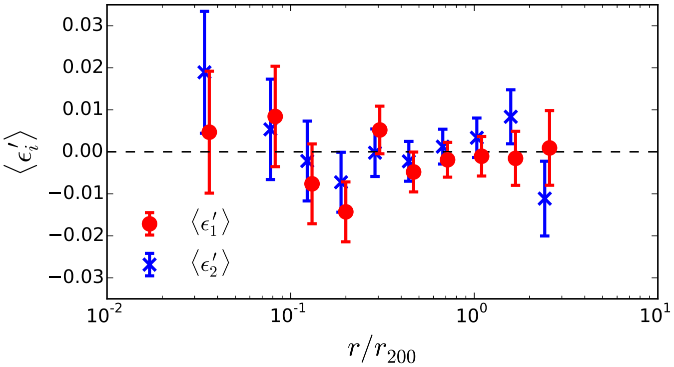

Figure 4.10: Mean ellipticity components of spectroscopic plus red sequence satellite galaxies in a frame rotated by the position angle of the BCG, probing the alignment of satellites with the cluster BCG. BCG position angles are measured with GALFIT, while the shapes of satellite galaxies are measured with KSB. Red circles show alignments with respect to the major ($\epsilon_1' > 0$) and minor ($\epsilon_1' < 0$) axes of the BCG, while blue crosses show alignments at 45° rotations.

Finally, we averaged not in annular bins but in cartesian coordinates $\{x, y\}$, to check if the satellite-BCG alignment could be happening only along a preferential direction, such that the azimuthal average would dilute the signal. We also found a null signal in this case (not shown).

4.5.3. Satellite-satellite alignment

We have shown in Section 4.5.1 that satellite galaxies are not aligned toward the centres of clusters. If galaxies reside within substructures themselves, then these substructures might have tidally aligned galaxies toward them. If the tidal torque of the cluster is not enough to overcome these substructure-scale alignments, then maybe we can observe an alignment signal at small separations, between satellite galaxies. After excluding data near the edges of the images (see Section 4.4.1.3), we use a total of 3.93×10^6 satellite pairs. Figure 4.11 shows the alignment signal between satellites averaged over all clusters, as a function of distance between satellites, for the full spectroscopic plus red sequence member sample. In this case we split the sample into two radial bins, namely (test) galaxies within and outside $0.25r_{200}$, which corresponds to the scale radius of a cluster with a concentration $c_{200} = 4$ (roughly what is expected for massive clusters; e.g., Duffy et al. 2008), but the results are similar when splitting the sample at other radii.

The leftmost bins in Figure 4.11 show the signal from substructure: outer bins probe the radial alignment between galaxies at large distances. It might be expected that substructure in the outskirts of clusters would contain an alignment signal since, presumably, they have been accreted more recently. As in the preceeding sections, we do not observe any alignment signal for the full cluster sample, nor for relaxed or disturbed clusters, at any radii. We note however that the last data point in Figure 4.11 is significantly nonzero, but so is the cross component. This suggests that at these distances measurements are affected by systematic effects, mainly because a large fraction of the pairs consist of two galaxies at the edges of the images. Moreover, this data point shows the alignments between satellites at opposite sides of the cluster; i.e., it is not a measurement of alignment within cluster substructure.

Since we do not detect any alignment signal for clusters at different redshifts and at different dynamical stages, we conclude that tidal torques in clusters, or in substructures within them, do not result in significant alignments of the stellar content of galaxies at any scale (neither toward the centre nor between galaxies). It may be possible to bring this in line with the strong alignments measured in N-body simulations by invoking a misalignment between the stellar and dark matter distributions (e.g., Okumura et al. 2009; Tenneti et al. 2014). However, such analysis is beyond the scope of this paper.

4.5.4. Is there an agreement on the level of galaxy alignments in groups and clusters?

As discussed above, previous studies have reported various levels of alignment of satellite galaxies in clusters using different estimators. We expect such a lack of agreement to arise for two main reasons: the quality of the images used to measure galaxy shape parameters, and the use of shape measurements that are prone to systematic effects, e.g., isophotal measurements. The latter effect was studied by Hao et al. (2011) in detail; they found significant radial alignments only when using isophotal shape measurements, and that the strength of these alignments depends on apparent magnitude but *not* on absolute magnitude, a strong suggestion that the detection is an artifact. Specifically, isophotal measurements are subject to severe contamination from the BCG, which can extend over a few hundred kpc in the case of massive clusters. As to the first cause, the quality of imaging data used by different groups varies significantly. To our knowledge, Plionis et al. (2003) were the first to use CCD photometry to measure galaxy alignments. They found a significant anisotropy in the (isophotal) position angles of satellite galaxies of Abell 521 (though they used photographic plates for their statistical study of alignments in clusters). There are also recent studies, however, who used position angle measurements extracted from scanned photographic plates (e.g., Baier et al. 2003; Panko et al. 2009; Godłowski et al. 2010), both of which are of noticeably lower quality than present-day observations. Moreover, these works typically used single-band information to select cluster members, yielding an unknown (and likely low) sample purity.

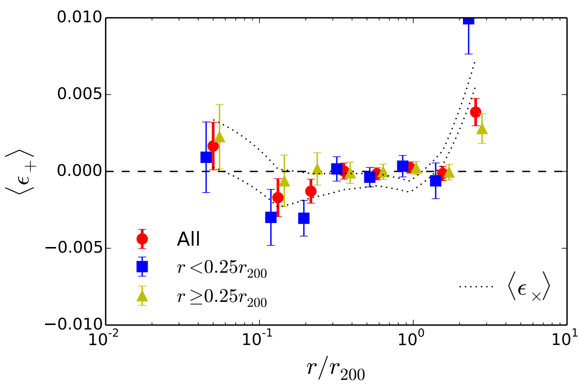

Figure 4.11: Satellite-satellite alignment as a function of the distance between satellites, for the full spectroscopic plus red sequence member sample. Red circles show all galaxies, while blue squares and yellow triangles show the signal with respect to galaxies inside and outside $0.25r_{200}$. Data points show the radial (positive) and tangential (negative) signal, while the dashed lines show the 68% range of the cross component, linearly interpolated. Uncertainties do not account for covariance between data points. Note that the vertical scale is smaller than in Figures 4.8 to 4.10.

Most recent studies have used data from SDSS because of its unmatched statistical power. These data, while of very high quality compared to photographic plate measurements, are several magnitudes shallower than our MegaCam data and taken under less ideal conditions (with seeing a factor 2 larger). Conversely, Hung & Ebeling (2012) have used deep, high-quality HST imaging to measure galaxy alignments, finding no evidence for galaxy alignments within clusters. As in our analysis, Hung & Ebeling (2012) have considered spectroscopically-confirmed cluster members, thus in addition to the superior photometry, both works have a cleaner member sample, which is key to the interpretation of the signal. Schneider et al. (2013) also used a sample of spectroscopically-confirmed group members, plus a shape measurement method that was specifically calibrated to weak lensing measurements (Mandelbaum et al. 2005), and found no significant evidence for alignments. Finally, Chisari et al. (2014) measured galaxy alignments in photometrically-selected galaxy groups and clusters in SDSS Stripe 82, fully accounting for photometric redshift uncertainties, and constrain alignments to similar values as those found here.

The fact that all recent measurements that use high-quality imaging and properly calibrated shape measurements have yielded null detections (Hao et al. 2011; Hung & Ebeling 2012; Schneider et al. 2013; Chisari et al. 2014, plus the present study) leads us to conclude that there is no evidence for intrinsic alignments of satellite galaxies in galaxy groups or clusters to the level of uncertainty achievable with current datasets (both statistical and systematic).

4.6. Contamination to cosmic shear measurements

In this section we explore the impact that the measured galaxy alignments in clusters can have on future cosmic shear measurements. We quantify the contribution of intrinsic alignments to cosmic shear measurements through the matter and intrinsic alignment power spectra, which can be defined as

$$\begin{aligned}\left\langle \tilde{\gamma}^{I*}(\mathbf{k})\tilde{\gamma}^{I}(\mathbf{k}')\right\rangle &= (2\pi)^3\delta_D^{(3)}\left(\mathbf{k}-\mathbf{k}'\right)P_{II}(\mathbf{k})\\ \left\langle \delta^{*}(\mathbf{k})\tilde{\gamma}^{I}(\mathbf{k}')\right\rangle &= (2\pi)^3\delta_D^{(3)}\left(\mathbf{k}-\mathbf{k}'\right)P_{GI}(\mathbf{k})\,.\end{aligned} \tag{4.11}$$

Here, $\tilde{\gamma}^I = (1+\delta_g)\gamma^I$ is the (projected) ellipticity field weighted by the galaxy density, δ_g, and $P_{II}(\mathbf{k})$ and $P_{GI}(\mathbf{k})$ are the II and GI contributions to the power spectrum including a prescription for nonlinear evolution (i.e, nonlinear power spectra, see Smith et al. 2003; Bridle & King 2007), respectively; δ^* is the complex conjugate of the Fourier transform of the matter density contrast, $\delta(\mathbf{r}) = (\rho(\mathbf{r})-\bar{\rho})/\bar{\rho}$ is the matter overdensity with respect to the average density of the Universe, $\tilde{\gamma}^{I*}$ indicates the complex conjugate of $\tilde{\gamma}^I$, and δ_D is a Dirac delta function.

Additionally, we translate the 3-dimensional power spectra discussed above into (observable) angular power spectra, C_ℓ, using the Limber (1953) approximation (e.g., Kaiser 1992). We use a source redshift distribution given by

$$p(z) \propto z^\alpha \exp\left[-(z/z_0)^\beta\right], \tag{4.12}$$

where we fix the parameters α, β, and z_0 so that the median redshift of the model distribution reproduces the median redshift of the Kilo-Degree Survey (KiDS, de Jong et al. 2013), $z_{\rm med} \simeq 0.7$ (Kuijken et al., in prep). We split the lens sample in redshift bins of half-width $\Delta z = 0.1$ to illustrate the results obtained from a tomographic cosmic shear analysis (e.g., Heymans et al. 2013). We use a narrow redshift bin covering $0.6 < z < 0.8$ for the GG and II power spectra, since this range is close to the one that maximizes the lensing signal in a KiDS-like tomographic analysis. The GI power spectrum is better captured by cross-correlating this redshift bin with one at low redshift; we choose $0.2 < z < 0.4$ as a compromise between a high intrinsic alignment efficiency and a large enough volume observed.

4.6.1. Linear alignment model

The simplest models for galaxy alignments predict that elliptical galaxies are aligned with a strength that is proportional to the tidal field (Catelan et al. 2001) while spiral galaxies, which are aligned by angular momentum acquired during gravitational collapse, are aligned with a strength that is proportional to the square of the tidal field (Pen et al. 2000). On sufficiently large scales, all galaxies are predicted to experience an alignment proportional to the large scale gravitational potential (Hui & Zhang 2002). Thus a linear alignment model is usually employed to characterize large scale galaxy alignments (e.g., Kirk et al. 2010; Joachimi et al. 2011; Mandelbaum et al. 2011; Heymans et al. 2013).[9] We normalize the intrinsic alignment power spectra as in previous studies (Hirata & Seljak 2004; Bridle & King 2007; Schneider & Bridle 2010), matching to the SuperCOSMOS measurements of Brown et al. (2002). This normalization is also consistent with more recent observations (Heymans et al. 2004; Mandelbaum et al. 2006a; Joachimi et al. 2011).

Solid lines in Figure 4.12 show the angular power spectra, C_ℓ, from the linear alignment model. This model includes no contribution from alignments within haloes (so-called 1-halo terms) and therefore the II and GI power spectra are subdominant to the matter power spectrum at all scales.

Figure 4.12 also shows the expected angular power spectrum measurements of a reference cosmic shear survey with properties similar to KiDS with a redshift distribution as described above, with a sky coverage of 1,500 sq. deg. and a background source density of $n_{\rm gal} = 10\,{\rm arcmin}^{-2}$. We assume a coverage $30 \leq \ell \leq 3000$, and compute the expected C_ℓ measurements and uncertainties following Cooray & Hu (2001), in logarithmic bins in ℓ. The bottom panel of Figure 4.12 shows that the II contribution remains safely subdominant to statistical uncertainties expected for KiDS, but the GI contribution cannot be ignored, contaminating the GG power spectrum at the $\sim 10\%$ level.

4.6.2. Halo model

The linear alignment model aims to describe alignments at large scales and the alignments between central galaxies, because these are expected to be aligned with the host halo by the large scale gravitational potential. On smaller, nonlinear scales, galaxy formation will tend to misalign baryonic and dark matter (e.g., Pereira & Bryan 2010; Tenneti et al. 2014), so the large-scale results from N-body simulations are probably not directly applicable to galaxy alignments within haloes. Galaxy formation can also have a major impact on the power spectra (van Daalen et al. 2011; Semboloni et al. 2011), and the way these two effects interplay is unclear. We therefore require a prescription to predict the power spectra accounting for 1-halo term galaxy alignments. To this end, we employ the halo model of radial alignments introduced by Schneider & Bridle (2010).

The main assumption of the halo model is that galaxies form and reside in dark matter haloes whose masses directly influence the (observable) properties of the galaxies they host. Additionally, one can assume that satellite galaxies in a halo are radially aligned toward the centre with a strength that can in principle be a function of the galaxy position in the halo, the host halo mass, and redshift. This is known as a *satellite radial alignment model*. The total alignment can be separated into a prescription for galaxies in haloes (the 1-halo

[9] This model is typically referred to as "nonlinear alignment model." However, this is a misnomer, since intrinsic alignments are still modeled as depending linearly on the tidal field; instead the name arises from the use of the nonlinear power spectrum in Equation 4.11. We therefore refer to it as linear alignment model throughout.

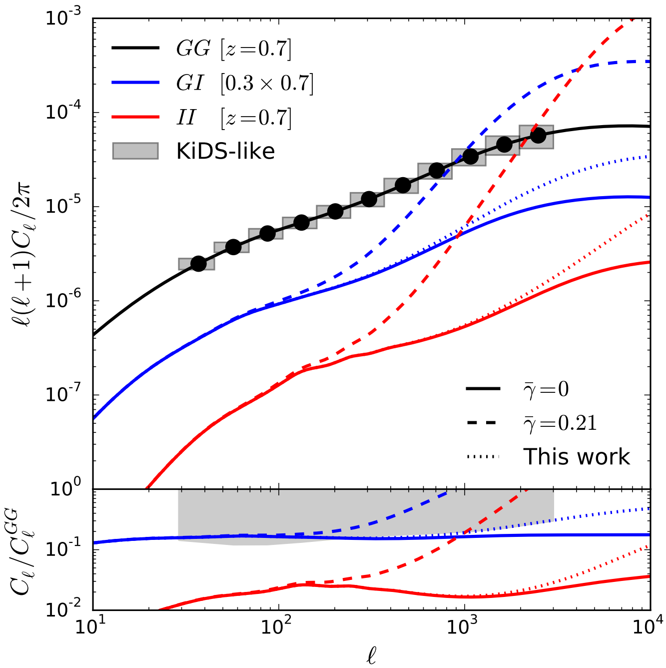

Figure 4.12: Effect of intrinsic alignments on the angular power spectra. *Top panel:* The black line shows the GG power spectrum, while blue and red lines show the GI and II power spectra, respectively. Solid lines show the linear alignment model with no small-scale intrinsic alignments, while dashed and dotted lines model the contribution of satellite galaxies with $\bar{\gamma} = 0.21$ as in Schneider & Bridle (2010) and with the mass-dependent 2σ upper limit on the alignment signal derived in this work (see Section 4.6.3), respectively. Grey boxes with black circles show the expected uncertainty levels on a KiDS-like survey covering 1,500 sq. deg. and with $n_{\rm gal} = 10\,\mathrm{arcmin}^{-2}$. The *bottom panel* shows the ratio between the GI and II power spectra and the GG power spectrum, for each model. The shaded region shows values above the 1σ uncertainties in the anglar power spectrum for a KiDS-like survey, where GI and II contributions would dominate over statistical uncertainties.

term), and one between haloes (the 2-halo term). We assume that galaxies populate haloes following the halo occupation distribution of Cacciato et al. (2013) and the halo mass and bias functions of Tinker et al. (2010). More details about the ingredients of this halo model can be found in Schneider & Bridle (2010). Given a model for radial alignments, $\gamma^I(\mathbf{r}, M, z)$, we calculate the power spectra through Equation 4.11.

This model only incorporates the information about the radial alignments studied in Section 4.5.1, by definition. In principle, it would be possible to include further constraints on the alignments from measurements such as those explored in Sections 4.5.2 and 4.5.3. However, these would be second order corrections to the cluster-scale radial component. In particular, the satellite-satellite alignment constraints woud be relevant on scales smaller than what will be probed by current and upcoming experiments; we therefore choose not to include them in the present analysis.

4.6.3. Impact of alignments within haloes on the power spectra

The halo model requires a prescription for the strength of small-scale radial alignments. In its simplest form this strength is constant with radius and halo mass. The power spectra derived from this model are shown as dashed lines in Figure 4.12, for an alignment strength

$\bar{\gamma} = 0.21$ ($\bar{\gamma}$ is the 3-dimensional alignment strength derived from a projected measurement, γ^I; see Schneider & Bridle 2010). This is the fiducial value adopted by Schneider & Bridle (2010). In this work, we extend this prescription by assuming a radial alignment that depends on halo mass but not on distance within the halo. Such a model is fully consistent with our results, since we find a null signal at all radii.

We construct a mass-dependent alignment model using the present results, plus the intrinsic alignment measurements in galaxy groups from the Galaxy and Mass Assembly (GAMA) survey (Schneider et al. 2013). We assume a power law for $\gamma^I(M)$, such that the mean ellipticity of satellite galaxies has the 2σ upper limits obtained in this study. We use the results for the augmented spectroscopic plus red sequence member sample, and choose to use the KSB measurement because, although the GALFIT constraint is less tight (i.e., more conservative), the contribution of each mass scale is weighted by the mass function. Since the mass function is an exponential function of mass, the overall alignment signal is dominated by lower mass objects. Since we use the constraint found for GAMA groups as a pivot, a smaller alignment strength in clusters will mean a larger overall contribution of alignments to a cosmic shear survey. Specifically, we use $\epsilon_+ < 0.0019$ at $M \simeq 10^{15}\,\mathrm{M}_\odot$ and $\epsilon_+ < 0.019$ at a typical mass $M \simeq 10^{13}\,\mathrm{M}_\odot$, corresponding to the 2σ upper limit for GAMA groups with $N_{\rm gal} \geq 5$ (Schneider et al. 2013). Our model is therefore $\gamma^I(M) = (M/M_0)^\alpha$, constant with redshift, with $M_0 = 1.19 \times 10^9\mathrm{M}_\odot$ and $\alpha = -0.5$.[10] We note that the assumption of a single power law at all masses has no justification other than its simplicity. A more detailed halo model for intrinsic alignments will be presented in a forthcoming study (Cacciato et al., in prep), where we explore the impact of halo model assumptions on the predictions of the II and GI power spectra.

Dotted lines in Figure 4.12 show the intrinsic alignment power spectra predicted by the halo model for our adopted $\gamma^I(M)$. Since we constructed the model using 2σ upper limits on the measured alignments, the regions between the solid and dotted lines should be regarded as conservative estimates of the current uncertainties on the GI and II power spectra due to 1-halo term intrinsic alignments. As can be seen, both the GI and II power spectra remain subdominant to the GG power spectrum, which is not the case with the fiducial $\bar{\gamma} = 0.21$ model used by Schneider & Bridle (2010). The GI angular power spectrum including our 1-halo term is ~70% higher than that predicted by the linear alignment model at $\ell \sim 3000$, which translates into an excess on the total (GG+GI+II) angular power spectrum of $\approx 10\%$, comparable to the statistical uncertainties expected at these scales. Note that at larger scales the GI power spectrum is dominated by linear alignments and the satellite contribution is well below the statistical uncertainties of KiDS. Therefore, we do not expect that cosmic shear analyses with KiDS will need to include a contribution by satellite galaxies in the modeling of intrinsic alignments, and we conclude that the linear alignment model should be a sufficient treatment of intrinsic alignments for KiDS. We note that for a bin at $0.2 < z < 0.4$, the II power spectrum can be $> 10\%$ of the lensing (GG) power spectrum at the same redshift, but the uncertainties of a KiDS-like survey are much larger than at $z \sim 0.8$ because of the smaller volume probed. In any case, the linear alignment model captures any II contribution to sufficient accuracy. Therefore a treatment of intrinsic alignments in KiDS cosmic shear analyses can rely on the linear alignment model, similar to the cosmic shear analysis of CFHTLenS data by Heymans et al. (2013). We expect the situation to be similar for the Dark Energy Survey (DES)[11], which will have three times as much area as KiDS but otherwise

[10] The conversion between ellipticity and shear is given by $\gamma = \epsilon_+/2\mathscr{R}$, where $\mathscr{R}$ is the shear responsivity, which we assume to be equal to 0.87.

[11] `http://www.darkenergysurvey.org`

similar characteristics. This may not be the case for larger surveys, for which the contribution of satellite galaxies to intrinsic alignments must be characterized to higher precision.

4.7. Conclusions

We have compiled a large sample of galaxies with spectroscopic redshifts in the direction of 90 galaxy clusters in the redshift range $0.05 < z < 0.55$, selected as part of MENeaCS and CCCP. We select cluster members using the shifting gapper technique, which uses phase space information, for a total 14,576 cluster members. We use these members to estimate dynamical masses using the simulation-based scaling relation between velocity dispersion and cluster mass of Evrard et al. (2008). The sample has a median redshift $z = 0.14$ and a median mass $M_{200} \sim 7 \times 10^{14}\,\mathrm{M}_{\odot}$, in good agreement with the weak lensing masses estimated by Hoekstra et al. (2012).

We quantify the alignment of galaxies within clusters using 14,250 cluster members for which we are able to measure their shapes either with KSB or GALFIT, after showing that the ellipticities measured by both methods are consistent (Figure 4.6). Both methods take different approaches to measuring galaxy shapes and therefore provide an important consistency check. We confirm that our analysis is free of significant systematic effects by measuring the average alignment of both foreground galaxies and stars. The signal from foreground galaxies is consistent with zero; the signal from stars is significantly different from zero, but at a level of $\langle\epsilon_+\rangle \sim 10^{-4}$, an order of magnitude lower than measurement uncertainties (Figure 4.7).

We measure three different alignments: the radial alignment of satellite galaxies toward the BCG, the alignment of satellites with the BCG orientation, and the radial alignment of satellites toward each other. Each probes a different, but not necessarily independent, effect. We find no evidence for any of these alignments (Figures 4.8 to 4.11). In particular, we constrain the average ellipticity of satellites toward BCGs to $\langle\epsilon_+\rangle = -0.0037 \pm 0.0027$ with KSB and $\langle\epsilon_+\rangle = 0.0004 \pm 0.0031$ with GALFIT, at 68% confidence, within r_{200}. Similarly, there is no evidence of galaxy alignments when splitting the sample by cluster (redshift, mass, or dynamical state) or galaxy (color or luminosity) properties. Selecting additional cluster members through the red sequence allows us to extend the sample to ~20,000 galaxies with an estimated contamination of $< 10\%$ from red sequence interlopers (Figure 4.4). All signals from this enlarged sample are also consistent with zero.

We include this constraint on the radial alignment of galaxies within high-mass haloes, together with a measurement at the group scale (Schneider et al. 2013), in a halo model framework, and derive the current uncertainty on the angular power spectrum given by intrinsic alignments within haloes (a 1-halo term). We find that the total (GG+GI+II) angular power spectrum predicted from our alignment model (see Section 4.6.3) is, at most, 10% higher than the total power spectrum predicted by the linear alignment model at the smallest scales probed by KiDS, $\ell \sim 3000$. This level of contribution from satellite galaxies will not be relevant for cosmic shear measurements with KiDS or DES (see Figure 4.12). We conclude that the linear alignment model is a sufficient description of intrinsic alignments for KiDS, but the situation may be different for significantly larger surveys.

5 | The masses of satellites in GAMA galaxy groups from 100 square degrees of KiDS weak lensing data

We use the first 100 sq. deg. of overlap between the Kilo-Degree Survey (KiDS) and the Galaxy And Mass Assembly (GAMA) survey to determine the galaxy halo mass of ~10,000 spectroscopically-confirmed satellite galaxies in massive ($M > 10^{13}h^{-1}\mathrm{M}_\odot$) galaxy groups. Separating the sample as a function of projected distance to the group centre, we jointly model the satellites and their host groups with Navarro-Frenk-White (NFW) density profiles, fully accounting for the data covariance. The probed satellite galaxies in these groups have total masses $\log M_\mathrm{sub}/(h^{-1}\mathrm{M}_\odot) \approx 11.7-12.2$ consistent across group-centric distance within the errorbars. Given their stellar masses, $\log M_{\star,\mathrm{sat}}/(h^{-2}\mathrm{M}_\odot) \sim 10.5$, such total masses imply stellar mass fractions of $M_{\star,\mathrm{sat}}/M_\mathrm{sub} \approx 0.04\,h^{-1}$. The average subhalo hosting these satellite galaxies has a mass $M_\mathrm{sub} \sim 0.015M_\mathrm{host}$ independent of host halo mass, in broad agreement with the expectations of structure formation in a ΛCDM universe.

Cristóbal Sifón, Marcello Cacciato, Henk Hoekstra, et al.,
2015, MNRAS, 454, 3938

5.1. Introduction

Following a hierarchical build-up, galaxy groups grow by accretion of smaller groups and isolated galaxies. Tidal interactions tend to transfer mass from infalling galaxies to the (new) host group, with the former becoming group satellites. The favoured cosmological scenario posits that galaxies are embedded in larger dark matter haloes, with masses that largely exceed the stellar masses, a conclusion supported by a variety of observations (see, e.g., the reviews by Trimble 1987; Einasto 2013). Accordingly, satellite galaxies are hosted by 'subhaloes,' whose masses and distribution contain information on the properties of dark matter itself (e.g., Libeskind et al. 2013).

Because dark matter is (at least to a good approximation) dissipationless and baryons are not, it is subject to stronger tidal disruption than the baryonic component: energy losses cause baryons to sink to the centre of the potential more efficiently than dark matter, and therefore baryons are more resistant to tidal disruption (White & Rees 1978). This latter fact produces a unique prediction of the dark matter hypothesis: a satellite galaxy will be preferentially stripped of its dark, rather than stellar, matter. Thus, tidal stripping can be observed by comparing the total and stellar masses of satellite galaxies, such that galaxies accreted earlier have smaller mass-to-light ratios than galaxies accreted recently or (central) galaxies that have not been subject to tidal stripping by a larger host (e.g., Chang et al. 2013a).

Numerical simulations predict that tidal stripping is stronger within more centrally concentrated host haloes, and is more severe for more massive satellites (e.g., Tormen et al. 1998; Taffoni et al. 2003; Contini et al. 2012). Different infall timescales and concentrations induced by baryons (compared to dark matter-only simulations) can alter both the radial distribution and density profiles of subhaloes, consequently affecting tidal stripping in a radially-dependent manner (Romano-Díaz et al. 2010; Schewtschenko & Macciò 2011), although this baryon-induced radial dependence could plausibly be (partially) compensated by feedback from active galactic nuclei (AGN; Romano-Díaz et al. 2010).

Observationally, the primary difficulty lies in estimating the total masses of satellite galaxies. Weak gravitational lensing is currently the only option available to measure the total mass of statistical samples of galaxies. So-called (weak) galaxy-galaxy lensing provides a direct measure of the masses of lensing galaxies through the observation of their distortion of the images of background galaxies, without assumptions about the dynamical state of the system (e.g., Brainerd et al. 1996; Courteau et al. 2014). Weak lensing is an intrinsically statistical observational measurement: outside the strong lensing regime (typically a few tenths of arcsecond) the distortion induced in each background galaxy is much smaller than the typical galaxy ellipticity. Such measurements require high-quality multi-colour images that allow both accurate shape measurements and photometric redshift determination of faint, distant background sources. Measuring the lensing signal around satellite galaxies (hereafter 'satellite lensing', see, e.g., Yang et al. 2006) is particularly challenging because of i) the small relative contribution of the satellite galaxy to the lensing signal produced by the host galaxy group; ii) source blending at small separations, which hampers our ability to measure shapes reliably (and which is enhanced in high-density regions); and iii) particular sensitivity to contamination by field galaxies. This latter point is critical: since the dark matter haloes around satellite galaxies are expected to be stripped, isolated galaxies will significantly contaminate the lensing signal since they are not stripped, thus complicating a meaningful interpretation of the signal. Therefore, satellite lensing requires a clean sample of satellite galaxies to allow a proper interpretation of the signal. Satellite galaxies can usually be identified easily in massive galaxy clusters with high purity by use of, for instance, the red sequence (e.g., Rozo et al. 2015, see also Chapter 4), which in principle requires only two-band photometry. Indeed, most satellite lensing measurements so far have concentrated on massive galaxy clusters with deep Hubble Space Telescope (HST) observations in which bright cluster members can be easily identified (Natarajan et al. 2002; Limousin et al. 2007; Natarajan et al. 2009), sometimes with the aid of strong lensing measurements (Natarajan et al. 2007). Some of these studies have claimed detections of satellite truncation, but it seems likely that they are mostly attributable to the parameterization of subhalo density profiles rather than direct detections (Pastor Mira et al. 2011).

Because galaxy groups have fewer satellites than massive clusters, lensing measurements of galaxy group satellites require larger samples and have only been possible thanks to recent large optical surveys with high image quality. Furthermore, because the red sequence is generally not so well established in galaxy groups compared to galaxy clusters, accurate group membership determination requires high-completeness spectroscopic observations. Lacking such data, most measurements in galaxy groups to date have relied on more indirect means of estimating subhalo masses. Gillis et al. (2013) used an optimized density estimator on galaxies selected from Canada-France-Hawaii Telescope Lensing Survey (CFHTLenS, Heymans et al. 2012; Erben et al. 2013) and showed that the lensing signal of galaxies in high-density environments is inconsistent with the predictions of a model that does not include halo stripping, providing indirect evidence for tidal stripping in galaxy groups. Such differentiation was only possible because their high-density environment galaxies were mostly satellites, due to their carefully calibrated density estimator. Recently, Li et al. (2014) presented the first direct detection of the lensing signal from satellite galaxies in galaxy groups. They took advantage of the overlap between deep imaging from the CFHT-Stripe82 Survey (CS82, e.g., Comparat et al. 2013) and the Sloan Digital Sky Survey (SDSS, York et al. 2000) Data Release 7 (Abazajian et al. 2009) spectroscopic catalogue. Yang et al. (2007) used this SDSS catalogue to construct a clean galaxy group catalogue with centrals and satellites identified individually; although Li et al. (2014) had only ~1,000 lens galaxies, their sample was essentially free of contamination by central galaxies. This allowed them to use weak lensing to directly measure the masses of satellites in galaxy groups for the first time, albeit with limited constraining power.

In this paper we present a direct measurement of the lensing signal from satellite galaxies in galaxy groups by combining a sample of spectroscopically confirmed galaxy groups from the Galaxy And Mass Assembly survey (GAMA, Driver et al. 2011), and background galaxies with high-quality shape measurements from the Kilo-Degree Survey (KiDS, de Jong et al. 2013; Kuijken et al. 2015). We use these measurements to constrain the masses of satellite galaxies as a function of projected distance from the group centre. By converting, in an average sense, these projected distances into 3-dimensional distances, we can study the evolution of satellite masses as they fall into galaxy groups.

This chapter is organized as follows. In Section 5.2 we describe the galaxy samples we use as lenses and lensed background sources. In Section 5.3 we summarize the measurement of galaxy-galaxy lensing and describe our modelling of satellites and their host groups. We present our results in Section 5.4 and summarize in Section 5.5. We adopt a flat ΛCDM cosmology with $\Omega_\mathrm{m} = 0.315$, consistent with the latest cosmic microwave background measurements (Planck Collaboration 2015a), and $H_0 = 100h\,\mathrm{km\,s^{-1}Mpc^{-1}}$. We explicitly include the dependence on h where appropriate. Throughout we use the symbol $\langle X\rangle$ to refer to the median of distribution X.

5.2. Galaxy samples

5.2.1. Lens galaxies: satellites in the GAMA galaxy group catalogue

GAMA[1] is a spectroscopic survey which measured redshifts for 238,000 galaxies over a total of $286\,\mathrm{deg}^2$ carried out with the AAOmega spectrograph on the Anglo-Australian Telescope (AAT). GAMA is 98% spectroscopically complete down to $m_r = 19.8$ even in the most crowded regions (Baldry et al. 2010; Driver et al. 2011; Liske et al. 2015). Here we use data over three different regions on the sky, centred at right ascensions 9h, 12h and 15h (the G09, G12 and G15 fields), which overlap with SDSS data. Below we briefly describe the GAMA galaxy group sample constructed by Robotham et al. (2011), who discuss the properties, possible systematics, and limitations of the catalogue in greater detail. Galaxy photometric properties such as luminosity and stellar mass are measured from the five-band optical SDSS imaging. In particular, we use the stellar masses derived by Taylor et al. (2011) by fitting Bruzual & Charlot (2003) synthetic stellar spectra to the broadband SDSS photometry.

The GAMA galaxy group catalogue was constructed using a 3-dimensional Friends-of-Friends (FoF) algorithm, linking galaxies in projected and line-of-sight separations. We use version 7 of the group catalogue (G^{3}Cv7), which contains 23,838 groups with $N_{\mathrm{FoF}} \geq 2$, where N_{FoF} is the number of spectroscopic members grouped together by the FoF algorithm (each group has $N_{\mathrm{FoF}} - 1$ satellites). Group properties such as velocity dispersion and total luminosity[2] were calibrated to mock galaxy catalogues processed in the same way as the real data and were optimized for groups with $N_{\mathrm{FoF}} \geq 5$. A visual inspection of the phase space (distance-velocity plane) of GAMA groups confirms that groups with $N_{\mathrm{FoF}} < 5$ are significantly contaminated by interlopers, while member selection for groups with $N_{\mathrm{FoF}} \geq 5$ is in better agreement with the expectation of a smooth distribution of galaxies with a maximum velocity that decreases with radius (e.g., Mamon et al. 2010). We therefore restrict our study to groups with $N_{\mathrm{FoF}} \geq 5$, in the 68.5 sq. deg. of unmasked area overlapping with the first release of KiDS lensing data (see Section 5.2.2). In all, we use 9683 satellites hosted by 1467 different groups[3]. These are the same groups used by Viola et al. (2015).

Robotham et al. (2011) identified the central galaxy in each group using three definitions of group centre: the weighted centre of light, an iterative method rejecting the galaxy farthest away from the center of light until one galaxy remained (the 'iterative' centre), and the brightest cluster galaxy (hereafter BCG). All galaxies that are not centrals are classified as satellites. In most cases (~90%) the iterative central galaxy coincides with the BCG, while the centre of light is more discrepant. Viola et al. (2015) performed a detailed analysis of the lensing signal of GAMA groups comparing the different centre definitions and confirm the results of Robotham et al. (2011): the BCG and the iterative centre both represent the group centre of mass to a good degree, while the centre of light is a very poor indicator of the group centre. In this work we use the central-satellite classification that uses the BCG as the central, and therefore measure the lensing signal around all group members except the BCGs.

---

[1] http://www.gama-survey.org/

[2] The total luminosity of a group is the sum of the luminosities of its member galaxies, corrected for spectroscopic incompleteness at the low-mass end (see Robotham et al. 2011).

[3] This is the total number of satellites considered in this work, and includes satellites that do not fall within the currently available KiDS data but reside in a group which is less than $2\,h^{-1}\mathrm{Mpc}$ away from the center of the closest KiDS field. 9357 (97%) of these satellites fall within the KiDS footprint (see Table 5.1).

Table 5.1: Median properties of satellite galaxies binned by projected distance to the group centre, $R_{\rm sat}$. $N_{\rm sat}$ is the total number of satellites considered while $N_{\rm sat}^{\rm KiDS}$ is the number of satellites that fall within the 100 sq. deg. of KiDS imaging used in this work. Errorbars are 16th and 84th percentiles.

Bin	$R_{\rm sat}$ range (h^{-1}Mpc)	$N_{\rm host}$	$N_{\rm sat}$	$N_{\rm sat}^{\rm KiDS}$	$\langle N_{\rm FoF}\rangle$	$\langle R_{\rm sat}\rangle$ (h^{-1}Mpc)	$\langle z_{\rm sat}\rangle$	$\log\langle M_{\star,\rm sat}\rangle$ ($h^{-2}\rm M_\odot$)	$\log\langle L_{\rm host}\rangle$ ($h^{-2}\rm L_\odot$)
1	$0.05 - 0.20$	1263	3714	3541	7^{+5}_{-2}	$0.12^{+0.05}_{-0.05}$	$0.17^{+0.09}_{-0.09}$	$10.45^{+0.26}_{-0.09}$	$11.10^{+0.17}_{-0.23}$
2	$0.20 - 0.35$	1235	3152	3042	7^{+5}_{-2}	$0.25^{+0.05}_{-0.04}$	$0.19^{+0.10}_{-0.09}$	$10.51^{+0.22}_{-0.10}$	$11.15^{+0.14}_{-0.26}$
3	$0.35 - 1.00$	785	2817	2773	8^{+7}_{-3}	$0.43^{+0.16}_{-0.08}$	$0.21^{+0.10}_{-0.07}$	$10.66^{+0.15}_{-0.14}$	$11.33^{+0.10}_{-0.25}$

5.2.2. Lensed background sources: the Kilo-Degree Survey

KiDS[4] is an ESO Public Survey being conducted with the 2.6 m VLT Survey Telescope (VST) in Cerro Paranal, Chile, which surveys the sky in the $ugri$ bands. Each 1 sq. deg. pointing is observed four times ('exposures') in the u-band and five times in the other bands. Upon completion, KiDS will cover 1,500 sq. deg.: half of the survey area will be on a 9°-wide patch around the celestial equator and the other half on a similarly-shaped region around a declination of −31° (de Jong et al. 2013). In total, KiDS overlaps with four GAMA patches: three in the equator (the three used in this work) and one in the south (G23), for a total of 240 sq. deg.. In this work, we use an unmasked area of 68.5 sq. deg. over ~ 100 sq. deg. of overlap currently available (de Jong et al. 2015).

KiDS data were reduced using two different pipelines: a reduction based on Astro-WISE (McFarland et al. 2013) used to measure Gaussian-weighted aperture photometry (Kuijken 2008) and photometric redshifts with the Bayesian Photometric Redshift (BPZ) code (Benítez 2000), and a THELI reduction (Erben et al. 2013) used to measure galaxy shapes with *lens*fit (Miller et al. 2007, 2013; Kitching et al. 2008). We briefly describe each in the following and refer to de Jong et al. (2015) and Kuijken et al. (2015) for details, including tests of systematic effects on shape measurements and photometric redshifts.

5.2.2.1. Photometric redshifts

Photometric redshifts use the coadded images from the KiDS public data releases DR1 and DR2 (de Jong et al. 2015) as input. These were processed using a pipeline largely based on the Astro-WISE optical pipeline (McFarland et al. 2013) which includes crosstalk and overscan corrections, flat fielding, illumination correction, satellite track removal and background subtraction, plus masking for bad pixels, saturation spikes and stellar haloes. A common astrometric solution was calculated per filter using a second-order polynomial. Individual exposures were regridded and co-added using a weighted mean procedure. Photometric zero-points were first derived per CCD by comparing nightly standard star observations to SDSS DR8 (Aihara et al. 2011) and zero-point offsets were subsequently applied to the gri data, based on a comparison of the photometry between the CCDs in the five exposures. This yields a homogeneous photometry over 1 sq. deg..

The point spread function (PSF) of the stacked images was homogenized by convolving them with a Gaussian kernel with varying width, such that each resulting image has a circular, Gaussian PSF with constant width across the field of view. A 'Gaussian Aperture and PSF' (GAaP, Kuijken 2008) photometry can be obtained such that the resulting aperture photometry is independent of seeing (see Appendix A of Kuijken et al. 2015). The flux of a galaxy can then be measured consistently within the same physical aperture in all bands, which is necessary for unbiased galaxy colour estimates.

GAaP photometry was finally compared to SDSS photometry in order to obtain an absolute photometric calibration. Photometric redshifts were estimated using GAaP magnitudes with BPZ, following Hildebrandt et al. (2012). Kuijken et al. (2015) compared the photometric redshifts to ~17,000 spectroscopic redshifts in the zCOSMOS (Lilly et al. 2007) and ESO/GOODS (Vanzella et al. 2008; Balestra et al. 2010) surveys. They found that the peak of the posterior distribution, z_B, is biased by less than 2% in the range $0.005 < z_B < 1.0$. However, for lenses at $z_l \lesssim 0.3$, as in our case, the lensing efficiency (cf. Equation 5.2) does not vary significantly for sources beyond $z_s = 0.5$. In order to have a larger number of sources

[4] http://kids.strw.leidenuniv.nl/

for which to measure shapes, we therefore use all galaxies in the range $0.005 < z_B < 1.2$. In the context of the CFHTLenS survey, Benjamin et al. (2013) have shown that the stacked photometric redshift posterior distribution, $p(z)$, estimated by Hildebrandt et al. (2012) in this z_B range is a fair representation of the true (i.e., spectroscopic) redshift distribution. We therefore use the full $p(z)$ in our lensing analysis (see Section 5.3).

5.2.2.2. Shape measurements

The r-band data were also reduced with the THELI pipeline (Erben et al. 2013), independently of the ASTRO-WISE pipeline, in order to measure the shapes of galaxies. We used only the r-band data for shape measurements, since the r-band observing conditions are significantly better than in the other three bands (see de Jong et al. 2013); combining different bands is not expected to result in a useful improvement in shape measurements. We used SEXTRACTOR (Bertin & Arnouts 1996) to detect objects on the stacked r-band image, and used the resulting catalogue as input to *lens*fit, which is used to simultaneously analyze the single exposures. *Lens*fit is a Bayesian method that returns for each object an ellipticity and an associated weight, w_s, which quantifies the measurement uncertainty after marginalizing over galaxy position, size, brightness, and bulge-to-disk ratio. It interpolates the PSF over a 2-dimensional polynomial across the image in order to estimate the PSF at the location of each galaxy. The number density of galaxies in the unmasked region that pass the photometric redshift cuts having $w_s > 0$ is $n_{\rm gal} = 8.88\,{\rm gal\,arcmin^{-2}}$ and the effective number of galaxies is $n_{\rm eff} = (\sigma_\epsilon / A) \sum_i w_{s,i} = 4.48\,{\rm gal\,arcmin^{-2}}$ (see Chang et al. 2013b; Kuijken et al. 2015); the root-mean-square (rms) ellipticity of galaxies is $\sigma_\epsilon = 0.279$. We correct for *noise bias*, which produces a signal-to-noise ratio (S/N) -dependent correction factor, m, between the mean ellipticity measurements and the shear (e.g., Melchior & Viola 2012; Refregier et al. 2012; Viola et al. 2014, see Section 5.3), using the correction calculated for CFHTLenS using extensive image simulations by Miller et al. (2013), which Kuijken et al. (2015) demonstrate is appropriate for the current KiDS catalogue. We also correct the galaxy shapes for an additive bias, c, introduced by imperfect PSF modelling following Heymans et al. (2012). See Kuijken et al. (2015) for details.

In performing the lensing analysis we have decided to blind ourselves to the final results. By doing this we ensure that the analysis does not depend on the results, and minimize the risk of confirmation bias. This is an especially important concern in this era of precision cosmology. At the start of the project we contacted an external person (unknown to all members of the KiDS collaboration except for the contact person), who generated three additional catalogues by rescaling the galaxy ellipticities by factors unknown to us. We carried out the full analysis four times, one for each ellipticity catalogue. Only when the team was convinced about the analysis *carried out with the four ellipticity catalogues*, the analysis was frozen *with no further changes to the results* and we contacted the external person again to reveal the true catalogue. A detailed description of the shape analysis and catalogue blinding of KiDS data is given in Kuijken et al. (2015).

5.3. Galaxy-galaxy lensing of satellite galaxies

Gravitational lensing produces a differential deflection of light coming from background galaxies when it passes through an inhomogeneous mass distribution, and most strongly along a mass concentration. The observable effect is a coherent distortion on both the shape and the size of background sources around the lens. The shape distortion, $\gamma_{\rm t}$, is referred to as *shear*, and in the weak lensing limit is much smaller than the typical ellipticities of galaxies and can only be measured statistically by averaging over many background sources. The average tangential shear relates to the excess surface mass density (ESD) at a projected distance[5] R of the lens, $\Delta\Sigma(R)$, through

$$\Delta\Sigma(R) \equiv \bar{\Sigma}(<R) - \bar{\Sigma}(R) = \Sigma_{\mathrm{c}}\gamma_{\mathrm{t}}(R)\,, \tag{5.1}$$

where $\bar{\Sigma}(<R)$ is the average surface density within R, $\bar{\Sigma}(R)$ is the average surface density *at* R (more precisely, within a thin shell $R+\delta R$) and the critical density, Σ_{c}, is as a geometrical factor that accounts for the lensing efficiency,

$$\Sigma_{\mathrm{c}} = \frac{c^2}{4\pi G}\frac{D(z_{\mathrm{s}})}{D(z_{\mathrm{l}})D(z_{\mathrm{l}},z_{\mathrm{s}})}. \tag{5.2}$$

Here, $D(z_{\mathrm{l}})$, $D(z_{\mathrm{s}})$, and $D(z_{\mathrm{l}},z_{\mathrm{s}})$ are the angular diameter distances to the lens, to the source and between the lens and the source, respectively. Therefore the redshifts of the lenses and sources are essential to relate the tangential distortions of the sources to the projected mass density of the lens.

We calculate $D(z_{\mathrm{l}})$ for each lens galaxy using its spectroscopic redshift from GAMA and marginalize over the full probability distribution of the photometric redshift of each background source, $p(z_s)$. Specifically, for every lens-source pair we calculate

$$\tilde{\Sigma}^{-1}_{\mathrm{c},ls} = \frac{4\pi G}{c^2}D(z_{\mathrm{l}})\int_{z_l}^{\infty}\mathrm{d}z_s\,p(z_s)\frac{D(z_{\mathrm{l}},z_{\mathrm{s}})}{D(z_{\mathrm{s}})}. \tag{5.3}$$

Each lens-source pair is then assigned a weight that combines the *lens*fit weight and the lensing efficiency,

$$w_{ls} = w_s\tilde{\Sigma}^{-2}_{\mathrm{c},ls}. \tag{5.4}$$

The ESD in a bin centred on a projected distance R is then calculated as

$$\Delta\Sigma(R) = \left(\frac{\sum_{ls} w_{ls}\epsilon_{\mathrm{t}}\tilde{\Sigma}_{\mathrm{c},ls}}{\sum_{ls} w_{ls}}\right)\frac{1}{1+K(R)} \tag{5.5}$$

where the sum is over all lens-source pairs in the radial bin, ϵ_{t} is the tangential component of the ellipticity of each source around each lens, and

$$K(R) = \frac{\sum_{ls} w_{ls}m_s}{\sum_{ls} w_{ls}} \simeq 0.1, \tag{5.6}$$

where m is the multiplicative correction for noise bias (Miller et al. 2013; Kuijken et al. 2015).

The ESD around a satellite galaxy at a projected distance R_{sat} from the group centre, $\Delta\Sigma_{\mathrm{sat}}(R|R_{\mathrm{sat}})$, is given by

$$\Delta\Sigma_{\mathrm{sat}}(R|R_{\mathrm{sat}}) = \Delta\Sigma_{\mathrm{sub}}(R) + \Delta\Sigma_{\mathrm{host}}(R|R_{\mathrm{sat}})\,, \tag{5.7}$$

where $\Delta\Sigma_{\mathrm{sub}}$ is the ESD of the subhalo in which the satellite galaxy resides and $\Delta\Sigma_{\mathrm{host}}$ is the ESD of the host galaxy group, measured around the satellite galaxy. We describe the measured satellite lensing signal in Section 5.3.1 before discussing our modelling of both terms of Equation 5.7 in Sections 5.3.2 and 5.3.3. In doing this, we follow the discussion by Yang et al. (2006).

[5] As a convention, we list 3-dimensional distances in groups with lower case r, and distances projected in the plane of the sky with capital R.

5.3.1. The satellite lensing signal

We show in Figure 5.1 the stacked ESD of all 9683 satellites residing in groups with $N_{\rm FoF} \geq 5$. We also show the ESD around all galaxies in the GAMA catalogue, which is dominated by (central) field galaxies (Robotham et al. 2011). The lensing signal around the two samples is qualitatively different. In terms of Equation 5.7, the ESD of central galaxies can be described by $\Delta\Sigma_{\rm host}(R|R_{\rm sat}=0)$ alone (see van Uitert et al. (2016) for a detailed comparison of the lensing signal of different lens samples). The bottom panel of Figure 5.1 shows $\Delta\Sigma_\times$, which is defined analogously to Equation 5.1 using the shear measured at 45° rotations from the direction tangential to the lens. $\Delta\Sigma_\times$ should be consistent with zero because of parity symmetry (Schneider 2003), and therefore serves as a check for systematic effects. As shown in Figure 5.1, $\Delta\Sigma_\times$ is consistent with zero for both samples at all lens-source separations.

Although in Figure 5.1 we show the lensing signal for separations $0.01 \leq R/(h^{-1}{\rm Mpc}) \leq 10$, we only use measurements of $\Delta\Sigma$ in the range $0.02 \leq R/(h^{-1}{\rm Mpc}) \leq 2$ in our analysis. Separations outside this range are marked in Figure 5.1 by grey bands. At smaller separations, blending with and obscuration by group members become significant and therefore the S/N is very low; at larger separations the coverage is highly incomplete due to the patchiness of the current KiDS data, making measurements less reliable. We assess the effect of the patchy coverage by measuring the lensing signal around random locations on the images, which should be consistent with zero. The signal is indeed consistent with zero for separations $R \lesssim 5\,h^{-1}$Mpc, but at separations $R \gtrsim 5\,h^{-1}$Mpc the lensing signal around random points deviates significantly from zero (see Viola et al. 2015). This indicates that systematic effects are affecting the shear estimation at such distances. We do not try to correct for such effects and instead conservatively discard measurements at separations $R > 2\,h^{-1}$Mpc.

The errorbars in Figure 5.1 correspond to the square root of the diagonal elements of the covariance matrix, described in Section 5.A. In principle, the lensing covariance matrix includes contributions from shape noise and sample ('cosmic') variance. Shape noise arises because galaxies are intrinsically elliptic and because noise in the images introduces additional uncertainties in the shape measurements (see, e.g., Hoekstra et al. 2000), while sample variance accounts for the finite fraction of the sky observed. As we show in Section 5.A, the contribution from sample variance can be safely neglected for our purposes and we therefore include only the contribution from shape noise, which can be cal-

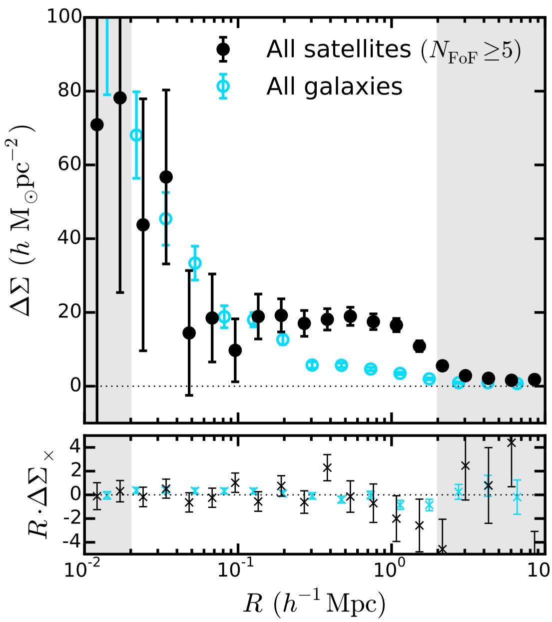

Figure 5.1: Top: Excess surface density around all satellites residing in groups with $N_{\rm FoF} \geq 5$ (black points) and around all galaxies in the GAMA catalogue (cyan circles). Bottom: corresponding cross signals, multiplied by projected separation, R, to make the errorbars of comparable size throughout the radial range (units are omitted for clarity). Dotted horizontal lines in both panels show $\Delta\Sigma = 0$. We used different bins to measure the signal of each sample for clarity. The grey bands show projected separations that are not used in our analysis.

culated directly from the data (see Section 3.4 of Viola et al. 2015). In addition to the covariance between data points (as in the case of Figure 5.1), we also compute the covariance between data points around lenses in different bins of projected distance from the group centre, $R_{\rm sat}$ (see Figure 5.8).

The signal shown in Figure 5.1 has a high S/N, but its interpretation is complicated by the mixing of satellites with a wide range of properties. van Uitert et al. (2016) use this satellite sample to study the stellar-to-halo mass relation by binning the sample in stellar mass and redshift. Here, we bin the sample by projected distance to the group centre; this binning is shown in the top-left panel of Figure 5.2 (see also Table 5.1). We find that this particular binning allows us to study each bin with high enough S/N. We take the distance from the group centre as a proxy for time since infall to the group (e.g., Gao et al. 2004; Chang et al. 2013a) and study the evolution of the mass in satellites as these galaxies interact with their host groups. As shown in Figure 5.2 (top right), the three radial bins have similar stellar mass distributions, their medians differing by only 0.2 dex (Table 5.1). In contrast, the group redshift and luminosity distributions of bin 3 are different from the other two bins. Because we separate groups by satellite distance, we essentially split groups by size. Only the most massive (i.e., the most luminous) groups in the sample have satellites at $R_{\rm sat} > 0.35\,h^{-1}{\rm Mpc}$. Additionally, because GAMA is a magnitude-limited survey, groups at high redshift are on average more luminous (i.e., more massive), which causes the different redshift distributions.

5.3.2. Host group contribution

The average density profile of galaxy groups is well described by a Navarro-Frenk-White (NFW, Navarro et al. 1995) profile,

$$\rho_{\rm NFW}(r) = \frac{\delta_c \rho_m}{(r/r_s)(1+r/r_s)^2}, \tag{5.8}$$

where $\rho_m(z) = 3H_0^2(1+z)^3\Omega_M/(8\pi G)$ is the mean density of the Universe at redshift z and

$$\delta_c = \frac{200}{3}\frac{c^3}{\ln(1+c) - c/(1+c)}. \tag{5.9}$$

The two free parameters, r_s and $c \equiv r_{200}/r_s$, are the scale radius and concentration of the profile, respectively. However, we use the concentration and the mass[6], M_{200}, as the free parameters for convenience. We further assume the mass-concentration relation, $c(M,z)$, of Duffy et al. (2008), allowing for a free normalization, $f_c^{\rm host}$. That is,

$$c(M_{200}, z) = f_c^{\rm host}\left[10.14\left(\frac{M_{200}}{2\times10^{12}h^{-1}{\rm M}_\odot}\right)^{-0.089}(1+z)^{-1.01}\right]. \tag{5.10}$$

The average surface density of the host group measured at a projected distance $R_{\rm sat}$ from the group centre is simply the azimuthal average of $\Sigma_{\rm host}$ around the satellite,

$$\bar{\Sigma}_{\rm host}(R|R_{\rm sat}) = \frac{1}{2\pi}\int_0^{2\pi} {\rm d}\theta\, \Sigma_{\rm NFW}\left(\sqrt{R_{\rm sat}^2 + R^2 + 2RR_{\rm sat}\cos\theta}\right), \tag{5.11}$$

and the contribution to the satellite ESD follows from Equation 5.1. We use the analytical expression for the projected surface density of an NFW profile, $\Sigma_{\rm NFW}(R)$, derived by Wright & Brainerd (2000).

[6]Here M_{200} is the mass within a radius r_{200}, which encloses a density $\rho(< r_{200}) = 200\rho_m(z)$.

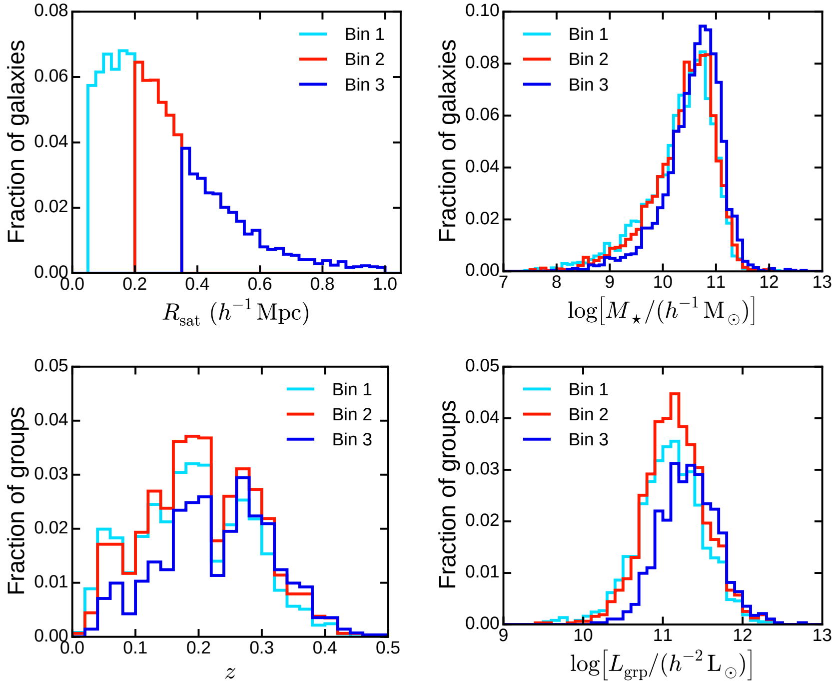

Figure 5.2: Top: Satellite distributions of distance to the BCG (left) and stellar mass (right); bottom: Group distributions of redshift (left) and total luminosity (right); for the radial bins defined in Table 5.1. Note that each group can contribute to more than one bin in the lower panels.

In reality we observe a sample of satellites at different distances to their respective group centres; therefore the total group contribution is

$$\Delta\Sigma_{\rm host}(R|n(R_{\rm sat})) = \frac{\int_{R_{\rm sat}^{\rm min}}^{R_{\rm sat}^{\rm max}} {\rm d}R_{\rm sat}\, n(R_{\rm sat})\Delta\Sigma_{\rm host}(R|R_{\rm sat})}{\int_{R_{\rm sat}^{\rm min}}^{R_{\rm sat}^{\rm max}} {\rm d}R_{\rm sat}\, n(R_{\rm sat})}, \tag{5.12}$$

where $n(R_{\rm sat})$ is the number density of satellites at $R_{\rm sat}$. We use Equation 5.12 to model the host group contribution to Equation 5.7 throughout. Our implementation differs from that introduced by Yang et al. (2006) and applied by Li et al. (2014) in that they fit for $R_{\rm sat}$, whereas we use the measured separations to fix $n(R_{\rm sat})$.

We illustrate the difference between $\Delta\Sigma_{\rm host}(R|R_{\rm sat})$ and $\Delta\Sigma_{\rm host}(R|n(R_{\rm sat}))$ in the left panel of Figure 5.3, for the innermost bin considered in this work (see Table 5.1 and the top left panel of Figure 5.2). The left panel of Figure 5.3 shows that $\Delta\Sigma_{\rm host}(R|R_{\rm sat})$ of a single group-satellite pair has a sharp minimum at $R = R_{\rm sat}$ where $\Sigma(R)$ is maximal and therefore $\Delta\Sigma < 0$; $\Delta\Sigma_{\rm host}(R|R_{\rm sat})$ increases abruptly further out and then drops back to the group's outer profile, matching the group profile measured around the group centre. Accounting for the distribution of group-centric distances shifts this minimum to $R < \langle R_{\rm sat}\rangle$, and makes both the peak and the dip significantly less pronounced; including the distribution of projected distances is critical to properly model the statistical properties of the lensing signal which cannot be captured by fitting for an average value. Similarly, the middle and right panels of Figure 5.3

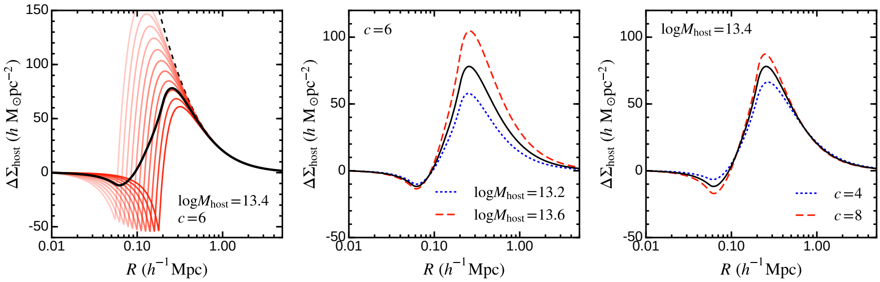

Figure 5.3: Illustration of the contribution from the host group, $\Delta\Sigma_{\rm host}(R|n(R_{\rm sat}))$, to Equation 5.7. Left: Red lines show the contribution to the signal around satellites at different distances from the group centre in logarithmic bins, with opacity scaling with the number density of objects in each bin, $n(R_{\rm sat})$, corresponding to the cyan histogram in the top-left panel of Figure 5.2. The thick black line is the weighted average of the red lines (cf. Equation 5.12) and represents the group contribution to the lensing signal around our sample of satellites with $0.05 \le R_{\rm sat}/(h^{-1}{\rm Mpc}) \le 0.20$ in a group with $\log M_{200} = 13.4$ and $c = 6$, and is reproduced in the middle and right panels. The black dashed line shows the excess surface density of the same group when measured around the group centre. Middle: Varying group mass at fixed concentration. Right: Varying group concentration at fixed mass. Note that the vertical scale in the middle and right panels is zoomed in with respect to the left panel. All masses are in units of $h^{-1}{\rm M}_\odot$.

show the effect of different host masses and concentrations on $\Delta\Sigma_{\rm host}(R|n(R_{\rm sat}))$. A higher mass increases its amplitude at all scales where the host contribution dominates, whereas a higher concentration mostly enhances the ESD signal around the peak and produces a more pronounced dip.

Our model ignores the contribution from baryons in the central group galaxy, which are noticeable at scales $R < 0.05\,h^{-1}$Mpc (Viola et al. 2015). Because baryons are more concentrated than dark matter, they can make the total density profile steeper than a pure NFW. Viola et al. (2015) have shown, however, that the amplitude of the baryonic contribution (modelled as a point mass) is not degenerate with any other group parameter in their halo model. Therefore we expect baryons in the BCG to have no impact on our results.

5.3.3. Satellite contribution

Pastor Mira et al. (2011) studied the density profiles of subhaloes in the Millenium simulation (Springel et al. 2005) and found that they are well fit by an NFW profile, with no evidence for truncation at any separation from the group centre. As discussed by Hayashi et al. (2003), while tidal disruption removes mass preferentially from the outskirts, tidal heating causes the subhalo to expand after every orbit. The two effects compensate in terms of the density distribution such that a defined truncation radius cannot be discerned in subhaloes. We therefore model subhaloes as NFW profiles (Equation 5.8). We assume the $c(M,z)$ relation of Duffy et al. (2008); in analogy to Equation 5.10, we set $f_c^{\rm sub} = 1$. To account for the baryonic contribution to the subhalo mass, we include a point mass in the centre with a mass equal to the median stellar mass for each bin (Table 5.1). Our model for the satellites therefore has a single free parameter per radial bin, namely $M_{\rm sub}(<r_{200})$.

For comparison, we also implement a theoretically-motivated model where subhaloes are tidally stripped by the host potential. In this model, a subhalo in a circular orbit is truncated at the radius at which the accelerations due to the tidal force from the host halo equals that

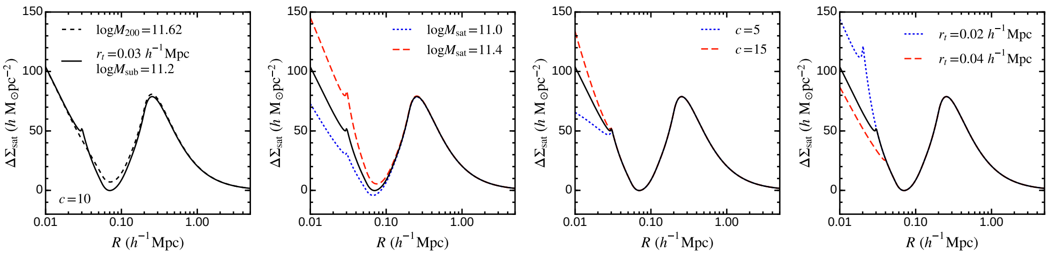

Figure 5.4: The satellite lensing signal, $\Delta\Sigma_{\rm sat}$, for different satellite properties. The group contribution is kept fixed at the fiducial value (i.e., the thick solid line) from Figure 5.3. Top left: The dashed line shows the excess surface density of a NFW profile with $c = 10$ and $\log M_{200} = 11.62$. Truncating this profile through Equation 5.15 at $r_{\rm t} = 0.03\,h^{-1}{\rm Mpc} \approx 2.6 r_s$ produces the solid line, with a total mass $\log M_{\rm sub} = 11.2$, which is reproduced in all other panels. The glitch in the solid line is produced by the sharp truncation of the density profile and is continuous but non-differentiable. Top right: Varying $M_{\rm sub}$, keeping both $c = 10$ and $r_{\rm t} = 0.03\,h^{-1}{\rm Mpc}$ fixed. Bottom left: Varying the concentration, keeping both $\log M_{\rm sub} = 11.2$ and $r_{\rm t} = 0.03\,h^{-1}{\rm Mpc}$ fixed. Bottom right: Varying the truncation radius, keeping both $c = 10$ and $\log M_{\rm sub} = 11.2$ fixed. Note that the normalization of the inner profile changes because we fix the mass *within the truncation radius*, which is itself changing. All masses are in units of $h^{-1}{\rm M}_\odot$.

arising from the gravitational force of the subhalo itself. This radius is given by

$$r_{\rm t} = \left[\frac{M_{\rm sub}(<r_{\rm t})}{(3 - \partial \ln M/\partial \ln r)\, M_{\rm host}(<r_{\rm sat})}\right]^{1/3} r_{\rm sat} \tag{5.13}$$

(King 1962; Binney & Tremaine 1987; Mo et al. 2010), where, for an NFW profile,

$$\frac{\partial \ln M_{\rm NFW}}{\partial \ln r} = \frac{r^2}{(r_s + r)^2}\left[\ln\left(\frac{r_s + r}{r_s}\right) - \frac{r}{r_s + r}\right]^{-1} \tag{5.14}$$

and r_s is the scale radius of the host halo. Note that in Equation 5.13 the truncation radius, $r_{\rm t}$, depends on the 3-dimensional distance to the group centre, $r_{\rm sat}$, which is not an observable. We draw 3-dimensional radii randomly from an NFW profile given the distribution of projected separations, $R_{\rm sat}$, for each bin. We additionally force $r_{\rm t} \le r_{200}$, although the opposite rarely happens.

We model the truncation itself in a simple fashion, with an NFW profile instantaneously and completely stripped beyond $r_{\rm t}$,

$$\rho_t(r) = \begin{cases} \rho_{\rm NFW}(r) & r \le r_{\rm t} \\ 0 & r > r_{\rm t}. \end{cases} \tag{5.15}$$

Note that, in addition to $r_{\rm t}$, this profile is defined *mathematically* by the same parameters, c and M_{200}, as a regular NFW, even though they are not well-defined physically; when referring to truncated models we report the proper physical masses, $M_{\rm sub} \equiv M_{\rm sub}(<r_{\rm t})$. We use the analytical expression for the ESD of the density profile given by Equation 5.15 derived by Baltz et al. (2009). In the leftmost panel of Figure 5.4 we show the ESD corresponding to such profile, compared with the ESD obtained assuming our fiducial NFW profile. The sharp truncation of the profile creates a glitch in the ESD around satellite galaxies at the radius of truncation which is continuous but non-differentiable and which, given our errorbars (cf. Figure 5.1), has no impact on our results. The other panels show the effect of the three parameters describing the truncated subhalo density profile, Equation 5.15 (the full NFW profile follows the same description but without the sharp cut at $r_{\rm t}$): as for the group profile,

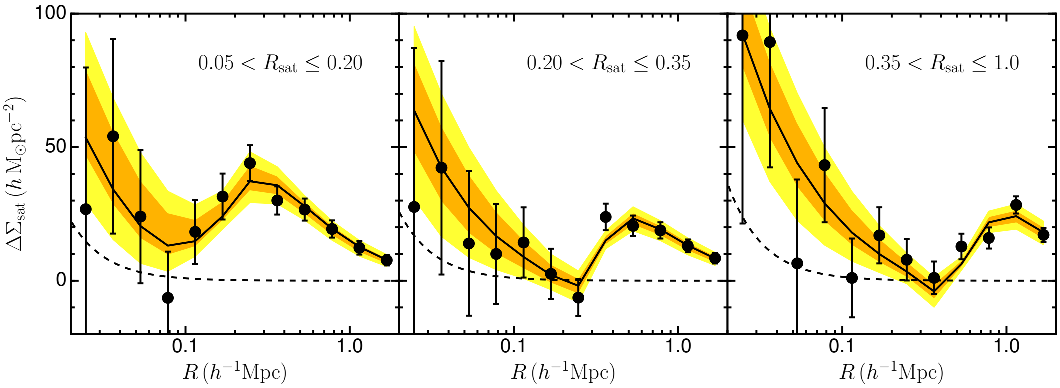

Figure 5.5: Excess surface density around satellite galaxies in the three radial bins summarized in Table 5.1 and shown in the legends in units of h^{-1}Mpc. Black points show lensing measurements around GAMA group satellites using KiDS data; errorbars correspond to the square root of the diagonal elements of the covariance matrix. The solid black line is the best-fit model where subhaloes are modelled as having NFW density profiles, and orange and yellow shaded regions mark 68% and 95% credible intervals, respectively. Dashed lines show the contribution of a point mass with a mass equal to the median stellar mass of each bin, which is included in the model.

the mass and concentration affect the normalization and slope of the profile, respectively; the rightmost panel shows changes in $r_{\rm t}$ for the same subhalo mass *within* $r_{\rm t}$, which is why the normalization of the different curves is different.

5.4. Results

We show the ESD around satellites in each of the three radial bins in Figure 5.5. Qualitatively, the signal looks similar to that of Figure 5.1, and the features described in Section 5.3 are clearly seen in each of the panels. The dip in the signal close to the typical $R_{\rm sat}$ is smooth, as anticipated in Section 5.3.2, and moves to higher R with increasing $R_{\rm sat}$, as expected. As in Figure 5.1, the errorbars correspond to the square root of the diagonal elements of the covariance matrix (see Section 5.A).

After describing the fitting procedure in Section 5.4.1, we summarize our constraints on group properties in Section 5.4.2 and on the satellite masses in Section 5.4.3. In Section 5.4.4 we carry out a proof-of-concept comparison of our results to predictions from semi-analytical models of subhalo statistics and we discuss the effect of contamination in the group sample in Section 5.4.5.

5.4.1. Fitting procedure

We fit the data in Figure 5.5 with the model described in Section 5.3 for each of the radial bins, using the median redshift of each galaxy sample, $\langle z_{\rm sat}\rangle$, as listed in Table 5.1. We use a single normalization $f_c^{\rm host}$ for the $c(M,z)$ relation of groups in the three bins. Our model therefore has seven free parameters: the three (weighted average) masses of the satellites, the three group masses, and a normalization to the $c(M,z)$ relation of Duffy et al. (2008) which applies to all groups across satellite radial bins.

We implement the model described above in a Markov Chain Monte Carlo (MCMC)

Table 5.2: Priors, marginalized posterior estimates and derived parameters of the satellites and host groups in the three radial bins. All priors are uniform in linear space in the quoted range. We use medians as central values and all uncertainties are 68% credible intervals. The normalization of the group $c(M,z)$ relation, $f_c^{\rm host}$, is the same for the three radial bins. The best-fit model has $\chi^2 = 24.7$ with 28 degrees of freedom (PTE = 0.64).

Parameter	Units	Prior	Bin 1	Bin 2	Bin 3
$\log M_{\rm sub}$	$h^{-1}\mathrm{M}_\odot$	[7,13]	$11.84^{+0.24}_{-0.34}$	$11.84^{+0.24}_{-0.35}$	$12.18^{+0.19}_{-0.24}$
$f_c^{\rm host}$	1	[0,2]	$0.53^{+0.19}_{-0.14}$	✓	✓
$\log M_{\rm host}$	$h^{-1}\mathrm{M}_\odot$	[10,15]	$13.58^{+0.07}_{-0.07}$	$13.62^{+0.07}_{-0.08}$	$14.11^{+0.07}_{-0.07}$
			Derived Parameters		
$\langle M_{\star,\rm sat}\rangle/\langle M_{\rm sub}\rangle$	h^{-1}	–	$0.04^{+0.02}_{-0.03}$	$0.04^{+0.02}_{-0.03}$	$0.03^{+0.01}_{-0.02}$
$\langle M_{\rm sub}/M_{\rm host}\rangle$	1	–	$0.018^{+0.014}_{-0.010}$	$0.016^{+0.013}_{-0.009}$	$0.012^{+0.007}_{-0.005}$
$\langle M_{\rm host}\rangle/\langle L_{\rm host}\rangle$	$h\mathrm{M}_\odot/\mathrm{L}_\odot$	–	300^{+49}_{-45}	265^{+46}_{-42}	386^{+66}_{-61}

using `emcee`[7] (Foreman-Mackey et al. 2013), which is based on an affine-invariant ensemble sampler. This sampler works by using a number of 'walkers' (in our case, a few hundred), each of which starts at a slightly different position in parameter space. Each step is drawn for each walker from a Metropolis-Hastings proposal based on the positions of all other walkers at the previous step (see Goodman & Weare 2010, for details about the algorithm). The likelihood $\mathscr{L}$ is given by

$$\mathscr{L} = \frac{1}{(2\pi)^{9/2}} \prod_{m=1}^{3}\prod_{n=1}^{3} \frac{1}{\sqrt{|C_{mn}|}} \exp\left[-\frac{1}{2}(\mathbf{O}-\mathbf{E})_m^T C_{mn}^{-1} (\mathbf{O}-\mathbf{E})_n\right], \tag{5.16}$$

where $\mathbf{O}_m$ and $\mathbf{E}_m$ are the measurements and model predictions in radial bin m, respectively; C_{mn}^{-1} is the element of the inverse covariance matrix that accounts for the correlation between radial bins m and n; and $|C_{mn}|$ is the corresponding determinant. We therefore account for covariance both within and between radial bins in our MCMC. We assume flat, broad priors for all parameters, as listed in Table 5.2.

The data are well fit by the model of Section 5.3. The best-fit model is shown in Figure 5.5 and gives $\chi^2 = 24.7$ with 28 degrees of freedom, with a probability to exceed $\mathrm{PTE} = 0.64$. Joint 2-dimensional posterior distributions for the seven free parameters are shown[8]. Marginalized posterior estimates for all seven parameters, together with 68% credible intervals, are reported in Table 5.2, which also lists the stellar mass fractions, fractional satellite masses, and group mass-to-light ratios derived from the posterior mass estimates.

5.4.2. Group masses and mass-concentration relation

Before discussing the results for the satellite galaxies, we explore the constraints on group masses and the group $c(M,z)$ relation. The masses of the same galaxy groups have been directly measured by Viola et al. (2015), which provides a valuable sanity check of our estimates.

We find that the normalization of the $c(M,z)$ relation is significantly lower than the fiducial Duffy et al. (2008) relation, $f_c^{\rm host} = 0.53^{+0.19}_{-0.14}$ (where the fiducial value is $f_c^{\rm host} = 1$). This normalization implies concentrations $c \approx 3$ for these groups. For comparison, using the same

[7] `http://dan.iel.fm/emcee/current/`

[8] We show and list the results in logarithmic space for convenience, but the analysis has been carried out in linear space and the reported uncertainties correspond to the uncertainties in linear space expressed on a logarithmic scale.

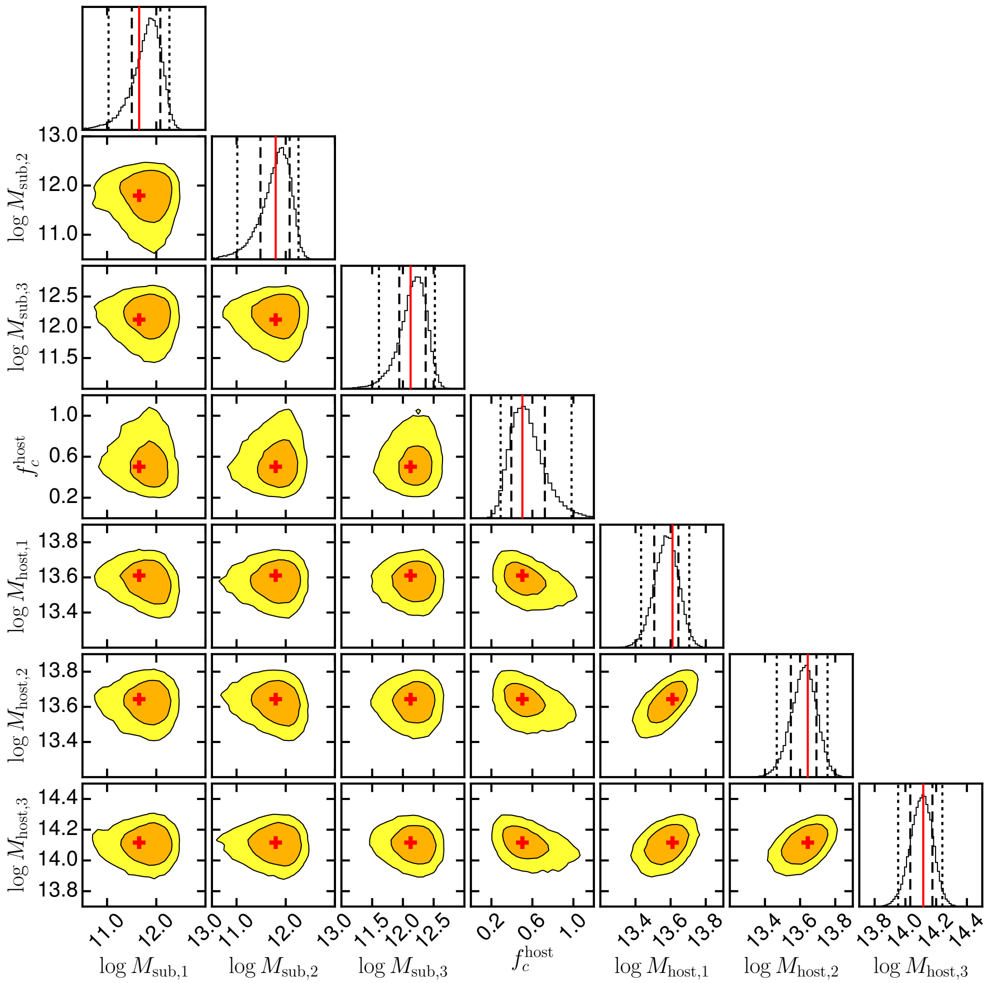

Figure 5.6: Joint 2-dimensional (lower off-diagonal panels, with contours at 68 and 95% joint credible regions) and marginalized 1-dimensional (diagonal panels) posterior distributions of free parameters of the model described in Section 5.3, with subhaloes modelled with NFW density profiles. In the diagonal panels, black dashed and dotted lines mark marginalized 68 and 95% credible intervals, respectively, and vertical red solid lines mark the maximum likelihood estimate. Red crosses in off-diagonal panels show the joint best-fit values. All masses are in units of $h^{-1}\mathrm{M}_\odot$ and are numbered according to the radial bin to which they correspond.

parameterization as we do, Viola et al. (2015) measured $f_c^{\rm host} = 0.84^{+0.42}_{-0.23}$. Our smaller errorbars are due to the fact that we do not account for several nuisance parameters considered by Viola et al. (2015) in their halo model implementation. Most notably, accounting for miscentring significantly increases the uncertainty on the concentration, since both affect $\Delta\Sigma$ at similar scales (Viola et al. 2015). Indeed, when they do not account for miscentring, Viola et al. (2015) measure $f_c^{\rm host} = 0.59^{+0.13}_{-0.11}$, consistent with our measurement both in the central value and the size of the errorbars. While this means that our estimate of $f_c^{\rm host}$ is biased, accounting for extra nuisance parameters such as miscentring is beyond the scope of this work; our aim is to constrain satellite masses and not galaxy group properties. As shown in Figure 5.6, $f_c^{\rm host}$ is not correlated with any of the other model parameters and therefore this bias in $f_c^{\rm host}$ does not affect our estimates of the satellite masses.

Group masses are consistent with the results from Viola et al. (2015) (with the same caveat that the small errorbars are an artifact produced by our simplistic modelling of the host groups). Specifically, our average mass-to-light ratios follow the mass-luminosity masses are slightly correlated because they are forced to follow the same mass-concentration relation determined by Equation 5.10. Groups in the third bin are on average $\sim 3.4 \pm 0.8$ times more massive than groups in the first radial bin. This is a selection effect, arising because groups in each bin must be big enough to host a significant number of satellites at the characteristic radius of each bin. For example, groups in the first radial bin have[9] $\log\langle M_{\rm host,1}/(h^{-1}{\rm M}_\odot)\rangle = 13.46^{+0.06}_{-0.06}$ and $\langle c_1\rangle \approx 3.3$, which implies a scale radius $\langle r_{s,1}\rangle = 0.19\,h^{-1}{\rm Mpc}$, beyond which the density drops as $\rho \propto r^{-3}$ (cf. Equation 5.8). The average 3-dimensional distance of satellites to the group centre (see Section 5.3.3) in the third radial bin is $\langle r_{\rm sat,3}\rangle = 0.46\,h^{-1}{\rm Mpc}$. At this radius, the average density in groups in the first radial bin is seven times smaller than at $\langle r_{s,1}\rangle$. relation found by Viola et al. (2015), $M_{200} \propto L_{200}^{1.16\pm0.13}$. As shown in Figure 5.6, group

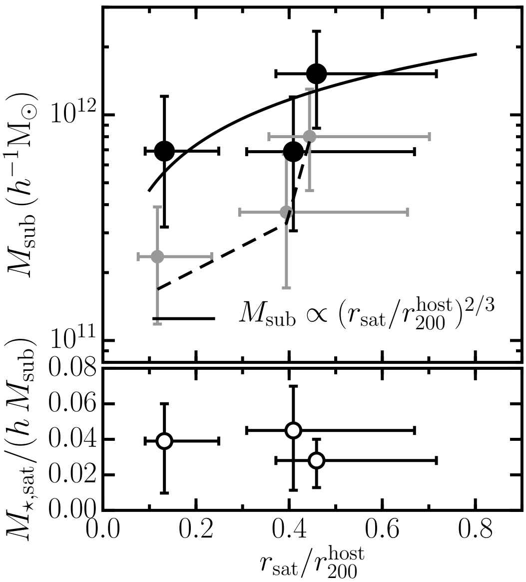

Figure 5.7: Top: Marginalized posterior mass estimates of satellite galaxies from the full NFW (black, large points) and truncated NFW (grey, small points) models, and the dashed black line shows the NFW masses within the same truncation radii for comparison. Horizontal errorbars are 68% ranges in (3-dimensional) $r_{\rm sat}/r_{200}$ per bin. The black solid line shows the radial dependence of subhalo mass predicted by the numerical simulations of Gao et al. (2004) with an arbitrary normalization. Bottom: Stellar-to-total mass ratios in each bin.

As mentioned above, our simplistic modelling of groups does not affect the posterior satellite masses significantly. Therefore it is sufficient that our group masses are consistent with the results of Viola et al. (2015), and we do not explore more complex models for the group signal. For a more thorough modelling of the lensing signal of groups in the KiDS-GAMA overlap region, see Viola et al. (2015).

5.4.3. The masses of satellite galaxies

We detect the signal from satellites with significances >99% in all three radial bins. Satellite masses are consistent across radial bins. We show the marginalized posterior estimates and 68% credible intervals in Figure 5.7 as a function of 3-dimensional group-centric distance, $r_{\rm sat}$ (in units of the group radius r_{200}).

[9]Throughout, we quote masses and radii for a given radial bin by adding an index from 1 to 3 to the subscript of each value.

Figure 5.7 also shows the subhalo mass as a function of 3-dimensional separation from the group centre found in numerical simulations by Gao et al. (2004). Note that we compare here only the trend with radius, not the normalization. Fitting a power law, $M_{\rm sub} \propto (r_{\rm sat}/r_{200})^a$, to the data in Figure 5.7 we find $a = 0.3 \pm 0.5$ (ignoring horizontal errorbars), consistent with the trend predicted by Gao et al. (2004) but also with no dependence on group-centric distance. The bottom panel shows the average stellar mass fractions, which are also consistent with each other, $\langle M_{\star,\rm sat}/M_{\rm sub}\rangle \sim 0.04\,h^{-1}$.

We also show in Figure 5.7 the results obtained for the truncated theoretical model. The difference between each pair of points depends on the posterior $r_{\rm t}$ estimated in each bin through Equation 5.13. Specifically, we find $\langle r_{\rm t}\rangle = \{0.04^{+0.02}_{-0.01}, 0.06^{+0.03}_{-0.02}, 0.09^{+0.04}_{-0.02}\}$ h^{-1}Mpc. We remind the reader that these are theoretical predictions from Equation 5.13 rather than observational results. For comparison, we also show in Figure 5.7 the masses obtained by integrating the posterior NFW models up to said truncation radii, shown by the dashed line. These masses are fully consistent with the truncated model, implying that the difference between the black and grey points (which show $M_{\rm sub}(<r_{200})$ and $M_{\rm sub}(<r_{\rm t})$, respectively) in Figure 5.7 is only a matter of presentation; the data cannot distinguish between these two models.

After we submitted this work, Li et al. (2016) presented similar, independent satellite lensing measurements. They used ∼7,000 satellites in the redMaPPer galaxy group catalogue (Rykoff et al. 2014) with background sources from CS82 and also measured the lensing signal in three bins in projected radius. They find comparable constraints that are consistent with ours.

5.4.4. The average subhalo mass

We can link the results presented in Section 5.4.3 to predictions from numerical simulations. Comparisons of the satellite populations of observed galaxies (or groups) provide valuable insights as to the relevant physical processes that dominate galaxy formation, as highlighted by the well known ‘missing satellites’ (Klypin et al. 1999; Moore et al. 1999) and ‘too big to fail’ (Boylan-Kolchin et al. 2011) problems, which suggest either that our Universe is not well described by a ΛCDM cosmology, or that using numerical simulations to predict observations is more complicated than anticipated. While the former may in fact be true, the latter is now well established, as the formation of galaxies inside dark matter haloes depends strongly on baryonic physics not included in N-body simulations, and the influence of baryons tends to alleviate these problems (Zolotov et al. 2012).

Here we specifically compare the average subhalo-to-host mass ratio, $\psi \equiv M_{\rm sub}/M_{\rm host}$, to ΛCDM predictions through the subhalo mass function, which describes the mass distributions of subhaloes for a given dark matter halo mass. In numerical simulations, the resulting subhalo mass function is a function only of ψ (e.g., van den Bosch et al. 2005; Jiang & van den Bosch 2016). As summarized in Table 5.2, we find typical subhalo-to-host mass ratios in the range $\langle\psi\rangle \sim 0.015$, statistically consistent across group-centric distance. We obtain these values by taking the ratio $M_{\rm sub}/M_{\rm host}$ at every evaluation in the MCMC. For comparison, the values we obtain using the truncated model are $\langle\psi_{\rm tNFW}\rangle \approx 0.005$, also consistent across radial bins.

We compare our results to the analytical *evolved* (that is, measured after the subhaloes have become satellites of the host halo, as opposed to one measured at the time of infall) subhalo mass function proposed by van den Bosch et al. (2005),

$$\frac{\mathrm{d}N}{\mathrm{d}\psi} \propto \frac{1}{\psi}\left(\beta/\psi\right)^{\alpha}\exp\left(-\psi/\beta\right), \tag{5.17}$$

where $\alpha = 0.9$ and $\beta = 0.13$, and calculate the average subhalo-to-host mass ratio,

$$\langle\psi\rangle = \left[\int_{\psi_{\min}}^{\psi_{\max}} \frac{\mathrm{d}N}{\mathrm{d}\psi}\mathrm{d}\psi\right]^{-1} \int_{\psi_{\min}}^{\psi_{\max}} \psi\frac{\mathrm{d}N}{\mathrm{d}\psi}\mathrm{d}\psi, \tag{5.18}$$

where $\psi_{\min} \approx 10^{-3}$ is approximately the minimum fractional satellite mass we observe given the results of Section 5.4.3, and $\psi_{\max} = 1$ is the maximum fractional satellite mass by definition. Integrating in this range gives $\langle\psi\rangle = 0.0052$.

There are many uncertainties involved in choosing a $\psi_{\min}$ representative of our sample, such as survey incompleteness and the conversion between stellar and total mass; we defer a proper modelling of these uncertainties to future work. For reference, changing $\psi_{\min}$ by a factor 5 modifies the predicted $\langle\psi\rangle$ by a factor ~3. Considering the uncertainties involved, all we can say at present is that our results are consistent with ΛCDM predictions.

5.4.5. Sensitivity to contamination in the group catalogue

Two sources of contamination in the group catalogue have been neglected in this analysis. The spectroscopic group satellite catalogue used in this work has a high, but not 100%, purity. For groups with $N_{\rm FoF} \geq 5$ the purity approaches 90%; groups with fewer members have significantly lower purity (Robotham et al. 2011). Li et al. (2013a) have shown that a contamination fraction of 10% in the satellite sample would lead to a +15% bias in the inferred satellite masses, well within the reported uncertainties (which amount to up to a factor two).

The second source of contamination is the misidentification of the central galaxy in a group, such that the true central galaxy would be included in our satellite sample. This effect is similar to that explained above, except that contaminating galaxies now reside in particularly massive halos (namely, the groups themselves). Based on comparisons to GAMA mock galaxy catalogues, Robotham et al. (2011) found that the fraction of BCGs correctly identified with the central galaxy of dark matter halos is around $70-75$% for groups with $N_{\rm FoF} \geq 5$. Viola et al. (2015) have directly measured the offset probability of BCGs from the true minimum of the potential well. They found that the BCG is as good a proxy for the centre as the iterative centre of Robotham et al. (2011), which according to mock group catalogues are well centred in ~ 90% of the groups. There are very few groups with $N_{\rm FoF} \gg 5$ (Robotham et al. 2011), and therefore the lensing signal of a central galaxy in our sample would probably have $\Delta\Sigma(R \approx 0.05\,h^{-1}\mathrm{Mpc}) \approx 100\,h\mathrm{M}_\odot\,\mathrm{pc}^{-2}$ (see Figure 7 of Viola et al. 2015). If we assume (conservatively) that 20% of the BCGs do not correspond to the central galaxy in their groups, then $0.20/7 = 3$% (where $\langle N_{\rm FoF}\rangle \sim 7$, cf. Table 5.1) of our satellites would be central galaxies. Therefore the total signal in the inner regions ($R \approx 0.05\,h^{-1}\mathrm{Mpc}$) would be $\Delta\Sigma_{\rm tot} = 0.03 \times 100 + 0.97 \times \Delta\Sigma_{\rm sub}^{\rm true} \simeq 40\,h\mathrm{M}_\odot\,\mathrm{pc}^{-2}$, which yields $\Delta\Sigma_{\rm sub}^{\rm true} = 38\,h\mathrm{M}_\odot\,\mathrm{pc}^{-2}$. Therefore central galaxy misidentification induces a +5% bias on the signal, which implies roughly a +15% bias on the mass.

Together, these two effects add up to a $\sim 20-25$% bias in our satellite mass estimates. Such a bias is safely within our statistical uncertainties. Therefore our results are insensitive to plausible levels of contamination in the group catalogue, both from satellites that are not really group members and from misidentified central galaxies.

5.5. Conclusions

We used the first 100 sq. deg. of optical imaging from KiDS to measure the excess surface mass density around spectroscopically confirmed satellite galaxies from the GAMA galaxy group catalogue. We model the signal assuming NFW profiles for both host groups and satellite galaxies, including the contribution from the stellar mass for the latter in the form of a point source. Taking advantage of the combination of statistical power and high image quality, we split the satellite population into three bins in projected separation from the group centre, which serves as a (high-scatter) proxy for the time since infall. We fit the data with a model that includes the satellite and group contributions using an MCMC (see Section 5.3 and Figure 5.5), fully accounting for the data covariance. As a consistency check, we find group masses in good agreement with the weak lensing study of GAMA galaxy groups by Viola et al. (2015), even though we do not account for effects such as miscentring or the contribution from stars in the BCG.

This model fits the data well, with $\chi^2/\mathrm{d.o.f.} = 0.88$ ($\mathrm{PTE} = 0.64$). We are able to constrain total satellite masses to within ~ 0.3 dex or better. Given these uncertainties, the estimated masses are insensitive to the levels of contamination expected in the group catalogue. Satellite galaxies have similar masses across group-centric distance, consistent with what is found in numerical simulations (accounting for the measured uncertainties). Satellite masses as a function of group-centric distance are influenced by a number of effects. Tidal stripping acts more efficiently closer to the group centre, while dynamical friction makes massive galaxies sink to the centre more efficiently, an effect referred to as mass segregation (e.g., Frenk et al. 1996). In addition, by binning the sample in (projected) group-centric distance we are introducing a selection effect such that outer bins include generally more massive groups, which will then host more massive satellites on average. Future studies with increased precision may be able to shed light on the interplay between these effects by, for instance, selecting samples residing in the same host groups or in bins of stellar mass.

As a proof of concept, we compare our results to predictions from N-body simulations. These predict that the subhalo mass function is a function only of the fractional subhalo mass, $\psi \equiv M_{\mathrm{sub}}/M_{\mathrm{host}}$. Our binning in satellite group-centric distance produces a selection effect on host groups, such that each bin probes a (slightly) different group population, which allows us to test such prediction. The average fractional mass in all three bins is consistent with a single value (within large errorbars), $\langle\psi\rangle \sim 0.015$. This is broadly consistent with the predictions of numerical simulations. We anticipate that weak lensing of satellite galaxies will become an important tool to constrain the physical processes incorporated in semi-analytic models of galaxy formation and, ultimately, hydrodynamical simulations.

5.A. Full satellite lensing correlation matrix and the contribution from sample variance

As mentioned in Section 5.3.1, we calculate the covariance matrix directly from the data including only the contribution from shape noise (see Section 3.4 of Viola et al. 2015). In Figure 5.8 we show the corresponding correlation matrix, defined as

$$\mathbf{C}'_{mnij} = \frac{C_{mnij}}{\sqrt{C_{mmii}C_{nnjj}}}, \tag{5.19}$$

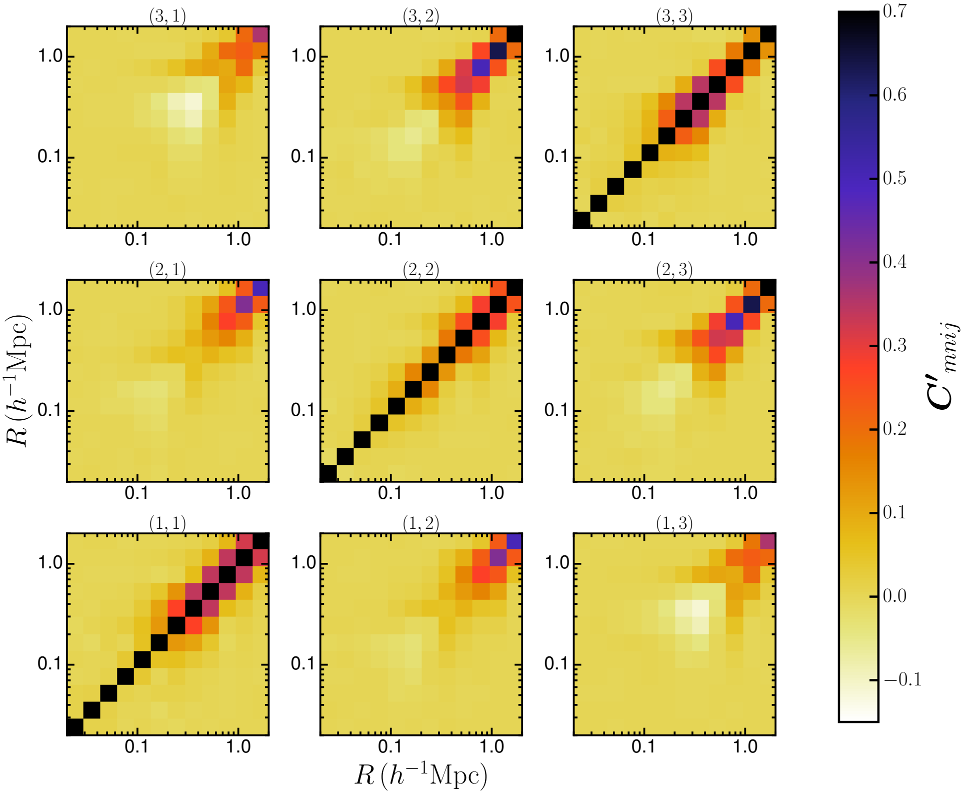

Figure 5.8: Full satellite lensing correlation matrix within and between radial bins as shown by the label at the top of each plot.

where C_{mnij} is the covariance between the i-th and j-th elements of radial bins m and n, respectively (where $m, n = 1, 2, 3$). In reality the lensing covariance also includes a contribution from sample ('cosmic') variance, but we have ignored it in our analysis. Below we justify this decision.

The contribution from sample variance can in principle be estimated by bootstrapping the lensing signal over individual KiDS fields. However, there are two caveats to this approach. First, the 101 KiDS fields used here do not produce enough independent bootstrap samples to properly estimate the full covariance matrix for our satellite samples, which is a symmetric 36×36 matrix (containing 648 independent elements) including sample variance for the three radial bins. Second, using single KiDS fields as bootstrap elements means that the elements are not truly independent from each other, because lenses in one field do contribute to signal in neighbouring fields. In fact, we calculate the lensing signal of each galaxy including background galaxies in neighbouring fields.

The latter point is not crucial for our analysis since, as shown in Figure 5.5, the signal produced by satellite subhaloes is confined to the smallest scales, $R \lesssim 0.3\,h^{-1}\mathrm{Mpc}$. Therefore, we can estimate the relative contribution from sample variance to the covariance matrix by comparing the diagonal sub-panels of the covariance matrices estimated directly from the data (the 'analytical' covariance) and by bootstrapping over KiDS fields. Note that the bootstrap covariance also accounts for shape noise in addition to sample variance. Therefore the ratio between the bootstrap and analytical covariances is a measure of the relative contribution of sample variance to the satellite lensing covariance. It should be noted, however, that the bootstrap covariance can be biased high by as much as 40% (Norberg et al. 2009).

We show this comparison in Figure 5.9 for each of the three radial bins, where we compare $\sqrt{C_{mmii}}$ estimated from the analytic (i.e., data) and bootstrap covariances. Both methods lead to similar values up to the largest angular separations. There is a hint of a nonzero contribution from sample variance at scales $R > 0.3\,h^{-1}\mathrm{Mpc}$, where the bootstrap variance is $\sim 10\%$ larger than the analytical variance. As stated above, the satellite contribution to $\Delta\Sigma$ is confined to scales smaller than these. We conclude that, for the purpose of this work, we can safely ignore sample variance.

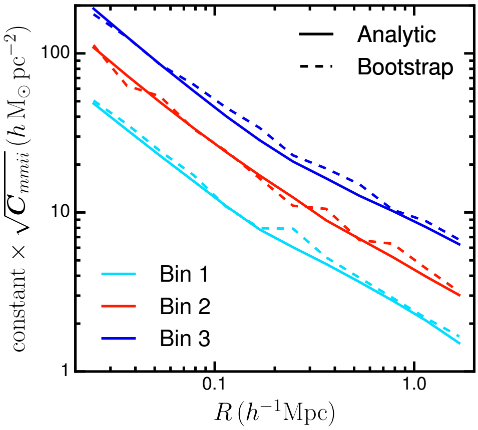

Figure 5.9: Comparison of the variances calculated analytically (solid), which account only for shape noise, and by bootstrapping (dashed), which also account for sample variance, for the diagonal sub-panels of the covariance matrix as per Figure 5.8. The red and blue lines have been offset vertically for clarity.

6 | The galaxy-subhalo connection in low-redshift galaxy clusters from weak gravitational lensing

We measure the gravitational lensing signal around satellite galaxies in galaxy clusters at $z < 0.15$ by combining high-quality imaging data from the Canada-France-Hawaii Telescope with a large sample of spectroscopically-confirmed cluster members. We use extensive image simulations to assess the accuracy of shape measurements of faint, background sources in the vicinity of bright satellite galaxies. We find a small but significant bias, as light from the lenses makes the shapes of backgroud galaxies appear more radial than they really are. We account for this bias by applying a correction that depends on both lens size and magnitude. We also determine and apply a scale-dependent boost factor to account for contamination of the source sample by cluster members. We measure the satellite lensing signal robustly down to scales of roughly 30 kpc, but we cannot constrain the matter density profiles of subhaloes. We estimate the subhalo mass as the mass bound to the subhalo, consistent with the definition of common subhalo finders, and provide a direct measurement of the subhalo-to-stellar-mass relation, $\log m_{\rm bg}/\mathrm{M}_\odot = (11.73 \pm 0.05) + (0.77 \pm 0.11) \log[m_\star/(2 \times 10^{10}\,\mathrm{M}_\odot)]$, broadly consistent with the corresponding relation for central galaxies. The slope of this relation is robust to both the adopted mass-concentration relation and the definition of subhalo mass. We also constrain the mass segregation of subhaloes by measuring the lensing signal as a function of projected cluster-centric distance. We find no statistically significant evidence for mass segregation, in qualitative agreement with predictions from numerical simulations.

Cristóbal Sifón, Ricardo Herbonnet, Henk Hoekstra, et al.,
in preparation

6.1. Introduction

According to the hierarchical structure formation paradigm, galaxy clusters grow by the continuous accretion of smaller galaxy groups and individual galaxies. Initially, each of these systems is hosted by their own dark matter halo, but as a galaxy falls into a larger structure, tidal interactions transfer mass from the infalling galaxy into the new host. The galaxy then becomes a satellite and its dark matter halo, a subhalo.

Detailed studies on the statistics of subhaloes from numerical N-body simulations have revealed that subhaloes are severely affected by their host haloes. Dynamical friction makes more massive subhaloes sink towards the centre faster, while tidal stripping removes mass preferentially from the outskirts of massive subhaloes closer to the centre. These two effects combined destroy the most massive subhaloes soon after infall (e.g., Tormen et al. 1998; Taffoni et al. 2003), a result exaggerated in simulations with limited resolution (e.g., Klypin et al. 1999; Taylor & Babul 2005; Han et al. 2016). Tidal stripping makes subhaloes more concentrated than field haloes of the same mass (e.g., Ghigna et al. 1998; Springel et al. 2008; Moliné et al. 2016), and counterbalances the spatial segregation induced by dynamical friction (van den Bosch et al. 2016).

One of the most fundamental questions is how these subhaloes are linked to the satellite galaxies they host, which are what we can observe in the real Universe. Taking N-body simulations at face value results in serious inconsistencies with observations, the most famous of which are known as the “missing satellites” (Klypin et al. 1999; Moore et al. 1999) and “too big to fail” (Boylan-Kolchin et al. 2011) problems. It has since become clear that these problems may arise because baryonic physics has a strong influence on the small-scale distribution of matter. Energetic feedback from supernovae at the low-mass end, and active galactic nuclei at the high-mass end, of the galaxy population affect the ability of dark matter (sub)haloes to form stars and retain them. In addition, the excess mass in the centre of galaxies (compared to dark matter-only simulations) can modify each subhalo’s susceptibility to tidal stripping (e.g., Zolotov et al. 2012).

Despite these difficulties, given the current technical challenges of generating cosmological high-resolution hydrodynamical simulations (in which galaxies form self-consistently), N-body simulations remain a valuable tool to try to understand the evolution of galaxies and (sub)haloes. In order for them to be applied to real observations, however, one must post-process these simulations in some way that relates subhaloes to galaxies, taking into account the aforementioned complexities (and others). For instance, semi-analytic models contain either physical or phenomenological recipes whether or not to form galaxies in certain dark matter haloes based on the mass and assembly history of haloes (e.g., Bower et al. 2006; Lacey et al. 2015). A different method involves halo occupation distributions (HODs), which assume that the average number of galaxies in a halo depends only on host halo mass. Because they provide an analytical framework to connect galaxies and dark matter haloes, HODs are commonly used to interpret galaxy-galaxy lensing and galaxy clustering measurements through a conditional stellar mass (or luminosity) function (e.g., Seljak 2000; Peacock & Smith 2000; Mandelbaum et al. 2006b; Cacciato et al. 2009; van den Bosch et al. 2013).

One of the key aspects of these prescriptions is the stellar-to-halo mass relation. While many studies have constrained the stellar-to-halo mass relation of central galaxies (e.g., Hoekstra et al. 2005; Heymans et al. 2006b; Mandelbaum et al. 2006b, 2016; More et al. 2011; van Uitert et al. 2011, 2016; Leauthaud et al. 2012; Velander et al. 2014), this is not the case for satellite galaxies, whose stellar-to-*sub*halo mass relation (SHSMR) remains essentially unexplored, and the constraints so far are limited to indirect measurements. Rodríguez-

Puebla et al. (2012) used abundance matching (the assumption that galaxies rank-ordered by stellar mass can be uniquely mapped to [sub]haloes rank-ordered by total mass) to infer the SHSMR using the satellite galaxy stellar mass function, and Rodríguez-Puebla et al. (2013) extended these results using galaxy clustering measurements. They showed that the SHSMR is significantly different from the central stellar-to-total mass relation, and that assuming an average relation when studying a mixed population can lead to biased results (see also Yang et al. 2009).

Instead, only stellar dynamics and weak gravitational lensing provide direct ways to probe the total gravitational potential of a galaxy. However, the quantitative connection between stellar velocity dispersion and halo mass is not straightforward (e.g., Li et al. 2013b; Old et al. 2015), and only weak lensing provides a direct measurement of the total surface mass density (Fahlman et al. 1994; Clowe et al. 1998). Using deep Hubble Space Telescope (HST) observations, Natarajan et al. (1998, 2002, 2007, 2009) measured the weak (and also sometimes strong) lensing signal of galaxies in six clusters at $z = 0.2 - 0.6$. After fitting a truncated density profile to the ensemble signal using a maximum likelihood approach, they concluded that galaxies in clusters are strongly truncated with respect to field galaxies. Using data for clusters at $z \sim 0.2$ observed with the CFH12k instrument on the Canada-Hawaii-France Telescope (CFHT), Limousin et al. (2007) arrived at a similar conclusion. Halkola et al. (2007) and Suyu & Halkola (2010) used strong lensing measurements of a single cluster and a small galaxy group, respectively, and also found evidence for strong truncation of the density profiles of satellite galaxies. However, Pastor Mira et al. (2011) have argued that the conclusion that cluster galaxies are truncated from these (strong and weak) galaxy-galaxy lensing measurements are driven by the parametrization of the galaxy density profiles rather than constraints from the data themselves.

Recent combinations of large weak lensing surveys with high-purity galaxy group catalogues have allowed direct measurements of the average subhalo masses associated with satellite galaxies using weak galaxy-galaxy lensing (Li et al. 2014, 2016, **Chapter 5**). However, these studies did not focus on the SHSMR but on the segregation of subhaloes by mass within galaxy groups, by measuring subhalo masses at different group-centric distances. The observational results are consistent, within their large errorbars, with the mild segregation seen in numerical simulations and semi-analytic models (Han et al. 2016; van den Bosch et al. 2016).

In this work, we present weak gravitational lensing measurements of the total mass of satellite galaxies in 50 massive galaxy clusters at $z < 0.15$. Our images were taken with the MegaCam instrument on CFHT, which provides a larger field of view (1 sq. deg.) than CFH12k. This large field of view allows us to focus on very low redshift clusters and take advantage of the $< 1''$ seeing (corresponding to 1.84 kpc at $z = 0.1$) of our observations. We can therefore probe the lensing signal close to the galaxies themselves, at a physical scale equivalent to what can be probed in a cluster at $z \sim 0.5$ with HST, but out to the clusters' virial radii. In addition, the low-redshift clusters we use have extensive spectroscopic observations available from various data sets, compiled in **Chapter 4**, so we do not need to rely on uncertain photometric identification of cluster members.

This chapter is organized as follows. We summarize the galaxy-galaxy lensing formalism in Section 6.2. We describe our data set in Section 6.3, taking a close look at the source catalogue and the shapes of background sources in Section 6.4. We present our modelling of the satellite lensing signal in Section 6.5, and discuss the connection between mass and light in satellite galaxies in Section 6.6.

We adopt a flat Λ cold dark matter (ΛCDM) cosmology with $\Omega_\mathrm{m} = 0.315$, based on the latest results from cosmic microwave background observations by Planck Collaboration (2015a), and $H_0 = 70\,\mathrm{km\,s^{-1}Mpc^{-1}}$. In this cosmology, $10'' = \{9.8, 18.4, 26.1\}\,\mathrm{kpc}$ at $z = \{0.05, 0.1, 0.15\}$. As usual, stellar and (sub)halo masses depend on the Hubble constant as $m_\star \sim 1/H_0^2$ and $m \sim 1/H_0$, respectively.

6.2. Weak galaxy-galaxy lensing

Gravitational lensing distorts the images of background ("source") galaxies as their light passes near a matter overdensity along the line-of-sight. This produces a distortion in the shape of the background source, called *shear*, and a *magnification* effect on the source's size (and consequently its brightness). Starting from a measurement of the shape of an object in a cartesian frame with components (γ_1, γ_2) (see Section 6.4.1), the shear can be computed as

$$\begin{pmatrix}\gamma_\mathrm{t}\\ \gamma_\times\end{pmatrix} = \begin{pmatrix}-\cos 2\phi & -\sin 2\phi\\ \sin 2\phi & -\cos 2\phi\end{pmatrix}\begin{pmatrix}\gamma_1\\ \gamma_2\end{pmatrix}, \tag{6.1}$$

where ϕ is the azimuthal angle of the lens-source vector, γ_t measures the ellipticity in the tangential ($\gamma_\mathrm{t} > 0$) and radial ($\gamma_\mathrm{t} < 0$) directions and $\gamma_\times$ measures the ellipticity in directions $45°$ from the tangent. Because of parity symmetry, we expect $\langle\gamma_\times\rangle = 0$ for an ensemble of lenses (Schneider 2003) and therefore $\gamma_\times$ serves as a test for systematic effects.

The shear is related to the excess surface mass density (ESD), $\Delta\Sigma$, via

$$\Delta\Sigma(R) \equiv \bar\Sigma(<R) - \bar\Sigma(R) = \gamma_\mathrm{t}\Sigma_\mathrm{c}, \tag{6.2}$$

where $\bar\Sigma(<R)$ and $\bar\Sigma(R)$ are the average surface mass density within a radius[1] R and within a thin annulus at distance R from the lens. The critical surface density, Σ_c, is a geometrical factor that accounts for the lensing efficiency,

$$\Sigma_\mathrm{c} = \frac{c^2}{4\pi G}\frac{D_\mathrm{s}}{D_\mathrm{l}D_\mathrm{ls}}, \tag{6.3}$$

where, D_l, D_s, and D_ls are the angular diameter distances to the lens, to the source and between the lens and the source, respectively. The ESD is then

$$\Delta\Sigma = \Sigma_\mathrm{c}\frac{\sum_i w_i\gamma_{\mathrm{t},i}}{\sum_i w_i}, \tag{6.4}$$

where the sums run over all lens-source pairs and the weight of each source is given by

$$w_i = \frac{1}{\langle\epsilon_\mathrm{int}^2\rangle + (\sigma_{\gamma,i})^2}. \tag{6.5}$$

Here, σ_γ is the measurement uncertainty in γ_t due to shot noise in the images (see Section 6.4.1). We set the intrinsic root-mean-square galaxy ellipticity, $\langle\epsilon_\mathrm{int}^2\rangle^{1/2}$, to 0.25.

In fact, the weak lensing observable is the *reduced* shear, $g \equiv \gamma/(1-\kappa)$ (where $\kappa = \Sigma/\Sigma_\mathrm{c}$ is the lensing convergence), but in the weak limit $\kappa \ll 1$ so that $g \approx \gamma$. However, close to the centres of clusters $\kappa \sim 1$, so this approximation is not accurate anymore. To account for this,

[1] As a convention, we denote three-dimensional distances with lower case r and two-dimensional distances (that is, projected on the sky) with upper case R.

the lensing model presented in Section 6.5 is corrected using

$$g(R) = \frac{\gamma(R)}{1-\bar{\Sigma}(R)/\Sigma_\mathrm{c}} = \frac{\Delta\Sigma(R)/\Sigma_\mathrm{c}}{1-\bar{\Sigma}(R)/\Sigma_\mathrm{c}}. \tag{6.6}$$

6.2.1. Statistical errors: data covariance

Because the gravitational potential of satellites in a cluster is traced by the same background source galaxies, data points in the ESD are correlated. Following Viola et al. (2015), we can re-arrange Equation 6.4 to reflect the contribution from each *source* galaxy. The data covariance can then be written as

$$\mathbf{Cov}_{mnij} = \langle\epsilon^2\rangle^{1/2} \frac{\sum_s \left(C_{si,m}C_{sj,n} + S_{si,m}S_{sj,n}\right)}{\left(\sum_s Z_{si,m}\right)\left(\sum_s Z_{sj,n}\right)}, \tag{6.7}$$

where index pairs m,n and i,j run over the observable bins (e.g., stellar mass) and lens-source separation, R, respectively, and C, S and Z are sums over the lenses:

$$\begin{aligned} C_{si} &= -\sum_l w_{ls}\Sigma_{\mathrm{c},ls}^{-1}\cos 2\phi_{ls}, \\ S_{si} &= -\sum_l w_{ls}\Sigma_{\mathrm{c},ls}^{-1}\sin 2\phi_{ls}, \\ Z_{si} &= \sum_l w_{ls}\Sigma_{\mathrm{c},ls}^{-2}, \end{aligned} \tag{6.8}$$

and we assume zero covariance between clusters. In Equations 6.7 and 6.8, we explicitly allow for the possibility that the source weight, w, may be different for each lens-source pair (as opposed to a unique weight per source). This is the case when we consider the corrections to the shape measurements from lens contamination discussed in Section 6.4.1.

In addition to the data covariance there is, in principle, a contribution to the measurement uncertainty from sample variance. By comparing Equation 6.7 to uncertainties estimated by bootstrap resampling, in **Chapter 5** we showed that the contribution from sample variance is less than 10% for satelite galaxy-galaxy lensing measurements when limited to small lens-source separations ($R \lesssim 2$ Mpc).

6.3. Data set

In this section we describe the lens and source galaxy samples we use in our analysis. In the next section, we make a detailed assessment of the shape measurement and quality cuts on the source sample using extensive image simulations.

6.3.1. Cluster and lens galaxy samples

The Multi-Epoch Nearby Cluster Survey (MENeaCS, Sand et al. 2012) is a targeted survey of 57 galaxy clusters in the redshift range $0.05 \lesssim z \lesssim 0.15$ observed in the g and r bands with MegaCam on the Canada-France-Hawaii Telescope (CFHT). The image processing is described in detail in van der Burg et al. (2013); all images have seeing $\lesssim 0.8''$. In **Chapter 4**, we compiled a large sample of spectroscopic redshift measurements in the direction of 46 of these clusters, identifying a total of 7945 spectroscopic members. Since,

Table 6.1: Average properties of stellar mass and cluster-centric distance bins used in Sections 6.6.1 and 6.6.2. Each column corresponds to the values of the fiducial spectroscopic-plus-red-sequence sample, the sample of galaxies (both spectroscopic and red sequence) that have a stellar mass measurement, and the spectroscopic-only sample (with and without stellar mass measurements). Note that the 'with-$m_\star$' columns reflect the number of clusters that have three- or four-band photometry, as opposed to those that have only two. See Section 6.3.1 for details on these samples.

Binning observable	Bin label	Range	$N_{\rm sat}$			$\langle R_{\rm sat}/{\rm Mpc}\rangle$			$\log\langle m_\star/{\rm M}_\odot\rangle$		
			spec+RS	with-$m_\star$	spec	spec+RS	with-$m_\star$	spec	spec+RS	with-$m_\star$	spec
$\log(m_\star/{\rm M}_\odot)$	M1	[9.0 – 10.0)	4199	1546	1756	0.69	0.71	0.92	9.59	9.60	9.64
	M2	[10.0 – 10.4)	2501	1591	1742	0.80	0.81	0.93	10.19	10.20	10.20
	M3	[10.4 – 10.7)	1396	1035	1105	0.84	0.86	0.93	10.54	10.54	10.54
	M4	[10.7 – 11.2]	963	737	811	0.88	0.92	0.94	10.88	10.87	10.88
$R_{\rm sat}$ (Mpc)	D1	[0.05 – 0.40)	2509	2021	1044	0.24	0.24	0.24	9.94	9.94	10.14
	D2	[0.40 – 0.70)	2433	1989	1145	0.55	0.55	0.55	9.93	9.94	10.16
	D3	[0.70 – 1.20)	2817	2358	1633	0.90	0.91	0.94	9.96	9.97	10.16
	D4	[1.20 – 2.00]	1821	1655	1818	1.57	1.57	1.57	10.17	10.17	10.17

Rines et al. (2016) have published additional spectroscopic redshifts for galaxies in 12 MENeaCS clusters, six of which are included in **Chapter 4** but for which the observations of Rines et al. (2016) represent a significant increase in the number of member galaxies. We select cluster members in these 12 clusters in an identical way as in **Chapter 4**. From the member catalogue of **Chapter 4** we exclude all brightest cluster galaxies (BCGs), and refer to all other galaxies as satellites. Because the shapes of background galaxies near these members is very likely to be contaminated by light from the BCG, we also exclude all satellite galaxies within 10″ of the BCGs to avoid severe contamination from extended light. Finally, we impose a luminosity limit $L_{\rm sat} < \min(2L^\star, 0.5L_{\rm BCG})$, where $L^\star(z)$ is the r-band luminosity corresponding to the characteristic magnitude, $m^\star_{\rm phot}(z)$ of the Schechter (1976) function, fit to red satellite galaxies in redMaPPer galaxy clusters over the redshift range $0.05 < z < 0.7$ (Rykoff et al. 2014).[2] We choose the maximum possible luminosity, $2L^\star$, because the BCGs in our sample have $L_{\rm BCG} \gtrsim 3L^\star$, so this ensures we do not include central galaxies of massive (sub)structures that could, for instance, have recently merged with the cluster. In addition, we only include satellites within 2 Mpc of the BCG. At larger distances, contamination by fore- and background galaxies becomes an increasingly larger problem. Our final spectroscopic sample consists of 5414 satellites in 51 clusters.

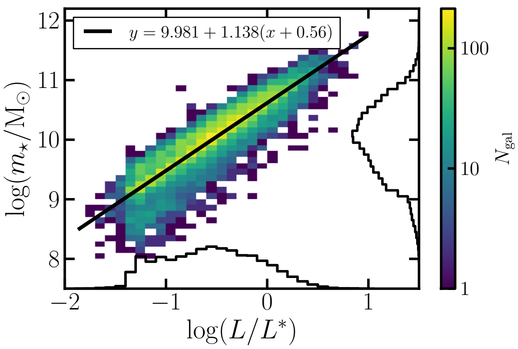

Figure 6.1: Relation between stellar mass and r-band luminosity for all satellites with stellar mass measurements. The color scale shows the two-dimensional histogram while the bottom and right histograms show the individual distributions. The black line is the best-fit relation, shown in the legend.

In addition, we include red sequence galaxies in all MENeaCS clusters in order to improve our statistics. We measure the red sequence by fitting a straight line to the colour-magnitude relation of red galaxies in each cluster using a maximum likelihood approach (C. Sifón et al., in prep.). Following the results of **Chapter 4**, we include only red sequence galaxies brighter than $M_{\rm r} = -19$ and within 1 Mpc of the BCG.[3] When we include red sequence galaxies, we also use the seven clusters without spectroscopic cluster members. Therefore our combined spectroscopic plus red sequence sample includes 9059 cluster members in 57 clusters. Throughout, we refer to the spectroscopic and spectroscopic plus red sequence samples as 'spec' and 'spec+RS', respectively.

Using u- and i-band data taken with either MegaCam or the Wide-Field Camera on the Isaac Newton Telescope in La Palma, van der Burg et al. (2015) estimated stellar masses for the 46 clusters with spectroscopic data from **Chapter 4**. Stellar masses were estimated by fitting each galaxy's spectral energy distribution using FAST (Kriek et al. 2009) assuming a Chabrier (2003) initial mass function. The only factor determining whether a particular galaxy has a stellar mass estimate or not is whether the cluster it resides in has u- and i-band

[2] Equation 9 of Rykoff et al. (2014) provides a fitting function for the i-band $m^\star_{\rm phot}(z)$, which we convert to r-band magnitudes assuming a quiescent spectrum, appropriate for the majority of our satellites, using EzGal (`http://www.baryons.org/ezgal/`, Mancone & Gonzalez 2012).

[3] Here, $M_{\rm r}$ is the $k+e$–corrected absolute magnitude in the r-band, calculated with EzGal using a passively evolving Charlot & Bruzual (2007, unpublished, see Bruzual & Charlot 2003) model with formation redshift $z_{\rm f} = 5$.

data. We therefore regard the subsample of satellites with stellar masses as a representative subsample of our full catalogue. We therefore also include galaxies in clusters without stellar mass catalogues (corresponding to roughly 15% of the galaxies) by assigning stellar masses to them based on a fit to the stellar masses as a function of r-band luminosity, $L^\star$. For each galaxy, we assign its stellar mass from a normal distribution centred on this relation and with a spread given by the scatter in Figure 6.1. The relation we use is

$$\log m_\star = (9.981 \pm 0.002) + (1.138 \pm 0.005)\left(\log L/L^* + 0.56\right), \tag{6.9}$$

and is shown in Figure 6.1. We have checked that the inclusion of galaxies without stellar masses through the above procedure does not bias any of our results.

In order to characterize the connection between satellite galaxies and their host subhaloes, we split the sample by stellar mass (Section 6.6.1) and cluster-centric distance (Section 6.6.2), each time splitting the sample in four bins. We show the stellar mass and cluster-centric distributions of the resulting subsamples in Figure 6.2, and list the average values in Table 6.1.

6.3.2. Source galaxy sample

We construct the source catalogues in an identical manner to Hoekstra et al. (2015), except for one additional constraint discussed in Section 6.4. The biases in the shape measurements of the sources, depending on how the source sample is defined, have been characterized in great detail by Hoekstra et al. (2015). Although the study of Hoekstra et al. (2015) refers to a different cluster sample, both samples have been observed with the same instrument under very similar conditions of high image quality, so we can safely take the analysis of Hoekstra et al. (2015) as a reference for our study. Specifically, we select only sources with r-band magnitudes[4] $20 < m_{\rm phot} < 24.5$, with sizes $r_{\rm h} < 5$ pix and an additional constraint on $\delta m_{\rm phot}$, the difference in estimated magnitude before and after the local background subtraction (see Section 6.4). Compared to Hoekstra et al. (2015), who used $22 < m_{\rm phot} < 25$, we choose different limits at the bright end because our cluster sample is at lower red-

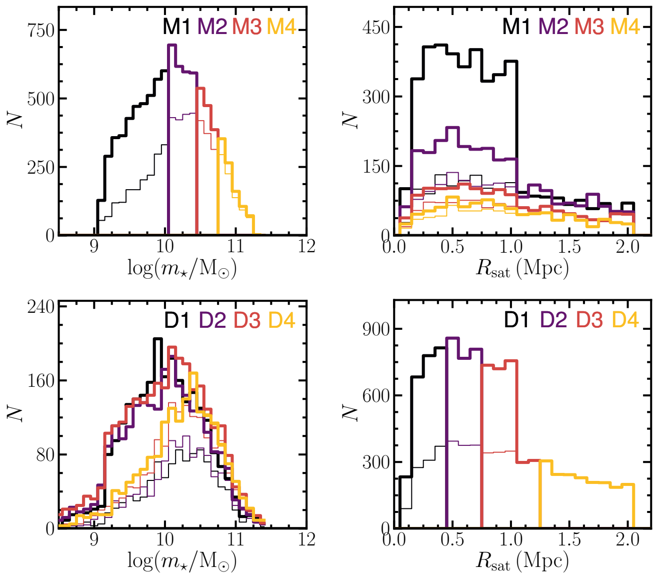

Figure 6.2: Stellar mass and cluster-centric distributions for the four bins in stellar mass used in Section 6.6.1 (top) and in cluster-centric distance used in Section 6.6.2 (bottom). Thin and thick histograms show the distributions of the spectroscopic and the spectroscopic-plus-red-sequence samples, respectively.

[4] We denote r-band magnitudes with $m_{\rm phot}$ in order to avoid confusion with subhalo masses, which we denote with lower case m and subscripts depending on the definition (see Section 6.5.2).

shift and therefore cluster members are brighter, and at the faint end because our data are slightly shallower, complicating the shape measurements of very faint sources.

The source density after applying these cuts is $n_s = 10.5$ arcmin^{-2}. Unlike most cluster lensing studies (e.g., Hoekstra et al. 2012; Applegate et al. 2014; Umetsu et al. 2014), we do not apply a colour cut to our source sample, since this only reduces contamination by ~30% (Hoekstra 2007). Instead, we follow Hoekstra et al. (2015) and correct for contamination in the source sample by applying a 'boost factor' to the measured lensing signal to account for the dilution by cluster members (e.g., Mandelbaum et al. 2005), defined here as

$$\mathscr{B}(\theta_{\rm ls}) = \frac{n_{\rm s,data}(\theta_{\rm ls})}{n_{\rm s,sim}(\theta_{\rm ls})}\frac{\langle n_{\rm s,sim}(\infty)\rangle}{\langle n_{\rm s,data}(\infty)\rangle}. \tag{6.10}$$

We define $n_s(\infty)$ as the number density as far as possible from the cluster, such that the measurement is contaminated by cluster members as least as possible. Because of the low redshift of our cluster sample, the field of view is sometimes not sufficient to probe a region truly devoid of cluster galaxies, but this has no impact on our results.

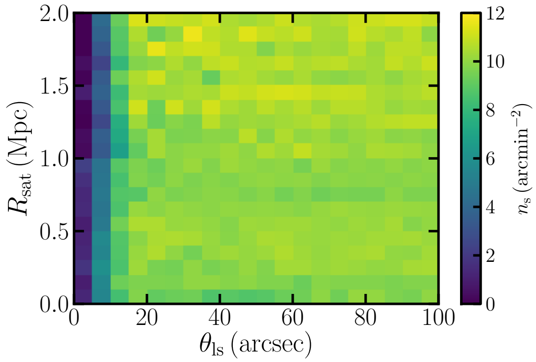

Figure 6.3: Observed number density of background sources as a function of lens-source separation, $\theta_{\rm ls}$, and distance from the lens to the cluster centre, $R_{\rm sat}$, for all 57 MENeaCS clusters, after applying all the cuts described in Section 6.3.

In the case of satellite galaxy-galaxy lensing there is a particularly high number density of lenses, which act as masks in our source sample in the regions where we most care about the signal—as close as possible to the lenses. In Figure 6.3, we show the source density as a function of both lens cluster-centric distance, $R_{\rm sat}$, and lens-source separation, $\theta_{\rm ls}$. The source density is fairly independent of both quantities, except for a sharp decrease at $\theta_{\rm ls} < 20''$, caused by the presence of cluster members which hide background sources (see Section 6.4.2). There is also a slight (~10%) decrease in n_s around lenses closer to the cluster centre, which can similarly be attributed to the higher lens density.

Roughly 20% of our satellites reside in clusters at $z < 0.06$, at which redshift the maximum distance from the centre within the 1 sq. deg. field of view of MegaCam (i.e., $30'$) corresponds to 2 Mpc. At larger radii the average signal may be biased since progressively fewer lenses from fewer clusters contribute to the measurements. We therefore only consider lens-source separations $R < 2\,{\rm Mpc}$ (where $R = D_A(z)\theta_{\rm ls}$) for our analysis.

6.4. Bias assessment and calibration through image simulations

In order to assess the impact of the lenses on our source sample (Section 6.4.2) and shape measurements (Section 6.4.1), we inject bright galaxies into the image simulations produced by Hoekstra et al. (2015). We place round galaxies modelled by Sérsic (1968) profiles with index $n = 4$ in a regular grid in the simulated images, separated at least $60''$ from each other. Figure 6.4 shows the distribution of magnitudes, $m_{\rm phot}$, and sizes, $s_{\rm eff}$, in the data, and the parameter space sampled with the simulations. The light profiles of the simulated lenses are truncated at $5 \times s_{\rm eff}$, where $s_{\rm eff}$ is the effective, or half-light, radius of the Sérsic profile. Galaxies are truncated to avoid confusion of light coming from different lenses, which would alter the inferred bias.

6.4.1. Shape measurements

To measure the galaxy-galaxy lensing signal we must be able to accurately infer the shear field around the lenses by measuring the shapes of as many background galaxies as possible. Most of these sources are faint and of sizes comparable to the image resolution, quantified by the point spread function (PSF). Blurring by the PSF leads to a multiplicative bias, μ, while an anisotropic PSF introduces an additive bias, c (e.g., Heymans et al. 2006a). The measured (or observed) shear is therefore related to the true shear by

$$\gamma^{\rm obs}(\theta) = \left(1+\mu\right)\gamma^{\rm true}(\theta)\mathscr{B}^{-1}(\theta) + c\,. \tag{6.11}$$

Note that μ, c and $\mathscr{B}(\theta)$ depend on both the shape measurement method and the dataset on which the method is applied. As with any bias, it is not the magnitude of μ or c that is important but the accuracy with which it is known; this determines the accuracy to which they can be corrected for.

We measure galaxy shapes by calculating the moments of galaxy images using the KSB method (Kaiser et al. 1995; Luppino & Kaiser 1997), incorporating the modifications by Hoekstra et al. (1998, 2000). Hoekstra et al. (2015) used extensive image simulations to assess the performance of KSB depending on the observing conditions and background source ellipticity, magnitude and size distributions. We adopt the size– and signal-to-noise–dependent multiplicative bias correction obtained by Hoekstra et al. (2015). Instead of correcting each source's measured shape, we apply an average correction to each data point, since the latter is more robust to uncertainties in the intrinsic ellipticity distribution (Hoekstra et al. 2015).

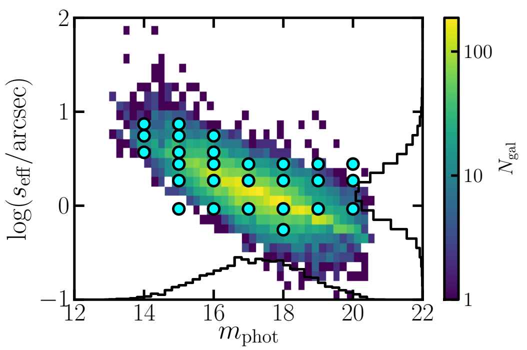

Figure 6.4: Magnitude and size distribution of satellites in the MENeaCS spec+RS sample. The logarithmic color scale shows the number of galaxies per two-dimensional bin, while black histograms show the one-dimensional distributions. Cyan circles show the coordinates used in the image simulations.

As is customary in galaxy-galaxy lensing studies (and similarly in cluster lensing studies), Hoekstra et al. (2015) ignored the additive bias in Equation 6.11 because the azimuthal averaging of source shapes washes out any spatial anisotropy (in other words, additive biases in γ_1 and γ_2 vanish when projected into $\gamma_{\rm t}$). However, unlike the case of cluster lensing, our measurements are focused on the immediate surroundings of thousands of lenses, such that galaxy light may bias the shape measurements of fainter background sources. Given that the light profile always decreases radially, the azimuthal averaging can introduce an additive bias in $\gamma_{\rm t}$ (as opposed to $\gamma_{1,2}$). In Section 6.A we show, using the image simulations described above, that we can model this (negative) bias, $c_{\rm t}$, as a function of lens-source separation, lens magnitude and size, and we correct each source's shape measurement for this bias. For reference, a fraction of order 10^{-6} lens-source pairs have $|c_{\rm t}| > 0.01$.

For illustration, we show in Figure 6.5 the average $c_{\Delta\Sigma} \equiv \Sigma_c c_t$ obtained for real galaxies binned into four stellar mass bins (see Section 6.6.1). As expected, the correction is larger for more massive galaxies, which are on average larger.

6.4.1.1. Sensitivity to background subtraction

The shape measurement algorithm proceeds in two steps. The first is to detect sources using a global background measurement, while the second is to measure the shapes of these detected objects. In the second step, a local background is determined by measuring the brightness in an annulus with inner and outer radii of 16 and 32 pixels, with all detected galaxies masked. This annulus is split into four quadrants and the background is subtracted by fitting a plane through them. This background subtraction works well in general, but in some cases, the background subtraction significantly modifies the estimated magnitude of the test galaxy. Since the simulations do not have a diffuse background component, a proper background subtraction would leave the galaxy magnitude untouched. Therefore changes in the magnitude pre- and post-background subtraction, which we denote $\delta m_{\rm phot}$, suggest that the shape measurement process is not robust for that particular galaxy. The simulations indeed contain a population of sources with large values of $\delta m_{\rm phot}$. We discard all source galaxies that meet the following criteria:

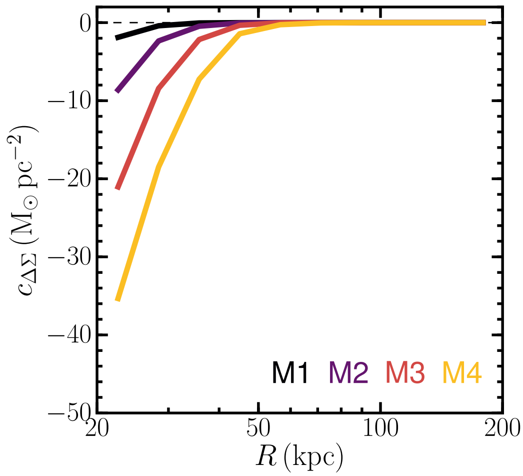

Figure 6.5: Average tangential additive bias, $c_{\Delta\Sigma} \equiv \Sigma_c c_t$, for the four stellar mass bins studied in Section 6.6.1, from low (M1) to high (M4) stellar mass. Note the smaller extent of the horizontal axis compared to other similar figures.

$$\begin{aligned} &\delta m_{\rm phot} > 0.0607 + 0.0363 m_{\rm phot} - 0.0152 m_{\rm phot}^2 + 0.0053 m_{\rm phot}^3, \\ &\quad \text{or} \\ &\delta m_{\rm phot} < -0.1607 - 0.0363 m_{\rm phot} + 0.0152 m_{\rm phot}^2 - 0.0053 m_{\rm phot}^3, \end{aligned} \tag{6.12}$$

which represent the edges of the distribution of $\delta m_{\rm phot}$, after accounting for the spread as a function of $m_{\rm phot}$ that arises due to measurement noise. Inspecting the location of the galaxies thus discarded in the real data, we find that they are mostly located either near bright, saturated stars (which have been discarded in previous steps by masking stellar spikes and ghosts), or close to big galaxies with resolved spiral arms or other similar features, that make the plane approximation of the background a very bad fit of the local background. Equation 6.12 therefore effectively acts as a step to identify blended objects. We have verified that the calibration of the shape measurements by Hoekstra et al. (2015) remains unchanged when discarding these galaxies (which were included in their sample). Typically, an additional 10–12 % of sources are masked by Equation 6.12.

6.4.2. Obscuration and contamination by cluster members

Lens galaxies affect the number of detected objects in their vicinity for two reasons: big lenses act as masks on the background source population, while small ones enter the source sample. We refer to these effects as obscuration and contamination, respectively. Since cluster galaxies are randomly oriented (see **Chapter 4**), contamination by cluster members dilutes the recovered lensing signal. Obscuration, in turn, has two effects: it reduces the statistical power of small-scale measurements, and it complicates the determination of contamination, since number density of sources is also affected by it. We resort to the image simulations described above to assess these two effects.

Figure 6.6 shows the source densities measured in the data (i.e., Figure 6.3 collapsed over the vertical axis) and in the real simulations, as a function of lens-source separation, $\theta_{\rm ls}$. The simulated average source densities have been obtained by performing a weighted sum of the source densities measured in simulations with different lens properties. Here, the weights correspond to the number of lenses in the MENeaCS sample with the same magnitude and size of each image simulation setup as per Figure 6.4. Both the data and the simulations show a sharp decrease in the source number density at lens-source separations $\theta_{\rm ls} < 20''$. This decrease effectively means that we have no constraining power below scales $\theta_{\rm ls} \sim 10''$, corresponding to 18 kpc at the median redshift of our sample, $z = 0.1$. This is well beyond the half-light radius of our lenses (see Figure 6.4), and severely limits our ability to constrain the density profile of galaxies at the smallest scales. One possibility to overcome this is to model and subtract lens galaxies from the images to be able to recover a larger source density in the innermost regions; we will explore this in future work.

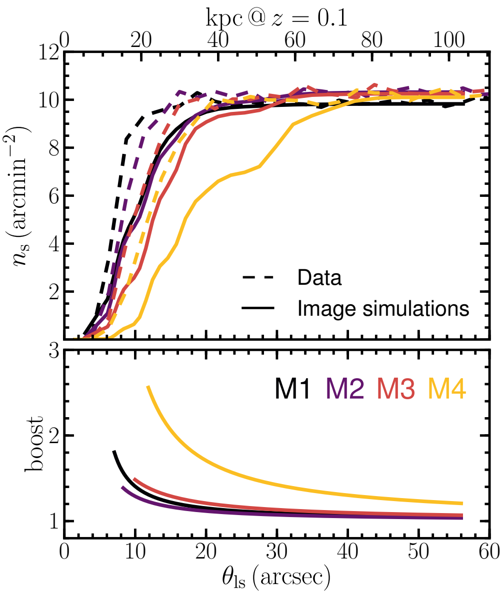

Figure 6.6: Top: average number densities of background sources in the data (dashed) and the image simulations (solid), as a function of lens-source separation, for four bins in stellar mass. The decrease in source density towards $\theta_{\rm ls} = 0$ is produced by obscuration, while the excess density in the data compared to the image simulations corresponds to contamination, by cluster members. Bottom: best-fit boost factors. Lens-source separations below which the source density is less than half of the large-scale value are masked.

While both the data and the simulations show a sharp decline in the source density at small scales, the source density profiles are in fact different in an important way. The number density in the image simulations start to decrease at larger scales and do so more slowly than the number densities measured from the data. This difference is produced by cluster members contaminating our source sample, which tends to compensate for the obscuration produced by the lens galaxy on the fainter sources. The bottom panel of Figure 6.6 shows the excess of source galaxies in the real data compared to the simulations, which represents the boost factor defined in Equation 6.10.

Therefore to correct the lensing signal, we repeat the procedure above separately for each considered bin (e.g., in stellar mass). That is, we first generate a two-dimensional histogram of $m_{\rm phot}$ and $\log s_{\rm eff}$ and weight-average the number densities measured in the image simulations.

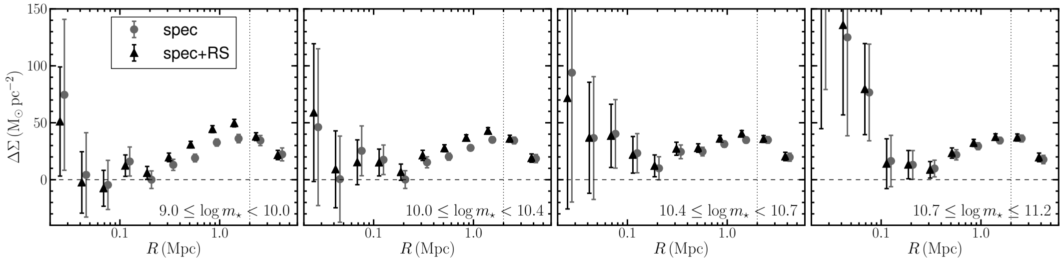

Figure 6.7: Excess surface mass density (ESD) of satellite galaxies binned by stellar mass. Grey circles and black triangles show the ESD of the spectroscopic and spectroscopic-plus-red sequence samples, respectively. Errorbars are the square roots of the diagonal terms of the covariance matrix. The dashed horizontal line shows $\Delta\Sigma = 0$ for reference. In our analysis we only use data points up to 2 Mpc, marked by the vertical dotted line.

We fit for a boost factor of the form $\mathscr{B}(\theta_{\rm ls}) \propto 1/\theta_{\rm ls}$, which we find provides a good description of the data (shown for the four stellar mass bins in the bottom panel of Figure 6.6). Finally, we average $D_{\rm A}(z)\mathscr{B}(\theta_{\rm ls})$ weighting by the lens distribution to obtain $\mathscr{B}(R)$, and apply the latter to the average $c_{\rm t}$-corrected signal per bin.

Due to lensing, sources are magnified as well as sheared, and this may bias the inferred source number counts discussed in this section, which would have an effect on the boost correction. The increase in flux boosts the number counts relative to an unlensed area of the sky, but the decrease in effective area works in the opposite direction. The net effect depends on the intrinsic distribution of source galaxies as a function of magnitude, and cancels out for a slope $d\log N_{\rm source}/dm_{\rm phot} = 0.40$ (Mellier 1999). In fact, this slope is 0.38–0.40 for the MegaCam r-band data (Hoekstra et al. 2015), so we can safely assume that contamination by cluster members fully explains the excess $n_{\rm s}$ seen in Figure 6.6.

6.4.3. Resulting lensing signal

Figure 6.7 shows the resulting lensing signal from satellites in MENeaCS clusters, corrected by both $c_{\rm t}(\theta_{\rm ls})$ and $\mathscr{B}(R)$. We make the distinction in the arguments of both corrections because the former is applied to each lens-source pair, while the latter is applied as an average correction after stacking all lenses in each bin. We compare the ESDs of the four bins in satellite stellar mass for the spec and spec+RS samples. The signals from the two samples are consistent at the scales where the subhalo dominates, $R \lesssim 100\,\mathrm{kpc}$. In more detail, the signal from the spec+RS sample is slightly lower than the signal from the spec sample at the smallest scales. This is expected, as in general the more massive galaxies have been targeted in the spectroscopic observations; this is reflected also in the average stellar masses listed in Table 6.1. We base our analysis is on the spec+RS sample, which contains a larger sample of lenses.

At intermediate scales, $0.3 \lesssim R/\mathrm{Mpc} \lesssim 2$, the two samples produce different signals. In particular, the signal from the spec+RS sample is higher. This is a consequence of the fact that we only include red sequence galaxies out to 1 Mpc, so the spec+RS sample is on average closer to the cluster centre than the spec sample. Therefore, the peak of the host cluster signal happens at smaller R. Beyond the peak the two signals are consistent, because all galaxies come from the same clusters. See Figure 5.3 for a graphical representation.

6.5. Satellite galaxy-galaxy lensing model

We interpret the galaxy-galaxy lensing signal produced by subhaloes following the formalism introduced by Yang et al. (2006, see also Li et al. 2013a), and applied to observations by Li et al. (2014, 2016) and in **Chapter 5**. This formalism assumes that measurements are averages over a large number of satellites *and* clusters, such that the stacked cluster is (to a sufficient approximation) point-symmetric around their centres and well-described by a given parametrization of the density profile. A similar method was introduced by Pastor Mira et al. (2011), which however does not rely on such parametrization by virtue of subtracting the signal at the opposite point in the host cluster. A different approach is to perform a maximum likelihood reconstruction of the lensing potential of cluster galaxies accounting for the cluster potential, which must be well known a priori (e.g., Natarajan & Kneib 1997; Geiger & Schneider 1998) or modelled simultaneously with the cluster galaxies (Limousin et al. 2005). This method has been applied in several observational studies (e.g., Natarajan et al. 1998, 2009; Limousin et al. 2007). By nature, however, this maximum likelihood approach is well-suited for studies of galaxies in single, rather than stacked, clusters. We discuss results from the literature using either method after presenting our analysis, in Section 6.6. In the following we describe our modelling of the satellite galaxy-galaxy lensing signal.

The ESD measured around a satellite galaxy is a combination of the contributions from the subhalo (including the galaxy itself) at small scales, and that from the host halo at larger scales,

$$\Delta\Sigma_{\rm sat}(R) = \Delta\Sigma_\star(R|m_\star) + \Delta\Sigma_{\rm sub}(R|m_{\rm bg}, c_{\rm sub}) + \Delta\Sigma_{\rm host}(R|M_{\rm h}, c_{\rm h}), \tag{6.13}$$

where $\Delta\Sigma_\star$ represents the contribution from baryons in the satellite galaxy, which we model as a point source contribution throughout, such that

$$\Delta\Sigma_\star(R|m_\star) = \frac{m_\star}{\pi R^2}. \tag{6.14}$$

Here, we take $m_\star$ to be the median stellar mass of all satellites in the corresponding sample (e.g., a given bin in satellite luminosity). In Equation 6.13, R refers to the lens-source separation in physical units; $m_{\rm bg}$ is the average subhalo mass (see below) and $c_{\rm sub}$ its concentration; and $M_{\rm h}$ and $c_{\rm h}$ are the average mass and concentration of the host clusters. In the remainder of this section we describe the other two components in Equation 6.13. Detailed, graphical descriptions of these components can be found in Yang et al. (2006), Li et al. (2013a) and **Chapter 5**.

6.5.1. Host cluster contribution

Numerical simulations reveal that the density profiles of dark matter haloes are well described by a Navarro-Frenk-White (NFW, Navarro et al. 1995) profile,

$$\rho_{\rm NFW}(r) = \frac{\delta_c\,\rho_{\rm m}}{r/r_{\rm s}\,(1+r/r_{\rm s})^2}, \tag{6.15}$$

where $\rho_{\rm m}(z) = 3H_0^2(1+z)^3\Omega_{\rm m}/(8\pi G)$ is the mean density of the Universe at redshift z and

$$\delta_c = \frac{200}{3}\,\frac{c^3}{\ln(1+c) - c/(1+c)}. \tag{6.16}$$

The two free parameters, $r_{\rm s}$ and $c \equiv r_{200}/r_{\rm s}$, are the scale radius and concentration of the profile, respectively. Stacked weak lensing measurements have shown that this theoretical profile is a good description, on average, of real galaxy clusters as well (Oguri et al. 2012; Umetsu et al. 2016). We therefore adopt this parametrization for the density profile of the host clusters.

The concentration parameter is typically anti-correlated with mass. This relation, referred to as $c(M)$ hereafter, has been the subject of several studies (e.g., Bullock et al. 2001; Duffy et al. 2008; Macciò et al. 2008; Prada et al. 2012; Dutton & Macciò 2014). Most of these studies parametrize the $c(M)$ relation as a power law with mass (and some with redshift as well), with the mass dependence being typically very weak. Since our sample covers relatively narrow ranges in both quantities (i.e., cluster mass and redshift), the exact function adopted is of relatively little importance. We therefore parametrize the mass-concentration relation as a power law with mass,

$$c_{\rm h}(M_{200,\rm h}) = a_{\rm c}\left(\frac{M_{200,\rm h}}{10^{15}\rm M_\odot}\right)^{b_{\rm c}} \tag{6.17}$$

where $M_{200,\rm h}$ is the host halo mass within $r_{200,\rm h}$, and $a_{\rm c}$ and $b_{\rm c}$ are free parameters that we marginalize over. As in **Chapter 5**, we account for the observed separations between the satellites and the cluster centre (which we assume to coincide with the BCG) in each observable bin to model the total host halo contribution to Equation 6.13.

6.5.2. Subhalo contribution

Although in numerical simulations satellite galaxies are heavily stripped by their host cluster, the effect on their density profile is not well established. For instance, Hayashi et al. (2003) found that, although tidal stripping removes mass in an outside-in fashion, tidal heating causes the subhalo to expand; the resulting density profile is similar in shape to that of a central galaxy (which has not been subject to tidal stripping). Similarly, Pastor Mira et al. (2011) found that the NFW profile is a better fit than truncated profiles for subhaloes in the Millenium Simulation (Springel et al. 2005), and that the reduction in mass produced by tidal stripping is reflected only as an overall decrease in the amplitude of the density profiles of subhaloes accreted earlier.

We therefore assume that the density profile of subhaloes can also be described by an NFW profile. However, we adopt the subhalo mass-concentration relation recently derived by Moliné et al. (2016), which depends on both the subhalo mass and its position within the halo,

$$c_{\rm sub}(m_{200}, x) = c_0\left(1 + \sum_{i=1}^{3}\left[a_i \log\left(\frac{m_{200}}{10^8\,h^{-1}\rm M_\odot}\right)\right]^i\right) \times \left[1 + b\log x\right], \tag{6.18}$$

where $x \equiv r_{\rm sat}/r_{\rm h,200}$ (defined in three-dimensional space), $c_0 = 19.9$, $a_i = \{-0.195, 0.089, 0.089\}$ and $b = -0.54$.

Note that the quantity m_{200} is used for mathematical convenience only, but is not well defined physically. Instead, we report subhalo masses within the radius at which the subhalo density matches the background density of the cluster at the distance of the subhalo in question (which we denote $r_{\rm bg}$), and refer to this mass simply as m. This radius $r_{\rm bg}$ scales roughly with cluster-centric distance as $r_{\rm bg} \propto (R_{\rm sat}/r_{200,\rm h})^{2/3}$ (see also Natarajan et al. 2007, for a comparison between m and m_{200}). The reported subhalo masses are therefore similar to those that would be measured by a subhalo finder based on local overdensities such as SUBFIND (Springel et al. 2001a).

Because the density profile is a steep function of cluster-centric distance, we take the most probable three-dimensional cluster-centric distance, $\langle r_{\rm sat}\rangle$, to be equal to the weighted average of the histogram of two-dimensional distances, $R_{\rm sat}$:

$$\langle r_{\rm sat}\rangle = \frac{\sum_i n(R_{{\rm sat},i})R_{{\rm sat},i}}{\sum_i n(R_{{\rm sat},i})}, \tag{6.19}$$

where the index i runs over bins of width $\Delta R_{\rm sat} = 0.1\,{\rm Mpc}$ (see Figure 6.2).

6.5.3. Fitting procedure

We fit the model presented above to the data using the affine-invariant Markov Chain Monte Carlo (MCMC) ensemble sampler EMCEE (Foreman-Mackey et al. 2013). This sampler uses a number of walkers (set here to 5000) which move through parameter space depending on the position of all other walkers at a particular step, using a Metropolis Hastings acceptance criterion (see Goodman & Weare 2010, for a detailed description). The loss function to be maximized is defined as

$$\mathscr{L} = \frac{1}{(2\pi)^{k^2/2}}\prod_{m=1}^{k}\prod_{n=1}^{k}\frac{1}{\sqrt{\det(C_{mn})}} \times \exp\left[-\frac{1}{2}(\mathbf{O}-\mathbf{E})_m^T C_{mn}^{-1}(\mathbf{O}-\mathbf{E})_n\right], \tag{6.20}$$

where $k=4$ is the number of bins into which the sample is split (i.e., stellar mass or cluster-centric distance bins); $\mathbf{O}$ and $\mathbf{E}$ are the observation data vector and the corresponding model predictions, respectively; C is the covariance matrix; $\det(\cdot)$ is the determinant operator; and the index pair (i,j) runs over data points in each bin (m,n). As implied by Equation 6.20, we account for the full covariance matrix, including the covariance both within and between observable bins.

We adopt flat priors for all parameters. For subhalo and host halo masses, the priors are non-zero over the ranges $10^7 \leq m/{\rm M}_\odot \leq 10^{15}$ and $10^{13} \leq M_{\rm h}/{\rm M}_\odot \leq 10^{16}$, respectively. We also adopt flat priors for the parameters characterizing the host density profile, in the ranges $0 \leq a_{\rm c} \leq 10$ and $-1 \leq b_{\rm c} \leq 1$.

6.6. The connection between mass and light in satellite galaxies

6.6.1. The subhalo-to-stellar mass relation

We first bin the sample by stellar mass, as shown in the top-left panel of Figure 6.2. The ESD of the four bins, along with the model fit, are shown in Figure 6.8. The model is a good description of the data. For reference, this model has $\chi^2 = 14.0$. Since there are 36 data points and 9 free parameters, there are nominally 26 degrees of freedom, but we caution that 'degrees of freedom' is ill-defined for nonlinear models with covariant data points (Andrae et al. 2010), so the interpretation of the χ^2 statistic is not straightforward. The best-fit masses resulting from this model are shown in Figure 6.9. We fit a power law relation between subhalo and stellar masses using the BCES $X_2|X_1$ estimator (Akritas & Bershady 1996), and find a sub-linear relation,

$$\frac{m_{\rm bg}}{{\rm M}_\odot} = 10^{11.89\pm0.07}\left(\frac{m_\star}{2\times10^{10}{\rm M}_\odot}\right)^{0.77\pm0.11}. \tag{6.21}$$

We remind the reader that this relation applies to the subhalo mass, $m_{\rm bg}$, within the radius $r_{\rm bg}$ where the subhalo density equals the host halo background density. If we replace $m_{\rm bg}$ with

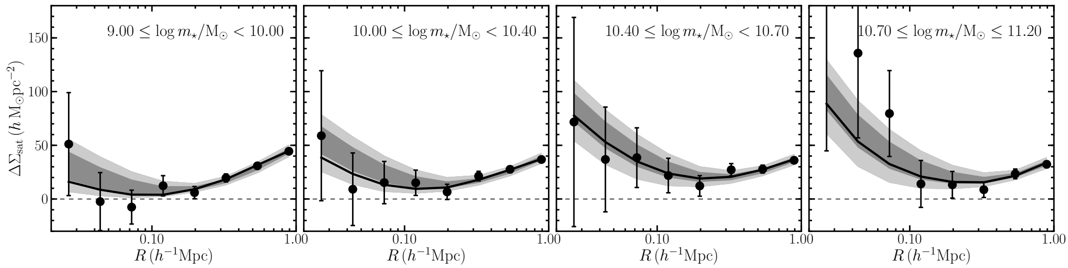

Figure 6.8: Excess surface mass density of the spec+RS sample, binned by stellar mass as shown in the legends (same as the black triangles in Figure 6.7). The black line shows the best-fitting model from the MCMC and the dark and light grey regions show the 68 and 95% credible intervals, respectively. The horizontal dashed line shows $\Delta\Sigma = 0$ for reference.

m_{200}, the normalization increases by a factor 2.45 but the best-fit slope is indistinguishable from that reported in Equation 6.21.

We also assess the robustness of the SHSMR to the parametrization of the $c(M)$ relation by adopting that of Duffy et al. (2008) instead of that of Moliné et al. (2016). The slope of the SHSMR is 0.75 ± 0.07, fully consistent with Equation 6.21. However, subhalo masses are then on average $(81 \pm 12)\%$ of those shown in Figure 6.9. Therefore while subhalo masses are somewhat dependent on the adopted $c(M)$ relation, the slope of the SHSMR is insensitive to it.

Rodríguez-Puebla et al. (2013) combined galaxy clustering measurements and abundance matching predictions to obtain the SHSMR[5] in galaxy groups, separating centrals from satellites a priori using the galaxy spectroscopic group catalogue of Yang et al. (2007). As shown in Figure 6.9, their results differ substantially from our measurements, underestimating the subhalo mass by almost an order of magnitude at approximately the pivot stellar mass $m_\star \sim 2 \times 10^{10}\,\mathrm{M}_\odot$. It may be that this difference arises because of the different halo masses probed in both works. To get a sense of this effect, we use the fact that the subhalo mass function, $n\,(m|M_\mathrm{h})$, depends on host halo mass such that the *normalized* subhalo mass function, $n\,(m/M_\mathrm{h})$ is universal, and the slope of the SHSMR quoted in Equation 6.21. The groups used by Rodríguez-Puebla et al. (2013) have typical masses slightly above $M_\mathrm{h} = 10^{13}\,\mathrm{M}_\odot$ (Yang et al. 2007), so the average subhalo could be up to 50 times more massive in the MENeaCS clusters. On the other hand, the SHSMR has a slope ~ 0.8, so we estimate "corrected" stellar masses through $m_{\star,1}/m_{\star,0} = (m_1/m_0)^{0.8} = 50^{0.8} \approx 23$ (where subscripts "0" and "1" refer to the original and adjusted masses, respectively). Therefore, the SHSMR should be increased by a factor $50/23 \approx 2.2$. As shown by the thin brown line in Figure 6.9, this correction significantly reduces the difference, and brings the results of Rodríguez-Puebla et al. (2013) in excellent agreement with measurements in EAGLE. (Note that EAGLE probes halo masses $M_\mathrm{h} \sim 10^{14}\,\mathrm{M}_\odot$, so the same argument would push the EAGLE SHSMR up by a factor 1.4.) Of course, this correction is inaccurate, and only meant to give a rough idea of the effect of halo mass. In particular, the correction assumes a constant slope for $m(m_\star)$ over the full stellar mass range, which is obviously not the case for the SHSMR of Rodríguez-Puebla et al. (2013).

We also show in Figure 6.9 various determinations of the stellar-to-halo mass relation

[5]Rodríguez-Puebla et al. (2013) used their measurements to fit for $m_\star(m)$, which due to intrinsic scatter cannot be directly inverted to obtain $m(m_\star)$. Instead, we invert it by Monte Carlo-sampling their relation, including intrinsic scatter, and binning the data points by $m_\star$.

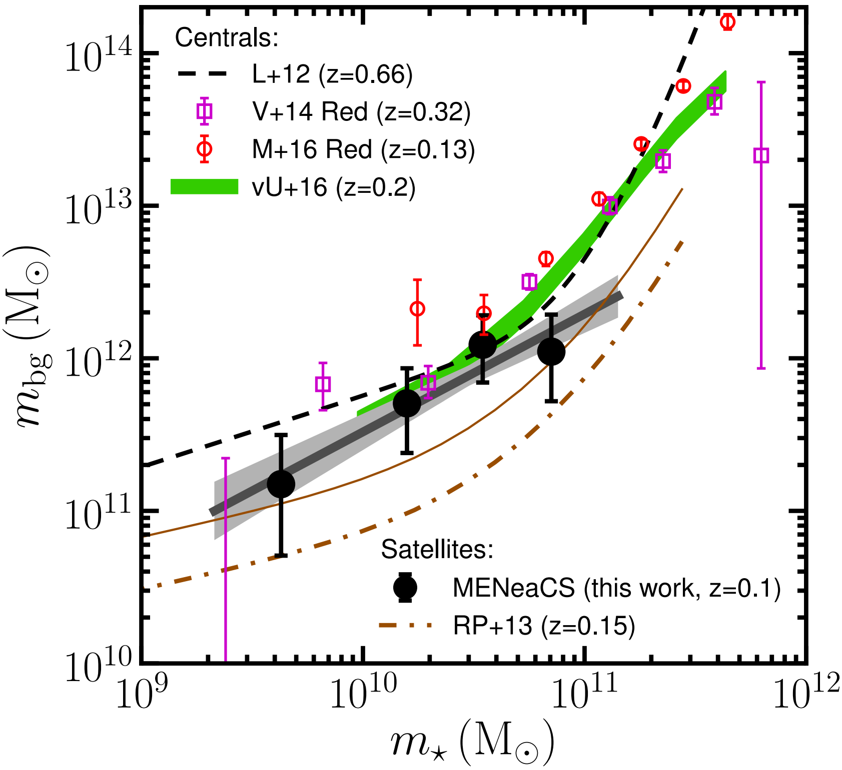

Figure 6.9: Stellar-to-subhalo mass relation. Black circles correspond to the best-fit subhalo masses of spectroscopic plus red sequence satellites, assuming the subhalo mass-concentration relation of Moliné et al. (2016). The grey line and shaded regions show the best-fit linear relation using the BCES $X_2|X_1$ estimator and the 68% confidence interval on the fit, respectively. Subhalo masses refer to the mass within $r_{\rm bg}$ (see Section 6.5.2). We show for comparison the subhalo-to-stellar mass relation of satellites in galaxy groups derived from clustering measurements applied to abundance matching by Rodríguez-Puebla et al. (2013), and the stellar-to-halo mass relations (where halo mass refers to $M_{200,\rm h}$) of central galaxies from galaxy-galaxy lensing measurements by Leauthaud et al. (2012) and van Uitert et al. (2016) and specifically of *red* central galaxies by Velander et al. (2014) and Mandelbaum et al. (2016). The thin brown line shows the SHSMR of Rodríguez-Puebla et al. (2013) boosted by a factor 2.2 to illustrate the effect of the different halo masses of groups used in that work.

(SHMR) of central galaxies from the literature (Leauthaud et al. 2012; Velander et al. 2014; Mandelbaum et al. 2016; van Uitert et al. 2016), where halo mass refers to $M_{200,\rm h}$.[6] These have all been determined with weak lensing measurements, and are broadly consistent with each other. Both Velander et al. (2014) and Mandelbaum et al. (2016) divided their samples into red and blue centrals, and we only show the results for red galaxies since MENeaCS satellites are in their great majority red as well (see van der Burg et al. 2015).

The comparison between the central SHMR and the satellite SHSMR is however not straightforward. In principle, we may consider in the case of central galaxies that $M_{\rm bg} = M_{200,\rm h}$, so at least the mass definitions are consistent. Even then, identifying the progenitors of present-day satellites is not an easy task, as there is evidence that most satellites in massive clusters today were part of smaller groups long before entering their current hosts. In the context of the decreased star formation of satellite galaxies, this is usually referred to as 'pre-

[6] We scale all these relations to the value of H_0 adopted in this work.

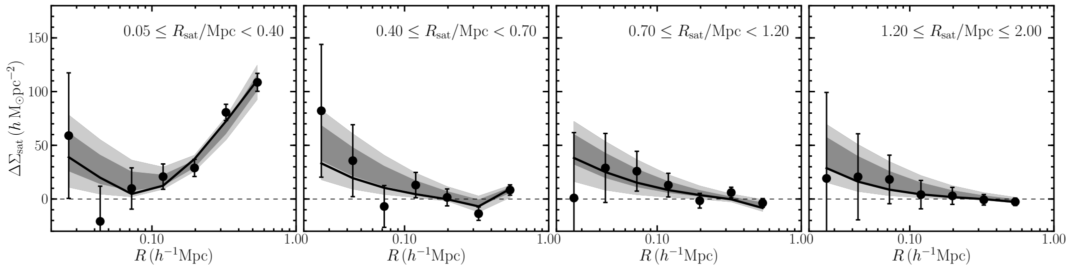

Figure 6.10: Excess surface mass density of satellites binned by cluster-centric distance as shown in the legends. Lines and symbols are the same as Figure 6.8.

processing' (e.g., McGee et al. 2009; Gabor & Davé 2015; Haines et al. 2015). The impact of this pre-processing on the total mass content of present-day satellites is not known.

The SHMR of central galaxies, like that of satellite galaxies derived by Rodríguez-Puebla et al. (2013), follows a broken power law, with a transition stellar mass of approximately $5 \times 10^{10}\,{\rm M_\odot}$. Given the few data points and the limited range in stellar mass covered here, a double power law fit is not justified, and we cannot place strong constraints on the shape of the SHSMR, beyond noting that a single power law is a good description given the current observational constraints.

6.6.2. Subhalo mass segregation

In this section we explore the dependence of subhalo mass and the ratio between total and stellar masses on the distance to the cluster centre. van den Bosch et al. (2016) have shown using N-body simulations that, even after collapsing the line-of-sight component, the projected halo-centric distance still preserves some of the correlation of subhalo physical parameters with the binding energy, which is closely related to the time a subhalo has spent in the halo. However, after multiple orbits the correlation is significantly reduced because at any particular (projected) distance from the halo centre there are subhaloes with a wide range of infall times. In an average sense, therefore, binning by cluster-centric distance, $R_{\rm sat}$, is binning by time since infall (although with very large uncertainties on the binning quantity). We might therefore expect satellites at similar $R_{\rm sat}$ to have been part of a similar halo-subhalo interaction. Hence the reason to bin by $R_{\rm sat}$ is to test whether we can infer a different degree of transformation for subhaloes in different bins.

Figure 6.10 shows the measured ESD and best-fit model when we split the satellite sample into four $R_{\rm sat}$ bins. Because of the finite extent of our data, we cannot draw full circles with large lens-source separations around most lenses, so additive biases do not cancel out. For this reason, in this section we only use measurements out to $R = 0.6$ Mpc. At larger separations the signal is dominated by the host clusters, with little to no contribution from the subhaloes, and we have verified that subhalo masses are not affected by this cut. The best-fit model shown in Figure 6.10 has $\chi^2 = 14.3$ with 17 'nominal' degrees of freedom (see discussion in Section 6.6.1). We also note that when binning by $m_\star$ as in Section 6.6.1, cluster-centric distances are mixed such that these biases effectively cancel out, and therefore large lens-source separations are not significantly affacted by the finite extent of our images.

van den Bosch et al. (2016) have also shown that the parameter that correlates most strongly with both binding energy and halo-centric distance is the ratio $m/m_{\rm acc}$, where $m_{\rm acc}$ is the mass of the subhalo at the time of its accretion onto the main halo. This is because

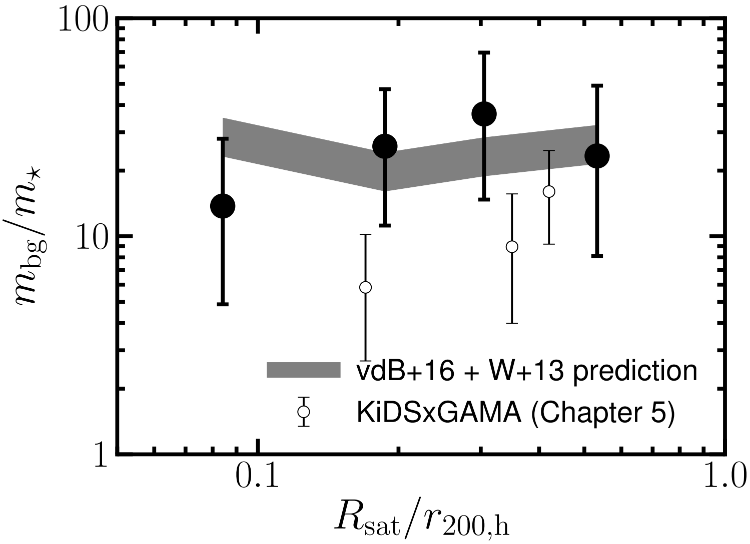

Figure 6.11: Best-fit subhalo-to-stellar mass ratio as a function of projected distance to the cluster centre, in units of the best-fit r_{200} of the host cluster. Small open circles show the results of **Chapter 5** for satellites in galaxy groups. Uncertainties show 68% credible intervals. As in Figure 6.9, all subhalo masses refer to the mass within $r_{\rm bg}$. The grey band shows a prediction for the total-to-stellar mass ratio from numerical simulations from van den Bosch et al. (2016), which give $m/m_{\rm acc}$ as a function of cluster-centric distance, combined with the $m_{\rm acc}(m_\star)$ predictions from Wang et al. (2013), taking the median stellar masses in each $R_{\rm sat}$ bin (cf. Table 6.1). The width of the grey band shows a 20% uncertainty on the model, adopted for illustration.

of the average relation between time a subhalo has spent in the host halo (or the accretion redshift, for a given redshift of observation) and the subhalo's distance to the halo centre, combined with the strong dependence of the mass ratio to the time since accretion as a result of tidal stripping.

We show the ratio of total (subhalo) mass to (galaxy) stellar mass as a function of cluster-centric distance in Figure 6.11. Consistent with **Chapter 5**, we find no statistically significant evidence for a dependence of $m_{\rm bg}/m_\star$ with $R_{\rm sat}$. The values obtained in **Chapter 5** are also shown for comparison, but note that they have been obtained under different assumptions for the concentration of subhaloes and their spatial extent (cf. Sections 5.3.3 and 6.5.2). To allow a fair comparison (which should nevertheless be taken with caution), we adjust the subhalo masses obtained in **Chapter 5** to be consistent with those reported in this Chapter. In **Chapter 5**, we adopted the mass-concentration relation of Duffy et al. (2008) for the density profiles of subhaloes. Following the discussion of the previous section, we divide the masses reported in **Chapter 5** by 0.81 to correct for the different concentrations. We also calculate $m_{\rm bg}$ for the subhaloes in **Chapter 5**, taking the best-fit host halo masses (cf. Table 5.2) and average group-centric distances (Table 5.1). At $R_{\rm sat} \sim 0.2 - 0.3\,\mathrm{Mpc}$, the total-to-stellar mass ratio in galaxy groups derived in **Chapter 5** is marginally smaller (at the $\sim 2\sigma$ level) than that in galaxy clusters derived here. This may point to a host halo mass dependence of the subhalo-to-stellar masses, but a definitive claim requires smaller errorbars.

We also show a prediction from numerical simulations and semi-analytic models. For this, we first use the average $m/m_{\rm acc}$ (where $m_{\rm acc}$ is the subhalo mass at the time of accretion) as a function of projected distance from van den Bosch et al. (2016).[7] We combine these predictions with the predictions for $m_{\rm acc}(m_\star)$ from Wang et al. (2013), assuming four different values for the stellar masses, given by the median masses for each bin quoted in Table 6.1, including a 20% uncertainty for illustration.[8] These predictions are in good agreement with our measurements, and show that we do not expect to see a trend with cluster-centric distance even when normalizing by stellar mass, if the stellar masses increase with $R_{\rm sat}$, as in our case (cf. Table 6.1 and Figure 6.2). Furthermore, any segregation at fixed stellar mass is too mild to be detected with current uncertainties. Several previous observational studies have focused on the mass segregation of subhaloes. However, differences in the adopted density profiles, mass definitions, and the fact that some works did not report the masses of the host clusters (nor normalized cluster-centric distance by host cluster size), preclude a detailed comparison with our results. To contextualize our results, we nevertheless compare these studies to the present one in a qualitative sense.

Using galaxy-galaxy lensing measurements of subhaloes in redMaPPer clusters (which have an average mass $M_{\rm h} \sim 10^{14}\,{\rm M}_\odot$; Rykoff et al. 2014), Li et al. (2016) found that the subhalo-to-stellar mass ratio increases by an order of magnitude from $R_{\rm sat} \sim 0.2\,{\rm Mpc}$ to $R_{\rm sat} \sim 1\,{\rm Mpc}$, when assuming a truncated NFW density profile, marginalizing over both the truncation radius and the concentration. Their trend with projected distance is stronger than that found here and than that predicted by N-body simulations and semi-analytical models (Han et al. 2016, see also Figure 6.11). As hinted by the comparison of the present results with **Chapter 5**, this may be due to a dependence of the mass segregation on the mass of the host cluster, but again we note that the uncertainties in both our studies and in Li et al. (2016) also allow for both no segregation and no dependence on cluster mass. Interestingly, Roberts et al. (2015) found a strong dependence of the segregation of *stellar* mass on host cluster mass, such that galaxies in more massive clusters are not segregated. Note that the segregation in stellar mass measured by Roberts et al. (2015) is, as expected, opposite that suggested by Li et al. (2016) for the total-to-stellar mass ratio, because the former is not as prone to tidal stripping as it is to dynamical friction.

Okabe et al. (2014) measured the lensing signal of galaxy- and group-scale subhaloes in the Coma cluster using observations with the Subaru telescope. They found that, while subgroup-scale subhaloes (which they analyzed individually) are better fit by truncated profiles, a stack of individual luminous galaxies is well-fit by a simple NFW model like the one adopted in this work, with no discernible truncation radius. This suggests that, maybe, the stacking of subhaloes with varying truncation radii, produces an average signal in which a truncation radius is no longer discernible, consistent with the findings of Pastor Mira et al. (2011) using the Millenium simulation (Springel et al. 2005). However, this contrasts with the results of Natarajan et al. (1998, 2002, 2007, 2009) and Limousin et al. (2007), who found evidence for galaxy truncation when studying galaxies in a few galaxy clusters at $z = 0.2-0.6$. Moreover, these studies found significant evidence for smaller truncation radii (or, equivalently, more compact cores) in galaxies closer to the cluster centres. It is unclear whether the methodology itself allowed the latter set of authors to detect a truncation radius while our

[7]van den Bosch et al. (2016) used subhalo masses obtained by the subhalo finder ROCKSTAR (Behroozi et al. 2013), which uses phase-space information to determine the membership of dark matter particles to a given subhalo, and has been shown to give larger subhalo masses than SUBFIND, especially at low halo-centric radii (Knebe et al. 2013). Therefore the comparison between the predictions and observational results in Figure 6.11 should be done with care.

[8]Wang et al. (2013) report the $m_\star(m_{\rm acc})$, which because of intrinsic scatter cannot be directly inverted to obtain $m_{\rm acc}(m_\star)$. Instead, we obtain the latter by sampling the $m_\star(m_{\rm acc})$ relation including intrinsic scatter, and then taking the average $m_{\rm acc}$ when binning by $m_\star$.

Table 6.2: Marginalized posterior estimates of fits to the satellite lensing signal. Masses are in units of $\mathrm{M}_\odot$. Uncertainties correspond to 68% credible intervals. All parameters have flat priors, in the following ranges: $10^7 \leq m_{\mathrm{bg}}/\mathrm{M}_\odot \leq 10^{15}$, $10^{13} \leq M_{\mathrm{h}}/\mathrm{M}_\odot \leq 10^{16}$, $0 \leq a_{\mathrm{c}} \leq 10$ and $-1 \leq b_{\mathrm{c}} \leq 1$.

Observable	$\log\langle m_1\rangle$	$\log\langle m_2\rangle$	$\log\langle m_3\rangle$	$\log\langle m_4\rangle$	a_{c}	b_{c}	$\log\langle M_{\mathrm{h},1}\rangle$	$\log\langle M_{\mathrm{h},2}\rangle$	$\log\langle M_{\mathrm{h},3}\rangle$	$\log\langle M_{\mathrm{h},4}\rangle$
$m_\star$	$11.17^{+0.31}_{-0.47}$	$11.69^{+0.23}_{-0.32}$	$12.10^{+0.18}_{-0.23}$	$12.06^{+0.22}_{-0.30}$	$4.8^{+1.0}_{-1.2}$	$-0.73^{+0.38}_{-0.16}$	$15.33^{+0.30}_{-0.23}$	$15.23^{+0.34}_{-0.20}$	$15.39^{+0.32}_{-0.25}$	$15.54^{+0.29}_{-0.29}$
R_{sat}	$11.07^{+0.30}_{-0.45}$	$11.36^{+0.26}_{-0.37}$	$11.55^{+0.28}_{-0.39}$	$11.59^{+0.31}_{-0.46}$	$3.8^{+1.5}_{-1.5}$	$-0.13^{+0.27}_{-0.26}$	$15.20^{+0.27}_{-0.33}$	$15.88^{+0.09}_{-0.17}$	$15.60^{+0.30}_{-0.53}$	$15.69^{+0.23}_{-0.48}$

methodology is more limiting in this respect (see Section 6.1 for a discussion of the different formalisms) , or if the parametrization of the subhalo mass density profile has any influence on this discrepancy, as argued by Pastor Mira et al. (2011). We do note that the azimuthal averaging necessarily washes out anisotropic information which is in fact used by the maximum likelihood approach. We have verified that, even if we bin the sample into only two or three bins (rather than four), we still cannot constrain the shape of the density profiles, due to the hard limit imposed by obscuration by cluster members (Section 6.4). Since the papers above do not show the signal from which their results are derived, it is difficult to assess the origin of the different conclusions we reach compared to theirs. The papers by Natarajan et al. used Hubble Space Telescope observations, which opens up that the possibility that a measurement of the density profiles of subhaloes requires data taken from space. However, this is not the case of Limousin et al. (2007), who in fact also used CFHT data for their measurements. As shown in Figure 6.6, the source density drops to roughly 50% at a distance of 20 kpc (at $z = 0.1$) due to obscuration by cluster members. It is therefore unlikely that truncation radii of order 10–20 kpc, as measured by Limousin et al. (2007), can be detected directly with weak lensing measurements using ground-based observations, irrespective of the method employed. Subtracting the light of lens galaxies from the images before the source sample is constructed might improve small-scale measurements; we will explore this in future work.

6.6.3. Host clusters

As discussed in the previous sections, in modelling the satellite lensing signal we must model the contribution from the host halo as well, even if it has little impact on the subhalo masses. However, since our measurements extend at most to $R = 1\,\mathrm{Mpc}$, we cannot break the degeneracy between host mass and concentration. Nevertheless, we list for completeness the best-fit values for the host clusters in Table 6.2. When binning by stellar mass, the best-fit power law for the concentration is significantly steeper than the values $b_\mathrm{c} \sim -0.1$ suggested by numerical simulations (e.g., Duffy et al. 2008; Dutton & Macciò 2014), but this is due to the strong degeneracy of the concentration with mass, which pushes the average masses to unrealistically large values. As shown in **Chapter 5**, the mass and concentration of the host clusters produce different changes in the satellite lensing signal, which are easily discernible if the measurements extend beyond the turnover of the host signal (at $R \gtrsim 2\,\mathrm{Mpc}$ for massive clusters). Since this is not our case, our data can accomodate varying values for both concentrations (which change the slope of the increase in signal at intermediate scales) and masses (which reflect as an overall normalization at intermediate to large scales). These uncertainties in the parameters of the density profile of host haloes has no significant impact on the constraints on subhalo masses.

6.7. Conclusions

We present the average masses of satellite galaxies in massive galaxy clusters at $0.05 < z < 0.15$ using weak galaxy-galaxy lensing measurements. We use a combination of deep, high-quality, wide-field observations of galaxy clusters (Sand et al. 2012) and extensive archival spectroscopic data (compiled in **Chapter 4**). Using extensive image simulations of bright lenses in the foreground of a population of field galaxies resembling the sources in the analysis, we model and account for biases arising from (i) shape measurements, due to confusion of light from the lens with the faint sources, and (ii) contamination of the source sample by faint cluster members (Section 6.4).

We model the lensing signal from subhaloes using an NFW profile and the subhalo mass-concentration relation measured from N-body simulations by Moliné et al. (2016), which depends on cluster-centric distance as well. We split the sample in bins of stellar mass and measure the subhalo-to-stellar mass relation (SHSMR) of galaxies in massive clusters. This is the first measurement of the SHSMR from weak lensing. Fitting the resulting masses with a power-law relation, we find $\log m_{\rm bg} = (11.73 \pm 0.05) + (0.77 \pm 0.11) \log m_\star$. The slope of this relation is robust to both the adopted subhalo mass-concentration relation and the subhalo mass definition. The SHSMR is broadly consistent with the corresponding relation for central galaxies, but a more detailed comparison requires the use of simulations.

We also study the masses of subhaloes at different cluster-centric distances with the aim of studying the evolution of subhaloes within clusters. Similar to recent results, we cannot constrain the truncation radii of subhaloes, while previous studies based on a different formalism have claimed significant detections. We also find no statistically significant evidence for mass segregation, consistent with recent results and with predictions from a combination of numerical simulations and semi-analytic models. Although direct comparison with the observational literature is complicated by the use of different definitions and conventions, the results of this chapter are consistent with **Chapter 5**, but most other works have found at least some evidence for mass segregation (e.g., Natarajan et al. 2002; Li et al. 2016). The origin of these discrepancies is not clear, and more work is needed to elucidate it.

Our measurements of mass segregation are broadly consistent with predictions from numerical simulations, while the SHSMR is almost an order of magnitude higher than that inferred from abundance matching applied to galaxy clustering measurements. A more detailed interpretation of our measurements in the context of these predictions requires a detailed analysis of hydrodynamic simulations, where both the satellites and their host haloes can be selected to match the observational situation. With these simulations we would also be able to test some assumptions of our model, most notably the concentration of the subhalo density profile, and reveal the origin of the observed connection between mass and light in cluster galaxies.

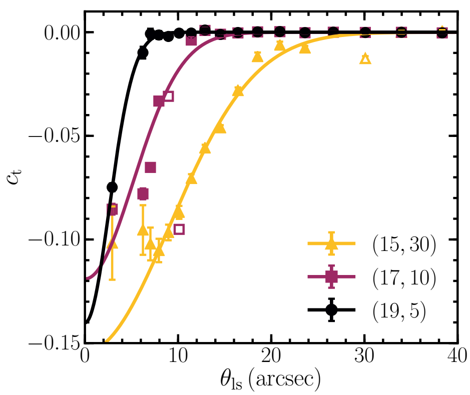

Figure 6.12: Tangential biases measured in three sets of image simulations. The legend shows the magnitude and size (in pixels) of each set. The three examples correspond to big bright (yellow triangles), average (brown squares), and small faint (black circles) simulated lenses, and illustrate the range of biases in our sample. The relevance of each set with respect to the real satellite galaxies can be seen in Figure 6.4. Data points with errorbars show measured tangential shear and solid lines show Gaussian fits to each set of simulations. Empty points are biased because they are adjacent the chosen truncation radius of the lenses, and are excluded from the fits.

6.A. Lens-induced bias on the shape measurements

Extended light from bright lens galaxies affects measurements of sources, such that their shapes are estimated to be more radially elongated than they really are. This induces a negative additive bias *in the coordinate frame of the lens galaxy*, which we label c_t.

In order to account for this bias we measure the shapes of galaxies in the image simulations of Hoekstra et al. (2015), after injecting bright lens galaxies in a grid pattern (separated by 1 arcmin from each other). These injected lenses are modelled as a Sérsic (1968) profile (i.e., $I(r) \propto r^{1/n}$) using GALSIM (Rowe et al. 2015), with a power-law index $n = 4$. Details about the simulated source population can be found in Hoekstra et al. (2015). The image simulations have a constant shear applied to them, which cancels out when we average shape measurements tangentially around the lenses. Therefore any measured shear in the tangential frame can be attributed to a bias induced by extended light from the lenses. The lenses we inject into the simulations span the ranges $14 \le m_{\rm phot} \le 20$ and $3 \le s_{\rm eff}/{\rm pix} \le 40$ (corresponding to $0.''55 \le s_{\rm eff} \le 7.''40$), and are compared to the magnitude and size distribution (as measured with GALFIT in **Chapter 4**) in the MENeaCS data in Figure 6.4.

We show the measured c_t for three sample sets of simulations in Figure 6.12. We find that the bias profiles can be well modelled in each bin as a Gaussian centred at $\theta_{\rm ls} = 0$,

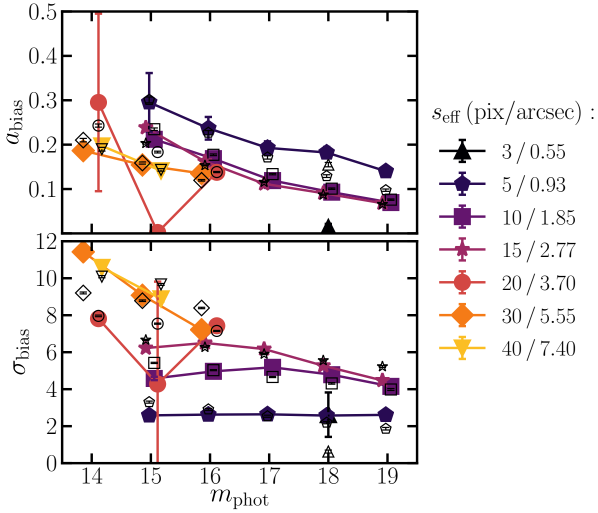

Figure 6.13: Amplitude and width of Gaussian fits to the additive bias c_t (solid symbols), and the results from an overall fit to each panel given in Equation 6.23 (empty symbols). Solid lines connect simulation sets with the same half-light radius as shown in the legend.

$$c_t(\theta_{\rm ls}) = a_{\rm bias} \exp\left[\frac{-\theta^2}{2\sigma^2_{\rm bias}}\right]. \tag{6.22}$$

We then fit the best-fit parameters $a_{\rm bias}$ and $\sigma_{\rm bias}$ as functions of lens magnitude and size,

$$\begin{aligned} a_{\rm bias} &= -0.81 - 1.22(m_{\rm phot} - 16) - 0.36\log(s_{\rm eff}/15\,{\rm pix}), \\ \sigma_{\rm bias} &= 6.27 - 14.01\log(m_{\rm phot}/16) + 7.04\log(s_{\rm eff}/15\,{\rm pix}). \end{aligned} \tag{6.23}$$

Figure 6.13 shows the best-fit individual values of $a_{\rm bias}$ and $\sigma_{\rm bias}$ and the values predicted by Equation 6.23. While at face value Equation 6.23 is not a good description of the measurements in the simulations for the full $(m_{\rm phot}, s_{\rm eff})$ space (and especially for $\sigma_{\rm bias}$), the discrepancy is limited to the extremes of this space. One notable discrepancy is roughly a 25% difference in the prediction of $\sigma_{\rm bias}$ for $(m_{\rm phot}, s_{\rm eff}) = (14, 30)$ (here, sizes are given in pixels). However, as shown in Figure 6.4, this combination of magnitude and size accounts for much less than 1% of the lenses in our sample. The other notable difference happens at $(m_{\rm phot}, s_{\rm eff}) = (18, 3)$, but the bias introduced by such small, faint galaxies is negligible to start with. Moreover, as can be seen in Figure 6.13, the difference arises because of the degeneracy between the amplitude and width of the Gaussian, such that the predicted bias is negligible as well.

Bibliography

Abazajian K. N., et al., 2009, ApJS, 182, 543
Abell G. O., 1958, ApJS, 3, 211
Abraham R. G., Yee H. K. C., Ellingson E., Carlberg R. G., Gravel P., 1998, ApJS, 116, 231
Afshordi N., 2008, ApJ, 686, 201
Agustsson I., Brainerd T. G., 2006, ApJL, 644, L25
Ahn C. P., et al., 2012, ApJS, 203, 21
Ahn C. P., et al., 2014, ApJS, 211, 17
Aihara H., et al., 2011, ApJS, 193, 29
Akritas M. G., Bershady M. A., 1996, ApJ, 470, 706
Alam S., et al., 2015, ApJS, 219, 12
Allen S. W., Evrard A. E., Mantz A. B., 2011, ARA&A, 49, 409
Alpher R. A., Bethe H., Gamow G., 1948, Physical Review, 73, 803
Altay G., Colberg J. M., Croft R. A. C., 2006, MNRAS, 370, 1422
Andersson K., et al., 2011, ApJ, 738, 48
Andrae R., Schulze-Hartung T., Melchior P., 2010, preprint, (arXiv:1012.3754)
Andreon S., 2015, A&A, 582, A100
Andreon S., de Propris R., Puddu E., Giordano L., Quintana H., 2008, MNRAS, 383, 102
Annis J., et al., 2014, ApJ, 794, 120
Applegate D. E., et al., 2014, MNRAS, 439, 48
Arnaud M., Pratt G. W., Piffaretti R., Böhringer H., Croston J. H., Pointecouteau E., 2010, A&A, 517, A92
Baier F. W., Godłowski W., MacGillivray H. T., 2003, A&A, 403, 847
Baldry I. K., et al., 2010, MNRAS, 404, 86
Balestra I., et al., 2010, A&A, 512, A12
Balogh M. L., et al., 2016, MNRAS, 456, 4364
Baltz E. A., Marshall P., Oguri M., 2009, JCAP, 1, 015
Barrena R., Boschin W., Girardi M., Spolaor M., 2007, A&A, 469, 861
Barrena R., Girardi M., Boschin W., Dasí M., 2009, A&A, 503, 357
Barrena R., Girardi M., Boschin W., de Grandi S., Eckert D., Rossetti M., 2011, A&A, 529, A128
Barrena R., Girardi M., Boschin W., 2013, MNRAS, 430, 3453
Battaglia N., Bond J. R., Pfrommer C., Sievers J. L., 2012, ApJ, 758, 74
Battaglia N., et al., 2016, JCAP, 8, 013
Becker R. H., White R. L., Helfand D. J., 1995, ApJ, 450, 559
Beers T. C., Flynn K., Gebhardt K., 1990, AJ, 100, 32

Behroozi P. S., Wechsler R. H., Wu H.-Y., 2013, ApJ, 762, 109

Belloni P., Roeser H.-J., 1996, A&AS, 118, 65

Benítez N., 2000, ApJ, 536, 571

Benjamin J., et al., 2013, MNRAS, 431, 1547

Benson B. A., et al., 2013, ApJ, 763, 147

Bernstein G. M., Norberg P., 2002, AJ, 124, 733

Bertin E., 2012, in Ballester P., Egret D., Lorente N. P. F., eds, Astronomical Society of the Pacific Conference Series Vol. 461, Astronomical Data Analysis Software and Systems XXI. p. 263

Bertin E., Arnouts S., 1996, A&AS, 117, 393

Bertin E., Mellier Y., Radovich M., Missonnier G., Didelon P., Morin B., 2002, in Bohlender D. A., Durand D., Handley T. H., eds, Astronomical Society of the Pacific Conference Series Vol. 281, Astronomical Data Analysis Software and Systems XI. p. 228

Binggeli B., 1982, A&A, 107, 338

Binney J., Tremaine S., 1987, Galactic dynamics

Biviano A., Murante G., Borgani S., Diaferio A., Dolag K., Girardi M., 2006, A&A, 456, 23

Blanton M. R., et al., 2003, ApJ, 592, 819

Blazek J., Mandelbaum R., Seljak U., Nakajima R., 2012, JCAP, 5, 041

Bleem L. E., et al., 2015, ApJS, 216, 27

Blumenthal G. R., Faber S. M., Primack J. R., Rees M. J., 1984, Nature, 311, 517

Bocquet S., et al., 2015, ApJ, 799, 214

Böhringer H., et al., 2010, A&A, 514, A32

Bonamente M., Joy M., LaRoque S. J., Carlstrom J. E., Nagai D., Marrone D. P., 2008, ApJ, 675, 106

Boschin W., Girardi M., Barrena R., Biviano A., Feretti L., Ramella M., 2004, A&A, 416, 839

Boschin W., Barrena R., Girardi M., 2009, A&A, 495, 15

Bower R. G., Benson A. J., Malbon R., Helly J. C., Frenk C. S., Baugh C. M., Cole S., Lacey C. G., 2006, MNRAS, 370, 645

Boylan-Kolchin M., Bullock J. S., Kaplinghat M., 2011, MNRAS, 415, L40

Braglia F. G., Pierini D., Biviano A., Böhringer H., 2009, A&A, 500, 947

Brainerd T. G., Blandford R. D., Smail I., 1996, ApJ, 466, 623

Bridle S., King L., 2007, New Journal of Physics, 9, 444

Brinchmann J., Charlot S., White S. D. M., Tremonti C., Kauffmann G., Heckman T., Brinkmann J., 2004, MNRAS, 351, 1151

Brown M. L., Taylor A. N., Hambly N. C., Dye S., 2002, MNRAS, 333, 501

Bruzual G., Charlot S., 2003, MNRAS, 344, 1000

Bullock J. S., Kolatt T. S., Sigad Y., Somerville R. S., Kravtsov A. V., Klypin A. A., Primack J. R., Dekel A., 2001, MNRAS, 321, 559

Burgh E. B., Nordsieck K. H., Kobulnicky H. A., Williams T. B., O'Donoghue D., Smith M. P., Percival J. W., 2003, in Iye M., Moorwood A. F. M., eds, SPIEVol. 4841, Instrument Design and Performance for Optical/Infrared Ground-based Telescopes. pp 1463–1471, doi:10.1117/12.460312

Cacciato M., van den Bosch F. C., More S., Li R., Mo H. J., Yang X., 2009, MNRAS, 394, 929

Cacciato M., van den Bosch F. C., More S., Mo H., Yang X., 2013, MNRAS, 430, 767

Carlberg R. G., 1994, ApJ, 433, 468

Catelan P., Kamionkowski M., Blandford R. D., 2001, MNRAS, 320, L7

Cava A., et al., 2009, A&A, 495, 707

Chabrier G., 2003, PASP, 115, 763

Chang J., Macciò A. V., Kang X., 2013a, MNRAS, 431, 3533

Chang C., et al., 2013b, MNRAS, 434, 2121

Chang Y.-Y., van der Wel A., da Cunha E., Rix H.-W., 2015, ApJS, 219, 8

Chisari N. E., Mandelbaum R., Strauss M. A., Huff E. M., Bahcall N. A., 2014, MNRAS, 445, 726
Christlein D., Zabludoff A. I., 2003, ApJ, 591, 764
Ciotti L., Dutta S. N., 1994, MNRAS, 270, 390
Clowe D., Luppino G. A., Kaiser N., Henry J. P., Gioia I. M., 1998, ApJL, 497, L61
Colín P., Klypin A. A., Kravtsov A. V., 2000, ApJ, 539, 561
Colless M., et al., 2001, MNRAS, 328, 1039
Colless M., et al., 2003, ArXiv Astrophysics e-prints,
Comparat J., et al., 2013, MNRAS, 433, 1146
Condon J. J., Cotton W. D., Greisen E. W., Yin Q. F., Perley R. A., Taylor G. B., Broderick J. J., 1998, AJ, 115, 1693
Contini E., De Lucia G., Borgani S., 2012, MNRAS, 420, 2978
Cooray A., Hu W., 2001, ApJ, 554, 56
Courteau S., et al., 2014, Reviews of Modern Physics, 86, 47
Coziol R., Andernach H., Caretta C. A., Alamo-Martínez K. A., Tago E., 2009, AJ, 137, 4795
Crawford S. M., et al., 2010, in Observatory Operations: Strategies, Processes, and Systems III. p. 773725, doi:10.1117/12.857000
Crawford S. M., Wirth G. D., Bershady M. A., Hon K., 2011, ApJ, 741, 98
Czoske O., Kneib J.-P., Soucail G., Bridges T. J., Mellier Y., Cuillandre J.-C., 2001, A&A, 372, 391
Danese L., de Zotti G., di Tullio G., 1980, A&A, 82, 322
Dekel A., 1985, ApJ, 298, 461
Dicke R. H., Peebles P. J. E., Roll P. G., Wilkinson D. T., 1965, ApJ, 142, 414
Dietrich J. P., Clowe D. I., Soucail G., 2002, A&A, 394, 395
Djorgovski S., 1983, ApJL, 274, L7
Dressler A., 1980, ApJ, 236, 351
Dressler A., Gunn J. E., 1992, ApJS, 78, 1
Dressler A., Shectman S. A., 1988, AJ, 95, 985
Dressler A., Smail I., Poggianti B. M., Butcher H., Couch W. J., Ellis R. S., Oemler Jr. A., 1999, ApJS, 122, 51
Drinkwater M. J., et al., 2010, MNRAS, 401, 1429
Driver S. P., et al., 2011, MNRAS, 413, 971
Duffy A. R., Schaye J., Kay S. T., Dalla Vecchia C., 2008, MNRAS, 390, L64
Dünner R., et al., 2013, ApJ, 762, 10
Durret F., Felenbok P., Lobo C., Slezak E., 1998, A&AS, 129, 281
Dutton A. A., Macciò A. V., 2014, MNRAS, 441, 3359
Ebeling H., Edge A. C., Henry J. P., 2001, ApJ, 553, 668
Ebeling H., Ma C.-J., Barrett E., 2014, ApJS, 211, 21
Eddington A. S., 1913, MNRAS, 73, 359
Einasto J., 2013, Brazilian Journal of Physics, 43, 369
Ellingson E., Yee H. K. C., Abraham R. G., Morris S. L., Carlberg R. G., Smecker-Hane T. A., 1997, ApJS, 113, 1
Erben T., et al., 2013, MNRAS, 433, 2545
Evrard A. E., 1989, ApJL, 341, L71
Evrard A. E., et al., 2008, ApJ, 672, 122
Evrard A. E., Arnault P., Huterer D., Farahi A., 2014, MNRAS, 441, 3562
Fadda D., Girardi M., Giuricin G., Mardirossian F., Mezzetti M., 1996, ApJ, 473, 670
Fahlman G., Kaiser N., Squires G., Woods D., 1994, ApJ, 437, 56
Faltenbacher A., Diemand J., 2006, MNRAS, 369, 1698
Faltenbacher A., Hoffman Y., Gottlöber S., Yepes G., 2007a, MNRAS, 376, 1327
Faltenbacher A., Li C., Mao S., van den Bosch F. C., Yang X., Jing Y. P., Pasquali A., Mo H. J.,

2007b, ApJL, 662, L71
Faltenbacher A., Jing Y. P., Li C., Mao S., Mo H. J., Pasquali A., van den Bosch F. C., 2008, ApJ, 675, 146
Feretti L., Giovannini G., Govoni F., Murgia M., 2012, A&ARv, 20, 54
Ferrari C., Maurogordato S., Cappi A., Benoist C., 2003, A&A, 399, 813
Fisher D., Fabricant D., Franx M., van Dokkum P., 1998, ApJ, 498, 195
Foreman-Mackey D., Hogg D. W., Lang D., Goodman J., 2013, PASP, 125, 306
Fowler J. W., et al., 2007, ApOpt, 46, 3444
Frenk C. S., White S. D. M., 2012, Annalen der Physik, 524, 507
Frenk C. S., Evrard A. E., White S. D. M., Summers F. J., 1996, ApJ, 472, 460
Gabor J. M., Davé R., 2015, MNRAS, 447, 374
Gao L., White S. D. M., Jenkins A., Stoehr F., Springel V., 2004, MNRAS, 355, 819
Geiger B., Schneider P., 1998, MNRAS, 295, 497
Geller M. J., Hwang H. S., Diaferio A., Kurtz M. J., Coe D., Rines K. J., 2014, ApJ, 783, 52
George M. R., et al., 2012, ApJ, 757, 2
Ghigna S., Moore B., Governato F., Lake G., Quinn T., Stadel J., 1998, MNRAS, 300, 146
Gifford D., Miller C., Kern N., 2013, ApJ, 773, 116
Gillis B. R., et al., 2013, MNRAS, 431, 1439
Gilmour R., Best P., Almaini O., 2009, MNRAS, 392, 1509
Girardi M., Giuricin G., Mardirossian F., Mezzetti M., Boschin W., 1998, ApJ, 505, 74
Girardi M., Barrena R., Boschin W., Ellingson E., 2008, A&A, 491, 379
Gladders M. D., Yee H. K. C., 2000, AJ, 120, 2148
Godłowski W., Baier F. W., MacGillivray H. T., 1998, A&A, 339, 709
Godłowski W., Piwowarska P., Panko E., Flin P., 2010, ApJ, 723, 985
Goodman J., Weare J., 2010, Communications in Applied Mathematics and Computational Science, 5, 65
Gruen D., et al., 2014, MNRAS, 442, 1507
Gunn J. E., Gott III J. R., 1972, ApJ, 176, 1
Guo H., et al., 2015a, MNRAS, 446, 578
Guo H., et al., 2015b, MNRAS, 453, 4368
Guth A. H., 1981, PhRvD, 23, 347
Haines C. P., et al., 2013, ApJ, 775, 126
Haines C. P., et al., 2015, ApJ, 806, 101
Halkola A., Seitz S., Pannella M., 2007, ApJ, 656, 739
Hall A., Taylor A., 2014, MNRAS, 443, L119
Han J., Cole S., Frenk C. S., Jing Y., 2016, MNRAS, 457, 1208
Hao J., et al., 2009, ApJ, 702, 745
Hao J., et al., 2010, ApJS, 191, 254
Hao J., Kubo J. M., Feldmann R., Annis J., Johnston D. E., Lin H., McKay T. A., 2011, ApJ, 740, 39
Hasselfield M., et al., 2013, JCAP, 7, 008
Hawley D. L., Peebles P. J. E., 1975, AJ, 80, 477
Hayashi E., Navarro J. F., Taylor J. E., Stadel J., Quinn T., 2003, ApJ, 584, 541
Heymans C., Heavens A., 2003, MNRAS, 339, 711
Heymans C., Brown M., Heavens A., Meisenheimer K., Taylor A., Wolf C., 2004, MNRAS, 347, 895
Heymans C., et al., 2006a, MNRAS, 368, 1323
Heymans C., et al., 2006b, MNRAS, 371, L60
Heymans C., et al., 2012, MNRAS, 427, 146
Heymans C., et al., 2013, MNRAS, 432, 2433

High F. W., Stubbs C. W., Rest A., Stalder B., Challis P., 2009, AJ, 138, 110

High F. W., et al., 2010, ApJ, 723, 1736

Hildebrandt H., et al., 2012, MNRAS, 421, 2355

Hill J. M., Oegerle W. R., 1993, AJ, 106, 831

Hilton M., et al., 2013, MNRAS, 435, 3469

Hirata C. M., Seljak U., 2004, PhRvD, 70, 063526

Hirata C. M., Mandelbaum R., Ishak M., Seljak U., Nichol R., Pimbblet K. A., Ross N. P., Wake D., 2007, MNRAS, 381, 1197

Hoekstra H., 2007, MNRAS, 379, 317

Hoekstra H., Franx M., Kuijken K., Squires G., 1998, ApJ, 504, 636

Hoekstra H., Franx M., Kuijken K., 2000, ApJ, 532, 88

Hoekstra H., Hsieh B. C., Yee H. K. C., Lin H., Gladders M. D., 2005, ApJ, 635, 73

Hoekstra H., Mahdavi A., Babul A., Bildfell C., 2012, MNRAS, 427, 1298

Hoekstra H., Herbonnet R., Muzzin A., Babul A., Mahdavi A., Viola M., Cacciato M., 2015, MNRAS, 449, 685

Hook I. M., Jørgensen I., Allington-Smith J. R., Davies R. L., Metcalfe N., Murowinski R. G., Crampton D., 2004, PASP, 116, 425

Hopkins A. M., et al., 2003, ApJ, 599, 971

Hubble E. P., 1925, Popular Astronomy, 33

Hubble E. P., 1929, Proceedings of the National Academy of Science, 15, 168

Huchra J. P., et al., 2012, ApJS, 199, 26

Hudson M. J., et al., 2015, MNRAS, 447, 298

Hui L., Zhang J., 2002, ArXiv Astrophysics e-prints,

Hung C.-L., Ebeling H., 2012, MNRAS, 421, 3229

Jäger K., Ziegler B. L., Böhm A., Heidt J., Möllenhoff C., Hopp U., Mendez R. H., Wagner S., 2004, A&A, 422, 907

Jee M. J., Hoekstra H., Mahdavi A., Babul A., 2014a, ApJ, 783, 78

Jee M. J., Hughes J. P., Menanteau F., Sifón C., Mandelbaum R., Barrientos L. F., Infante L., Ng K. Y., 2014b, ApJ, 785, 20

Jiang F., van den Bosch F. C., 2016, MNRAS, 458, 2848

Joachimi B., Bridle S. L., 2010, A&A, 523, A1

Joachimi B., Schneider P., 2008, A&A, 488, 829

Joachimi B., Schneider P., 2010, A&A, 517, A4

Joachimi B., Mandelbaum R., Abdalla F. B., Bridle S. L., 2011, A&A, 527, A26

Joachimi B., Semboloni E., Bett P. E., Hartlap J., Hilbert S., Hoekstra H., Schneider P., Schrabback T., 2013a, MNRAS, 431, 477

Joachimi B., Semboloni E., Hilbert S., Bett P. E., Hartlap J., Hoekstra H., Schneider P., 2013b, MNRAS, 436, 819

Jullo E., Kneib J.-P., Limousin M., Elíasdóttir Á., Marshall P. J., Verdugo T., 2007, New Journal of Physics, 9, 447

Kaiser N., 1992, ApJ, 388, 272

Kaiser N., Squires G., Broadhurst T., 1995, ApJ, 449, 460

Kassiola A., Kovner I., 1993, ApJ, 417, 450

Kelly P. L., et al., 2014, MNRAS, 439, 28

King I., 1962, AJ, 67, 471

King L. J., 2005, A&A, 441, 47

King L., Schneider P., 2002, A&A, 396, 411

Kirk D., Bridle S., Schneider M., 2010, MNRAS, 408, 1502

Kirk D., Rassat A., Host O., Bridle S., 2012, MNRAS, 424, 1647

Kirk B., et al., 2015, MNRAS, 449, 4010
Kitching T. D., Miller L., Heymans C. E., van Waerbeke L., Heavens A. F., 2008, MNRAS, 390, 149
Kitching T. D., et al., 2013, ApJS, 205, 12
Klypin A., Holtzman J., 1997, ArXiv Astrophysics e-prints,
Klypin A., Gottlöber S., Kravtsov A. V., Khokhlov A. M., 1999, ApJ, 516, 530
Knebe A., et al., 2013, MNRAS, 435, 1618
Kneib J.-P., 1993, PhD thesis, Ph. D. thesis, Université Paul Sabatier, Toulouse, (1993)
Kneib J.-P., Natarajan P., 2011, A&ARv, 19, 47
Kneib J.-P., Ellis R. S., Smail I., Couch W. J., Sharples R. M., 1996, ApJ, 471, 643
Knowles K., et al., 2015, preprint, (arXiv:1506.01547)
Knuth K. H., 2006, ArXiv Physics e-prints,
Krause E., Pierpaoli E., Dolag K., Borgani S., 2012, MNRAS, 419, 1766
Kriek M., van Dokkum P. G., Labbé I., Franx M., Illingworth G. D., Marchesini D., Quadri R. F., 2009, ApJ, 700, 221
Kuhlen M., Diemand J., Madau P., 2007, ApJ, 671, 1135
Kuijken K., 2008, A&A, 482, 1053
Kuijken K., et al., 2015, MNRAS, 454, 3500
Kurtz M. J., Mink D. J., 1998, PASP, 110, 934
Lacey C. G., et al., 2015, preprint, (arXiv:1509.08473)
Lamareille F., 2010, A&A, 509, A53
Larson R. B., Tinsley B. M., Caldwell C. N., 1980, ApJ, 237, 692
Lau E. T., Nagai D., Kravtsov A. V., 2010, ApJ, 708, 1419
Laureijs R., et al., 2011, preprint, (arXiv:1110.3193)
Leauthaud A., et al., 2012, ApJ, 744, 159
Li R., Mo H. J., Fan Z., Yang X., Bosch F. C. v. d., 2013a, MNRAS, 430, 3359
Li C., Wang L., Jing Y. P., 2013b, ApJL, 762, L7
Li R., et al., 2014, MNRAS, 438, 2864
Li R., et al., 2016, MNRAS, 458, 2573
Liang H., Lémonon L., Valtchanov I., Pierre M., Soucail G., 2000, A&A, 363, 440
Libeskind N. I., Di Cintio A., Knebe A., Yepes G., Gottlöber S., Steinmetz M., Hoffman Y., Martinez-Vaquero L. A., 2013, PASA, 30, e039
Lilly S. J., et al., 2007, ApJS, 172, 70
Limber D. N., 1953, ApJ, 117, 134
Limousin M., Kneib J.-P., Natarajan P., 2005, MNRAS, 356, 309
Limousin M., Kneib J. P., Bardeau S., Natarajan P., Czoske O., Smail I., Ebeling H., Smith G. P., 2007, A&A, 461, 881
Limousin M., Morandi A., Sereno M., Meneghetti M., Ettori S., Bartelmann M., Verdugo T., 2013, Space Sci. Rev., 177, 155
Lin Y.-T., Mohr J. J., 2004, ApJ, 617, 879
Lin H. W., McDonald M., Benson B., Miller E., 2015, ApJ, 802, 34
Lindner R. R., et al., 2014, ApJ, 786, 49
Liske J., et al., 2015, MNRAS, 452, 2087
Luppino G. A., Kaiser N., 1997, ApJ, 475, 20
Macciò A. V., Dutton A. A., van den Bosch F. C., 2008, MNRAS, 391, 1940
Magnier E. A., Cuillandre J.-C., 2004, PASP, 116, 449
Mahdavi A., Hoekstra H., Babul A., Bildfell C., Jeltema T., Henry J. P., 2013, ApJ, 767, 116
Mamon G. A., Biviano A., Murante G., 2010, A&A, 520, A30
Mancone C. L., Gonzalez A. H., 2012, PASP, 124, 606
Mandelbaum R., et al., 2005, MNRAS, 361, 1287

Mandelbaum R., Hirata C. M., Ishak M., Seljak U., Brinkmann J., 2006a, MNRAS, 367, 611
Mandelbaum R., Seljak U., Kauffmann G., Hirata C. M., Brinkmann J., 2006b, MNRAS, 368, 715
Mandelbaum R., et al., 2011, MNRAS, 410, 844
Mandelbaum R., Wang W., Zu Y., White S., Henriques B., More S., 2016, MNRAS, 457, 3200
Mantz A., Allen S. W., Rapetti D., Ebeling H., 2010, MNRAS, 406, 1759
Marriage T. A., et al., 2011a, ApJ, 731, 100
Marriage T. A., et al., 2011b, ApJ, 737, 61
Marrone D. P., et al., 2012, ApJ, 754, 119
Martel H., Robichaud F., Barai P., 2014, ApJ, 786, 79
Martini P., Mulchaey J. S., Kelson D. D., 2007, ApJ, 664, 761
Massey R., et al., 2007, MNRAS, 376, 13
Mauch T., Murphy T., Buttery H. J., Curran J., Hunstead R. W., Piestrzynski B., Robertson J. G., Sadler E. M., 2003, MNRAS, 342, 1117
Maurogordato S., et al., 2008, A&A, 481, 593
Maurogordato S., Sauvageot J. L., Bourdin H., Cappi A., Benoist C., Ferrari C., Mars G., Houairi K., 2011, A&A, 525, A79
McDonald M., et al., 2012, Nature, 488, 349
McFarland J. P., Verdoes-Kleijn G., Sikkema G., Helmich E. M., Boxhoorn D. R., Valentijn E. A., 2013, Experimental Astronomy, 35, 45
McGee S. L., Balogh M. L., Bower R. G., Font A. S., McCarthy I. G., 2009, MNRAS, 400, 937
Medezinski E., Broadhurst T., Umetsu K., Oguri M., Rephaeli Y., Benítez N., 2010, MNRAS, 405, 257
Melchior P., Viola M., 2012, MNRAS, 424, 2757
Mellier Y., 1999, ARA&A, 37, 127
Menanteau F., et al., 2010a, ApJS, 191, 340
Menanteau F., et al., 2010b, ApJ, 723, 1523
Menanteau F., et al., 2012, ApJ, 748, 7
Menanteau F., et al., 2013, ApJ, 765, 67
Meneghetti M., Fedeli C., Zitrin A., Bartelmann M., Broadhurst T., Gottlöber S., Moscardini L., Yepes G., 2011, A&A, 530, A17
Mercurio A., Girardi M., Boschin W., Merluzzi P., Busarello G., 2003, A&A, 397, 431
Miller N. A., Owen F. N., Hill J. M., Keel W. C., Ledlow M. J., Oegerle W. R., 2004, ApJ, 613, 841
Miller N. A., Oegerle W. R., Hill J. M., 2006, AJ, 131, 2426
Miller L., Kitching T. D., Heymans C., Heavens A. F., van Waerbeke L., 2007, MNRAS, 382, 315
Miller L., et al., 2013, MNRAS, 429, 2858
Miyatake H., et al., 2013, MNRAS, 429, 3627
Mo H., van den Bosch F. C., White S., 2010, Galaxy Formation and Evolution
Moliné Á., Sánchez-Conde M. A., Palomares-Ruiz S., Prada F., 2016, preprint, (`arXiv:1603.04057`)
Moore B., Katz N., Lake G., Dressler A., Oemler A., 1996, Nature, 379, 613
Moore B., Ghigna S., Governato F., Lake G., Quinn T., Stadel J., Tozzi P., 1999, ApJL, 524, L19
Morandi A., Pedersen K., Limousin M., 2010, ApJ, 713, 491
More S., van den Bosch F. C., Cacciato M., Skibba R., Mo H. J., Yang X., 2011, MNRAS, 410, 210
Motl P. M., Hallman E. J., Burns J. O., Norman M. L., 2005, ApJL, 623, L63
Munari E., Biviano A., Borgani S., Murante G., Fabjan D., 2013, MNRAS, 430, 2638
Muzzin A., et al., 2014, ApJ, 796, 65
Nagai D., 2006, ApJ, 650, 538
Natarajan P., Kneib J.-P., 1997, MNRAS, 287, 833
Natarajan P., Kneib J.-P., Smail I., Ellis R. S., 1998, ApJ, 499, 600
Natarajan P., Kneib J.-P., Smail I., 2002, ApJL, 580, L11

Natarajan P., De Lucia G., Springel V., 2007, MNRAS, 376, 180

Natarajan P., Kneib J.-P., Smail I., Treu T., Ellis R., Moran S., Limousin M., Czoske O., 2009, ApJ, 693, 970

Navarro J. F., Frenk C. S., White S. D. M., 1995, MNRAS, 275, 720

Nelson K., Rudd D. H., Shaw L., Nagai D., 2012, ApJ, 751, 121

Ng K. Y., Dawson W. A., Wittman D., Jee M. J., Hughes J. P., Menanteau F., Sifón C., 2015, MNRAS, 453, 1531

Niederste-Ostholt M., Strauss M. A., Dong F., Koester B. P., McKay T. A., 2010, MNRAS, 405, 2023

Norberg P., Baugh C. M., Gaztañaga E., Croton D. J., 2009, MNRAS, 396, 19

Ntampaka M., Trac H., Sutherland D. J., Fromenteau S., Poczos B., Schneider J., 2015a, preprint, (`arXiv:1509.05409`)

Ntampaka M., Trac H., Sutherland D. J., Battaglia N., Póczos B., Schneider J., 2015b, ApJ, 803, 50

Nulsen P. E. J., 1982, MNRAS, 198, 1007

Ochsenbein F., Bauer P., Marcout J., 2000, A&AS, 143, 23

Oegerle W. R., Hill J. M., Fitchett M. J., 1995, AJ, 110, 32

Oguri M., Bayliss M. B., Dahle H., Sharon K., Gladders M. D., Natarajan P., Hennawi J. F., Koester B. P., 2012, MNRAS, 420, 3213

Okabe N., Futamase T., Kajisawa M., Kuroshima R., 2014, ApJ, 784, 90

Okumura T., Jing Y. P., Li C., 2009, ApJ, 694, 214

Old L., Gray M. E., Pearce F. R., 2013, MNRAS, 434, 2606

Old L., et al., 2014, MNRAS, 441, 1513

Old L., et al., 2015, MNRAS, 449, 1897

Owers M. S., Nulsen P. E. J., Couch W. J., 2011, ApJ, 741, 122

Pacaud F., et al., 2007, MNRAS, 382, 1289

Panko E., Juszczyk T., Flin P., 2009, AJ, 138, 1709

Pastor Mira E., Hilbert S., Hartlap J., Schneider P., 2011, A&A, 531, A169

Peacock J. A., 2002, in Metcalfe N., Shanks T., eds, Astronomical Society of the Pacific Conference Series Vol. 283, A New Era in Cosmology. p. 19 (`arXiv:astro-ph/0204239`)

Peacock J. A., Smith R. E., 2000, MNRAS, 318, 1144

Pen U.-L., Lee J., Seljak U., 2000, ApJL, 543, L107

Peng C. Y., Ho L. C., Impey C. D., Rix H.-W., 2002, AJ, 124, 266

Penzias A. A., Wilson R. W., 1965, ApJ, 142, 419

Pereira M. J., Bryan G. L., 2010, ApJ, 721, 939

Pereira M. J., Kuhn J. R., 2005, ApJL, 627, L21

Pereira M. J., Bryan G. L., Gill S. P. D., 2008, ApJ, 672, 825

Perlmutter S., et al., 1999, ApJ, 517, 565

Pimbblet K. A., Smail I., Edge A. C., O'Hely E., Couch W. J., Zabludoff A. I., 2006, MNRAS, 366, 645

Pinkney J., Roettiger K., Burns J. O., Bird C. M., 1996, ApJS, 104, 1

Planck Collaboration 2011a, A&A, 536, A8

Planck Collaboration 2011b, A&A, 536, A9

Planck Collaboration 2011c, A&A, 536, A11

Planck Collaboration 2011d, A&A, 536, A12

Planck Collaboration 2013, A&A, 550, A129

Planck Collaboration 2014a, A&A, 571, A16

Planck Collaboration 2014b, A&A, 571, A29

Planck Collaboration 2015a, preprint, (`arXiv:1502.01589`)

Planck Collaboration 2015c, preprint, (arXiv:1502.01597)
Planck Collaboration 2015b, preprint, (arXiv:1502.01598)
Plionis M., Benoist C., Maurogordato S., Ferrari C., Basilakos S., 2003, ApJ, 594, 144
Poole G. B., Babul A., McCarthy I. G., Fardal M. A., Bildfell C. J., Quinn T., Mahdavi A., 2007, MNRAS, 380, 437
Prada F., Klypin A. A., Cuesta A. J., Betancort-Rijo J. E., Primack J., 2012, MNRAS, 423, 3018
Proust D., Cuevas H., Capelato H. V., Sodré Jr. L., Tomé Lehodey B., Le Fèvre O., Mazure A., 2000, A&A, 355, 443
Quintana H., Carrasco E. R., Reisenegger A., 2000, AJ, 120, 511
Reese E. D., et al., 2012, ApJ, 751, 12
Refregier A., Kacprzak T., Amara A., Bridle S., Rowe B., 2012, MNRAS, 425, 1951
Reichardt C. L., et al., 2013, ApJ, 763, 127
Reid B. A., Spergel D. N., 2006, ApJ, 651, 643
Richard J., Kneib J.-P., Limousin M., Edge A., Jullo E., 2010, MNRAS, 402, L44
Riebe K., et al., 2013, Astronomische Nachrichten, 334, 691
Riess A. G., et al., 1998, AJ, 116, 1009
Rines K., Geller M. J., Diaferio A., Kurtz M. J., 2013, ApJ, 767, 15
Rines K. J., Geller M. J., Diaferio A., Hwang H. S., 2016, ApJ, 819, 63
Roberts I. D., Parker L. C., Joshi G. D., Evans F. A., 2015, MNRAS, 448, L1
Robotham A. S. G., et al., 2011, MNRAS, 416, 2640
Rodríguez-Puebla A., Drory N., Avila-Reese V., 2012, ApJ, 756, 2
Rodríguez-Puebla A., Avila-Reese V., Drory N., 2013, ApJ, 767, 92
Romano-Díaz E., Shlosman I., Heller C., Hoffman Y., 2010, ApJ, 716, 1095
Rood H. J., Sastry G. N., 1972, AJ, 77, 451
Rowe B. T. P., et al., 2015, Astronomy and Computing, 10, 121
Rozo E., et al., 2010, ApJ, 708, 645
Rozo E., Rykoff E. S., Bartlett J. G., Evrard A., 2014a, MNRAS, 438, 49
Rozo E., Evrard A. E., Rykoff E. S., Bartlett J. G., 2014b, MNRAS, 438, 62
Rozo E., Rykoff E. S., Becker M., Reddick R. M., Wechsler R. H., 2015, MNRAS, 453, 38
Rubin V. C., Ford W. K. J., . Thonnard N., 1980, ApJ, 238, 471
Ruel J., et al., 2014, ApJ, 792, 45
Rykoff E. S., et al., 2012, ApJ, 746, 178
Rykoff E. S., et al., 2014, ApJ, 785, 104
Sand D. J., et al., 2012, ApJ, 746, 163
Sarazin C. L., 1986, Reviews of Modern Physics, 58, 1
Saro A., Mohr J. J., Bazin G., Dolag K., 2013, ApJ, 772, 47
Sastry G. N., 1968, PASP, 80, 252
Schechter P., 1976, ApJ, 203, 297
Schewtschenko J. A., Macciò A. V., 2011, MNRAS, 413, 878
Schlafly E. F., Finkbeiner D. P., 2011, ApJ, 737, 103
Schneider P., 2003, A&A, 408, 829
Schneider M. D., Bridle S., 2010, MNRAS, 402, 2127
Schneider M. D., et al., 2013, MNRAS, 433, 2727
Scoville N., et al., 2007, ApJS, 172, 38
Sehgal N., et al., 2011, ApJ, 732, 44
Sehgal N., et al., 2013, ApJ, 767, 38
Seljak U., 2000, MNRAS, 318, 203
Semboloni E., Hoekstra H., Schaye J., van Daalen M. P., McCarthy I. G., 2011, MNRAS, 417, 2020

Sérsic J. L., 1968, Atlas de galaxias australes
Shapley H., Curtis H. D., 1921, Bulletin of the National Research Council, Vol. 2, Part 3, No. 11, p. 171-217, 2, 171
Shaw L. D., Holder G. P., Bode P., 2008, ApJ, 686, 206
Sifón C., et al., 2013, ApJ, 772, 25
Skibba R. A., van den Bosch F. C., Yang X., More S., Mo H., Fontanot F., 2011, MNRAS, 410, 417
Skielboe A., Wojtak R., Pedersen K., Rozo E., Rykoff E. S., 2012, ApJL, 758, L16
Skrutskie M. F., et al., 2006, AJ, 131, 1163
Smith R. E., et al., 2003, MNRAS, 341, 1311
Soucail G., Mellier Y., Fort B., Cailloux M., 1988, A&AS, 73, 471
Spergel D. N., et al., 2003, ApJS, 148, 175
Springel V., 2005, MNRAS, 364, 1105
Springel V., White S. D. M., Tormen G., Kauffmann G., 2001a, MNRAS, 328, 726
Springel V., White M., Hernquist L., 2001b, ApJ, 549, 681
Springel V., et al., 2005, Nature, 435, 629
Springel V., et al., 2008, MNRAS, 391, 1685
Sunyaev R. A., Zel'dovich Y. B., 1972, Comments on Astrophysics and Space Physics, 4, 173
Sunyaev R. A., Zeldovich I. B., 1980, ARA&A, 18, 537
Suyu S. H., Halkola A., 2010, A&A, 524, A94
Swetz D. S., et al., 2011, ApJS, 194, 41
Taffoni G., Mayer L., Colpi M., Governato F., 2003, MNRAS, 341, 434
Taylor J. E., Babul A., 2005, MNRAS, 364, 535
Taylor E. N., et al., 2011, MNRAS, 418, 1587
Tenneti A., Mandelbaum R., Di Matteo T., Feng Y., Khandai N., 2014, MNRAS, 441, 470
Thompson L. A., 1976, ApJ, 209, 22
Tinker J. L., Robertson B. E., Kravtsov A. V., Klypin A., Warren M. S., Yepes G., Gottlöber S., 2010, ApJ, 724, 878
Tormen G., Diaferio A., Syer D., 1998, MNRAS, 299, 728
Trevese D., Cirimele G., Flin P., 1992, AJ, 104, 935
Trimble V., 1987, ARA&A, 25, 425
Trimble V., 1995, PASP, 107, 1133
Trimble V., 2012, The Observatory, 132, 33
Trimble V., 2013, preprint, (`arXiv:1307.2289`)
Troxel M. A., Ishak M., 2014, PhRvD, 89, 063528
Umetsu K., et al., 2014, ApJ, 795, 163
Umetsu K., Zitrin A., Gruen D., Merten J., Donahue M., Postman M., 2016, ApJ, 821, 116
VanderPlas J., Connolly A. J., Ivezic Z., Gray A., 2012, in Proceedings of Conference on Intelligent Data Understanding (CIDU), pp. 47-54, 2012.. pp 47–54 (`arXiv:1411.5039`), doi:10.1109/CIDU.2012.6382200
Vanzella E., et al., 2008, A&A, 478, 83
Velander M., et al., 2014, MNRAS, 437, 2111
Verdugo T., Motta V., Muñoz R. P., Limousin M., Cabanac R., Richard J., 2011, A&A, 527, A124
Vikhlinin A., et al., 2009, ApJ, 692, 1060
Viola M., Melchior P., Bartelmann M., 2011, MNRAS, 410, 2156
Viola M., Kitching T. D., Joachimi B., 2014, MNRAS, 439, 1909
Viola M., et al., 2015, MNRAS, 452, 3529
Wang L., De Lucia G., Weinmann S. M., 2013, MNRAS, 431, 600
Wen Z. L., Han J. L., 2013, MNRAS, 436, 275
White S. D. M., Rees M. J., 1978, MNRAS, 183, 341

White M., Cohn J. D., Smit R., 2010, MNRAS, 408, 1818
Wik D. R., Sarazin C. L., Ricker P. M., Randall S. W., 2008, ApJ, 680, 17
Williamson R., et al., 2011, ApJ, 738, 139
Wojtak R., Łokas E. L., Mamon G. A., Gottlöber S., Prada F., Moles M., 2007, A&A, 466, 437
Wright C. O., Brainerd T. G., 2000, ApJ, 534, 34
Wright E. L., et al., 2010, AJ, 140, 1868
Wu H.-Y., Hahn O., Evrard A. E., Wechsler R. H., Dolag K., 2013, MNRAS, 436, 460
Yang X., Mo H. J., van den Bosch F. C., Jing Y. P., Weinmann S. M., Meneghetti M., 2006, MNRAS, 373, 1159
Yang X., Mo H. J., van den Bosch F. C., Pasquali A., Li C., Barden M., 2007, ApJ, 671, 153
Yang X., Mo H. J., van den Bosch F. C., 2009, ApJ, 693, 830
Yee H. K. C., Ellingson E., Carlberg R. G., 1996, ApJS, 102, 269
Yee H. K. C., Ellingson E., Morris S. L., Abraham R. G., Carlberg R. G., 1998, ApJS, 116, 211
York D. G., et al., 2000, AJ, 120, 1579
Yu L., Nelson K., Nagai D., 2015, ApJ, 807, 12
Zel'dovich Y. B., Sunyaev R. A., 1969, Ap&SS, 4, 301
Zhang P., 2010a, MNRAS, 406, L95
Zhang P., 2010b, ApJ, 720, 1090
Zitrin A., Broadhurst T., Bartelmann M., Rephaeli Y., Oguri M., Benítez N., Hao J., Umetsu K., 2012, MNRAS, 423, 2308
Zitrin A., Menanteau F., Hughes J. P., Coe D., Barrientos L. F., Infante L., Mandelbaum R., 2013, ApJL, 770, L15
Zolotov A., et al., 2012, ApJ, 761, 71
Zwicky F., 1933, Helvetica Physica Acta, 6, 110
da Silva A. C., Kay S. T., Liddle A. R., Thomas P. A., 2004, MNRAS, 348, 1401
de Jong J. T. A., et al., 2013, The Messenger, 154, 44
de Jong J. T. A., et al., 2015, A&A, 582, A62
van Daalen M. P., Schaye J., Booth C. M., Dalla Vecchia C., 2011, MNRAS, 415, 3649
van Dokkum P. G., 2001, PASP, 113, 1420
van Kampen E., Rhee G. F. R. N., 1990, A&A, 237, 283
van Uitert E., Hoekstra H., Velander M., Gilbank D. G., Gladders M. D., Yee H. K. C., 2011, A&A, 534, A14
van Uitert E., et al., 2016, MNRAS,
van den Bosch F. C., Tormen G., Giocoli C., 2005, MNRAS, 359, 1029
van den Bosch F. C., More S., Cacciato M., Mo H., Yang X., 2013, MNRAS, 430, 725
van den Bosch F. C., Jiang F., Campbell D., Behroozi P., 2016, MNRAS, 455, 158
van der Burg R. F. J., et al., 2013, A&A, 557, A15
van der Burg R. F. J., Hoekstra H., Muzzin A., Sifón C., Balogh M. L., McGee S. L., 2015, A&A, 577, A19
von der Linden A., et al., 2014a, MNRAS, 439, 2
von der Linden A., et al., 2014b, MNRAS, 443, 1973

Nederlandse Samenvatting

Wij zijn maar een progressieve soort apen op een kleine planeet rond een zeer gewone ster. Maar wij kunnen het Universum begrijpen. Dat maakt ons iets speciaals.

– Stephen Hawking

Het weidse Universum

Een blik naar de nachtelijke hemel vertelt ons dat sterren niet willekeurig geplaatst zijn. Het merendeel van de sterren bevindt zich in een dunne streep aan de hemel. Deze streep heet de *Melkweg* en is het sterrenstelsel waar onze zon zich bevindt. Er wordt geschat dat de zon een van de 100 miljard sterren is die de Melkweg rijk is. Het linker paneel van Figuur 1 laat een typisch spiraal sterrenstelsel zien, Messier 81 genaamd, dat ongeveer 12 miljoen lichtjaar van ons af ligt. De karakteristieke blauwe kleur van spiraal stelsels wordt veroorzaakt door jonge sterren, die ongeveer 100 miljoen jaar geleden ontstaan zijn. Ons sterrenstelsel is een deel van de *Lokale Groep*, een conglomeraat van ongeveer 50 sterrenstelsels, waarvan de Melkweg en het Andromeda stelsel (ongeveer 2.5 miljoen lichtjaar verwijderd van de Melkweg) de grootsten zijn.

De meeste sterrenstelsels in het universum bevinden zich in zulk soort conglomeraten, waarvan de Lokale Groep een voorbeeld is. Per conventie worden verzamelingen van rond de 50 sterrenstelsels *groepen* genoemd en verzamelingen van meer dan dat, *clusters* van sterrenstelsels. Clusters zijn de grootste objecten die zich tot nu toe hebben gevormd in het universum. Zo'n cluster kan meer dan duizend zichtbare sterrenstelsels bevatten en een massa van 10^{15} (1.000.000.000.000.000) zonnen hebben. Het rechter paneel van Figuur 1 toont de cluster van sterrenstelsels Abell 2218 (ontdekt door Amerikaanse astronoom George Abell). Het plaatje toont grote getalen van (elliptische) rossige sterrenstelsels, waarvan de meesten toebehoren aan het cluster. Het cluster Abell 2218 bevindt zich ongeveer 2 miljard lichtjaar van ons af.

Sterrenstelsels in clusters lijken rossig in tegenstelling tot de blauwe spiraalvormige sterrenstelsels, die vooral op zichzelf te vinden zijn. De reden voor dit verschil ligt in de zwaartekracht van het cluster, het gas in het cluster en de grote hoeveelheid andere sterrenstelsels in het cluster. Deze drie ontnemen het gas van sterrenstelsels in het cluster, wat anders gebruikt zou worden om nieuwe sterren te vormen. Het gebrek aan nieuwe jonge blauwe sterren zorgt ervoor dat het stelsel de rode kleur van zijn oudere sterren aanneemt.

Donkere materie

De sterrenstelsels die wij zien, met hun sterren, gas en stof, en alle atomen in het universum zijn maar ongeveer 20 procent van alle massa in het universum. Het grootste gedeelte

Figuur 1: Links: Spiraalvormig sterrenstelsel Messier 81. Het plaatje is een combinatie van waarnemingen met de Subaru Telescoop in Hawaii en de Hubble ruimtetelescoop. De blauwe kleur toont het licht van jonge sterren en het rode licht toont het stof in het sterrenstelsel. *Credit: Ken Crawford (Rancho del Sol Observatory).* **Rechts:** Cluster van sterrenstelsels Abell 2218, waargenomen met de Hubble ruimtetelescoop. Het merendeel van de rossige objecten zijn sterrenstelsels die bij het cluster horen. Het plaatje laat ook heldere bogen zien rondom de centrale stelsels van het cluster. Deze bogen zijn sterrenstelsels achter het cluster die vervormd zijn door de sterke lenswerking door de zwaartekracht van het cluster. *Credit: NASA, Andrew Fruchter en de ERO Team [Sylvia Baggett (STScI), Richard Hook (ST-ECF), Zoltan Levay (STScI)] (STScI).*

van alle massa zit verborgen in een mysterieus bestandsdeel van het universum, dat *donkere materie* wordt genoemd. Hoewel donkere materie niet direct waar te nemen is, kunnen we wel diens aanwezigheid bepalen aan de hand van de zwaartekracht die het uitoefent op zichtbare componenten van het Universum.

De ontdekking van donkere materie dateert uit 1933, toen Zwitserse astronoom Fritz Zwicky aantoonde dat clusters van sterrenstelsels een enorme hoeveelheid onzichtbare materie moesten hebben om alle sterrenstelsels bij elkaar te houden. De sterrenstelsels in clusters hadden namelijk zo'n hoge snelheid dat ze zouden moeten ontsnappen als ze niet door iets tegengehouden zouden worden. In 1980 toonde een studie, geleid door Amerikaanse astronome Vera Rubin, aan dat de sterren in spiraalvormige stelsels ook sneller gaan dan verwacht. Ook hier is een grote hoeveelheid donkere materie nodig om de sterren door middel van zwaartekracht aan het sterrenstelsel te binden. Sinds deze eerste studies zijn er steeds meer aanwijzingen gekomen voor het bestaan van donkere materie. Hoewel er nog geen definitief bewijs is voor het bestaan van donkere materie, is het wel een hypothese die door de meeste astronomen wordt aangenomen.

De bewegingen van sterren en sterrenstelsels

De relatie tussen de bewegingen van sterren in sterrenstelsels en de massa van sterrenstelsels is in principe vrij simpel. Net als een raket een specifieke snelheid (de *ontsnappingssnelheid*) nodig heeft om de atmosfeer van de aarde te ontsnappen, heeft een ster een specifieke snelheid nodig om aan diens sterrenstelsels te ontsnappen. De ontsnappingssnelheid is dus de maximale snelheid die een ster kan hebben in een sterrenstelsel en is direct gerelateerd aan de massa van het totale systeem. Daarom zijn metingen van de maximale snelheden van sterren in sterrenstelsels goed te verbinden aan de massa van het sterrenstelsel.

Voor spiraalvormige sterrenstelsels kan de *omloopsnelheid* van sterren (de snelheid waarmee de ster ronddraait rond het centrum van het stelsel) gebruikt worden om een *rotatiecurve* te bepalen. Deze rotatiecurve geeft de omloopsnelheid van de ster als functie van de afstand tot het centrum van het stelsel. In een universum zonder donkere materie zouden verafgelegen sterren een lagere snelheid moeten hebben dan centraler gelegen sterren, die rond het keerpunt liggen in de rotatiecurve. Het is echter in 1980 aangetoond door Vera Rubin en haar mede-onderzoekers dat de omloopsnelheid van sterren constant blijft tot de rand van het sterrenstelsel. Deze waarneming kan verklaard worden door een wolk van donkere materie die zich verder uitstrekt dan het stelsel, wiens zwaartekracht de sterren binnen het stelsel houdt.

In elliptische stelsels, en ook in groepen en clusters van sterrenstelsels, is er geen coherente rotatie van sterren. In plaats daarvan bewegen de objecten zich willekeurige rond en is hun *snelheidsspreiding* (de typische snelheid van bijvoorbeeld stelsels in een cluster) direct verbonden aan de massa door middel van het *viriaaltheorema*. Deze methode werd in 1933 door Fritz Zwicky gebruikt om de hypothese van donkere materie op te stellen.

Lenswerking door zwaartekracht

Het effect van lenswerking door zwaartekracht is de vervorming van het beeld van verre objecten door tussengelegen materie. Deze vervorming is een consequentie van de intieme relatie tussen de geometrie van de ruimte-tijd en de massa die het bevat. Deze relatie is beschreven in de wereldberoemde Algemene Relativiteitstheorie die precies 100 jaar geleden is gepubliceerd door Albert Einstein. Volgens deze theorie buigt massa de ruimte, waardoor het licht zich in een gebogen, in plaats van rechte, lijn voortbeweegt. De verbuiging van het lichtpad zorgt er ook voor dat het licht van verafgelegen sterrenstelsels, vooral als die achter een andere sterrenstelsel of een cluster van sterrenstelsels ligt, anders wordt waargenomen dan dat het is uitgezonden. Het waarnemen van zulke verbuigingen geeft ons dus een directe indicatie van de verdeling van massa in het object dat dienst doet als lens.

Het rechter paneel van Figuur 1 laat enkele dunne bogen zijn rondom het grootste sterrenstelsel. Deze bogen zijn eigenlijk stelsels achter het cluster waarvan het licht zo is verbogen door de zwaartekracht van het cluster. Als het effect van zwaartekracht zo duidelijk is, wordt dit fenomeen *sterke lenswerking door zwaartekracht* genoemd. Dit fenomeen kan alleen worden waargenomen in de kern van cluster van sterrenstelsels of in de buurt van hele massieve sterrenstelsels. Verder verwijderd van het centrum van clusters is *zwakke lenswerking door zwaartekracht* waar te nemen als minieme vervormingen van alle stelsels achter het cluster. In dit geval kan de massa verdeling worden geschat door de gemiddelde vervorming te bepalen voor duizenden achtergrond stelsels.

Beide effecten van lenswerking door zwaartekracht geven ons de mogelijkheid om de hoeveelheid massa van het object dat als lens fungeert (een sterrenstelsel of cluster van sterrenstelsels) te onderzoeken. In het ideale geval moeten deze effecten gecombineerd worden om de totale massa van het object gedetailleerd te bepalen. Echter is dit in de praktijk moeilijk haalbaar doordat zeer gedetailleerde observaties van grote delen van de hemel hiervoor nodig zijn. Zulke combinaties zijn dus alleen gemaakt voor een paar clusters van sterrenstelsels.

De relatie tussen massa en licht in sterrenstelsels en clusters van sterrenstelsels

Een eerste stap in de studie naar de relatie tussen donkere en lichtgevende materie (of simpel gezegd tussen “massa” en “licht”) is het differentiëren tussen verschillende typen

Figuur 2: Massa en licht in het cluster van sterrenstelsels El Gordo, een zeer massief systeem van ten minste twee op elkaar botsende clusters. Het achtergrond plaatje is waargenomen met de Hubble ruimtetelescoop. De blauwe gloed toont de distributie van donkere materie, wat is bepaald met behulp van zwaartekrachtslenzen, terwijl de rode gloed de distributie van het gas toont, wat is bepaald met behulp van waarnemingen van Röntgen licht. De enorme afstand tot het cluster, ongeveer 7 miljard lichtjaar, maakt het moeilijk om sterrenstelsels in dit plaatje te zien, maar het centrale stelsel kan worden gevonden iets ten links van de piek in de rode gloed van de verdeling van gas. De kolossale botsing heeft de donkere en lichtgevende materie in El Gordo duidelijk gescheiden. *Credit: NASA, ESA, J. Jee (Univ. of California, Davis), J. Hughes (Rutgers Univ.), F. Menanteau (Rutgers Univ. & Univ. of Illinois, Urbana-Champaign), C. Sifón (Leiden Obs.), R. Mandelbaum (Carnegie Mellon Univ.), L. Barrientos (Univ. Católica de Chile), and K. Ng (Univ. of California, Davis).*

sterrenstelsels: *centrale* en *satelliet* stelsels. In het algemeen bevatten clusters een dominant stelsel in het centrum, dat helderder is dan alle andere stelsels, wat wij het centrale stelsel noemen. Alle andere stelsels die bij het cluster behoren, zullen we satelliet stelsels noemen. In Abell 2218 (in het rechterpaneel van Figuur 1) is het centrale stelsels gemakkelijk te identificeren in de buurt van de rechterbovenhoek van het figuur, omringd door bogen gemaakt door sterke lenswerking.

Deze scheiding is belangrijk omdat de verschillende typen stelsels anders worden beïnvloed door hun omgeving. De reden hierachter is dat satelliet stelsels in de cluster omgeving ronddraaien en naar het centrale stelsel toevallen, waardoor het centrale stelsel groeit door elke fusie met een satelliet stelsel. Zo'n scheiding is in de praktijk moeilijk te bewerkstelligen. Voor elk sterrenstelsel moet bepaald worden of het geïsoleerd is, en dus een centraal stelsel is, of dat het een deel is van een groep, en dus ook een satelliet stelsel kan zijn. Er zijn nauwkeurige afstandsmetingen van alle stelsels nodig om dit te bepalen en dus onderscheid te maken tussen satelliet en centrale stelsels. Centrale stelsels zijn in het algemeen de helderste sterrenstelsels in hun buurt en dus makkelijker te bepalen dan satelliet stelsels. Dit heeft ervoor gezorgd dat centrale stelsels veel meer zijn onderzocht voor de relatie tussen massa en licht. De conclusie van die studies is dat, zoals verwacht, stelsels die helderder zijn ook massiever zijn en dat de stelsels aan de uitersten van de massa schaal meer donkere materie bevatten, terwijl stelsels met een gemiddelde massa een lagere fractie donkere materie bevatten. Clusters van sterrenstelsels lijken een vaste fractie aan donkere materie (van 80-85%) te hebben, ongeacht hun massa. Desondanks is de relatie tussen massa en licht nog niet in detail onderzocht. Gezien de radicale transformatie van stelsels als zij satellieten worden (vergelijk her linker en rechter paneel in Figuur 1), kan eenzelfde transformatie verwacht worden van hun donkere materie. De tweede helft van dit proefschrift is gewijd aan de relatie tussen massa en licht in satelliet stelsels in groepen en clusters van sterrenstelsels.

Sterrenstelsels in clusters zijn verantwoordelijk voor ongeveer 20% van het lichtgevende materiaal in het cluster (wat ongeveer gelijk is aan 4% van de totale massa). De overgebleven 80% zit in heet gas, met temperaturen van 10 miljoen graden Kelvin of meer, dat verspreid is in het cluster. De hoge temperatuur van het gas zorgt ervoor dat het Röntgen licht uitzendt. Figuur 2 toont de verdeling van massa in het cluster van sterrenstelsels “El Gordo”, wat zich ongeveer 7 miljard lichtjaar van ons vandaan bevindt. In dit cluster kunnen wij verschillende regios met grote hoeveelheden massa onderscheiden; totale (donkere) massa in het blauw, wat zich ergens anders bevindt dan het gas in het rood. Het figuur laat zien dat het cluster uit twee zeer massieve botsende en fuserende sub-clusters bestaat. Aangezien het hete gas het gros van de lichtgevende massa bevat, is de afstand tussen de totale massa en de lichtgevende massa een directe indicatie van het bestaan van donkere materie. De eerste helft van dit proefschrift is gemoeid met de relatie tussen de totale massa en de lichtgevende massa in enkele clusters van sterrenstelsels.

Dit proefschrift

Dit proefschrift begint met het uitzoeken van de globale relatie tussen de hoeveelheid massa en licht in clusters van sterrenstelsels door waarnemingen van het cluster gas te combineren met schattingen van de totale massa van het cluster. Daarna, bestuderen wij deze relatie direct voor sterrenstelsels in groepen en clusters.

In **Hoofdstuk 2** bestuderen wij het cluster van sterrenstelsels PLCK G004.5-19.5 (zo genoemd vanwege diens coordinaten aan de hemel). Wij gebruiken de sterke lenswerking van het cluster om de totale massa ervan te meten en vinden dat het lager is dan verwacht aan de hand van metingen van de wolk van cluster gas. De reden voor deze discrepantie is niet duidelijk met behulp van de beschikbare data. Wij gebruiken ook waarneming van licht met radio golflengten om een voorzichtige hypothese op te stellen dat het cluster een botsing ondergaat met een kleiner systeem. Zo’n botsing kan de bovengenoemde discrepantie in massa verklaren, aangezien beide massa metingen aannemen dat het cluster geïsoleerd is. In de toekomst zullen wij nieuwe waarnemigen gebruiken om meer informatie in te winnen over deze cluster en onze hypothese te testen.

In **Hoofdstuk 3** passen wij een statistische aanpak toe en vergelijken we de massa’s van 44 cluster, die zijn bepaald met behulp van eigenschappen van het cluster gas en de snelheidsspreiding van de cluster stelsels. Een belangrijk deel van dit hoofdstuk is gewijd aan de bespreking van de sterke en zwakke punten van het gebruik van de snelheidsspreiding om massa’s van clusters te bepalen. We vinden dat massa’s, die bepaald zijn aan de hand van de snelheidsspreiding, gemiddeld genomen consistent zijn met massa’s, die bepaald zijn aan de hand van de eigenschappen van het cluster gas. Desondanks zijn er te veel factoren die deze resultaten beïnvloeden. Deze factoren beperken de toepassing van de snelheidsspreiding om nauwkeurige massametingen uit te voeren.

In **Hoofdstuk 4** verleggen wij onze aandacht naar satelliet stelsels in clusters en onderzoeken wij een ander aspect van de relatie tussen massa en licht: de oriëntatie van elk. Een cluster van sterrenstelsels oefent een sterke getijdenkracht uit op satelliet stelsels en in dit hoofdstuk zoeken wij uit of deze getijdenwerking ervoor zorgt dat satelliet stelsels een voorkeursrichting hebben richting het cluster centrum. Dit fenomeen is duidelijk zichtbaar in simulaties van donkere materie, maar directe voorspellingen voor het universum blijven uit. Wij onderzoeken ongeveer 14000 sterrenstelsels in 90 verschillende clusters en vinden geen voorkeursrichting van stelsels in clusters richting het centrum van het cluster noch richting elkaar.

Een belangrijk aspect van de resultaten in **Hoofdstuk 4** is de verbinding tussen het voorkeursrichting van sterrenstelsels en metingen van de lenswerking door zwaartekracht. Metingen van zwakke zwaartekrachtslenzen worden uitgevoerd door naar de coherente vervorming van stelsels achter het cluster te kijken, die daardoor ook uitgelijnd worden. Onze resultaten suggereren dat enige uitlijning binnen het cluster door getijdenkracht erg klein is en niet metingen van zwakke zwaartekrachtslenzen beïnvloed. Toekomstige experimenten zullen met meer precisie zwaartekrachtslenzen bekijken en het moet nog uitgezocht worden of onze conclusie ook voor die metingen stand houdt.

In **Hoofdstuk 5** meten wij het effect van zwakke lenswerking door de zwaartekracht van satelliet stelsels in groepen van sterrenstelsels. Deze studie is pas de tweede die dit fenomeen bekijkt. Wij vinden dat deze sterrenstelsels een totale massa hebben, die ongeveer 20 keer groter is dan de massa die in hun sterren zit . Deze fractie is vergelijkbaar met de waarde voor centrale sterrenstelsels. We hebben ook laten zien, als richtlijn voor de toekomst, hoe preciezere metingen van dit fenomeen gebruikt zouden kunnen worden om verschillende kosmologische modellen uit te testen.

Uiteindelijk breiden wij in **Hoofdstuk 6** het onderzoek in **Hoofdstuk 5** uit naar de massieve clusters van sterrenstelsels, die ook gebruikt zijn in **Hoofdstuk 4**. We gebruiken dezelfde techniek van zwakke lenswerking door zwaartekracht om de hoeveelheid donkere materie in deze clusters te bepalen. Wij maken gebruik van de betere kwaliteit van de data in vergelijking met **Hoofdstuk 5** om de resultaten te ijken aan theoretische voorspellingen. Onze resultaten zijn consistent met deze voorspellingen: alle cluster stelsels hebben ongeveer dezelfde fractie van donkere materie van ongeveer 95%. In de toekomst zullen wij vergelijkbare metingen in computer simulaties onderzoeken. Dit zal ons in staat stellen om onze resultaten te vergelijken met voorspellingen en de onderliggende natuurkundige principes uit te zoeken.

Resumen en Castellano

Somos sólo una clase avanzada de monos en un planeta menor en una estrella cualquiera. Pero podemos entender el Universo. Eso nos hace algo muy especial.

– Stephen Hawking

El Universo a gran escala

Al mirar al cielo en una noche oscura, podemos notar que las estrellas no están distribuidas aleatoriamente sino que, en su mayoría, se ubican en una delgada banda que cruza el cielo. Esta banda corresponde a la *Vía Láctea*, la galaxia espiral en la que se encuentra el Sol. Junto con el Sol, se estima que la Vía Láctea contiene unos 100 millones de estrellas. El panel izquierdo de la Figura 1 muestra una típica galaxia espiral, denominada Messier 81, a unos 12 millones de años luz de la Vía Láctea. Su color azul, característico de las galaxia espirales, corresponde al color de la luz que emiten las estrellas "jóvenes", formadas hace unos 100 millones de años o menos. Nuestra Galaxia es parte del llamado *Grupo Local*, que corresponde a un aglomerado de unas 50 galaxias dominado por la Vía Láctea y la galaxia Andrómeda, situada a unos 2,5 millones de años luz de la Vía Láctea.

La mayoría de las galaxias en el Universo viven en agrupaciones, y el Grupo Local es sólo un ejemplo de éstas. Como convención, llamamos *grupos* de galaxias a agrupaciones más bien pequeñas, de unas 50 galaxias o menos, y llamamos *cúmulos* a las agrupaciones más grandes. Estos cúmulos de galaxias son los objetos más grandes que se han formado hasta ahora en el Universo. Un cúmulo de galaxias puede llegar a tener más de mil galaxias visibles, y una masa equivalente a 10^{15} (es decir, 1.000.000.000.000.000) veces la masa del Sol. El panel derecho de la Figura 1 muestra el cúmulo de galaxias Abell 2218 (descubierto por el astrónomo estadounidense George Abell). En la imagen se distinguen decenas de galaxias elípticas de color anaranjado, la mayoría de ellas pertenecientes al cúmulo. Este enorme cúmulo se encuentra a unos 2 mil millones de años luz de nosotros.

Las galaxias en un cúmulo se ven anaranjadas y no azules como las galaxias espirales, que típicamente se encuentran más bien aisladas. La razón es que la gravedad del cúmulo, además del gas que lo permea y las otras cientos de galaxias en el cúmulo, se encargan de remover todo el gas que Sin poder formar nuevas estrellas, la galaxia toma el color rojizo de sus estrellas viejas.

Materia oscura

Las galaxias que podemos ver, incluyendo sus estrellas, gas y polvo, además de todos los átomos del Universo, sólo componen aproximadamente un 20 por ciento de la materia del Universo. La mayoría de la materia corresponde a un componente misterioso al que llamamos

Figura 1: Izquierda: galaxia espiral Messier 81. La imagen es una combinación de observaciones hechas por el telescopio Subaru en Hawaii y el Telescopio Espacial Hubble. El color azul muestra la luz emitida por estrellas jóvenes, mientras que el color rojo muestra polvo en la galaxia. *Crédito: Ken Crawford (Rancho del Sol Observatory).* **Derecha:** cúmulo de galaxias Abell 2218, observado con el Telescopio Espacial Hubble. La mayoría de los objetos de color anaranjado son galaxias perteneciantes al cúmulo. También se distinguen múltiples arcos alrededor de las galaxias principales; éstos corresponden a galaxias deformadas por el efecto de lente gravitacional fuerte. *Crédito: NASA, Andrew Fruchter y el Equipo ERO [Sylvia Baggett (STScI), Richard Hook (ST-ECF), Zoltan Levay (STScI)] (STScI).*

materia oscura. Aunque no podemos ver la materia oscura directamente, podemos inferir su presencia por su influencia en la materia que sí vemos, a través de la gravedad.

El descubrimiento de la materia oscura se remonta al año 1933, cuando el astrónomo búlgaro Fritz Zwicky mostró que los cúmulos de galaxias deben contener una gran cantidad de materia no visible que mantenga las galaxias unidas, porque éstas se mueven demasiado rápido y, de otra manera, escaparían del cúmulo. En 1980, un estudio liderado por la astrónomo estadounidense Vera Rubin mostró que las estrellas en galaxias espirales también se mueven más rápido de lo esperado, y que se requieren grandes cantidades de materia oscura para mantener a las estrellas dentro de la galaxia. A partir de entonces, la evidencia a favor de la materia oscura ha ido creciendo y, aunque aún no se ha confirmado su existencia, la mayoría de los astrónomos acepta la hipótesis de la existencia de la materia oscura.

Por lo tanto, para poder entender la formación y evolución de las galaxias, debemos estudiar también la materia oscura que las rodea. Existen dos técnicas para investigar directamente la materia oscura a través de su efecto gravitatorio: los movimientos de las estrellas y galaxias, y las lentes gravitacionales.

Los movimientos de las estrellas y galaxias

La relación entre los movimientos de las estrellas en galaxias y la masa de las últimas es en teoría relativamente sencilla. Tal como un cohete necesita alcanzar una cierta rapidez para escapar la atmósfera terrestre (conocida como la *velocidad de escape*), existe una máxima velocidad que las estrellas pueden tener antes de escapar de su galaxia huésped. Esta velocidad está directamente relacionada con la masa total del sistema. Por lo tanto, midiendo la velocidad máxima de las estrellas en una galaxia se obtiene una medida de la masa de dicha galaxia.

En el caso de galaxias espirales, podemos usar las *velocidades rotacionales* de las estrellas (es decir, la velocidad con la que orbitan la galaxia) para medir la *curva de rotación* de la galaxia: la velocidad rotacional de sus estrellas en función de la distancia al centro de la galaxia. Sin materia oscura, las estrellas más alejadas del centro deberían tener velocidades rotacionales menores que las estrellas en un radio "pivote". Sin embargo, como mostraron por primera vez Vera Rubin y sus colaboradores en 1980, la velocidad de rotación de las estrellas se mantiene constante hasta que termina la galaxia. Esto puede explicarse por la mayor extensión de la materia oscura, que logra mantener a las estrellas dentro de la galaxia.

En el caso de grupos y cúmulos de galaxias sus galaxias no rotan coherentemente, y lo mismo ocurre con las estrellas en una galaxia elíptica. En cambio, las galaxias en un cúmulo de galaxias siguen trayectorias aleatorias, y su *dispersión de velocidades*—es decir, la velocidad típica de las galaxias en un cúmulo—está directamente relacionada con la masa del cúmulo a través del *Teorema del Virial*. Éste fue el método utilizado por Fritz Zwicky en 1933, que lo llevó a proponer la existencia de materia oscura por primera vez.

Lentes gravitacionales

El efecto de lente gravitacional corresponde a la aparente deformación de objetos lejanos, debido a la materia que se encuentra entre estos objetos y nosotros. Este efecto es una consecuencia de la íntima conexión entre la geometría del espacio y su contenido de materia, descrita en la famosa Teoría General de Relatividad, publicada por Albert Einstein hace exactamente 100 años. De acuerdo a esta teoría, la materia curva el espacio, de manera que la luz viaja a través de caminos curvos en lugar de rectos, y por lo tanto las galaxias que están detrás de otra galaxia o cúmulo de galaxias se ven deformadas. Por lo tanto, al observar una lente gravitacional se puede inferir directamente la distribución de materia del objeto que la produce.

En el panel derecho de la Figura 1 se distingue un gran número de arcos alargados y muy finos que rodean las galaxias principales. Estos arcos corresponden a galaxias detrás del cúmulo que se ven deformadas por la lente gravitatoria producida por el cúmulo. Cuando el efecto es tan notorio, se conoce como lente gravitacional *fuerte*, y sólo se puede observar en la zona central de cúmulos de galaxias o galaxias muy masivas. Más lejos del centro, sólo se puede observar el efecto de lente gravitacional *débil*, en el que la luz de cada galaxia de fondo sufre sólo una pequeña distorsión. En este caso, la distribución de materia en el cúmulo es revelada por la deformación promedio de miles de galaxias de fondo.

Ambos efectos permiten medir directamente el contenido de materia de la galaxia o el cúmulo que produce la lente gravitacional. Idealmente, estos efectos se deben combinar para determinar de manera completa y detallada la distribuición total de materia en la galaxia o el cúmulo. En la práctica, esto requiere de observaciones muy detalladas en regiones grandes del cielo, y sólo ha sido posible hasta ahora en unos pocos cúmulos de galaxias.

La conexión entre masa y luz en galaxias y cúmulos de galaxias

Como primer paso para estudiar la conexión entre materia oscura y materia luminosa (o simplemente entre "masa" y "luz"), es importante distinguir dos clases de galaxias: las galaxias *centrales* y las galaxias *satélites*. En general, los cúmulos (o grupos) de galaxias contienen una galaxia dominante en el centro, más brillante que todas las demás galaxias, a la que se denomina galaxia central. Las demás galaxias se denominan satélites. En Abell 2218, mostrado en el panel derecho de la Figura 1, se identifica claramente la galaxia central dominante a la derecha de la imagen, rodeada por arcos producidos por lentes gravitacionales.

Figura 2: Masa y luz en el cúmulo de galaxias El Gordo, un gigantesco sistema compuesto por al menos dos cúmulos en proceso de colisión. La imagen de fondo fue tomada con el Telescopio Espacial Hubble. El tono azul muestra la distribución de materia oscura, determinada con el método de lentes gravitacionales débiles, mientras que el tono rojizo muestra la distribución de gas, determinada con observaciones de rayos X. Dada la enorme distancia a este cúmulo, de unos 7 mil millones de años luz, es dificil identificar las galaxias a simple vista, pero destaca la galaxia central justo a la izquierda de la zona con mayor concentración de gas. Debido a la enorme colisión, la materia oscura y la luz en El Gordo están claramente disociadas. *Crédito: NASA, ESA, J. Jee (Univ. of California, Davis), J. Hughes (Rutgers Univ.), F. Menanteau (Rutgers Univ. & Univ. of Illinois, Urbana-Champaign), C. Sifón (Leiden Obs.), R. Mandelbaum (Carnegie Mellon Univ.), L. Barrientos (Univ. Católica de Chile), y K. Ng (Univ. of California, Davis).*

Esta distinción es importante porque ambas clases de galaxias se ven afectadas de manera muy distinta por su entorno. La razón es que las galaxias satélites caen hacia la galaxia central, y la galaxia central crece a través de sucesivas fusiones con galaxias satélites. Para cada galaxia, se debe determinar si está aislada y es por lo tanto una galaxia central, o si es parte de un grupo, en cuyo caso podría ser también una galaxia satélite. En la práctica, resulta difícil diferenciar ambos tipos de galaxias; para esto se requieren mediciones precisas de las distancias de las galaxias. Las galaxias centrales son en general más fáciles de identificar, ya que son las galaxias más brillantes en su vecindad, y la mayoría de los estudios de la conexión entre masa y luz hasta ahora se han centrado en ellas. La conclusión principal es que las galaxias más luminosas son también más masivas (algo no del todo sorpresivo), y que las galaxias en los extremos (las menos y las más luminosas) tienden a tener una mayor fracción de materia oscura, mientras que las galaxias intermedias tienen una menor fracción. Sin embargo, la relación entre masa y luz en galaxias satélites prácticamente no ha sido explorada. Dada la transformación radical que sufren las galaxias al convertirse en satélites de otras galaxias (como se puede apreciar comparando los paneles izquierdo y derecho de la Figura 1), se puede esperar una transformación similar en su contenido de materia oscura. La segunda mitad de esta tesis está dedicada precisamente a estudiar la conexión entre masa y luz en galaxias satélites en grupos y cúmulos de galaxias.

Las galaxias en un cúmulo de galaxias componen sólo un 20% de la masa luminosa del cúmulo (es decir, aproximadamente un 4% de su masa total). El 80% restante es un gas caliente, a una temperatura de unos 10^7 grados o más, que permea el cúmulo. Dada su temperatura, este gas se puede observar en ondas de rayos X. La Figura 2 muestra la distribución de masa en el cúmulo de galaxias "El Gordo", a unos 7 mil millones de años de distancia. En este cúmulo se distinguen dos regiones con grandes cantidades de materia (principalmente materia oscura, en azul en la Figura), que no coincide con la distribución de gas (mostrada en rojo). Esta imagen muestra que este cúmulo está compuesto por dos subcúmulos muy masivos que están en proceso de colisión. Dado que la mayoría de la materia luminosa corresponde precisamente al halo de gas, esta separación entre materia luminosa y masa total provee evidencia directa de la existencia de materia oscura. En la primera mitad de esta tesis estudiamos la relación entre la masa total de un número de cúmulos de galaxias y su halo de gas caliente.

Esta tesis

Esta tesis comienza explorando la conexión global entre la cantidad de masa y luz en cúmulos de galaxias combinando observaciones del gas de los cúmulos con determinaciones de su masa total, para luego estudiar más directamente esta conexión en las galaxias pertenecientes a estos cúmulos.

En el **Capítulo 2** estudiamos el cúmulo de galaxias PLCK G004.5−19.5 (llamado así por sus coordenadas en el cielo). Usamos el efecto de lente gravitacional fuerte para medir la cantidad de masa total en el cúmulo, y encontramos que es menor que la esperada a partir de las propiedades del halo de gas. La razón de esta diferencia no queda clara con los datos disponibles. Además, usando datos en ondas de radio pudimos concluir tentativamente que el cúmulo está en proceso de colisión con un sistema más pequeño. Esta colisión podría explicar la diferencia en la masa inferida usando el gas del cúmulo y la masa medida con lentes gravitacionales, ya que estas determinaciones de la masa asumen que el cúmulo está aislado. En el futuro usaremos nuevas observaciones para obtener mayor información sobre este cúmulo.

En el **Capítulo 3** tomamos una perspectiva más estadistica para comparar la cantidad de masa estimada usando las propiedades del gas, y la inferida a través de la dispersión de las velocidades de las galaxias en 44 cúmulos de galaxias. Parte importante de este capítulo es una discusión detallada de las fortalezas y debilidades inherentes al uso de las velocidades de galaxias para determinar la masa de los cúmulos. Encontramos que la masas inferidas usando las velocidades de las galaxias son, en promedio, consistentes con aquéllas inferidas a partir del halo de gas. Sin embargo, existen demasiados factores que afectan estos resultados. Estos factores limitan la posibilidad de usar las velocidades de las galaxias para medir masas de cúmulos de galaxias con precisión.

En el **Capítulo 4** tornamos la atención hacia las galaxias que componen los cúmulos, y exploramos otro aspecto de la conexión entre masa y luz: la orientación de ambos componentes. Un cúmulo ejerce un fuerte efecto de marea sobre sus galaxias satélites, y en este capítulo exploramos si es que esta fuerza de marea es capaz de alinear estas galaxias hacia el centro del cúmulo. Este efecto se observa claramente en simulaciones de materia oscura, pero hasta hace poco no había observaciones directas. Usando unas 14.000 galaxias en 100 cúmulos distintos, no observamos ninguna señal de alineamiento de las galaxias hacia el centro del cúmulo, ni con las demás galaxias.

Un aspecto importante de los resultados del **Capítulo 4** es la conexión entre la alineación de las galaxias y las mediciones de lentes gravitacionales, ya que este efecto se observa a través de la alineación de galaxias detrás de las lentes. Nuestras mediciones sugieren que cualquier alineamiento de las galaxias en cúmulos debe ser muy débil, y no afecta de manera significativa las mediciones de lentes gravitacionales con experimentos actuales. Habrá que obtener resultados aún más precisos para sacar conclusiones sobre proyectos futuros que medirán lentes gravitacionales con mayor precisión.

En el **Capítulo 5** medimos el efecto de lentes gravitacionales débiles que producen las galaxias satélites en grupos de galaxias. Ésta es sólo la segunda vez que se logra tal medición. Encontramos que estas galaxias tienen una masa total aproximadamente 20 veces mayor que su masa estelar, similar a las masas de galaxias centrales. También mostramos cómo se podrían utilizar mediciones más precisas de este efecto incluso para examinar modelos cosmológicos.

Finalmente, en el **Capítulo 6** extendimos el estudio del **Capítulo 5** a cúmulos más masivos—aquéllos usados en el **Capítulo 4**. Usamos la misma técnica de lentes gravitacionales débiles para medir la cantidad de materia oscura en galaxias en estos cúmulos. Aprovechando la mejor calidad de los datos usados en este capítulo (comparado con los datos del **Capítulo 5**), comparamos nuestros resultados con predicciones teóricas. Por el momento, nuestros resultados son consistentes con las predicciones: en promedio, todas las galaxias en cúmulos masivos tienen más o menos la misma fracción de materia oscura: aproximadamente un 95%. Para investigar los mecanismos físicos que dan origen a estos resultados, en el futuro exploraremos mediciones similares en simulaciones computacionales, que podremos contrastar con nuestras observaciones.

Curriculum Vitae

I was born on 11 May, 1986, in Punta Arenas, Chile, in one of the southernmost cities in the world. At the age of 2 my family and I moved some 1800 km north (still in the south of Chile) to Concepción, where we lived for two years. Finally, we settled in Santiago in 1990. After attending 5 different schools through primary and secondary education, I completed high school in 2004 in Colegio Pumahue Peñalolén.

I am not sure when I found out that I wanted to study astronomy, but it must have been two or three years before I finished high school. I enrolled to study astronomy in Universidad Católica de Chile, starting in March 2005. During the summer vacations of 2006/2007 and 2007/2008 I went to Sun Valley, ID, and Lake Tahoe, CA, in the US, respectively, to work in ski resorts for the entire seasons, first as a lift operator and then as a ski instructor. In the second half of 2009 I worked on my BSc thesis in the Gemini South Observatory in La Serena, Chile, under the supervision of Dr. Percy Gómez, studying the dynamics of the merging galaxy cluster Abell 1882, and I obtained my BSc in January 2010.

I started my MSc in astrophysics in Católica immediately thereafter, in March 2010. My MSc thesis was on measurements of dynamical masses of galaxy clusters selected with the Sunyaev-Zel'dovich effect by the Atacama Cosmology Telescope (ACT) under the supervision of Prof. Luis Felipe Barrientos. I have been an active ACT member since. I obtained my MSc in January 2012. I then worked on the development of a data reduction pipeline for the FLAMINGOS-2 instrument, which was under commissioning in Gemini South, until in September 2012 I joined Leiden University as a PhD student under the supervision of Dr. Henk Hoekstra.

During my PhD I worked on a variety of aspects on the connection between dark and luminous matter in galaxy clusters using optical imaging and spectroscopy, as part of both the ACT and Kilo-Degree Survey (KiDS) collaborations, and in independent work with Dr. Hoekstra. I have presented my work in international conferences in Huntsville, AL (USA), Tallinn (Estonia), Prato (Leiden), London (UK), Athens (Greece) and Leiden (Netherlands), and in universities in Canada, Chile and the US.

After defending my PhD thesis in September 2016, I will take a postdoctoral research position with David Spergel in Princeton University in NJ, US, to work on joint science with ACT and the HyperSuprime Cam survey.

Acknowledgements

Ha llegado el momento de la despedida, les quiero agradecer muchísimo … realmente estoy muy emocionado. Los quiero mucho, se los digo de verdad, lo siento no sólo como persona sino como ser humano. Lo que siento se resume en una palabra: mil gracias.

– Manuel Darío (Les Luthiers, *Unen Canto con Humor*, 1999)

The path to this PhD has been a long one, surely dating back much further than September 2012, but I'm not sure I can pinpoint when it all started. I am sure however that many people have taken part in it along the way, and some of them not less for being almost 12,000 km away from where these last four years have taken place.

Leiden is a wonderful, most beautiful place, and I could hardly have chosen a better location to spend these four years and carry out my PhD research. To add to this, the Sterrewacht is a lively, friendly place where I felt at all times welcome. There is a community atmosphere which always made me feel I could rely on anyone at anytime, for any matter at hand.

To our working group: Andrej, Fabian, Jelte, Koen, Maciej, Marco, Margot, Martin, Remco and Ricardo, thank you for making our group meetings both useful and enjoyable. I'm glad I got to work with some of you, and hope we'll do some more work together in the future. Marcello and Massimo, thank you for sharing your experience and wisdom with me. Most of all, thank you Henk for being a true advisor and not just a supervisor. I have learnt tremendously from my interactions with all of you, both within and outside the scientific context. I enjoyed every one of our group meetings (however hard to believe that may be), and the times we've shared outside of them even more.

I met some amazing people in the Sterrewacht, without whom these four years could not have been nearly as enjoyable. I'm happy I got to know you all through so many breaks, lunches, evenings and weekends. Adam, Allison, Alex North, Alex South, Andra, Berenice and Jesús, Clément, David, Emanuele, Gabi, Henriette, Irene, Jeroen, Leah, María, Marissa, Matteo, Mattia and Anna, Mieke, Monica, Nicola, Renske and Thanja. Maryam, Ali, we had a great time, and some great food, together. We're glad you got to love manjar as much as we do! Thank you for that wonderful weekend in Zurich. Tiffany, thank you for your advice throughout our three years as office mates, I really enjoyed our conversations, deep and shallow. Elena, Jarle and Huub, thank you for your advice, your help and your friendliness, academic and otherwise.

I am very fortunate that such a welcoming and friendly atmosphere extends to people I have interacted with beyond the Sterrewacht itself. It is a great honour and pleasure to be part of the KiDS collaboration. The weak lensing group is just a wonderful team to work with and get advice from. Special thanks to Benjamin, Catherine, Edo, Hendrik, Peter and

Tom for your interest and support. Our many meetings throughout the years have been much fun (and much work!), and I look forward to working more with all of you in the future.

It is also a great honour and pleasure to be part of the ACT collaboration. I start by thanking Felipe, my MSc advisor in Chile, for believing in me and for introducing me and making me part of such a great team, both in terms of the science carried out and the people involved. Arthur, Lyman, Matt, Matthew, Nick and Toby, thank you for your help and encouragement whenever it was needed, whether requested or not. Jack, Felipe, thank you for making work so much fun when I was just starting my career. From observing runs back several years ago to visits and remote discussions, thank you for helping me develop and grow both personally and scientifically, and for your enthusiasm on all matters. I look forward to seeing more of you in the coming years.

I have also made good friends in the Chilean community (broadly defined) in Leiden. You have been a great support throughout these four years. Andrea, Cami, Francisco, Håvar, Javi, Nico, Pablo, Seba, Sole and Vicente. Heather, thank you for taking care of me when I arrived, I really don't know what I would have done without you. Mariana, Mariano, we have found great friends and the most enjoyable company in you. You managed to make the best of the barbeques allowed by the variety of Dutch meat. We will miss you all. I hope our paths will cross again sometime in the near future

A mis amigos de toda la vida, que sin importar la distancia, siguen estando ahí siempre, viviendo mis logros conmigo, así como yo los de ustedes. Arruga, Chasca, Chino, Claudio, Mari, Nico, Pablito, Pame, Tatán, Topo, Watón, gracias a todos. Sé que la distancia no es ningún obstáculo para contar con ustedes para lo que sea, cuando sea, y ustedes saben que es recíproco. Algún día podremos por fin repetir esas tardes de puro tenis, quién sabe dónde.

A mi familia. A mis padres, gracias por creer en mí y apoyarme en este camino, y en todos los demás desde el comienzo, sin importar las condiciones. Está de más decirles que no habría podido llegar acá sin su cariño y apoyo. También agradezco a mi hermano, Matías, y a mi hermana, Bárbara, por su apoyo continuo e incondicional. Estoy muy feliz de que todos hayan podido venir a vernos. Sus visitas y los tantos viajes asociados viven en nuestra memoria como momentos maravillosos. A mis queridos abuelos y a mi querida Agüe, por su cariño y alegría, por sus enseñanzas y por los buenos momentos juntos. Gracias también Rosita por acompañarnos en este largo camino.

Finalmente y lo más importante, gracias Dani y Martina. Parte de esta sección está escrita en plural y no singular, porque nada de esto tendría sentido sin ustedes a mi lado. Dani, me siento tremendamente afortunado de tenerte conmigo y de tener a la Martina con nosotros. Gracias por tu amor, tus sonrisas, por acompañarme, soportarme, apoyarme, por darme ánimo y aterrizarme. Siempre sabes cuál corresponde. Martina, tu simpatía e ingenuidad llenan de alegría nuestra casa, eres lo más lindo que he visto en la vida. Las amo desde lo más profundo de mí.

Cristóbal Sifón Andalaft
Leiden, September 2016